HAL open science

Structured differential equations and multiscale approaches for human cell population dynamics

Samuel Bernard

▶ To cite this version:

Samuel Bernard. Structured differential equations and multiscale approaches for human cell population dynamics. Dynamical Systems [math.DS]. Université Claude Bernard Lyon 1, 2017. tel-01572434v1

HAL Id: tel-01572434
https://hal.science/tel-01572434v1

Submitted on 7 Aug 2017 (v1), last revised 24 Aug 2017 (v2)

HAL is a multi-disciplinary open access archive for the deposit and dissemination of scientific research documents, whether they are published or not. The documents may come from teaching and research institutions in France or abroad, or from public or private research centers.

L'archive ouverte pluridisciplinaire **HAL**, est destinée au dépôt et à la diffusion de documents scientifiques de niveau recherche, publiés ou non, émanant des établissements d'enseignement et de recherche français ou étrangers, des laboratoires publics ou privés.

Distributed under a Creative Commons Attribution - NonCommercial 4.0 International License

Institut Camille Jordan
UMR 5208 du CNRS

Structured differential equations and multiscale approaches for human cell population dynamics

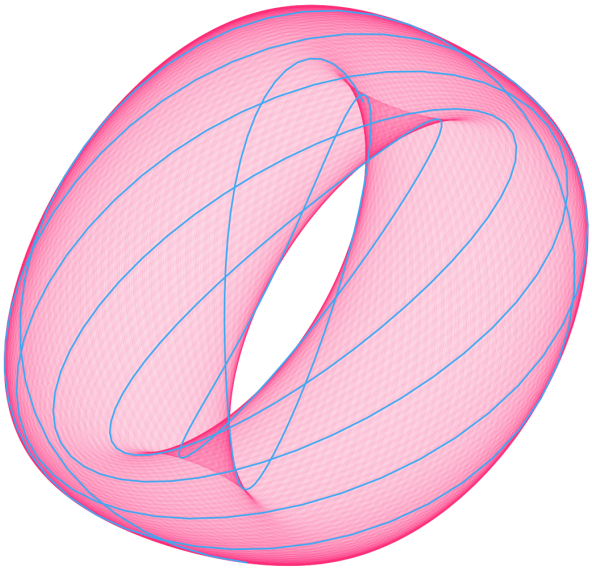

Samuel Bernard

Habilitation à diriger des recherches

Université Claude Bernard Lyon 1

Université Claude Bernard Lyon 1
École doctorale **InfoMath**, ED 512
Spécialité : **Mathématiques**
N. d'ordre 034–2017

Structured differential equations and multiscale approaches for human cell population dynamics

Habilitation à diriger des recherches

Soutenue publiquement le 12 juin 2017 par

Samuel Bernard

devant le Jury composé de:

Mme. Angélique Stéphanou	CR CNRS, Grenoble	Examinatrice
M. Franck Delaunay	PU, Nice	Examinateur
Mme Fahima Nekka	PR, Montreal	Rapporteur
M. Laurent Pujo-Menjouet	MCF, HDR, Lyon 1	Examinateur
M. David Rand	PR, Warwick	Rapporteur
M. Benoît Perthame	PU, Paris 6	Rapporteur

Contents

1 Remerciements **1**

2 Curriculum Vitae **5**

3 Introduction **15**

4 Delay equations **19**
4.1 Differential equations with distributed delays 20
4.2 G$\langle n \rangle$[dM] 22
4.3 Stability results 23
4.4 Positive feedback loops and robustness of oscillations 25

5 Circadian clocks **27**
5.1 The circadian clock 28
5.2 Damped versus sustained oscillators 28
5.3 Synchronization of biological oscillators 30
5.4 Synchronization of circadian oscillators 32

6 Cell proliferation **35**
6.1 Birth-and-death models and 14C dating 36
6.2 Renewal equations 37
6.3 14C model and data 39
6.4 Nonlinear fitting strategies 39
6.5 Cardiomyocyte renewal in humans 40
6.6 Tumor-immune interaction 41

7 Integrative approaches **43**
7.1 Multiscale modeling in biology 44
7.2 The cell division cycle and the circadian clock 44
7.3 Circadian clock and liver renewal 45
7.4 Modulation of cell population growth under circadian clock control 45
7.5 Simuscale 46

8 Outlook **49**

9 Selected papers **53**
9.1 Bernard S, Crauste F (2015) Optimal linear stability condition for scalar differential equations with distributed delay. Discrete Contin Dynam Systems Ser B 20:1855–1876 55
9.2 Bergmann O, Bhardwaj R, Bernard S, Zdunek S, Barnabé-Heider F, Walsh S, Zupicich J, Alkass K, Buchholz B, Druid H, Jovinge S, Frisén J (2009) Evidence for cardiomyocyte renewal in humans. Science 324:98–102 79

9.3 Bernard S, Gonze D, Čajavec B, Herzel H, Kramer A (2007) Synchronization-induced rhythmicity of circadian oscillators in the suprachiasmatic nucleus. PLOS Comput Biol 3:e68 85
9.4 Besse A, Clapp G, Bernard S, Nicolini F, Levy D, Lepoutre T (2017) Stability analysis of a model of interaction between the immune system and cancer cells in chronic myelogenous leukemia. Bull Math Biol *in press* 99
9.5 Chauhan A, Lorenzen S, Herzel H, Bernard S (2011) Regulation of mammalian cell cycle progression in the regenerating liver. J Theor Biol 283:103–112 129
9.6 El Cheikh R, Bernard S, El Khatib N (2014) Modeling circadian clock-cell cycle interaction effects on cell population growth rates. J Theor Biol 363:318–331 141

Chapter 1

Remerciements

There are so many people I would like to thank for making this thesis possible. I am very grateful to all of you. My first thanks go to the HDR thesis defence committee. To my reviewers, David Rand, Benoît Perthame and Fahima Nekka, thank you for taking the time to read the thesis carefully and review it in depth. I would like to thank the examiners, Franck Delaunay, Angélique Stéphanou and Laurent Pujo-Menjouet for accepting to be part of the defence committee. Having your names on the thesis cover means a great deal to me.

L'Institut Camille Jordan et le CNRS m'ont soutenu depuis mon arrivée à Lyon en 2007, je les en remercie. Je remercie aussi la direction de l'ICJ, Frank Wagner et Elisabeth Mironescu par le passé et maintenant Sylvie Benzoni, ainsi que Simon Masnou, chef de l'équipe MMCS à l'ICJ, pour leur soutien aux biomathématiques; le support informatique à l'ICJ, Laurent Azema et Thierry Dumont; et Régis Goiffon pour son enthousiasme à partager les maths à l'Université Ouverte. Je voudrais remercier le centre Inria Grenoble et sa direction pour l'accueil dans l'équipe Dracula et son soutien pour le développement de Simuscale, et David Parsons qui s'est investi personnellement dans ce projet. Un grand merci à l'IXXI pour son soutien financier et à son ex-directeur Guillaume Beslon, pour avoir promu l'interdisciplinarité en Rhône-Alpes et aidé à créer une atmosphère propice à l'épanouissement des biomathématiques. Un grand merci à Mostafa Adimy, directeur de l'équipe Inria Dracula, qui ne compte pas son temps pour que le nôtre puisse être consacré à la science.

I have a special thought for my collaborators past and present: Kirsty Spalding, Jonas Frisén, the 14C data is the best application of renewal equations one could think of; Peter Arner, for the precious data in the freezer; Mikael Rydén, Olaf Bergmann, Hagen Huttner, Aurélie Ernst, such fruitful collaborations; Henrik Druid, Brita Zilg, Kanar Alkass, I can't watch CSI with the same eye now; Jeff Mold, Pedro Réu, for the one last question; et Fanie Barnabé-Heider, pour l'accent du Québec à Stockholm. Didier Gonze, Hanspeter Herzel, Achim Kramer, Francis Lévi, Pål Westermark, modelling the circadian clock raises so much interesting questions; Vitaly Volpert, Nader El Khatib et Angélique vous avez motivé mon intérêt pour la modélisation multiéchelles/hybride.

La vie de labo ne serait pas la même sans les membres de l'équipe Dracula. Fabien Crauste, Thomas Lepoutre, Laurent, Céline Vial, Olivier Gandrillon, Léon Tine, vous êtes bien plus que des collègues. Fabien, merci d'y avoir cru quand j'ai eu des doutes. Merci aussi pour ton écoute, tes conseils et ton aide dans les bons moments comme dans les très mauvais, je n'oublierai pas les virées à Ikea, par exemple. Laurent, je n'oublierai pas le canot sur le lac Pilon, les papiers écrits sur la plage à Vancouver, et ton accueil à mon arrivée en France. Il y a aussi toutes celles et ceux que je croise à la salle café. C'est rassurant de voir qu'on peut toujours y trouver quelqu'un en train de se faire couler un espresso ou une infusion.

À mes doctorants et les étudiants avec qui j'ai travaillé, ici et ailleurs: Stephan Fischer, Charles Rocabert, Catherine Foley, Paulina Kurbatova, Pauline Mazzocco, ainsi que tous les stagiaires, c'est toujours un plaisir de travailler avec vous. Embla Steiner, Sofia Zdunek, thank you for the stimulating discussions. Apollos Besse, Raouf El Cheikh, Anuradha Chauhan, certains de ces chapitres n'auraient pas été possibles sans votre travail et votre persévérance. Merci de m'avoir fait confiance.

To my thesis directors and postdoc supervisors Michael Mackey, Jacques Bélair, Hanspeter, and Daphne Manoussaki, with whom it all got started. I learned a lot with you, thank you.

Un grand merci à toute l'équipe administrative de l'ICJ, et en particulier à Maria Konieczny, qui a été de toutes mes aventures administratives avec une bonne humeur indéfectible. Merci infiniement à Caroline Lothe pour sa grande patience à mon égard, je sais que je peux m'améliorer. Merci à Hédi Soula et Hubert Charles pour les opportunités d'enseignement en 3BIM INSA, et à Anne-Laure Fougères pour avoir pris en charge la direction du Master Maths en Action à l'UCBL.

À ma famille, Roseline, Sophie, Luc, Paul, Mélissa, François, Roxane, Marjolaine et Pierre, qui sont

toujours là même de loin. A Dora, Ella et Alex pour leur source inépuisable de joie et d'énergie, et pour les "tangled monster plots". Et enfin à Carole, sans qui cette thèse ne serait qu'un projet flou.

Chapter 2

Curriculum Vitae

Samuel Bernard

Institut Camille Jordan (CNRS UMR5208)
Bât. Jean Braconnier, 43 blvd du 11 novembre 1918,
F-69622 Villeurbanne-Cedex, France
Courriel: bernard@math.univ-lyon1.fr
Web: math.univ-lyon1.fr/~bernard/
Twitter: @samu6ernard

Né le 13/06/1976, Canada
Langues parlées: français et anglais courants, allemand intermédiaire

Expérience professionnelle

CNRS, France

Depuis octobre 2011 — Membre de l'Equipe-Projet Dracula, Inria Grenoble

Depuis octobre 2007 — Chargé de Recherche 1re classe
CNRS UMR5208 Institut Camille Jordan, Université de Lyon

Marie Curie Research Training Network, Grèce

2006 – 2007 — Chercheur Expérimenté (post-doctoral) avec Daphne Manoussaki
Marie Curie Research Training Network on Mathematical Methods and Computer Simulation of Tumour Growth and Therapy
Institute of Applied and Computational Mathematics Foundation for Research and Technology—Hellas, P.O. Box 1527, 71110 Héraklion, Crète, Grèce

Institute for Theoretical Biology, Germany

2004 – 2006, 2007 — Assistant de Recherche (post-doctoral) dans le groupe de Hanspeter Herzel
Institute for Theoretical Biology, Université Humboldt, Invalindenstr. 43, 10115 Berlin, Allemagne

Formation académique

Université de Montréal, Canada

2000 – 2003 — Ph.D. en Mathématiques Appliquées avec Jacques Bélair (Université de Montréal) et Michael C. Mackey (Université McGill)
Équations différentielles à retard et leur application en hématopoïèse, avec étude du cas de la neutropénie cyclique (2003).

Domaines d'expertise

Mathématiques — Mathématiques appliquées, dynamique non-linéaire, equations différentielles à retard, processus stochastiques, analyse numérique, modélisation de systèmes physiologiques, pharmacodynamique/pharmacocinétique, modélisation multiéchelles

Biology théorique — Horloge circadienne, désordres hématopoïétiques, cycle cellulaire et croissance tumorale, regulation transcriptionnelle, analyse de données ^{14}C pour le renouvellement de tissus à

	faible potential régénératifs
Programmation	Matlab, R, C, C++

Prix & subventions

2013 - aujourd'hui	Foreign Adjunct Professor, Institut Karolinska, Stockholm, Suède
2014 - aujourd'hui	Coordonnateur pour le projet Inria de développement logiciel software development project (Inria ADT) Simuscale: une plateforme de simulation multiéchelles pour la dynamique de populations cellulaires. https://gforge.inria.fr/projects/simuscale/
2013-2015	Coordonnateur Partenariat Hubert Curien, Projet Cèdre, Campus France, 30097ZA (18,000 €, 2 years)
2004	Prix de la meilleure thèse en sciences pures et appliquées de l'Université de Montréal remis par la Faculté des Études Supérieures

Enseignement

Dynamique des populations cellulaires (Master 2) Université Lyon 1, 15h par an.
http://math.univ-lyon1.fr/homes-www/bernard/popdyn.html

Algèbre linéaire et analyse matricielle (3e année de licence) INSA Lyon, 30h par an.
http://math.univ-lyon1.fr/homes-www/bernard/numalg.html

EDO pour les neurosciences (3e année de licence) INSA Lyon, 10h par an.
http://math.univ-lyon1.fr/~bernard/edoneuro.html

Direction de thèse

2014-2017	Directeur, **Apollos Besse**, Université Lyon 1 *Modélisation mathématique de la leucémie myéloïde chronique et de ses traitements*
2011-2015	Co-directeur, **Raouf El Cheik**, Université Lyon 1 *Modélisation multiéchelles de la regulation du cycle cellulaire par l'horloge circadienne: application à la chronothérapie*
2011-2015	Superviseur scientifique, ***Sofia Zdunek***, Insitut Karolinska, Stockholm *Analyse du renouvellement de cellules cardiaque chez l'humain par datation radiocarbone et modélisation mathématique*

2010-2013	Co-directeur, **Stephan Fischer**, INSA Lyon *Modélisation de l'évolution de la taille des génomes et de leur densité en gènes par mutations locales et grands réarrangements chromosomiques*
2006-2010	Superviseur scientifique, ***Anuradha Chauhan***, Université Humboldt, Berlin *Modèles du cycle cellulaire lors de la régénération d'hépatocytes chez les mammifères*

Publications

Chapitres de livre & revues

Bernard, S, How to Build a Multiscale Model in Biology (2013) *Acta biotheoretica*, 61(3), 291-303.

G Bordyugov, PO Westermark, A Korencivc, **S Bernard**, H Herzel, Mathematical modeling in chronobiology, in *Circadian clocks: Handbook of Experimental Pharmacology*, Volume 217, pp. 335-357, Springer, 2013.

S Bernard, Modélisation multi-échelles en biologie, in *Le vivant discret et continu*, Éditions Matériologiques (Ed.) pp. 65-89, 2013.

S Bernar, Nés pour sentir ? (2012) *Med Sci* (Paris) 28:937-939.

R El Cheikh, T Lepoutre, **S Bernard**, Modeling biological rhythms in cell populations (2012) *Math Model Nat Phenom*, 7(06), 107-125.

M Adimy, **S Bernard**, J Clairambault, F Crauste, S Génieys, L Pujo-Menjouet, Modélisation de la dynamique de l'hématopoïèse normale et pathologique (2008) *Hematologie* 14:339-350.

Articles dans des journaux internationaux (à comité de lecture)

KL Spalding, **S Bernard**, E Näslund, M Salehpour, G Possnert, L Appelsved, K-Y Fu, K Alkass, H Druid, A Thorell, M Rydén and P Arner, Impact of fat mass and distribution on lipid turnover in human adipose tissue (2017) *Nat Comm* 8:15253

R El Cheikh, **S Bernard** and N El Khatib, A multiscale modelling approach for the regulation of the cell cycle by the circadian clock (2017) *J Theor Biol*, DOI:10.1016/j.jtbi.2017.05.021

A Besse, GD Clapp, **S Bernard**, FE Nicolini, D Levy, T Lepoutre, Stability analysis of a model of interaction between the immune system and cancer cells in chronic myelogenous leukemia (2017) *Bull Math Biol*, doi:10.1007/s11538-017-0272-7

A Besse, T Lepoutre and **S Bernard**, Long-term treatment effects in chronic myeloid leukemia (2017) *J Math Biol*, DOI:10.1007/s00285-017-1098-5

S Bernard, Moving the Boundaries of Granulopoiesis Modelling (2016) *Bull Math Biol* 78:2358-2363.

R Yvinec, **S Bernard**, E Hingant and L Pujo-Menjouet, First passage times in homogeneous nucleation: Dependence on the total number of particles (2016) *J Chem Phys* 144:034106

GD Clapp, T Lepoutre, R El Cheikh, **S Bernard**, J Ruby, H Labussière-Wallet, FE Nicolini and D Levy, Implication of the autologous immune system in BCR-ABL transcript variations in chronic myelogenous leukemia patients

treated with imatinib, (2015) *Cancer Res* 75:4053

M Rydén, M Uzunel, JL Hård, E Borgström, JE Mold, E Arner, N Mejhert, DP Andersson, Y Widlund, M Hassan, CV Jones, KL Spalding, B-M Svahn, A Ahmadian, J Frisén, **S Bernard**, J Mattsson and P Arner, Transplanted Bone Marrow-Derived Cells Contribute to Human Adipogenesis (2015) *Cell Metabolism* 22:408-417

B Zilg, **S Bernard**, K Alkass, S Berg and H Druid, A new model for the estimation of time of death from vitreous potassium levels corrected for age and temperature (2015) *Forens Sci Int* 254:158-166

O Bergmann, S Zdunek, A Felker, M Salehpour, K Alkass, **S Bernard**, SL Sjostrom, M Szewczykowska, T Jackowska, C dos Remedios, T Malm, M Andrä, R Jashari, JR Nyengaard, G Possnert, S Jovinge, H Druid and J Frisén, Dynamics of cell generation and turnover in the human heart (2015) *Cell* 161:1566-1575

S Bernard and F Crauste, Optimal linear stability condition for scalar differential equations with distributed delay (2015) *Discr Contin Dyn Sys B* 20:1855-1876

R El Cheikh, **S Bernard** and N El Khatib, Modeling circadian clock-cell cycle interaction effects on cell population growth rates (2014) *J Theor Biol* 363:318-331

S Fischer, **S Bernard**, G Beslon and C Knibbe, A model for genome size evolution (2014) *Bull Math Biol* 76(9):2249-2291

Prokopiou SA, Barbarroux L, **Bernard S**, Mafille J, Leverrier Y, Arpin C, Marvel J, Gandrillon O and Crauste F, Multiscale Modeling of the early CD8 T-cell immune response in lymph nodes: an integrative study (2014) *Computation* 2:159-181

MSY Yeung, S Zdunek, O Bergmann, **S Bernard**, M Salehpour, K Alkass, S Perl, J Tisdale, G Possnert, L Brundin, H Druid, J Frisén, Dynamics of Oligodendrocyte Generation and Myelination in the Human Brain (2014) *Cell* 159:766-774

Ernst A, Alkass K, **Bernard S**, Salehpour M, Perl S, Tisdale J, Possnert G, Druid H, Frisén J, Neurogenesis in the Striatum of the Adult Human Brain (2014) *Cell* 156(5), 1072-1083

HB Huttner, O Bergmann, M Salehpour, A Rácz, J Tatarishvili, E Lindgren, T Csonka, L Csiba, T Hortobágyi, G Méhes, E Englund, BW Solnestam, S Zdunek, C Scharenberg, L Ström, P Ståhl, B Sigurgeirsson, A Dahl, S Schwab, G Possnert, **S Bernard**, Z Kokaia, O Lindvall, J Lundeberg and J Frisén, The age and genomic integrity of neurons after cortical stroke in humans (2014) *Nat Neurosci* 17:801-803

Alkass K, Saitoh H, Buchholz BA, **Bernard S**, Holmlund G, Senn DR, Spalding KL, Druid H, Analysis of radiocarbon, stable isotopes and DNA in teeth to facilitate identification of unknown decedents (2013) *PLoS One* 8:e69597

Rydén M, Andersson DP, **Bernard S**, Spalding K, Arner P, Adipocyte triglyceride turnover and lipolysis in lean and overweight subjects (2013) *J Lipid Res* 54:2909-13.

KL Spalding, O Bergmann, K Alkass, **S Bernard**, M Salehpour, HB Huttner, E Boström, I Westerlund, C Vial, BA Buchholz, G Possnert, DC Mash, H Druid, J Frisén, Dynamics of Hippocampal Neurogenesis in Adult Humans (2013) *Cell* 153:1219-1227

Frayn K, **Bernard S**, Spalding KL, Arner P, Adipocyte Triglyceride Turnover Is Independently Associated With Atherogenic Dyslipidemia (2012) *Journal of the American Heart Association* 1:e003467

Bergmann O, Liebl J, **Bernard S**, Alkass K, Yeung MS, Steier P, Kutschera W, Johnson L, Landén M, Druid H, Spalding KL, Frisén J, The age of olfactory bulb neurons in humans (2012) *Neuron* 74:634-639

O Bergmann, S Zdunek, J Frisén, **S Bernard**, H Druid, S Jovinge, Cardiomyocyte Renewal in Humans (2012) *Circ Res* 110: e17-e18

P Kurbatova, **S Bernard**, N Bessonov, F Crauste, I Demin, C Dumontet, S Fischer, V Volpert, Hybrid Model of Erythropoiesis and Leukemia Treatment with Cytosine Arabinoside (2011) *SIAM J Appl Math* 71:2246-2268

Arner P, **Bernard S**, Salehpour M, Possnert G, Liebl J, Steier P, Buchholz BA, Eriksson M, Arner E, Hauner H, Skurk T, Rydén M, Frayn KN, Spalding KL, Dynamics of human adipose lipid turnover in health and metabolic disease (2011) *Nature* 478:110-113

A Chauhan, S Lorenzen, H Herzel and **S Bernard**, Regulation of mammalian cell cycle progression in the regenerating liver (2011) *J Theor Biol* 283:103-112

O Bergmann, S Zdunek, K Alkass, H Druid, **S Bernard** and J Frisén, Identification of cardiomyocyte nuclei and assessment of ploidy for the analysis of cell turnover (2010) *Exp Cell Res* 317:188-194

S Bernard, B Čajavec Bernard, F Lévi, H Herzel, Tumor growth rate determines the timing of optimal chronomodulated treatment schedules (2010) *PLoS Comput Biol* 6(3): e1000712

E Arner, PO Westermark, KL Spalding, T Britton, M Rydén, J Frisén, **S Bernard**, P Arner, Adipocyte turnover: relevance to human adipose tissue morphology (2009) *Diabetes* 59:105-109

S Bernard, J Frisén, KL Spalding, A mathematical model for the interpretation of nuclear bomb test derived 14C incorporation in biological systems (2010) *Nucl Instr and Meth B* 268:1295-1298

O Bergmann, RD Bhardwaj, **S Bernard**, S Zdunek, F Barnabé-Heider, S Walsh, J Zupicich, K Alkass, BA Buchholz, H Druid, S Jovinge, and J Frisén, Evidence for cardiomyocyte renewal in humans (2009) *Science* 324:98-102

K Sriram, **S Bernard**, Complex dynamics in the Oregonator model with linear delayed feedback, (2008) *Chaos* 18:023126

Spalding KL, Arner E, Westermark PO, **Bernard S**, Buchholz BA, Bergmann O, Blomqvist L, Hoffstedt J, Näslund E, Britton T, Concha H, Hassan M, Rydén M, Frisén J, Arner P, Dynamics of fat cell turnover in humans, (2008) *Nature* 453:783-787

Bernard S, Gonze D, Čajavec B, Herzel H, Kramer A, Synchronization-induced rhythmicity of circadian oscillators in the suprachiasmatic nucleus, (2007) *PLoS Comput Biol* 3(4):e68

S Bernard and H Herzel, Why do cells cycle with a 24 h period? (2006) *Genome Informatics* 17:72-79

S Bernard, B Čajavec, L Pujo-Menjouet, MC Mackey, and H Herzel, Modelling transcriptional feedback loops--The role of Gro/TLE1 in Hes1 oscillations (2006) *Philos Transact A Math Phys Eng Sci* 364:1155-1170

B Čajavec, H Herzel, and **S Bernard,** Death of neuronal clusters contributes to variance of age at onset in Huntington's disease (2006) *Neurogenetics* 7:21-25

B Čajavec, **S Bernard**, and H Herzel, Aggregation in Huntington's disease: Insights through modelling (2005) *Genome Inform Ser Workshop Genome Inform* 16:262-271

C Foley, **S Bernard**, and MC Mackey, Cost-effective G-CSF therapy strategies for cyclical neutropenia: mathematical modelling based hypotheses (2006) *J Theor Biol* 238:754-63

D Gonze, **S Bernard**, C Waltermann, A Kramer, and H Herzel, Spontaneous synchronization of coupled circadian oscillators (2005) *Biophys J* 89:120-129

L Pujo-Menjouet, **S Bernard**, and MC Mackey, Long period oscillations in a Go model of hematopoietic stem cells (2005) *SIAM J Appl Dyn Sys* 4:312-332

S Bernard, J Bélair, and MC Mackey, Bifurcations in a white-blood-cell production model (2004) *CR Biologies* 327:201-210

S Bernard, J Bélair, and MC Mackey, Oscillations in cyclical neutropenia: new evidence based on mathematical modeling (2003) *J Theor Biol* 223: 283-298

S Bernard, L Pujo-Menjouet, and MC Mackey Analysis of cell kinetics using a cell division marker: mathematical modeling of experimental data (2003) *Biophys J* 84:3414-3424

S Bernard, J Bélair, and MC Mackey, Sufficient conditions for stability of linear differential equations with distributed delays (2001) *Discrete Contin Dyn Syst Ser B* 1:233-256

Développement logiciel

Simuscale Une plateforme de simulation multiéchelles pour la dynamique de populations cellulaires (C++), https://gforge.inria.fr/projects/simuscale/

Post-mortem Predictor Un outil pour la prediction d'intervalles post-mortem base sur la concentration de potassium de
l'humeur vitreuse
(R / shiny), https://slbd.shinyapps.io/pmi_app/

ODExp Un solveur EDO léger et rapide
(C), https://github.com/samubernard/odexp

cellDating Outils de modélisation et d'ajustement non-linéaire pour l'estimation des taux de renouvellement pour les tissus à faible potentiel de regeneration, basés sur des mesures d'incorporation de 14C dérivé des tests nucléaires
http://carbondating.gforge.inria.fr

Conférences invitées

2016 Hambourg, Allemagne, Atelier StemCellMathLab'16, From using models to using modelling in clinical applications
Conférence invitée: *Un point de vue dynamique des populations de la rémission sans traitement de la leucémie myéloïde chronique*

2015 St-Etienne, France, Journées MMCS
Conférence invitée: *Condition optimale pour la stabilité asymptotique linéaire pour les équations différentielles scalaires avec retards distribués*

2015 Lyon, France, Séminaire du Laboratoire de Biométrie et Biologie Évolutive
Conférence invitée: *Dynamique du renouvellement lent de tissus chez l'humain*

2013 Paris, France, GDR METICE

Conférence invitée: *Modélisation multiéchelles pour l'hématopoïèse - l'Équipe Inria Dracula*

2013 Lyon, France, Séminaire conjoint Dracula-Beagle
Conférence invitée: *La dynamique du renouvellement cellulaire chez l'humain*

2013 Lyon, France, Semestre thématique: Mathématiques et biologie
Conférence invitée: *Des boucles de rétroaction linéaires aux distribution de retards: applications aux réseaux de signalisation*

2012 Stockholm, Suède, Nobel Forum Minisymposium No.50 in the series Frontiers in Medicine, Lipid mobilization from adipose tissue - novel aspects on an old story
Conférence plénière: *Modelling in vivo data in human adipose tissue research*

2012 St-Flour, France, École d'été de la Société francophone de biologie théorique (SFBT)
Conférence invitée: *Modélisation multi-échelles en biologie*

2010 Rabat, Maroc, Conférence internationale de la Société marocaine de mathématiques appliquées (SM2A)
Conférence invitée: *Un modèle mathématique pour l'interprétation de l'incorporation dans les systèmes biologiques de 14C dérivé des tests de bombes nucléaires*

2010 Brighton, Angleterre, Université du Sussex
Conférence invitée: *Optimisation des horaires de traitement pour la chronothérapie des cancers*

2009 Stockholm, Suède, Institut Karolinska
Conférence invitée: *Le double rôle des neuropeptides dans la synchronisation et la maintenance des rythmes circadiens dans le noyau suprachiasmatique*

2009 Lyon, France, Entretiens Jacques Cartier
Conférence invitée: *L'âge de nos cellules par tests nucléaires*

2009 Dubrovnik, Croatie, École d'été en modélisation mathématique en biologie et en médecine
Conférence invitée: *Un modèle mathématique pour l'interprétation de l'incorporation dans les systèmes biologiques de 14C dérivé des tests de bombes nucléaires*

2009 Villejuif, France, BioSim Network Conference
Conférence invitée: *Horaires de traitement chronomodulés optimaux*

Organisation d'événements scientifiques

2013	Membre du comité d'organisation du semestre thématique: Mathématiques et biologie, Lyon, France.
2009	Co-directeur du comité d'organisation de l'École d'été en modélisation mathématique en biologie et en médecine, Dubrovnik, Croatia.

Communication avec le publique

2009 - present	Conférences publiques avec l'Université Ouverte de Lyon, Lyon, France.

- *L'âge de nos cellules par tests nucléaires*
- *Garder le rythme, c'est garder la santé*

Responsibilités

2011-2013	Membre du comité de direction de l'institut Rhône-alpin des systèmes complexes (IXXI, http://www.ixxi.fr).

Comités d'évaluation

Jury de soutenance de thèse

2013: Anne-Cécile Lesart, Université Joseph Fourier, Grenoble, France

Comités de recrutement

2012, 2015 Grant & Fellowships review, FNRS, Belgique

2012 Comité de recrutement pour un poste de maître de conférence, Université Joseph Fourier, Grenoble, France

Activité de relecture

Rapporteur dans les domaines de l'analyse d'équations différentielles, biologie computationnelle et dynamique de populations cellulaires (J. Math. Anal. Appl., J. Theor. Biol., Bull. Math. Biol., Biophys. J., and Math Biosci., Biophysical Journal, PLOS One, etc)

Chapter 3

Introduction

This manuscript is an overview of the research done in the past ten years or so. The motivation behind most of the work I have done with my collaborators is the observation that several interesting biological properties of tissues and organisms cannot be reduced to molecular mechanisms alone. Cell proliferation and death, and intercellular interaction act as filters between what happens at the cellular level and what is actually seen in at the cell population levels.

An illuminating example is the controversy that arose from the publication, two years ago, of a paper by Tomasetti and Vogelstein explaining the lifetime risks of cancers across tissues by the number of stem cell divisions in those tissues [61]. The paper failed to account for difference in cancer incidence among populations, and neglected the fact that several environmental factors are strongly correlated with cancer incidence, critics said [67, 6]. The correlation established by Tomasetti and Vogelstein spans 6 orders of magnitude in the number of stem cell divisions and 5 orders of magnitude in the lifetime risks of cancer. This means that, independently of any other factors, the risk of a cancer in a tissue is mainly determined by a cell proliferation index. By not taking the measure of the importance of cell proliferation, we are left looking for external causes to cancer [68]. In their most recent paper, Tomasetti and colleagues argue that even when there is a strong environmental link such as in lung cancer, cell proliferation may account for as much as 35% of all cancer driver mutations [62].

Another, less controversial example is the circadian clock pacemaker. The clock pacemaker is located in a region of the brain called the suprachiasmatic nucleus. The suprachiasmatic nuclei contain around 20,000 neurons. These neurons are circadian oscillators that synchronize to each other to form a robust clock. At the cellular level, the oscillator is a genetic oscillator formed by interlocked negative and positive post-translational feedback loops. Knock-out studies have identified which of the proteins are necessary for the maintenance of the rhythms in behavior. However, behavior does not necessarily reflect clock cell phenotype. In an elegant set of experiments combined with mathematical modelling, Liu and colleagues [45] have shown that the genes *Per1* and *Cry1* are not necessary for rhythmic behavior, but are necessary for individual clock neuron rhythmicity, and that intercellular coupling preserves rhythmicity. This is a nice case where cellular phenotype is masked by synchronization of a cell population.

The reductionist approach that has been used in molecular biology for the past 30 years consists in inferring biological function, often at the tissue or whole body level, from molecular observations. There are several areas where this approach does not work so well. If the average cellular phenotype is not representative of the whole population phenotype, no matter how finely individual cells will be characterized, there will be a mismatch between the prediction and the observation. For the reductionist approach to work, it must take into account what happens when cells are brought together, that is, the tissue ecology. Cell population dynamics, in a broad sense, is interested in the phenomena that occurs when many cells are brought in together, interact, proliferate and die. This is what we are interested in.

Presenting an overview of past research is not an easy task. Now that I look back at my publications, the temptation is great of trying to fix obvious holes in the studies that seemed so solid at the time of publication. On the upside, I am quite happy to see that some of the modeling predictions made 10 years ago seem to have been confirmed experimentally. Some other predictions have failed. One such prediction concerned the regulation of a genetic negative feedback loop by a co-repressor [19]. It was predicted that co-regulation was necessary to control transient response of the system to external signals, but experimental data published shortly after showed no evidence of such control.

Here is how this thesis is organized. In Chapter 4, we study the stability of a generic negative feedback loop with a delay, which is known to be prone to instabilities and oscillations [16, Article in Section 9.1]. The negative feedback loop can describes equally well genetic oscillators and nonlinear feedback regulation of cell population numbers. Understanding what affects stabil-

ity (or instability) is thus relevant for the two biological scales of interest here: the cell and the population.

In Chapter 5, we show how interaction (cell-cell communication though a diffusible factor) can transform a collection of sloppy oscillators into a robust, noise-resistant clock [20, Article in Section 9.3]. There is evidence that the clock neurons follow this design principle.

In Chapter 6, we take a step back and look at the long-term renewal capacity of tissues in human. We discuss how we can estimate the extent of cell renewal in the human heart ventricle [11, Article in Section 9.2]. The human heart has a limited capacity to regenerate after a stroke or during chronic heart failure, but tens of clinical trials involving stem cells injection in the heart are being conducted without clear understanding of fate of these cells after transplant. We also discuss a recent model for the tumor-immune interaction, and the role of the immune system in long-term remission in chronic myelogenous leukemia [22, Article in Section 9.4].

In Chapter 7, we discuss integrative approaches for multiscale (molecular/population) models. In a first study [25, Article in Section 9.5], we looked at how cell division during liver regeneration is gated by the circadian clock, based on a molecular model of the cell cycle. In a second study [28, Article in Section 9.6], we looked at the effect of a disruption of the circadian clock of cell proliferation.

The outlook in Chapter 8 is the opportunity to discuss the future. Finally, Chapter 9 contains the reprints of 6 selected papers.

Chapter 4

Stability of delay differential equations

4.1 Differential equations with distributed delays

Delay differential equations (DDEs), with their infinite-dimensional phase space, possess a rich dynamics and are better suited to study complex objects with long life history. However, delays can lead to non-biological solutions, even when introduced with care [15], which lead some researchers to criticize the use of DDEs. We try here to show why DDEs can be useful.

Delay differential equations are equations where some of the dynamical variables depend not only on present time t but also on the past. We consider here only scalar DDE, the idea being that any extra equations can be eliminated by introducing a **distributed time delay**

$$\frac{dx}{dt} = F\Big(x, \int_0^\infty x(t-\tau)f(\tau)d\tau\Big).$$

The history $x(t-\tau)$ is averaged against a probability density f on the positive real numbers. The density f is non-negative, $\int_0^\infty f(\tau)d\tau = 1$, and has non-negative finite expectation s,

$$s = \int_0^\infty \tau f(\tau)d\tau < +\infty. \tag{4.1}$$

Solutions are in a function space, where $x_t : [-\infty, 0] \to \mathbb{R}$ is the solution at time t. Initial conditions are usually taken in the Banach space of bounded continuous functions on $[-\infty, 0]$ with the supremum norm.

Steady-state solutions are constant functions $x_t = \bar{x}$ that satisfy $F(\bar{x}, \bar{x}) = 0$. For smooth nonlinear right-hand-side function F, linearisation around a steady-state yields

$$\frac{dx}{dt} = -ax - b\int_0^\infty x(t-\tau)f(\tau)d\tau, \tag{4.2}$$

with a and b the negatives of the derivatives of the instantaneous and the delayed parts of F. Negatives are taken because in the general setting, a represents a loss rate and b, the gain of a negative feedback loop, both of which are usually positive.

A much-studied delay distribution is the **Gamma distribution**. As a probability law, the Gamma delay distribution with parameters (q, β) represents the sum of q i.i.d. exponential laws of parameter β. Biologically, the Gamma distribution describes the time it take for the information component $x(t)$ to go through q successive stages, each with transition rate β. The delay can also consist in a positive linear combination of m Gamma distributions. This represents r possible paths for the information of x to go through, each having a probability p_i $i = 1, ..., m$ of being picked up. By a suitable choice of each of the m Gamma distributions, we can approximate any probability distribution.

It is possible to convert a DDE with a linear combination of Gamma distributions to an ODE system consisting of a main nonlinear ODE $\dot{x} = F(x, y)$ and a linear subsystem $\dot{y} = Ay$ where $y \in \mathbb{R}^{\tilde{q}}$ for some $\tilde{q}$ and A is a square of size $\tilde{q}$. This implies that the use of DDEs is not strictly necessary. However, arbitrary small perturbations of the delay distribution will destroy the structure of the corresponding ODE, in particular when q is not an integer. In that sense, ODEs are not robust against delay perturbations. Therefore, the choice between using a scalar DDE or a nonlinear ODE system is thus driven by what kind of perturbation to the system we are expecting. The DDE formalism should be favoured when the delay distribution is not known precisely.

The **characteristic equation** associated to the scalar linear delay equation defined by equation (4.2) is

$$\lambda + a + b\int_0^\infty \exp(-\lambda\tau)f(\tau)d\tau = 0. \tag{4.3}$$

For a fixed delay distribution, the **stability chart** in the (a, b)-plane is easy to represent. When $a > |b|$ there is no root with positive real part, the leading root is negative. If (a, b) are varied continuously, the only way for roots with positive real parts can appear is through the imaginary axis (they cannot appear in the right half complex plane or at $+\infty$). On the line $b = -a$ there is at least one root $\lambda = 0$. That root becomes positive when $b < -a$. When $b > |a|$, there are no real roots, and roots with positive real part appear when they cross the imaginary axis. Assuming $b > |a|$, and letting $\lambda = i\omega$ ($\omega > 0$), leads to two equations for the real and imaginary parts of the characteristic equation:

$$\begin{aligned} a + b\int_0^\infty \cos(\omega\tau)f(\tau)d\tau &= 0 \\ \omega - b\int_0^\infty \sin(\omega\tau)f(\tau)d\tau &= 0. \end{aligned}$$

These equations can be solved parametrically for a and b:

$$\begin{aligned} a(\omega) &= -b(\omega)\int_0^\infty \cos(\omega\tau)f(\tau)d\tau \\ b(\omega) &= \frac{\omega}{\int_0^\infty \sin(\omega\tau)f(\tau)d\tau}. \end{aligned}$$

The successive zeros ω_k, $k \geq 0$ of the function $S(\omega) = \omega / \int_0^\infty \sin(\omega\tau)f(\tau)d\tau$ delimit branches of the curve $(a(\omega), b(\omega))$. Let the interval $I_k = (\omega_k, \omega_{k+1})$ and the branch

$$B_k = \{\big(a(\omega), b(\omega)\big) | \omega \in I_k\}$$

For k odd and $\omega \in I_k$, $S(\omega) < 0$ and B_k lies below $b < -|a|$. Thus only branches with k even can determine the stability. The branch B_0 had two important properties

1. The branch B_0 always starts at $\big(a(0), b(0)\big) = \big(-s^{-1}, s^{-1}\big)$.
2. The branch B_0 always extends to $+\infty$ along the b-axis. Even when $S(\omega)$ does not admit any zero,

$$\lim_{\omega\to\infty} S(\omega) = 0.$$

Therefore, for $b > s^{-1}$, loss of stability is always due to pairs of complex roots crossing the imaginary axis.

Suppose that f is a **single discrete delay** at $\tau = s$, i.e. $f(\tau) = \delta(\tau - s)$ is a Dirac mass. Then the branches B_k, k even, are strictly ordered and the number of pairs of roots with positive real parts added is equal to the number of branches that have been crossed from right to left when looking in the direction of the branch for increasing values of ω. It follows that the first branch B_0 defines the boundary of stability of the linear scalar equation (4.2).

When f is not a Dirac mass, there is no such strict order on the branches. They can intersects at several points, so that the boundary of the stability region will be determined by the first branch crossed when moving continuously from the line $a = b$. For instance, when the delay distribution takes three distinct discrete delay, at least the four first branches are needed to determine the stability boundary (Figure 4.1). The stability chart in the (a, b)-space then becomes a *tangled monster plot*[1].

[1]This is how my daughter refers to her little brother's colorful drawings.

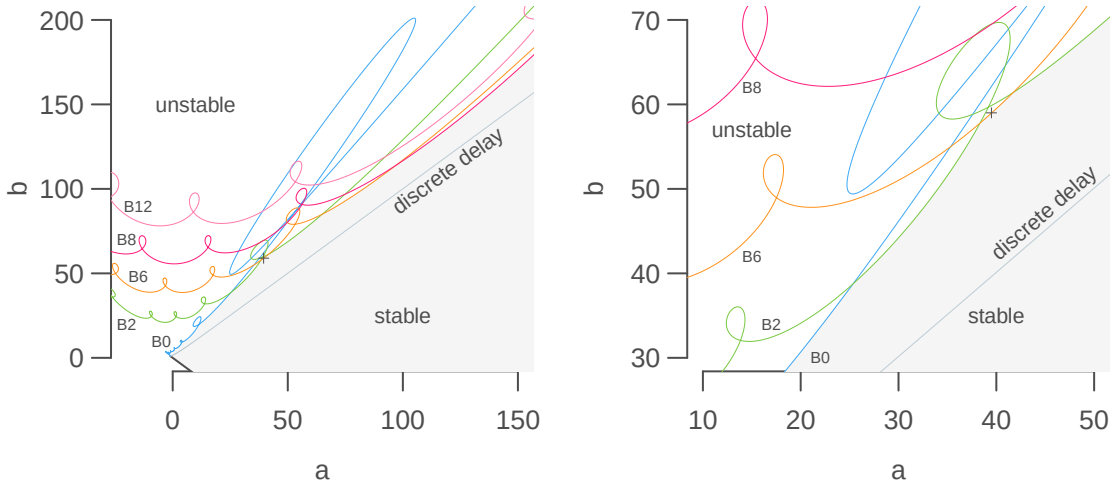

Figure 4.1: *Tangled monster plot* (stability chart) for the characteristic equation with three discrete delays $\lambda + a + b\sum_{i=1}^{3} p_i \exp(-\lambda\tau_i) = 0$, with $\tau = \{0.3731, 0.7090, 5.9701\}$ and $p = \{0.7, 0.2, 0.1\}$. The mean delay is $s = 1$. The stability region (*grey area: stable*) is located below the union of the branches (*colored curves:* B_0, B_2, B_6, B_8, *and* B_{12}*; the curves* B_4 *and* B_{10} *are not visible on these axes*) on which the characteristic equation admits imaginary roots $\pm i\omega$ with increasing values of ω. The stability boundary of the characteristic equation with a single delay at 1: $\lambda + a + b\exp(-\lambda) = 0$ lies entirely in the stable region (*grey curve: discrete delay*). The stability region with three delay is bounded by a non-trivial union of parametric curves (enlarged in *right panel*). For instance, at the point $(a, b) = (39.5, 59)$ (*point* $+$), the characteristic equation in unstable, but only because of branch B_6 (*orange*).

4.2 G$\langle n \rangle$[dM]

The **Goodwin model** is perhaps the best-known model of a genetic oscillator. Introduced in the 1960's by B. Goodwin [35], it describes the activity of a gene (mRNA expression x), its product (protein concentration y) and the formation of a negative regulator complex z that inhibit gene expression.

$$\begin{aligned}\frac{dx}{dt} &= P(z) - \alpha x,\\ \frac{dy}{dt} &= \beta[x - y],\\ \frac{dz}{dt} &= \beta[y - z],\end{aligned}$$

where the nonlinear function P is a **Hill function**

$$P(z) = k_0 \frac{1}{1 + z^h}.$$

The parameters α, β, k_0, h have all real, positive values. (The original Goodwin had different coefficients for each dynamical variable, but we keep things simple.) Parameter α is the mRNA degradation rate, β is the degradation rate of the protein products, k_0 is the maximal mRNA synthesis rate. Parameter h is the **Hill coefficient**. There are parameters for which the Goodwin model has unique, unstable, positive equilibrium, and a stable, positive limit cycle. However, the limit cycle exists only for relatively large values of the Hill coefficient, $h > 8$. There are several ways to modify the Goodwin model so that solutions will oscillate more easily. The reason the

Goodwin model can oscillate is that it is a system with a delayed, negative feedback loop. The loop is clear: x depends on z, which depends on x. It is negative because P is a decreasing function, and it is delayed because z is a delayed version of x. We can increase the length of the delay by adding more intermediary steps between x and z, i.e. by replacing y and z with $y_1, y_2, ..., y_q$ and defining the corresponding ODEs

$$\frac{dy_i}{dt} = \beta(y_{i-1} - y_i),\ i = 1, ..., q,$$

where, for ease of notation, $y_0 = x$ and $y_q = z$.

I became interested in the Goodwin oscillator in 2004 while I was working with Hanspeter Herzel at the Institute for Theoretical Biology in Berlin. There I met Didier Gonze, who was studying how circadian clocks could synchronize to form a pacemaker. The Goodwin model had been applied to the circadian clock already [56], and it seemed like a good compromise between the realism of complexity and the simplicity of abstraction. Robust synchronization of nonlinear oscillators is far from trivial, and we tried several versions of the Goodwin models as a core circadian oscillator with varying degree of success. To keep up with these different model versions, we developed a naming convention. We called the Goodwin model with one nonlinear equation and q auxiliary linear equations $\mathtt{G}\langle q+1\rangle$. Under this naming convention, the original Goodwin model is `G3`. It is the smallest model that admits a stable limit cycle. Model `G2` has only one auxiliary equation, and it is a classical result that no such 2-dimensional negative feedback system can admit a limit cycle. In general, the larger the q, the easier it is to produce stable limit cycles. In the limit $q \to \infty$ (while $q/\beta \to \tau > 0$), the Goodwin model becomes a scalar equation with a discrete delay

$$\frac{dx}{dt} = P(x_s) - \alpha x, \tag{4.4}$$

where $x_s = x(t-s)$. This model is denoted `G1d` (`d` for delay), and is equivalent to $\mathtt{G}\infty$.

Another way to modify the Goodwin model is to replace linear degradation term with nonlinear ones. We used in [34] a modified version of the Goodwin model where the degradation terms followed Michaelis-Menten kinetics,

$$v\frac{x}{K+x}. \tag{4.5}$$

These models are denoted $\mathtt{G}\langle n\rangle\mathtt{M}$ followed optionally with the indices of the variable for which the degradation rate is nonlinear. Introduction of nonlinear degradation rates helps producing sustained oscillations, but care must be taken to make sure solutions do not blow up.

4.3 Stability results

A Goodwin model $\mathtt{G}\langle n\rangle$ possesses exactly one positive equilibrium, given by the unique positive solution of $P(x) - \alpha x = 0$. Its asymptotic stability is determined by a characteristic polynomial of degree $n = q+1$. In practice, the roots can be inconvenient to locate, especially when n is large [18]. To avoid dealing with cumbersome high degree polynomials, we can use the **linear chain trick** to convert the system $\mathtt{G}\langle n\rangle$ into a scalar differential with a distributed delay. The linear chain trick consists in integrating the auxiliary variables y_i successively, keeping the dependence on x. This way z can be expressed as a linear functional on the history of x:

$$z(t) = \int_0^\infty x(t-\tau)g(\tau, q, \beta)d\tau, \tag{4.6}$$

where g is the Gamma distribution

$$g(\tau, q, \beta) = \frac{\beta^q}{\Gamma(q)} \tau^{q-1} e^{-\beta\tau}. \tag{4.7}$$

The mean delay $s = q/\beta$. Model $\mathtt{G}\langle n \rangle$ can then be expressed as

$$\frac{dx}{dt} = P(z) - \alpha x, \tag{4.8}$$

with z defined by equation (4.6). We note that q, the number of auxiliary equations, is now a ordinary parameter that can take any non-negative real value.

Let $\bar{x}$ be the unique positive equilibrium of equation (4.8), then the characteristic equation of the linear system at equilibrium is

$$\lambda + a + b \int_0^\infty g(\tau, q, \beta) e^{\lambda\tau} d\tau = 0. \tag{4.9}$$

Coefficients are $a = \alpha$ and $b = -dP/dx|_{\bar{x}} \geq 0$. For $q \in \mathbb{N}$, the characteristic equation has the same n roots as the characteristic polynomial, so no advantage can be gained analytically with the linear chain trick. The roots of the characteristic equation determine the **asymptotic stability** of the equilibrium $\bar{x}$. The equilibrium is asymptotically stable if and only if all roots have strictly negative real parts. However, we know how the roots of the characteristic equation behave when q goes to infinity, while $q/\beta \to s$. By continuity, the roots of the characteristic equation will converge to the roots of the characteristic equation associated to the model `G1d`. The characteristic equation for model `G1d` is

$$\lambda + a + be^{-\lambda s} = 0. \tag{4.10}$$

All roots of the equation (4.10) have strictly negative real parts if one of the conditions is satisfied

1. $a \geq |b|$ and $a > -b$,
2. $b > a$ and

$$s < \frac{\arccos(-a/b)}{\sqrt{b^2 - a^2}}. \tag{4.11}$$

If none of the conditions are satisfied, there is at least one root with nonnegative real part. Our main stability result [16, Article in Section 9.1] generalizes previous results [18]. It states that if either of the above conditions is satisfied, all roots of the characteristic equation (4.9) for model $\mathtt{G}\langle n \rangle$ also have strictly negative real parts. This stability results holds not only for delay equations with Gamma distributions, but for any distribution with at least an exponential tail. These sufficient conditions are also necessary when the distribution is a single discrete delay. Our stability results are optimal in the sense that if the stability conditions are not met, we can find a delay distribution with mean s such that the corresponding characteristic equation will possess a root with a nonnegative real part. Put another way, replacing a discrete delay by a distribution of delay cannot destabilize an equilibrium.

In practice, the bound defined by inequality (4.11) is quite conservative. Wide delay distributions tend to expand the region of stability in the (a, b)-space at s fixed. In Figure 4.1, the shaded area (*stable*) above the grey curve (*discrete delay*) is the region in the (a, b)-space that is stable for the distributed delay, but unstable for the single delay. For instance, at $a = 30$, the stability region is extended from $b \approx 30$ to $b \approx 40$. Despite the conservative conditions on a, b and s for stability, there are obvious advantages to be able to draw stability conclusions based only on three parameters: the coefficients a, b and the first moment of the distribution s.

4.4 Positive feedback loops and robustness of oscillations

The Goodwin model and its variants have been used to model anything from small gene regulatory networks involving *Hes1*, *p53*, and *NF-κB* [50] (G2d), or the circadian clock [56] (G3), to cell populations with density-dependent growth rates, as exemplified by a model for erythrocyte production [10] (G1d).

We have identified the ingredients needed to obtain oscillations in terms of the characteristic equation: a strong negative feedback loop $b > |a|$, and a significant delays. If the delay is discrete, then for any $a \geq 0$, there will be a critical value b for which a pair of complex roots of the characteristic equation will cross the imaginary axis. The Hopf bifurcation theorem states that (generically) a small amplitude limit cycle appears right there. There are often objections as to whether the negative-feedback+delay combo is *sufficient* for oscillations in real genetic oscillators and populations. The strength of the feedback is mostly determined by the Hill coefficient, and only very specific mechanisms can produce values much larger than 4 [65]. Moreover, the delay is likely to be smooth rather than "spiky", and this increases the region of stability. Our stability results tend to support these arguments that in practice it may be difficult to achieve a delay large enough to make sustained oscillations possible.

How can biological oscillators be robust then? It has been suggested that adding positive feedback could make an oscillator more robust [2, 63]. A simple positive feedback loop can be incorporated by slightly modifying the nonlinear term

$$P(x, z) = k_0 \frac{x^r}{1 + z^h}.$$

The coefficient r is a cooperativity coefficient. When $r < 1$, cooperativity is negative, and the positive feedback is most active for small values of x. When $r > 1$, cooperativity is positive, and the loop is active for large values of x. When $r = 1$, cooperativity is neutral. The introduction of a positive feedback loop can easily destabilize even a system that could never oscillate. This happens because positive feedback loops shifts the parameter a to the left. Therefore, for any $b \geq s^{-1}$ there will always be a value of $a > -b$, such that the characteristic equation has a pair of imaginary roots, and destabilization will occur through a Hopf bifurcation.

For instance, the characteristic equation for the model G2 with a positive feedback loop is

$$\lambda + \alpha(1 - r) + \frac{\alpha^2 h}{k_0} \bar{x}^{h-r+1} \int_0^\infty e^{-\lambda\tau} \beta e^{-\beta\tau} d\tau = 0.$$

The integral term simplifies to $\beta/(\lambda + \beta)$, and the characteristic equation reduces to the familiar second-order polynomial

$$\lambda^2 + \big(\beta + \alpha(1 - r)\big)\lambda + \frac{\alpha^2 h}{k_0} \bar{x}^{h-r+1} + \alpha\beta(1 - r) = 0.$$

We are looking for a pair of complex roots with positive real part. When $r = 0$, the case without positive feedback loop, the roots cannot be complex and have a positive real part, since the trace $-\alpha - \beta$ is negative. Another way to see that is that the characteristic equation possesses only one branch of imaginary roots for $b > |a|$, which is exactly the line $\big(a = -s^{-1}, b > s^{-1}\big)$. Because $a = \alpha > 0$ the stability boundary cannot be reached.

When $r > 1$, however, the trace $\alpha(r - 1) - \beta$ can be positive. At the same time, parameters k_0 and h can be chosen as to have a negative discriminant. Therefore, positive instantaneous feedback loops with positive cooperativity can destabilize stable fixed points through a Hopf bifurcation. As a rule of thumb, we can assume that increasing the cooperativity r has a destabilizing effect:

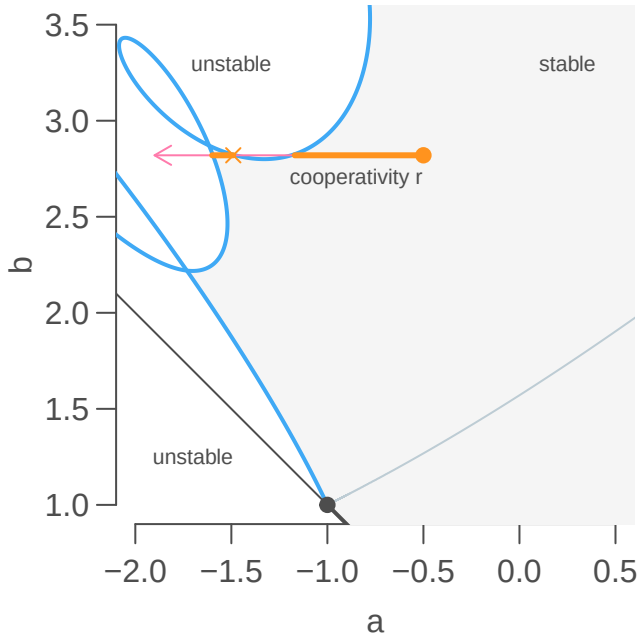

Figure 4.2: *Tangled monster plot* (stability chart) for the characteristic equation with three discrete delays with characteristic equation $\lambda + \alpha(1-r) + b\sum_{i=1}^{3} p_i \exp(-\lambda\tau_i) = 0$, with $\tau = \{0.3731, 0.7090, 5.9701\}$ and $p = \{0.7, 0.2, 0.1\}$ (delay parameters as in Figure 4.1, and $a = \alpha(1-r)$). Increasing the cooperativity coefficient r while keeping b constant always eventually destabilizes a steady state, but stability switches can occur ($\times$).

the real part of the leading eigenvalues of the characteristic equation increases with r. This is not always true, because **stability switches** can occur, as evidence by a close up on the *tangled monster plots* (Figure 4.2).

The main limitation of the sufficient condition for stability is that it cannot handle mixed delayed feedback loops, i.e. loops with negative and positive delayed components. What happens when the positive feedback loop is delayed is a bit more complicated. Intuitively, a positive loop with a sufficiently large delay should be destabilizing. The characteristic equation of the scalar mixed feedback loop equation would be

$$\lambda + a + be^{\lambda\tau_1} - ce^{\lambda\tau_2} = 0,$$

assuming $bc > 0$. This characteristic equation has been studied from different angles [36, 46, 24, 55]. We have recently obtained promising results concerning the locations of the roots (A Besse, 2017, *Ph.D. thesis in preparation*). Briefly, for τ_1 fixed, and c not too large, there is a smooth curve B in partitioning the region $b \geq |-a+c|$ such that

1. If $b < B$, for any $\tau_2 \geq 0$, all roots have negative real parts.
2. If $b > B$, there exists $\tau_2 \geq 0$ such that the leading roots have positive real parts.

The inequality $b < B$ is to be understood by the existence of $\bar{b} > b$ such that $(a, \bar{b}) \in B$, and $b > B$ if there is no such value. This curve B is the "lower" part of the envelope of the limit set of the parametric curve B_0 (and only B_0) when $\tau_2 \to \infty$. This result should be generalizable to delay distributions, where the curve B would be optimal when the negative feedback delay is discrete.

Chapter 5

Synchronization and rhythmicity of circadian clocks

5.1 The circadian clock

The **circadian clock** is a biological clock that controls daily rhythms in physiology and behavior. In mammals it is controlled by a pacemaker located in the suprachiasmatic nucleus (SCN) of the hypothalamus. In mice, the SCN is composed of 20,000 densely packed neurons. Each of these neurons possesses a gene regulatory network with interlocked positive and negative feedback loops that can generate 24 hour-period oscillations in molecular concentrations. Neurons in the SCN are organized in different regions, characterized by which neuropeptides or neurotransmitters they express and whether they can receive direct light input from the retina. The ventrolateral part of the SCN receives light from the retina and relays the information to the dorsomedial part. As a whole, the SCN is capable of producing a coherent daily rhythm. The disparate intracellular clocks form a coherent rhythm through mutual interaction, or coupling.

It was initially observed that neurons dispersed in cell culture mostly displayed cell-autonomous oscillations [66], but a more recent study showed that when neurons are dispersed at a lower density, most neurons display no or irregular oscillations [64]. When key circadian clock genes are knocked-out, making isolated cells arrhythmic, animal behavior can still be rhythmic, indicating that cell-cell interaction can rescue oscillations [45, 39].

So, based on available experimental data, we were looking for mechanisms to synchronize self-sustained oscillators. However, from a mathematical point of view, damped oscillators would be more appropriate. Damped oscillators can be entrained at any frequency, while entrainment of sustained oscillators can show complex periodic and non-periodic solutions.

5.2 Damped versus sustained oscillators

The idea that circadian rhythms could be generated by mutually coupled damped oscillators was already proposed by Enright in the 1980's [30]. Enright used mutually triggered damped, noisy relaxation oscillators, interconnected in such a way that when a given fraction of elements have fire up, all connected elements are triggered and reset to phase 0. Enright defines a damped relaxation oscillator so that when isolated, it will fire with an amplitude 1 at the first cycle, $k < 1$ at the second cycle, k^2 at the third cycle, and so on. Amplitude is reset to 1 when the oscillator is reset. It is intuitively clear such oscillators can become sustained through mutual entrainment, as soon as enough oscillators fire at each cycle. Enright's model shows how unreliable oscillators can produce a reliable timekeeping. However, the assumption that individual clocks can be modeled as relaxation oscillator is a strong one. Relaxation oscillators arise at short biological time scales. For instance in neuron action potentials or pancreatic beta cell insulin secretion occur at a time scales of milliseconds to minutes. It is not clear how much slower cycles, from circadian clocks to menstrual cycles can be considered as relaxation oscillators. Relaxation oscillators, with a fast-slow dynamics, such as the **van der Pol oscillator**, tend to have an all-or-none dynamics (Figure 5.1, *left panels*). The van der Pol oscillator is a non-linearly (negatively) damped oscillator

$$\ddot{x} - \varepsilon\omega_0(1 - x^2)\dot{x} + \omega_0^2 x = 0.$$

The damping coefficient $-\varepsilon\omega_0(1 - x^2)$ is negative for small values of $|x|$ and positive values of ε (assuming $\omega_0 > 0$), and negative for larger values of $|x|$. Poincaré-Bendixson theorem can be applied to show that the van der Pol oscillator admits a stable limit cycle.

Several experimental reports suggested that cellular clocks have sustained sinusoidal oscillations, even in isolated cells [66, 51]. Multiple genetic regulation feedback loops, both positive and negative, have been identified, but the experimental and theoretical consensus is that a delayed negative loop is sufficient to generate and maintain a 24h cycle in molecular levels [53]. The Goodwin

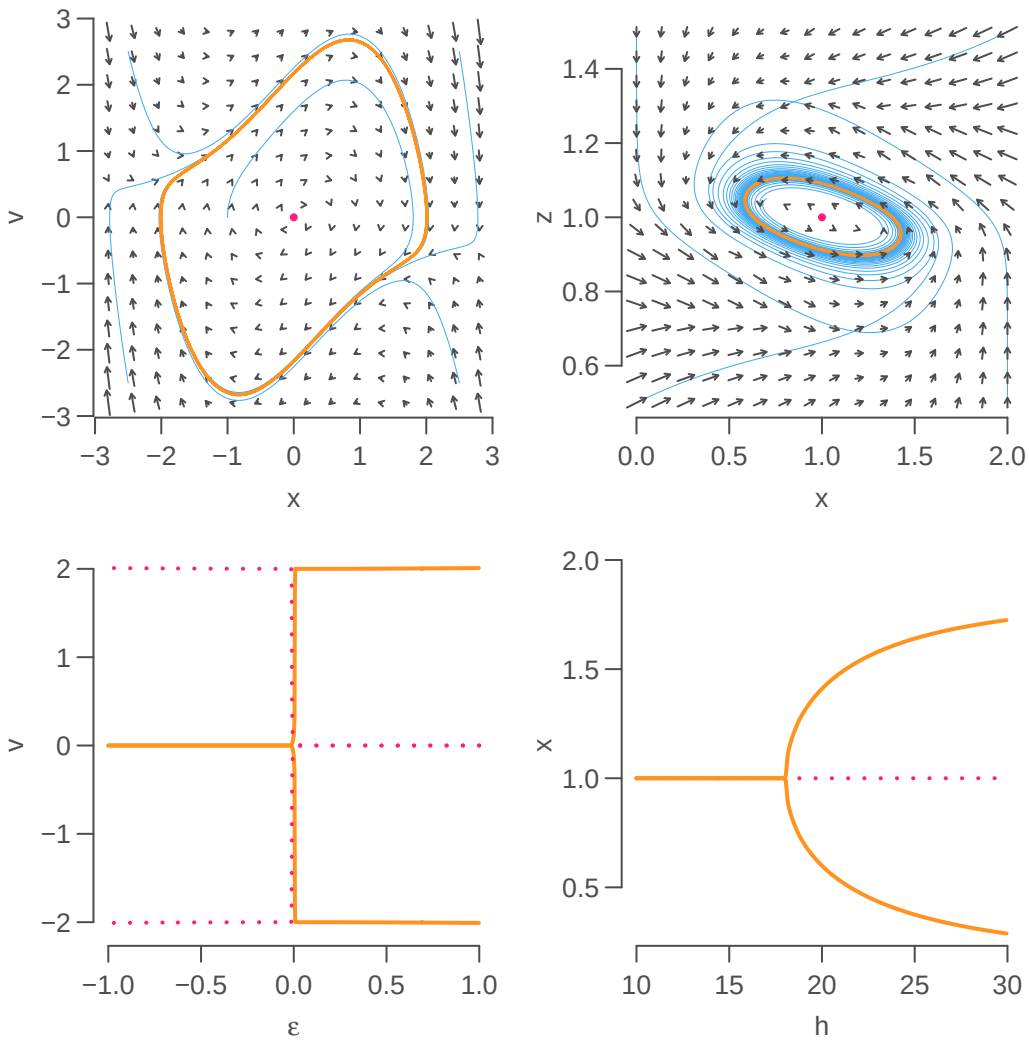

Figure 5.1: Van der Pol (*top left*, $\varepsilon = 1, \omega_0 = 1$) and G3 (*top right*, $\beta = 1, \alpha = 1, k_0 = 2, h = 20$) phase spaces. The phase space of G3 has been projected onto the xz-plane, for y interpolated from numerical solution: for (x, z), y was set to $y(t)$, where $||(x, z) - (x(t), z(t))||$ is minimized along all times t. Bifurcation diagrams of the van der Pol oscillator with respect to ε (*bottom left*) and G3 with respect to the Hill coefficient h (*bottom right*).

model G3, as defined in Section 4.2 is an instance of such a delayed negative loop, which for suitable parameter values, admits a stable limit cycle.

The generic process for the appearance of a limit cycle in Goodwin models is a Hopf bifurcation, through which an asymptotically stable steady state becomes unstable an small, stable amplitude limit cycle appears. The periodic solution is sinusoidal and there is no clear separation of time scales (Figure 5.1, *right panels*) unlike in the van der Pol model. Sinusoidal and relaxation oscillators have different responses to external perturbations, so care should be taken when choosing a system to study outside its equilibrium state. Here we have chosen to study sinusoidal oscillators, because of their immediate biological interpretation in terms of mRNA and protein concentrations. The observation that cellular clock are self-sustained indicates that the clocks should stand away from the Hopf bifurcation.

5.3 Synchronization of biological oscillators

Suppose we have a population of N non-identical oscillators. Each of the oscillator is modeled by a system of D ODEs

$$\frac{dx_i}{dt} = f_i(x_i),$$

with $x_i \in \mathbb{R}^D$. We assume that the right-hand-side of the ODEs can be parametrized with parameter sets $\theta_i \in \mathbb{R}^p$: $f_i(x) = f(x, \theta_i)$, where $\theta_i \neq \theta_j$, for $i \neq j$. We assume that there is a compact subset Θ_i such that oscillator i admits a unique stable limit cycle for $\theta_i \in \Theta_i$. Associated to the limit cycle is a unstable manifold that contains an unstable focus $\bar{x}_i$. In absence of any coupling between the oscillators, there are at least N pairs of complex eigenvalues associated with the Jacobian matrices of f_i at $\bar{x}_i$ with positive real parts. In the generic case the N oscillators orbit with their intrinsic period τ_i on an N dimensional torus. There are two ways of coupling the oscillators together, diffusive and direct coupling. A **diffusive coupling** term has a form

$$C_i^{diff} = \frac{K}{N} \sum_{j=1}^{N} c_{i,j} g_i(x_j - x_i)$$

with $g_i(0) = 0$, while a **direct coupling** has the form

$$C_i^{dir} = \frac{K}{N} \sum_{j=1}^{N} c_{i,j} h_i(x_j).$$

The parameter K is called **coupling strength**, and the $n \times n$ matrix c is a **connectivity matrix** where $c_{i,j}$ is the directional connection from oscillator j to i. Here we are mainly concerned with direct coupling. When g_i is linear, the diffusive coupling can be rewritten as

$$-g_i(x_i) \frac{K}{N} \sum_{j=1}^{N} c_{i,j} + \frac{K}{N} \sum_{j=1}^{N} c_{i,j} g_i(x_j).$$

The first term can be collected into the ODE right-hand-side function f_i, so both coupling types are interchangeable to some extent. **Phase synchronization** occurs when some oscillators adopt the same period. How can we achieve synchronization? All oscillators are phase synchronized if the coupling reduces the N-dimensional torus to a limit cycle. Essentially, one way to achieve that is to move all but one pair of the complex eigenvalues to the left half complex plane. Two difficulties arise when dealing with non-identical oscillators: partial phase synchronization, where only a fraction of the oscillators do synchronize, while the rest runs freely, and quasi-periodic solutions, where oscillators oscillate in coherence but not in phase.

We approached the problem by using weak **sinusoidal oscillators**, i.e. oscillators that are close to a Hopf bifurcation. As an illustration, we consider the normal form equations for the Hopf bifurcation, expressed in rectangular coordinates

$$\begin{aligned} \frac{dx}{dt} &= (\mu - r^2)x - \omega y, \\ \frac{dy}{dt} &= (\mu - r^2)y + \omega x, \\ r &= x^2 + y^2. \end{aligned}$$

For $\omega \neq 0$, the $(0, 0)$ steady state is

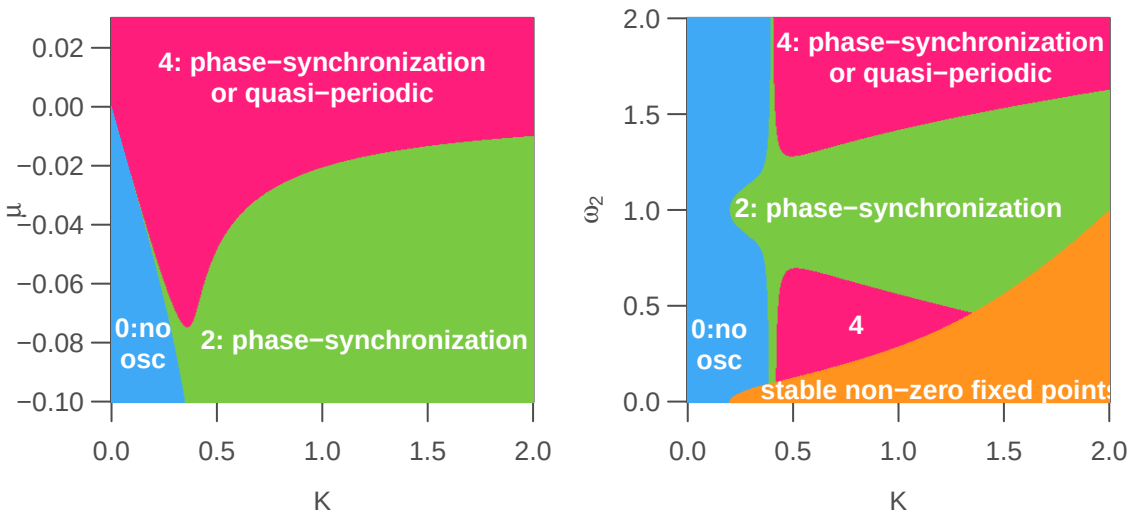

Figure 5.2: Number of complex eigenvalues with positive real parts (0: *blue* no self-sustained oscillations; 2: *green* stable limit cycle, phase synchronization; 4: *red* quasi-periodic or stable limit cycle; *orange* non-zero stable fixed-point. (Left) $\omega_1 = 0.9, \omega_2 = 1.1$. (Right) $\mu = -0.1, \omega_1 = 1$.

- a stable focus if $\mu < 0$,
- an unstable focus if $\mu > 0$.

At $\mu = 0$, there is a supercritical Hopf bifurcation and a stable limit cycle on appears the circle $r = \sqrt{\mu}$, with a frequency ω. Consider N such oscillators, with frequencies ω_i and bifurcation coefficient μ_i, $i = 1, ..., N$. We introduce the coupling term in x (the choice is semi-arbitrary: it is easier to synchronize x with x rather than y with x).

$$\begin{aligned}
\frac{dx_i}{dt} &= (\mu_i - r_i^2)x_i - \omega_i y_i + \frac{K}{N}\sum_{i=1}^{N} x_i, \\
\frac{dy_i}{dt} &= (\mu_i - r_i^2)y_i + \omega_i x_i, \\
r_i &= x_i^2 + y_i^2.
\end{aligned}$$

This is an instance of all-to-all, or global direct coupling. We compare how synchronization occurs in two cases: i) damped oscillators $\mu_i < \mu_0 < 0$, ii) sustained or weakly damped oscillators $\mu_i > \mu_0$.

When $\mu_i < 0$, for sufficiently small K, all eigenvalues are complex with negative real parts. When $\mu_i > \mu_0 \approx -0.08$, the system can go through three regimes: damped oscillations and convergence to 0 (Figure 5.2, Left panel, blue); quasi-periodic oscillations (red) and periodic, phase-synchronized solutions (green or red). When $\mu < \mu_0$, no sustained, quasi-periodic oscillations occurs. The system converges to a fixed point (blue), or to a stable periodic phase-synchronized state (green). Therefore, damped oscillators tend to exclude incoherent oscillatory solutions.

Simulations of $N = 100$ coupled sustained or damped oscillators shows that oscillation amplitude is much larger in sustained oscillators, but much less coherent. For the sustained oscillators, the center of mass of the oscillators shows large amplitude, long-period oscillations (Figure 5.3, *left panel, orange*), characteristic of quasi-periodic solutions (Figure 5.3, *right panel, orange*). For the damped oscillators, the center of mass is constant over long time scales (Figure 5.3, *left panel, blue*), indicating periodic solutions (Figure 5.3, right panel, blue).

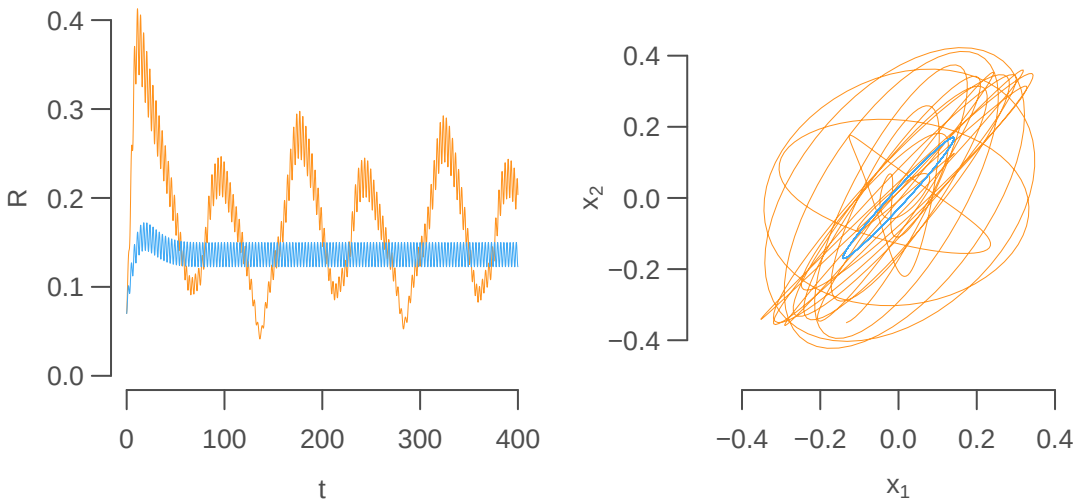

Figure 5.3: Synchronization of $N = 100$ globally-coupled (coupling matrix is one) non-identical oscillators with coupling strength $K = 0.4$, random frequencies $\omega \sim U[0.8, 1.2]$ and $\mu = 0.08$ (*orange*, sustained oscillators), $\mu = -0.08$ (*blue*, damped oscillators). (Left) Coherence parameter $R = ||\langle(x, y)\rangle||$. (Right) Orbits in the (x_1, x_2)-space.

5.4 Synchronization of circadian oscillators in the suprachiasmatic nucleus

Based on the previous section, it seems much easier to synchronize damped oscillators than sustained oscillators. So what about circadian oscillators of the suprachiasmatic nucleus? They form a dense coupled network with the following properties

1. Most if not all oscillating neurons are phase-synchronized [69].

2. Profiles are sinusoidal rather than "spiky" [69].

3. Individual amplitudes and phases vary among cells.

4. Loss of rhythmic behavior is due loss of rhythmicity in individual cells [7, 49], or loss of synchrony [52].

In practice, it is not so easy to phase-synchronize non-identical systems of genetic oscillators. Several modeling studies have explored the dynamics of coupled, non-identical circadian oscillators. Some of them used van der Pol oscillators [41, 3, 4], while others used Goodwin-type oscillators [34] or more realistic gene regulatory network models [60, 20]. It turns out van der Pol oscillators could not be reliably phased-synchronized in any of the mentioned studies, even if some degree of coherence could be achieved. Whether the requirement for phase-synchronization is biologically relevant remains an open question.

Our initial model [34] consisted of the core circadian oscillator `G3M` augmented with a fourth

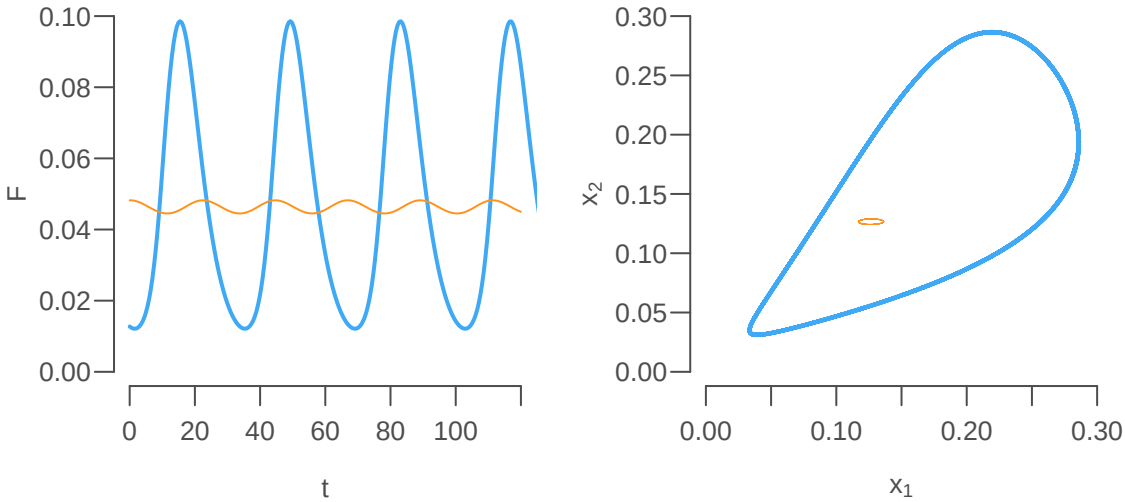

Figure 5.4: Synchronization of $N = 2$ coupled oscillators with with period ratio 0.9. (Left) Mean field F for $K = 1$ (*blue*) and $K = 0.3$ (*orange*). (Right) (X_1, X_2) phase space ($K = 1$, *blue*; $K = 0.3$, *orange*). The two oscillators are phase-synchronized for the two values of the coupling strength K.

auxiliary equation for the putative couple agent vasointestinal polypeptide (VIP):

$$\frac{dX_i}{dt} = v_1 \frac{K_1^n}{K_1^n + Z_i^n} - v_2 \frac{X_i}{K_2 + X_i} + v_c \frac{KF}{K_c + KF} + L, \tag{5.1}$$

$$\frac{dY_i}{dt} = k_3 X_i - v_4 \frac{Y_i}{K_4 + Y_i}, \tag{5.2}$$

$$\frac{dX_i}{dt} = k_5 Y_i - v_6 \frac{Z_i}{K_6 + Z_i}, \tag{5.3}$$

$$\frac{dV_i}{dt} = k_7 X_i - v_8 \frac{V_i}{K_8 + V_i}. \tag{5.4}$$

The variables represent: X the mRNA concentration of a clock gene (*Per* or *Cry*); Y the resulting protein PER or CRY concentration; and Z the concentration of the active (inhibitory) form of the protein. The variable V is the putative coupling agent concentration released. Each neuron is labeled i, $i = 1, ..., N$. We used $N = 10,000$. Coupling is assumed to be fast so as to make a **mean field** approximation for the concentration of the coupling agent

$$F = \frac{1}{N} \sum_{i=1}^{N} V_i. \tag{5.5}$$

The average concentration F of coupling agent V acts positively on the expression of the clock gene, while the clock gene is repressed through the delayed formation of the repressor Z. The ingredients are there to promote the existence of a clock. The parameter L is a light input, K is the sensitivity of the cells to the mean field F. Default parameters were: Hill coefficient $n = 4$, $v_1 = 0.7$ nM/h; $K_1 = 1$ nM; $v_2 = 0.35$ nM/h; $K_2 = 1$ nM; $k_3 = 0.7$/h; $v_4 = 0.35$ nM/h; $K_4 = 1$ nM; $k_5 = 0.7$/h; $v_6 = 0.35$ nM/h; $K_6 = 1$ nM; $k_7 = 0.35$ nM/h; $v_8 = 1$ nM/h; $K_8 = 1$ nM; $v_c = 0.4$ nM/h; $K_c = 1$ nM; $K = 0.5$; and $L = 0$. Parameters were chosen so that individual oscillators were sustained in absence of coupling. We obtained a random distribution of periods by rescaling rate constants, i.e. by dividing v_1, v_2, k_3, v_4, k_5, v_6, k_7 and v_8 by τ_i, $i = 1, ..., N$, where τ_i follows a Gaussian distribution with mean 1.0 and standard deviation 0.05. This way, the periods are distributed around 23.5h with a standard deviation of 5%. Coupling is direct, meaning

that even in case of perfect synchronization, the coupling term in non-zero. A bifurcation analysis showed the existence of a very small interval of phase-synchronization at low coupling strength, where a small amplitude stable limit cycle exists. At mid-strength levels, no sustained oscillations could occur. At larger coupling strengths, oscillators entered a regime of large-amplitude robust phase-synchronization ([34, Figure 2C]). The difference between the small and large amplitudes is quite striking (Figure 5.4)

To make sure the high-amplitude phase-synchronization regime was not due to sustained oscillators, we checked that under constant mean fields in the range observed for synchronization, individual oscillators were outside the range were stable limit cycles exist ([34, Figure 2A,B]).

In a follow-up study [20, Article in Section 9.3], we used a more realistic, yet simple model by Becker-Weimann and colleagues [9] for the circadian clock and spatially realistic coupling matrices. Parameters in the original circadian clock model were set so that it could produce stable large amplitude oscillations. We deliberately reduced the strength of the negative feedback loop to generate damped oscillators. We showed that globally coupled circadian clock could be phase-synchronized in a robust manner. However, when oscillators were only sparsely connected, a wide range of behaviors could be seen, from no oscillations at all, to mutually de-synchronized clusters of phase-synchronized cells. These results were robust to additive noise in the equations, and were also robust to the specific model used. In addition to the Becker-Weimann model, we also reproduced the same qualitative behavior with `G1d`, `G3M` and the 16-variable Leloup-Goldbeter model [43].

Chapter 6

Cell proliferation and tissue renewal

6.1 Birth-and-death models and 14C dating

Retrospective cell carbon dating is a method developed for dating long lived cells in humans by Kirsty Spalding at Jonas Frisén's lab [59]. The method is based on the variations in the atmospheric 14C levels over the past decades. Extensive atmospheric (above-ground) nuclear bomb testing between 1945 and 1963 lead to a rapid rise of the 14C levels in the atmosphere. In 1963, the Limited Test Ban Treaty signed in Moscow put an end to most atmospheric bomb testing. Since then, 14C levels are steadily decreasing, mainly because of the absorption in the oceans. Atmospheric carbon is integrated into the food chain through photosynthesis. 14C is incorporated into DNA during cell division, in an amount corresponding to the atmospheric levels around the time of division. Because DNA is a very stable molecule, the 14C content provides a date-stamp for the birth of the cell.

Cellular **Birth-and-death** models describe the dynamics of a cell population in an individual, in which cells can either be born or die. In an individual aged t years, we denote by $N(t)$ the cell number in the cell population. Keeping in mind that the atmospheric 14C data provides information on the birth-date of the cells, we also want to track the chronological age of each cell. The chronological age of a cell is defined as the time elapsed since its last division. To take into account the age of the cells, we brake down the population $N(t)$ into a continuum of age bins. We say that the population is structured in chronological cell age a. The new dynamical variable $n(t, a)$ is the cell density at age a at time t. The cell number and the cell density are related in the following way

$$N(t) = \int_0^t n(t, a)da. \tag{6.1}$$

Atmospheric 14C levels have been measured in the northern and southern hemispheres over the past decades (Figure 6.1, at distinct time points y_i, expressed in calendar years, $i = 1, ..., N_y$. In practice, we use an linear interpolation $K(y)$ of y_i. The function K is continuous and piecewise linear. It is expressed in Δ^{14}C, a measure of the 14C levels expressed in per mil variation relative to the baseline level of 1950 [54]. The level $K(1950) = 0$ by definition, and $K = 300‰$ corresponds to an increase of 30 percent. The 14C content is determined by accelerator mass spectrometry, normalized to a δ^{13}C baseline, and corrected for radioactive decay. The 14C half-life of 5568 years plays only a minor role for contemporary carbon dating. The 14C levels in a cells population measured at calendar year d (the collection date) is found by averaging the atmospheric profile K against the normalized density $n(t, a)$ [21],

$$c(t) = \int_0^t \frac{n(a, t)}{N(t)} K(d - a)da. \tag{6.2}$$

To describe the Birth-and-Death model completely, we make a set of hypotheses:

H1 Time- and age-dependent cell death rate. We assume that $\gamma \geq 0$, the death rate of a cell, can depend on its age a and on the age of the individual t. We suppose $\gamma(a, t)$ independent from the state of the cell population.

H2 At time $t_0 \geq 0$ before birth, all N_0 cells are aged 0. Tissues and organs start their development before birth, and in slowly renewing tissues, some cells may never be replaced at all. When $t_0 > 0$, to simplify the notation, we will shift the age of the individual by t_0, so that $t = 0$ corresponds to the start of development.

H3 Time-dependent birth rate. Cell renewal can be affected by factors external to the tissue, such as aging of the individual, change in lifestyle (diet, exercise, drug treatment), or accident. To reflect these extraneous factors, we assume that the birth rate $\beta \geq 0$ depend on

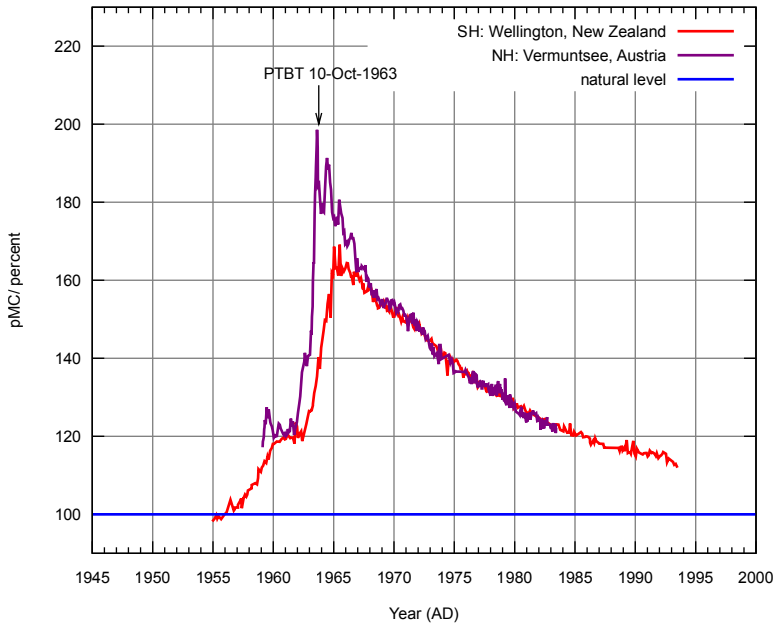

Figure 6.1: Atmospheric 14C, New Zealand and Austria. By Hokanomono. Data from the following sources: Manning, M.R., and W.H. Melhuish. 1994. Atmospheric 14C record from Wellington. In Trends: A Compendium of Data on Global Change. Carbon Dioxide Information Analysis Center, Oak Ridge National Laboratory, U.S. Department of Energy, Oak Ridge, Tenn., U.S.A.Levin, I., B. Kromer, H. Schoch-Fischer, M. Bruns, M. Münnich, D. Berdau, J.C. Vogel, and K.O. Münnich, 1994. δ14CO2 record from Vermunt. In Trends: A Compendium of Data on Global Change. Carbon Dioxide Information Analysis Center, Oak Ridge National Laboratory, U.S. Department of Energy, Oak Ridge, Tenn., U.S.A., Public Domain, https://commons.wikimedia.org/w/index.php?curid=634564

the age of the individual t. All cells are born with an age 0. We suppose $\beta(t)$ independent from the state of the cell population.

Under normal conditions, the time scale of the cell renewal dynamics is in years, but it may happen that sharp changes in cell number occurs almost instantly, after a stroke, or after a surgical intervention. To account for that fact, in general we assume that γ and β are generalized functions (or distributions).

6.2 Renewal equations

The Birth-and-Death model can be implemented as a linear first-order transport PDE with a linear death rate. Let n be the density of cells of age a in an individual of age t. Cell age a is the **chronological age**, i.e. the time elapsed since their last division, so the rate of aging is $da/dt = 1$. The **renewal equation** is

$$\frac{\partial n}{\partial t}(a,t) + \frac{\partial n}{\partial a}(a,t) = -\gamma(a,t)n(a,t) \tag{6.3}$$

on $a \in \Omega =]0, +\infty]$, for $t > 0$. We specify the initial boundary value problem with initial conditions $t = 0$ on $a \in \Omega$ and the boundary conditions for $t \geq 0$,

$$n(a, 0) = 0, \text{ for } a \in \Omega, \tag{6.4}$$

$$n(0, t) = \begin{cases} N_0 \delta(a) & \text{if } t = 0, \\ \beta(t) & \text{if } t > 0. \end{cases} \tag{6.5}$$

The death rate in the right-hand-side of equation (6.3) comes from H1. The Dirac mass δ in equation (6.5) comes from H2. The boundary condition $\beta(t)$ (6.5) comes from H3. The initial boundary value problem naturally satisfies the compatibility condition at $(a = 0, t = 0)$, even though it is not continuous at that point. Equation (6.3) is hyperbolic, and it propagates the regularity of the initial and the boundary conditions. The solution n defined on $\bar{\Omega}$ is expected to have the same regularity as the boundary condition. We want to make jumps (discontinuities) possible in the solution, either by adding or removing a certain number of cells. An appropriate way to add cells at certain points this is by letting β take singular values at a finite number of time points, i.e. β is a sum of a locally integrable function and Dirac masses. In the same way, removing cells can be done by letting γ be a sum of a locally integrable function and Dirac masses. We can choose β in the space of distributions $H^s(]0, T])$ with $s < -1/2$, and $\gamma \in H^s(]0, T],]0, T])$, spaces that contain Dirac masses. This is suitable if we look for weak solutions, for we are interested in evaluating 14C levels with equation (6.2). For all continuous and bounded functions f ($\in H^s(\mathbb{R})$, $s > 1/2$) and for all $t \geq 0$, the operator $\langle u_t, f \rangle$, with $u_t = n(a, t)/N(t)$ is linear and continuous. It is easily checked that $C = \langle u_t, f \rangle$, with $f(a) = K(d - a)$ satisfies $\min_{a \in [0,t]}\{f(a)\} \leq C \leq \max_{a \in [0,t]}\{f(a)\}$.

There exists a weak solution $n \in H^s(\Omega \times]0, T[)$ to the initial boundary value problem (6.3–6.5) if, for any $\varphi \in C_0^\infty(\Omega)$ and $t \in]0, T[$,

$$\int_\Omega \partial_t n \varphi da - \int_\Omega n \partial_a \varphi da = -\int_\Omega \gamma n \varphi da.$$

Theorem 1 *Set $-1 < s < -1/2$ and $T > 0$. Let $\beta \in H^s(]0, T[)$ and $\gamma \in H^s(\Omega \times]0, T[)$ be positive distributions. The initial boundary value problem (6.3–6.5) has a unique weak (or mild) solution $n \in H^s(\Omega \times]0, T[)$,*

$$n(a, t) = \begin{cases} \beta(t - a) \exp\left(-\int_0^a \gamma(t - a + s, s) ds\right) & \text{if } 0 < a < t, \\ N_0 \delta(a - t) \exp\left(-\int_0^t \gamma(s, s) ds\right) & \text{if } a \geq t. \end{cases} \tag{6.6}$$

The solution extends trivially to the boundary $\{0\} \times]0, T[$, where $n(0, t) = \beta(t)$. The total cell number $N(t) \in H^{s+1}(]0, T[) \subseteq L^q(]0, T[)$, for $q \leq +\infty$, and

$$N(t) = N_0 e^{-\int_0^t \gamma(s,s) ds} + \int_0^t \beta(t - a) e^{-\int_0^a \gamma(t-a+s,s) ds} da.$$

Proof 1 *The solution (6.6) is found by integrating along the characteristics $t = a + t_0$, with $0 \geq t_0 < T$. Note that if $\gamma \in H^s(\Omega \times]0, T[)$, then $\exp\left(-\int_0^a \gamma(t - a + s, s) ds\right) \in H^{s+1}(\Omega)$ and take values in $[0, 1]$. Multiplying β with this distribution does not change its regularity, so n is at least as regular as β for $a < t$ and as δ at $a = t$, and consequently, $n \in H^s(\Omega \times]0, T[)$. Extension on the boundary is obtained by extending along the characteristics.*

A particular situation of interest is when the cell number is assumed not to change significantly: $dN(t)/dt = 0$, for $t > 0$. This means that all dying cells are replaced, leading to a **Volterra equation** (of the second kind) on β,

$$\beta(t) = N_0 v(t, t) + \int_0^t v(t - a, t) \beta(a) da, \ t > 0, \tag{6.7}$$

where

$$v(a,t) = \gamma(a,t)\exp\Big(-\int_0^a \gamma(t-a+s,s)ds\Big). \tag{6.8}$$

There is no closed form solution in general for this equation, but it can easily be solved numerically. Existence and uniqueness of the solution to the Volterra equation for a continuous function $v(a,t)$ can be shown, (see for instance [40]).

Another situation of interest is when different subsets of cells with different renewal capacities are present in the sample. This happens for instance when the sample is spatially heterogeneous. In that case, a spatial or type structure $x \in [0,1]$ can be introduced, so that $n_x(a,t)\mathrm{d}x$ is the cell density of type. In case a finite number of types are present, a discrete index j can be used: $n_j(a,t)$ is the cell density of type j, $j = 1,..,m$. For each cell type, β and γ and N_0 are parametrized with the cell type index j, but cell cannot move from one type or another (no-transdifferentiation or movement) and each cell subset evolves independently of the other ones. Therefore the total cell density

$$n(a,t) = \sum_{j=1}^{m} n_j(a,t),$$

where each $n_j(a,t)$ is solved independently.

6.3 14C model and data

Samples come in the form (c_i, b_i, d_i), for individual i, $i = 1,...,n$, where c_i is the 14C level in the sample of interest, b_i is the birth date of the individual, and d_i is the date of collection of the biological sample. The collection date is the date at which we can assume that there is no more 14C exchange in the sample. For individuals aged $t_i = d_i - b_i$, $i = 1,...,n$ at date of collection, the problem is to find γ and β such that the predicted 14C levels $\tilde{c}_i$ are close to the measured levels c_i. We distinguish the global problem, in which we try to find a single γ and β that fits well the 14C for the all individuals, in the least-square sense

$$SSE = \sum_{i=1}^{n} w_i^2 \big(c_i - \tilde{c}_i\big)^2 \tag{6.9}$$

from the individual problem, in which we try to find γ_i and β_i for individual i that matches the 14C levels, $c_i = \tilde{c}_i$. The weights w_i, can be related to the experimental error on the measurement c_i, or to other "confidence" measure on the data. The mass of carbon measured, for instance, is a good indicator of the confidence that can be put in a sample measurement.

Equation (6.2) suggests that, at best, the 14C level provides information on the average age of the distribution $n(a,t)$. Therefore, it is unlikely, in practice, that much information about the shape of $n(a,t)$ can be extracted from the 14C data, even when the 14C level is available for wide ranges of ages t.

6.4 Nonlinear fitting strategies

To find birth and death rates that reproduce well the experimental data, it seems fair to parametrize β and γ: $\beta = \beta(t;\theta)$ and $\gamma = \gamma(a,t;\theta)$, where θ is a vector of real-valued parameters of size p. The **least-square problem** becomes: find $\theta \in \mathbb{R}^p$ such that the *SSE* (6.9) is minimized (locally).

The individual problem becomes: find $\theta \in \mathbb{R}^p$ such that $\tilde{c}_i(\theta) = c$. The least-square problem has always at least one solution, but the individual problem has in general two solutions, even for $p = 1$, given that the bomb curve is not monotonous. For the individual problem, we restrict ourselves to parametric models with $p = 1$.

The general strategy for finding adequate rates is to start with simple models, or **scenarios**, with few parameters, and to improve the goodness-of-fit by increasing the complexity of the scenarios. The **corrected Akaike Information Criterion** (AIC_c) is a useful tool to compare scenarios that have different numbers of parameters. The AIC_c is

$$AIC_c = n \log\Big(\frac{SSE}{n}\Big) + 2p + \frac{2K(K+1)}{n-K-1},$$

where n is the number of samples to fit and K the total number of parameters in the model, which also includes the unknown variance of the least-square, SSE/n, so that $K = p+1$, [23]. The third term accounts for the correction in the AIC_c, and penalizes scenarios with large numbers of parameters. This term is non-negligible when n is small, as it can be here.

The simplest model has a single parameter, a constant death rate: $\gamma(a,t) = \gamma$. The birth rate is set so that the total cell number is constant: $\beta = N_0\gamma$. In that case, the death rate γ is called **turnover rate**. The turnover rate corresponds approximately to the fraction renewed each year. The term turnover rate is also more loosely applied when the $N(t)$ is not constant but is only changing slowly.

6.5 Cardiomyocyte renewal in humans

The heart has a very limited regenerative capacity. After a stroke, the damaged tissue loses cardiomyocytes, the heart muscle cells, and consequently the pumping capacity is impaired. The heart heals by scaring and forming fibrous tissue instead of regenerating cardiomyocytes. Stem cell-based therapies aim improving heart capacity by inducing cardiomyocyte regeneration. Whether the heart has an endogenous potential for cardiomyocyte regeneration is fundamental for the success of these therapies.

The renewal capacity of the heart in human has been debated over the past few years. The 14C dating method provides a robust way to measure slow turnover rates. The method has been applied to measure the renewal rates in cardiomyocytes in healthy individual with wide range of age [11, Article in Section 9.2] and [13]. We explored several scenarios for the dynamics of cardiomyocyte renewal. The best scenario, based on goodness-of-fit, self-consistency and current knowledge, showed that turnover rates vary from around 1–2% per year in young adults and decreases slowly to reach around 0.5% in older individuals. The main challenge regarding modeling is to reconcile 14C samples from pre-bomb subjects (born before 1955) and from post-bomb subject (born after 1963). Fitting either group alone is very easy, but it is important to find a scenario that can recapitulate both group in a consistent way. A further issue with cardiomyocytes is that they polyploidize, i.e. they duplicate their DNA without mitosis or cell division, resulting in cell nuclei with 4 or 8 pairs of chromosomes. This has a direct impact on the interpretation of the 14C levels in DNA, which is likely to be much younger than the cell. A second issue is that one can ususally find two different turnover rates for pre-bomb subjects, one corresponding to very young cells and one corresponding to (very) old cells. This has been a source of confusion, leading some to conclude to increasing renewal rates in older subjects [38, 29].

We applied renewal models to other tissues, adipocytes (fat cells) [57] and lipids [5]; neurons of the hippocampus [58], striatum [31], and olfactory bulb [12], and the cortex [37]; oligodendrocytes [70]. Most of the measurements have been done in healthy subjects. The challenge is now to extend the results to pathological cases and to assess how cell renewal is affected.

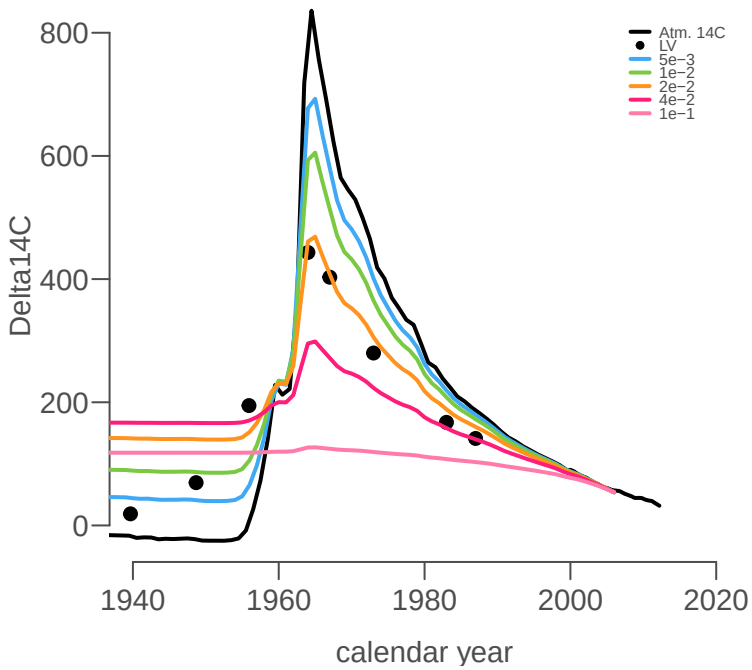

Figure 6.2: Atmospheric 14C profiles for different turnover rates. The atmospheric 14C levels between shows a steep rising phase between 1955 and 1963, and a slow decrease since then [44]. A tissue formed at a given calendar year and turning over at a constant rate will show a 14C content different from the atmospheric levels. The theoretical 14C levels are shown for 5 different turnover rates (per year): 1e-3 (*blue*), 1e-2 (*green*), 2e-2 (*orange*), 4e-2 (*red*), 1e-1 (*pink*). 14C content in left ventricle cardiomyocytes DNA from 12 subjects are plotted against the date of birth [11]. No single turnover rate can fit 14C levels from subjects born before 1955.

6.6 Tumor-immune interaction in chronic myelogenous leukemia

Chronic myelogenous leukemia (CML) is a haematopoietic stem cell disorder due to a chromosomal translocation that creates a chimeric gene from the fusion of genes *Bcr* and *Abl*. The development of the targeted CML treatment Imatinib revolutionized cancer treatment paradigms. Imatinib inhibits leukemic cell expansion durably, transforming a life-threatening disease into a chronic but asymptomatic condition. There is evidence that Imatinib cannot eradicate the disease, as BCR-ABL transcripts can still be detected in the blood of otherwise asymptomatic patients. Yet, recent clinical trials showed that a significant fraction of patients who responded well to Imatinib or similar drugs could discontinue treatment without compromising remission [47]. The immune system as been implicated in long-term remission.

A Besse [22, Article in Section 9.4] investigated under which conditions long-term remission could be explained by the immune system. The model describes proliferation and expansion of leukemic stem cells y_1, circulating leukemic cells y_2, and immune cells z. The three populations are described by a system of ODEs,

$$\frac{dy_1}{dt} = ry_1\left(1 - \frac{y_1}{K}\right) - \mu y_1 z, \tag{6.10}$$

$$\frac{dy_2}{dt} = \frac{a_1}{k_{inh}} y_1 - d_2 y_2 - \mu y_2 z, \tag{6.11}$$

$$\frac{dz}{dt} = s - f(y_2)z. \tag{6.12}$$

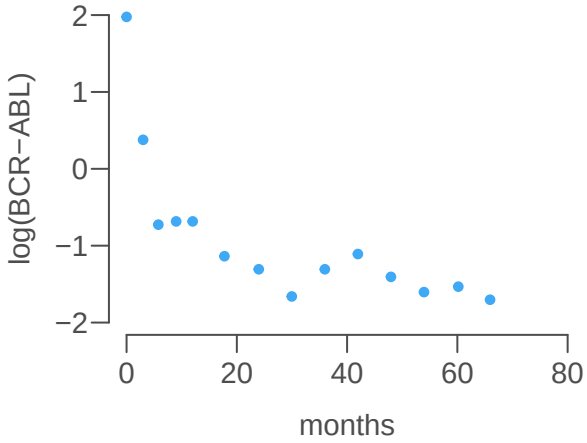

Figure 6.3: Log(BCR-ABL) levels during treatment (data from [27]).

This model is a reduced version of a model published previously [27]. The stem cell density self-renews and produces circulating leukemic cells. Immune cells are activated at a basal rate s and kill leukemic cells at a density-dependent rate μ. Immune cells also interact with leukemic cells through the term $f(y_2)z$. This term is the combination of two mechanisms. At low tumor density (y_2 small), f is just the natural immune cell death rate, so $f(0) > 0$. We assume that small tumors can induce a immune response, but larger tumors inhibit immune system. In term of functional form for f, this means that f is first decreasing (immune response) and then increasing (inhibition). If $d > \mu s/r$, the disease-free steady state $y_1 = 0, y_2 = 0, z = s/f(0)$ is unstable. Then, the existence and stability of the steady states depend on the number of zeros of f:

i) No zero, inability of the immune system to mount a proper response. There is a single, large stable disease steady-state $\bar{y}_2 > 0$.

ii) One zero y_{min}, effective immune response at all tumor densities. There is possibly a single low, stable disease steady state $\bar{y}_2 < y_{min}$.

iii) Two zeros $y_{min} \leq y_{max}$, effective immune response at low tumor density and inhibition at high densities. There are possibly several disease steady-states with $\bar{y}_2 \geq y_{max}$. The low disease steady-state $\bar{y}_2 \leq y_{min}$ can co-exist.

Based on the above steady state analysis, we may speculate that the large steady states for y_2 correspond to an untreated state, and that the low steady state corresponds to a remission state. When treatment is applied, the large steady state disappear, leaving the low disease steady state as the only stable state. It is hoped that treatment discontinuation preserves the low disease steady state and the remission.

One prediction of this model is that for a wide range of parameters, the low disease steady state, corresponding to remission, is a weakly attracting focus. This is similar to other tumor-immune interaction models [42]. It looks like in some treated patients, BCR-ABL transcript oscillate around low levels, even though the sampling frequency is not high enough to formally detect periodic behavior (Figure 6.3).

Chapter 7

Integrative and multiscale approaches

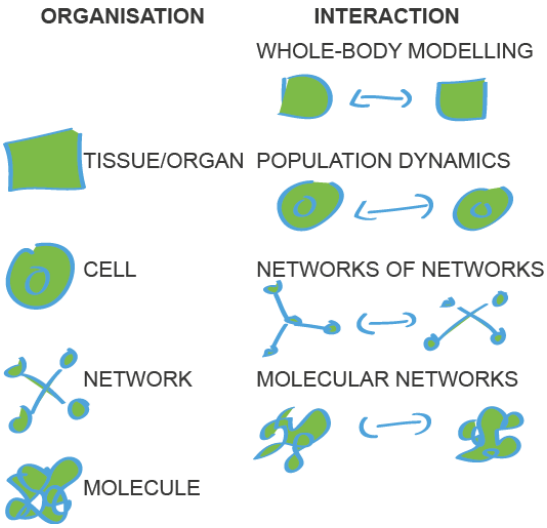

Figure 7.1: Organisation and interaction scales in biology. The key question in multiscale modeling is how to bridge the interaction (e.g. molecular networks) and the organization levels (e.g. the cell).

7.1 Multiscale modeling in biology

In this chapter we discuss some thoughts on multiscale and integrative modeling in biology. Most of these ideas are presented in reference [14]. The main problem we face in building multiscale models is linking or bridging the scales. Assuming the state of a cell at time t is $X(t) \in \mathbb{R}^d$, what can be said about the fate of the cell (Figure 7.1)? Even with a detailed model of the molecular processes going on inside the cell, it is difficult to infer the fate of the cell unambiguously. This is mainly because most of the existing data are based on average population measurements. If we are interested in a finite set of phenotypes Φ (survival, death, division, migration, etc), can we specify a deterministic function $F : \mathbb{R}^d \to \Phi$, or should we specify transition intensities $\lambda_{i,j}(X)$ from phenotype i to phenotype j, and treat cell phenotype as a stochastic process? Averages do not translate very well into discrete events such as cell division or death. It would seem best to link the fate of a cell to a probabilistic law based on the molecular state rather than a deterministic function.

Yet in practice assigning deterministic fate works quite well. In this chapter, we discuss two applications of integrative models: the regulation of mammalian cell cycle progression in the regenerating liver [25, Article in Section 9.5] and the how interaction between the circadian clock and cell cycle affects cell population growth rates [28, Article in Section 9.6]. Both are based on deterministic fate functions.

7.2 The cell division cycle and the circadian clock

At the molecular level, cell division is orchestrated by cell-cycle dependent oscillations of cyclin and cycling-dependent kinase (CDK) protein levels. Their sequential activation produces a well ordered succession of cell cycle phases: growth or first gap phase G1, DNA synthesis S, second gap phase G2, and mitosis M. Progression in the cell cycle is gated by the circadian clock. In hepatocytes, cell cycle protein Wee1 expression is clock-controlled; its expression oscillates with a 24-h period. Wee1 delays entry of the cells into mitosis, and a 24-h modulation has been shown in the timing of cell division [48]. Incidentally, reference [48] is one of two papers published within

weeks by Okamura's lab that provided much of my motivation for modeling the circadian clock. The other is reference [69].

We have explored the link between the cell cycle and the circadian clock. In a study with A. Chauhan [25, Article in Section 9.5], we looked at how cell division during liver regeneration is gated by the circadian clock based on a molecular model of the cell cycle. In a second study with R. El Cheikh [28, Article in Section 9.6], we looked at the effect of a disruption of the circadian clock on cell proliferation. Both models are based on the regulation of Wee1 levels by circadian clock genes.

7.3 Circadian clock and liver renewal

After partial hepatectomy (PH), when part of liver is removed, most of the hepatocytes de-differentiate and re-enter the cell division cycle synchronously for one or two rounds to restore liver mass. Matsuo and colleagues [48] have shown that the time of the day at which PH is performed affects how long it takes for cells to enter mitosis, but not DNA synthesis. We have developed an integrated model of the mammalian cell cycle based on sequential activation of cyclins [25]. The model is composed of 26 ODEs and 92 parameters. This might seem rather large, but the model is constructed in several modules: G1-S transition; E2F regulation; Wee1-gating; Mitosis, etc. The model recapitulates the priming and activation of the cell cycle after damage, the entry into G1 and progression through S and M phases and back to the G1 phase.

The model exhibits "bandpass filter" properties that allow cells to be primed only if damage signal is sustained and strong. Cyclin B controls M phase progression. First a switch-like increase in Cyclin B activity promotes entry into mitosis. Then Cyclin B proteolysis promotes exit from mitosis. Cyclin B total concentration and activities are finely tuned by several mechanisms. Two feedback loops control Cyclin B activity. First a double negative feedback loop from inhibitor Wee1, and a positive feedback loop from the activating phosphatase Cdc25. Total Cyclin B concentration is regulated through synthesis by E2F, and through degradation by APC^{Cdh1} and APC^{Cdc20}. A bifurcation analysis showed the presence of two threshold mechanisms controlling the progression of the cells through M phase. Cyclin B activation depends first on reaching a concentration high enough. This occurs through a transcritical bifurcation with respect to E2F. Cyclin B activation is maintained via positive loops. APC^{Cdc20} is then responsible for Cyclin B degradation. This induces a hysteresis, whereby Cyclin B activity shows bistability for a wide range of degradation rates. When we simulated the entrainment of the light-dark cycle by varying Wee1 synthesis, we could reproduce the 8h-delay in mitotic entry observed experimentally by Matsuo et al. [48].

7.4 Modulation of cell population growth under circadian clock control

Cell population growth rate depends not only on the mean interdivision intervals but also on the variability of the intervals. In a cell population with a distribution on interdivision intervals, faster cells contribute more to the population than their nominal share, resulting in an asymmetry in the growth rates. Likewise, variable (but determined) interdivision intervals also affect the population growth rate. Several studies have shown that in mammals, the cell cycle is gated by the circadian clock. It has been suggested that this gating could serve as a tumor suppressor [33], or enhance tissue regeneration after injury or during homeostasis [48]. The limited tissue regeneration capabilities in mammals has been explained by the need to keep tumor growth in check, so it is surprising that the same mechanism could account for both tissue regeneration and tumor

suppression abilities. Two independent factors need to be accounted for in the circadian control: the mean effect of the clock and the effect of the daily variation around the mean. Mathematically it has been shown that when the clock affect the proliferation rate (i.e. the interdivision intervals), there is a natural comparison of the growth rates with and without a clock. At fixed geometric mean effect, the presence of a clock speeds up the growth rate [26]. However, rather than the geometric mean, it is the arithmetic mean we would like to keep constant. In this case there is no systematic inequality in the growth rates, and a circadian variation of the proliferation rate can either speed up or slow down the growth rate. One of the main parameter determining whether the clock has a positive effect on the growth rate is the mean interdivision time. Growth rates will be enhanced for an interdivision times around multiples of 24h, and impaired when the interdivision times are far from multiples of 24h. It is tempting to speculate on an adaptive mechanism by which mammalian cells evolved to divide every 24h. Normal regeneration and homeostasis would be favored by the clock, while abnormal cells with a shortened cell cycle would be suppressed [17].

These theoretical results are based on age-structured population models, in which the cell cycle oscillator is only implicitly defined through the succession of phase transition. In a recent computational study, we explored how a molecular model of the cell cycle could be entrained by a circadian clock oscillator, and how that affected the growth rate at the population level [28]. We confirmed previous theoretical results that intrinsic interdivision times close to multiples of 24h are beneficial. This is remarkable, because our results imply that absolute growth rates can be *slower* in a population of fast cycling cells compared to slower cells. This effect is independent of cell death. The reason for that is that by cell division gating by the clock prevent a certain fraction of the otherwise fast cycling cells from progressing through the cell cycle. Therefore, although both autonomous single cells and cell population show rapid cycling, the resulting growth rate can be impaired. The opposite effect can also be seen, whereby slow cells can grow faster under circadian entrainment compared to no clock. These computational results emphasize the need for integrative models for understanding the link between molecular events and cell population behavior.

7.5 Simuscale

We have developed over the last few years a modeling framework for simulating multiscale models. *Simuscale* is a versatile multiscale modeling tool for efficient simulation of large, heterogeneous populations of interacting cells. Cells are modeled by visco-elastic balls under mechanical constraints. Each cell possesses an intrinsic intracellular dynamics. The intracellular states are coupled through each other via biochemical signals expressed on the surface of the cells. Macroscopic cell fate (division, death, growth, movement) is entirely dictated by the intracellular state of the cell. Physical and biochemical interactions evolves in a 3D environment. Simuscale takes the form of a *core* simulation engine on top of which biological model plug-ins can be added. Plug-ins are meant to be interoperable, so that different plug-ins (say, one for tumor cells and one for immune cells) can be used together without any problem. This feature relies on the fact that all cells share common properties: position, size, mechanical properties, and biochemical signals. The intracellular dynamics is encapsulated in each cells, so different types of formalism (e.g. Boolean networks, ODEs, stochastic differential equations, etc) can co-exist. This reduces the need for re-implementing existing models.

Simuscale is still in active development (Simuscale is hosted at `https://gforge.inria.fr/projects/simuscale`). As a proof-of-concept, we implemented the circadian clock model developed in [20] and coupled the cells through the diffusible factor. In addition to possess a circadian clock, cells were endowed with a basic molecular cell-cycle network

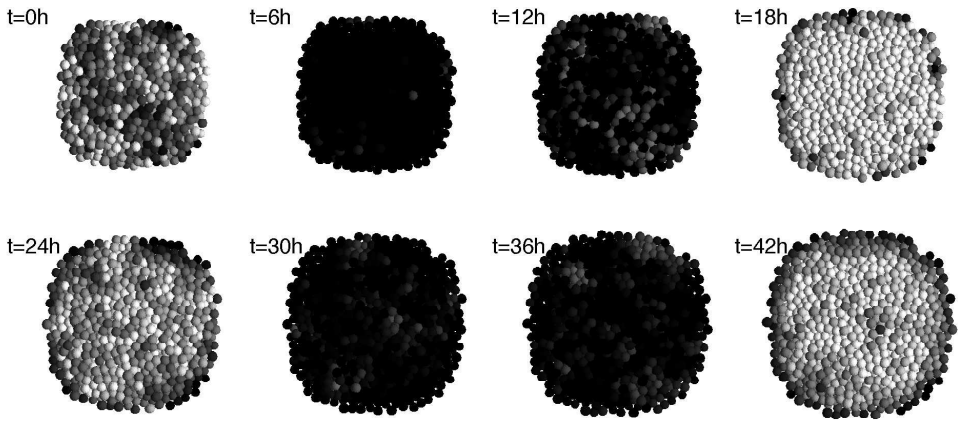

Figure 7.2: Synchronization of circadian clock in a proliferating cell population with *Simuscale*. Cells (*small balls*) is modeled as an visco-elastic ball. They can move but adhere to each other. They grow by random volume increments and divide according to a small cell-cycle network (approximately every 60h). The circadian clock comes from [20, Article in Section 9.3] Cells express a clock marker (represented by cell shading: *dark grey*, low levels; *light grey*, high levels). The circadian clock is coupled through cell-to-cell contact; cells sense the clock marker of their neighbors. Cells show a high degree of synchronization with a period of $\sim 24h$, despite the fact that they grow, move and divide.

[8], which determined the timing of cell division. Model parameters in each cells were perturbed to introduce cell-to-cell variability. Simulations show that cells divide in waves, and that the circadian clocks in each cell can synchronize when coupled locally, even in a population of several hundred cells (Figure 7.2).

Chapter 8

Outlook

I have tried while writing this thesis to patch holes in the published results, but I probably just managed to paper over the cracks. I leave several unanswered questions behind. How can we approximate nonlinear system of ODEs by scalar delay equations? What is the effect of distributed delays on positive feedback loops? How to make more rigorous statements on the robustness of synchronization of damped oscillators? Is it possible to make formal parameter identification for the 14C data? Can we solve the inverse problem for general birth and death functions?

I have tried to give in this thesis a sense of direction in my research that leans towards integrative and multiscale modeling. Multiscale modeling (in a wide sense) in biology is essential to understand what emerges from the complex interactions at the different organization levels. There is often a mismatch between available data or knowledge and the biological process of interest. For instance, genomic data on cancer provide a detailed picture of the heterogeneity present in tumor cells. However, cancer is a complex system, often likened to a ecological system, and the question of interest, whether the tumor will grow, is only remotely linked to any particular genetic profile.

We presented here two computational examples showing how problematic it can be to assign any particular outcome at the population level from an intracellular state. In the first example, we showed how a single-cell phenotype, a *damped oscillator*, could lead to a larger amplitude oscillations and more robust synchronization when observed in a population (Figure 8.1, left). Several experiments have supported this view of how clock neurons synchronize in the SCN.

In the second example, we have shown, using a computational model, that the growth rate of a cell population could be slowed down or sped up depending on the status of the circadian clock, is a way that cannot be inferred intuitively from the intracellular behavior of single cells (Figure 8.1, right). Theses results show that, if growth rate is used as a proxy for tumorigenesis, the circadian clock can be a tumor suppressor or promoter.

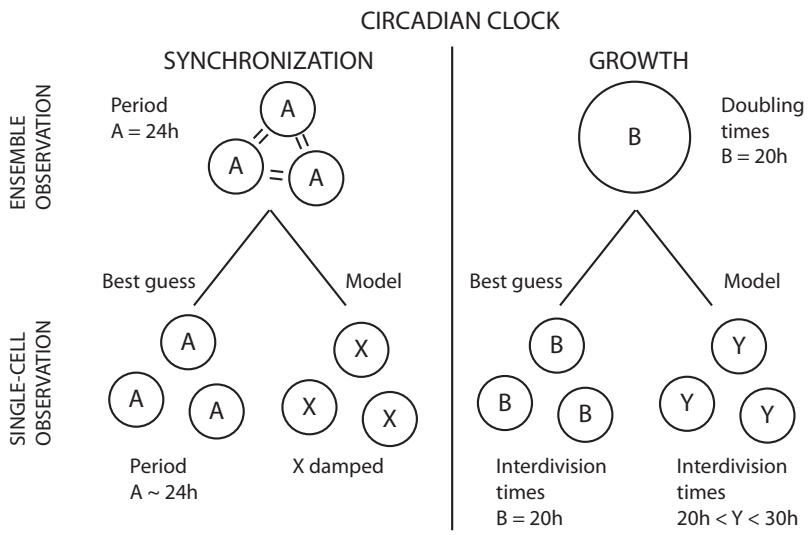

Figure 8.1: (Left) Synchronization in clock neurons. Ensemble observation of period $A = 24$h leads to *best guess* that each oscillator has a period similar to A. *Model* shows oscillators can be damped (X). (Right) Growth under circadian clock. Ensemble observation of doubling times $B = 20$h leads to *best guess* that single cells have an interdivision time similar to B. *Model* shows interdivision times Y can be anywhere between 20 and 30h.

In the synchronization examples, cell-cell communication is the key factor, while in the cell proliferation example, the key factor is the way the molecular network of the cell cycle couples with the actual cell division. These two types of coupling, between objects at the same levels, and

between levels, are the hallmarks of multiscale systems. Simuscale has been developed to make coupling among and between levels easy. With the help of such simulation tools, I expect more example of systems that are highly multiscale in nature to be uncovered. Two applications come to mind. First, an integrated model for the regulation of the adipose tissue. The rising prevalence of obesity in several parts of the world, and the difficulty to lose weight and maintain a healthy weight shows that this is a complex problem with no easy solution. The second application is of course cancer. How interactions between tumor cells and the host lead to malignant growth has been an important topic in mathematical biology for decades. It is becoming clear that integrative models are needed to progress in the understanding of the disease [1].

Even with all the potential for discovery, it is important to remain cautious about the real contribution of multiscale models in understanding complex system. Multiscale models are difficult to implement, and several non-trivial choices have to be made in terms of modeling formalism, coupling methodologies, spatial characterization, etc. In contrasts to single-scale models, it is hard even to list all the modeling assumptions. How do they affect the results is therefore impossible to assess. This makes predictions risky. This is why the development of simulation frameworks can help, by making modeling assumptions clearer, and speeding up the development and testing phases. Multiscale models are also hard to replicate. The codes are not always available to the community and the re-implementation of the model from scratch is usually impossible because not all information is specified or accurate in the publications. There are welcomed initiatives for curating multicellular data [32]. Such tools could be used to make simulation data and model specification easier to share.

Interaction is at the heart of physiological and pathological cell population dynamics. The computational results presented here show that our intuition is not sufficient to deal even with relatively simple interactions. Integrative computational models will be useful for exploring and testing hypotheses against our intuition.

Chapter 9

Selected papers

9.1 Bernard S, Crauste F (2015) Optimal linear stability condition for scalar differential equations with distributed delay. Discrete Contin Dynam Systems Ser B 20:1855–1876

DISCRETE AND CONTINUOUS
DYNAMICAL SYSTEMS SERIES B
Volume **20**, Number **7**, September **2015**

doi:10.3934/dcdsb.2015.20.1855

pp. **1855–1876**

OPTIMAL LINEAR STABILITY CONDITION FOR SCALAR DIFFERENTIAL EQUATIONS WITH DISTRIBUTED DELAY

Samuel Bernard and Fabien Crauste

Université de Lyon; CNRS UMR 5208
Université Lyon 1; Institut Camille Jordan
INRIA Team Dracula
43 blvd. du 11 novembre 1918, F-69622 Villeurbanne cedex, France

(Communicated by Tomas Gedeon)

Abstract. Linear scalar differential equations with distributed delays appear in the study of the local stability of nonlinear differential equations with feedback, which are common in biology and physics. Negative feedback loops tend to promote oscillations around steady states, and their stability depends on the particular shape of the delay distribution. Since in applications the mean delay is often the only reliable information available about the distribution, it is desirable to find conditions for stability that are independent from the shape of the distribution. We show here that for a given mean delay, the linear equation with distributed delay is asymptotically stable if the associated differential equation with a discrete delay is asymptotically stable. We illustrate this criterion on a compartment model of hematopoietic cell dynamics to obtain sufficient conditions for stability.

1. **Introduction.** Models of self-regulating systems often include discrete delays in the feedback loop to account for the finite time required to perform essential steps before the loop is closed. Such mathematical simplifications are especially welcome in biological applications, where knowledge about the loop steps is usually sparse. This includes maturation and growth times needed to reach reproductive age in a population [31, 40], signal propagation along neuronal axons [17], and post-translational protein modifications [15, 44]. Introduction of a discrete delay in an ordinary differential equation can destabilize steady states and generate complex dynamics, from limit cycles to chaos [36]. Although the linear stability properties of scalar equations with single discrete delays are fairly well characterized, lumping intermediate steps into a delayed term can produce broad and atypical delay distributions that deviate from discrete delays, and it is still not clear how that affects the stability of the equation [18].

The delayed feedback differential equation of the form

$$\dot{x} = F\Big(x, \int_0^\infty x(t-\tau)d\eta(\tau)\Big)$$

2010 *Mathematics Subject Classification.* Primary: 34K06, 34K20; Secondary: 92C30.

Key words and phrases. Delay differential equations, delay distribution, negative feedback loop, hematopoiesis.

Work supported by ANR grant ProCell ANR-09-JCJC-0100-01.

is a model paradigm in biology and physics [1, 5, 25, 42, 44, 46]. The first argument of F is the instantaneous part of the loop and the second one, the delayed or retarded part, which closes the feedback loop. The integral is taken in the Riemann-Stieltjes sense. The function η is a cumulative probability distribution function, it can be continuous, discrete, or a mixture of continuous and discrete elements. In most cases, the stability of the above equation is related to its linearized equation about one of its steady states $\bar{x}$,

$$\dot{x} = -ax - b\int_0^\infty x(t-\tau)d\eta(\tau) \tag{1}$$

where the constants a and $b \in \mathbb{R}$ are the negatives of the derivatives of the instantaneous and the delayed parts of F at $x = \bar{x}$,

$$a = -\frac{\partial}{\partial x}F(x,y)\Big|_{x=y=\bar{x}} \quad \text{and} \quad b = -\frac{\partial}{\partial y}F(x,y)\Big|_{x=y=\bar{x}}.$$

Eq. (1) is also called a linear retarded functional differential equation. Basic theory for delay differential equations and functional differential equations can be found in [9] and [28]. Additional applications can be found in previously mentioned references and in [24, 36].

Stability analysis of Eq. (1), when the distribution function η differs from the Dirac distribution, has been the subject of several works. In 1989, Boese [16] analyzed the stability of (1) for a Gamma distribution, and determined rather technical sufficient conditions for its asymptotic stability. Kuang [37], in 1994, considered a system of two differential equations with continuous distributed delay, possibly infinite. He focused on the existence of pure imaginary eigenvalues, and determined conditions for their nonexistence, obtaining sufficient conditions for the asymptotic stability of his system. In 2001, Bernard et al [13] considered (1) and determined sufficient conditions for its stability, mainly in the case where the distribution is symmetric about its mean. They then conjectured that the single Dirac measure would be the most destabilizing distribution of delays for (1). Atay [6] recently gave arguments in that direction. He focused on the stability of delay differential equations near a Hopf bifurcation, and for linear delay differential equations, such as (1), he showed that if the delay has a destabilizing effect, then the discrete delay is locally the most destabilizing delay distribution.

Huang and Vandewalle [30] and Tang [50] also analyzed the stability of equations similar to (1). The first authors were interested in the numerical stability of differential equations with distributed delay, but they proposed an interesting geometrical approach to determine conditions for the stability of (1) for a special delay distribution. Unfortunately, their method cannot be generalized to general distributions. In [50], Tang determined sufficient stability conditions for very general differential equations with distributed delay, but his results are very technical and not easy to handle in practice. Adimy et al [1] and Crauste [23] obtained sufficient conditions for the existence of a Hopf bifurcation when the delay density function is decreasing. In [45], Ozbay et al. investigated the stability of linear systems of equations with distributed delays, and applied their results to a model of hematopoietic stem cell dynamics. Considering an exponential distribution of delays, they obtained necessary and sufficient conditions for the stability using the small gain theorem and Nyquist stability criterion. Solomon and Fridman, using Linear Matrix Inequalities, also established sufficient conditions for exponential stability of systems with infinite distributed delays [47]. Berezansky and Braverman recently obtained

sufficient conditions for the stability of non-autonomous differential equations with distributed delay [11, 12].

Finally, let us mention the work of Anderson [2, 3], who focused on the stability of some delay differential equations, called *regulator models*, which are a particular form of (1). The theory developed by Anderson [2, 3] focuses on the properties of the probability distribution η. Although the results of Anderson are only valid for some class of probability measures, they stress the importance of the shape of the delay distribution. Moreover, Anderson mentions that "the more concentrated the probability measure, the worse the stability property of the model" [3].

Although it has been observed that in general a greater relative variance provides a greater stability, a property linked to geometrical features of the delay distribution [2], there are counter-examples to this principle. Yet, as mentioned above, it has been conjectured that among distributions with a given mean, the discrete delay is the least stable one [6, 13]. If this were true, a theorem due to Hayes [29] would provide a sufficient condition for the stability of the trivial solution of delay differential equations independently from the shape of the delay distribution. This conjecture has been proved by Krisztin using Lyapunov-Razumikhin functions when there is no instantaneous part [35], and by different authors for distributions that are symmetric about their means [6, 13, 33, 43]. It is possible to lump the non-delayed term into the delay distribution and use the condition found in [35], but the resulting stability condition is not optimal. Here we prove that the conjecture is true for all delay distributions with exponential tails. That is, for a given mean delay, the scalar linear differential equation with a distributed delay is asymptotically stable provided that the corresponding equation with a single discrete delay is asymptotically stable. This sufficient condition for stability is optimal in the sense that if it is not satisfied, we can find a distribution with distributed delay for which the equation is not stable. To illustrate this general result, we consider a compartment model of hematopoiesis that can be expressed as a scalar differential equation with an arbitrarily complex delay distribution, and we obtain a simple stability condition.

In section 2, we provide definitions and, in Section 3, we set the stage for the main stability results. In section 4, we show that a distribution of discrete delays is necessarily stable when the discrete distribution with a single delay equal to the mean is stable. In section 5, we present the generalization to any distribution, hence showing that distributions with distributed delays provide more stability than the discrete distribution with the same mean. Section 6 is devoted to the presentation of a model for hematopoiesis and the illustration of the stability problem.

2. **Definitions.**

We consider the linear retarded functional differential equation

$$\dot{x} = -ax - b\int_0^\infty x(t-\tau)d\eta(\tau) \tag{2}$$

with real constants a and b. We assume that η is a cumulative probability distribution function: $\eta : [0,\infty) \to [0,1]$ is monotone nondecreasing, right-continuous, $\eta(\tau) = 0$ for $\tau < 0$ and $\eta(+\infty) = 1$. The corresponding probability density functional $f(\tau)$ is given by the generalized derivative $d\eta(\tau) = f(\tau)d\tau$. The following definitions and Theorem 2.4 follow from Stépán [48].

Let B be the vector space of continuous and bounded functions on $[-\infty, 0] \to \mathbb{R}$. With the norm $||\phi|| = \sup_{\theta\in[-\infty,0]} |\phi(\theta)|$, $\phi \in B$, B is a Banach space.

Definition 2.1. The function $x : \mathbb{R} \to \mathbb{R}$ is a solution of Eq. (2) with the initial condition

$$x_\sigma = \phi,\ \sigma \in \mathbb{R},\ \phi \in B, \tag{3}$$

if there exists a scalar $\delta > 0$ such that $x_t \equiv x(t+\theta) \in B$ for $\theta \in [-\infty, 0]$ and x satisfies Eqs. (2) and (3) for all $t \in [\sigma, \sigma+\delta)$.

The notation $x_t(\sigma, \phi)$ is also used to refer to the solution of Eq. (2) associated with the initial conditions σ and ϕ.

Definition 2.2. The trivial solution $x = 0$ of Eq. (2) is stable if for every $\sigma \in \mathbb{R}$ and $\varepsilon > 0$ there exists $\delta = \delta(\varepsilon)$ such that $||x_t(\sigma, \phi)|| < \epsilon$ for any $t \geq \sigma$ and for any function $\phi \in B$ satisfying $||\phi|| < \delta$. The trivial solution $x = 0$ is called asymptotically stable if it is stable, and for every $\sigma \in \mathbb{R}$ there exists $\Delta = \Delta(\sigma)$ such that $\lim_{t\to\infty} ||x_t(\sigma, \phi)|| = 0$ for any $\phi \in B$ satisfying $||\phi|| < \Delta$.

Definition 2.3. The function $D : \mathbb{C} \to \mathbb{C}$ given by

$$D(\lambda) = \lambda + a + b \int_0^\infty e^{-\lambda\tau} d\eta(\tau),$$

is called the characteristic function of the linear equation (2). The equation $D(\lambda) = 0$ is called the characteristic equation of (2).

The following theorem [26, 48] gives a necessary and sufficient condition for the asymptotic stability of $x = 0$.

Theorem 2.4. *Suppose that there exists $\nu > 0$ such that the following inequality is satisfied:*

$$\int_0^\infty e^{\nu\tau} d\eta(\tau) < \infty. \tag{4}$$

The solution $x = 0$ of Eq. (2) is (exponentially) asymptotically stable if and only if all roots of the characteristic equation $D(\lambda) = 0$ have $\Re(\lambda) < 0$.

Theorem 2.4 is equivalent to the statement that solutions of Eq. (2) of the form $x(t) = \sum_{i=1}^\infty \nu_i(t) e^{\lambda_i t}$ where λ_i are the roots of the characteristic equation and $\nu_i(t)$ polynomials, are enough to determine the stability of $x = 0$. Other solutions, the small solutions, decay faster than any exponential; hence the exponential stability.

Inequality (4) implies that the mean delay value is finite,

$$E := \int_0^\infty \tau d\eta(\tau) < \infty.$$

We assume in the following that inequality (4) is always satisfied. For more details concerning retarded functional differential equations with infinite delays, see [26, 27].

When η represents a single discrete delay (η a heaviside function), the asymptotic stability of the zero solution of Eq. (2) is fully determined by the following theorem, originally due to Hayes [29].

Theorem 2.5. *Let $f(\tau) = \delta(\tau - E)$ a Dirac mass at E. The zero solution of Eq. (2) is asymptotically stable if and only if $a > -b$ and $a \geq |b|$, or if $b > |a|$ and*

$$E < \frac{\arccos(-a/b)}{\sqrt{b^2 - a^2}}.$$

More generally, the following statements always hold for any delay distribution:

(i) When $a \leq -b$, the characteristic equation of Eq. (2) has a positive real root.

(ii) When $a \geq |b|$ and $a > -b$, the characteristic equation of Eq. (2) has no root with positive real part.

Therefore, the stability of the solution $x = 0$ depends on the delay distribution only in the parameter space region $b > |a|$ and, from now on, we restrict the stability analysis to that region.

Assuming $b > 0$ and making the change of timescale $t \to bt$, we have $a \to a/b$, $b \to 1$ and $\eta(\tau) \to \eta(b\tau)$. Eq. (2) can be rewritten as

$$\dot{x} = -ax - \int_0^\infty x(t-\tau)d\eta(\tau). \tag{5}$$

The delay distributions affect the stability of Eq. (5) when $a \in]0, 1[$.

The characteristic equation is called stable if all roots have $\Re(\lambda) < 0$ [48]. To emphasize the relation between the stability and the delay distribution, we give a similar definition for the delay distribution.

Definition 2.6. The delay distribution η (or the density f) is called stable if all roots of the characteristic equation of Eq. (2), or Eq. (5), have $\Re(\lambda) < 0$. The delay distribution η (or the density f) is called unstable if there exists a characteristic root with $\Re(\lambda) > 0$.

According to Theorem 2.4 and using Definition 2.6, the solution $x = 0$ of Eq. (5) is asymptotically stable if and only if the delay distribution is stable. The characteristic equation of Eq. (5) is

$$D(\lambda) = \lambda + a + \int_0^\infty e^{-\lambda\tau} d\eta(\tau) = 0. \tag{6}$$

The integral term in Eq. (6) is the Laplace transform $\mathcal{L}$ of the distribution η. Along the imaginary axis $\lambda = i\omega$, the Laplace transform can be expressed as $(\mathcal{L}\eta)(i\omega) = C(\omega) - iS(\omega)$, where

$$C(\omega) = \int_0^\infty \cos(\omega\tau)d\eta(\tau), \qquad S(\omega) = \int_0^\infty \sin(\omega\tau)d\eta(\tau).$$

The strategy for determining the stability of distributed delays is the following. We use a geometric argument to bound the roots of characteristic equation (6) by the roots of the characteristic equation for a single discrete delay. More precisely, we will show that if the leading roots associated to the discrete delay are a pair of imaginary roots, then all the roots associated to the distribution of delays have negative real parts. We first state, in Section 3, a criterion for stability: if $S(\omega) < \omega$ whenever $C(\omega) = -a$, then the distribution is stable. We then show in Theorem 4.5 that a distribution of n discrete delays is more stable than a certain distribution with two delays (in the sense that $S(\omega) \leq S^*(\omega)$, where the distribution with n delays is denoted by η and the "special" distribution with two delays by η^*). We construct this most "unstable" distribution and determine that only one of the delays is positive, so that its stability can be determined using Theorem 2.5. We then generalize for any distribution of delays in Section 5.

3. General stability criteria.

Assume $a \in]-1, 1[$, and let η be a distribution with mean E. We consider the family of distributions, scaled with the parameter $\rho \geq 0$,

$$\eta_\rho(\tau) = \begin{cases} \eta(\tau/\rho), & \rho > 0, \\ H(\tau), & \rho = 0, \end{cases} \tag{7}$$

where $H(\tau)$ is the step or heaviside function at 0, corresponding to a single discrete delay vanishing at $\tau = 0$. The distribution η_ρ has a mean $\rho E \geq 0$. The notation D_ρ is used to refer to the characteristic equation associated with the scaled distribution η_ρ. The characteristic equation for the distribution η_0 is $D_0(\lambda) := \lambda + a + 1 = 0$.

The next proposition provides a necessary condition for instability. It is a direct consequence of Theorem 2.19 in [48].

Proposition 1. *If the distribution η is unstable, then there exists $\omega_s \in (0, \omega_c]$, $\omega_c = \sqrt{1-a^2}$, such that $C(\omega_s) = -a$ and $S(\omega_s) \geq \omega_s$.*

Proof. Suppose that the distribution η is unstable, i.e. that the characteristic equation has roots λ with $\Re(\lambda) \geq 0$. Consider the family of scaled distributions η_ρ. The roots of the characteristic equation $D_\rho = 0$ depend continuously on the parameter ρ and roots with positive real parts can only appear by crossing the imaginary axis. The scaled distribution η_ρ is stable for $\rho = 0$ (the only root is $\lambda = -(a+1) < 0$) and unstable for $\rho = 1$. Hence there exists a critical value $0 < \rho \leq 1$ at which η_ρ loses its stability, and this happens when the characteristic equation $D_\rho(\lambda) = 0$ has a pair of imaginary roots $\lambda = \pm i\omega$, with $\omega \geq 0$. Splitting the characteristic equation in real and imaginary parts, we have

$$\begin{cases} \Re(D_\rho(i\omega)) &= \displaystyle\int_0^\infty \cos(\omega\tau) d\eta_\rho(\tau) + a = 0, \\ \Im(D_\rho(i\omega)) &= \omega - \displaystyle\int_0^\infty \sin(\omega\tau) d\eta_\rho(\tau) = 0. \end{cases} \tag{8}$$

Since $-\omega$ satisfies the above system, we only look from now on and throughout this manuscript to positive values of ω. The upper bound on ω, $\omega_c = \sqrt{1-a^2}$, is obtained by applying Cauchy-Schwartz inequality,

$$a^2 + \omega^2 = \Big(\int_0^\infty \cos(\omega\tau) d\eta_\rho(\tau)\Big)^2 + \Big(\int_0^\infty \sin(\omega\tau) d\eta_\rho(\tau)\Big)^2 \leq 1.$$

Rewriting (8) in term of η, we have

$$\int_0^\infty \cos(\omega\rho\tau) d\eta(\tau) = -a, \qquad \int_0^\infty \sin(\omega\rho\tau) d\eta(\tau) = \omega.$$

Finally, setting $\omega_s := \rho\omega$, we obtain $0 < \omega_s \leq \omega \leq \omega_c$ and

$$C(\omega_s) = \int_0^\infty \cos(\omega_s\tau) d\eta(\tau) = -a, \qquad S(\omega_s) = \int_0^\infty \sin(\omega_s\tau) d\eta(\tau) = \omega \geq \omega_s.$$

This completes the proof. □

Proposition 1 provides a sufficient condition for asymptotic stability, stated in the following corollary.

Corollary 1. *The distribution η is stable if one of the two following conditions is satisfied:*

(i) $C(\omega) > -a$ for all $\omega \in [0, \omega_c]$,
(ii) $C(\omega) = -a$, for $\omega \in]0, \omega_c]$, implies that $S(\omega) < \omega$.

The condition $S(\omega) < \omega$ is not necessary for stability, as there are cases where $S(\omega) \geq \omega$ even though the distribution is stable. This happens when an unstable distribution switches back to stability as E is further increased (see [10] or [16]).

4. **Stability of a distribution of discrete delays.** In this section, we show that a distribution with n discrete delays and mean E is more stable than the distribution with a single discrete delay E. It is convenient to represent distributions of discrete delays by their densities. We denote a density of n discrete delays $\tau_i \geq 0$, and weights $p_i > 0$, $i = 1, ..., n$, $n \geq 1$, as

$$f_n(\tau) = \sum_{i=1}^{n} p_i \delta(\tau - \tau_i)$$

where $\delta(\tau - \tau_i)$ is a Dirac mass at τ_i, and

$$\sum_{i=1}^{n} p_i \tau_i = E, \quad \text{and} \quad \sum_{i=1}^{n} p_i = 1. \tag{9}$$

The characteristic equation associated with the density f_n is $D_n(\lambda) = \lambda + a + \sum_{i=1}^{n} p_i e^{-\lambda \tau_i} = 0$. Likewise, we denote

$$C_n(\omega) = \sum_{i=1}^{n} p_i \cos(\omega \tau_i), \qquad S_n(\omega) = \sum_{i=1}^{n} p_i \sin(\omega \tau_i).$$

Following Corollary 1, for f_n to be stable, it is enough to show that $S_n(\omega_s) < \omega_s$ whenever $C_n(\omega_s) = -a$, $\omega_s \leq \omega_c$. We now show that among all distributions satisfying $C_n(\omega_s) = -a$ for a fixed ω_s, there exists a density f^* that maximizes the values of $S_n(\omega_s)$. This density f^* has only one positive delay, making it easy to show that $S^*(\omega_s) < \omega_s$. This would imply that all discrete delay distributions are stable.

Definition 4.1. We define the constants $c \approx 0.7246$ and $\theta_c \approx 2.3311$, where c is the smallest positive value such that $\cos(\theta) \geq 1 - c\theta$ for all $\theta > 0$, found by solving the two equations $c = \sin(\theta)$ and $1 - \theta \sin(\theta) = \cos(\theta)$ for $c > 0$, $\theta > 0$, and θ_c is the positive value for which $\cos(\theta) = 1 - c\theta$. We define the convex function $g(x) : [0, \pi] \to [-1, 1]$ by

$$g(x) = \begin{cases} 1 - cx, & 0 \leq x < \theta_c, \\ \cos(x), & \theta_c \leq x \leq \pi. \end{cases}$$

Convexity implies $g(px_1 + (1-p)x_2) \leq pg(x_1) + (1-p)g(x_2)$, for $p \in [0, 1]$, and $x_1, x_2 \in [0, \pi]$. In addition, we have $g(x) \leq \cos(x)$.

The following lemmas show how to find the distribution that maximizes $S_n(\omega_s)$ for $n = 2$.

Lemma 4.2. *Assume $a \in]-1, 1[$ and $E > 0$ satisfies*

$$E < \frac{\arccos(-a)}{\omega_c}, \tag{10}$$

with $\omega_c = \sqrt{1 - a^2}$. Suppose that there exists $\omega_s \in [0, \omega_c]$ and a density f_2 with mean E, such that

$$C_2(\omega_s) := p_1 \cos(\omega_s \tau_1) + p_2 \cos(\omega_s \tau_2) = -a. \tag{11}$$

Then $\omega_s E < \theta_c$ and $\cos(\omega_s E) > -a$.

Proof. From inequality (10), one gets $\omega_c E < \arccos(-a) < \pi$, so $\cos(\omega_c E) > -a$. Moreover, since $\omega_c \leq 1$, the inequality $\omega_s \leq \omega_c$ implies $\cos(\omega_s E) \geq \cos(\omega_c E)$. Consequently, $\cos(\omega_s E) > -a$ and, using (11), we then deduce that $\cos(\omega_s E) > C_2(\omega_s)$.

Furthermore, we have

$$C_2(\omega_s) := p_1 \cos(\omega_s \tau_1) + p_2 \cos(\omega_s \tau_2) \geq p_1 g(\omega_s \tau_1) + p_2 g(\omega_s \tau_2) \geq g(\omega_s E).$$

The first inequality comes from the definitions of c and g (see Definition 4.1): $\cos(x) \geq 1 - cx$ for $x \geq 0$. The second inequality is the convexity property of g. Thus, we deduce $\cos(\omega_s E) > g(\omega_s E)$. Since $g(x) = \cos(x)$ for $x \geq \theta_c$, this means that $\omega_s E < \theta_c$. □

Lemma 4.3. *Assume $a \in]-1, 1[$ and $E > 0$ satisfies (10). Suppose that there exists $\omega_s \in [0, \omega_c]$ and a density f_2 with mean E, such that equality (11) is satisfied. Then there exists a unique density f^* with two discrete delays τ_1^* and τ_2^*, mean E, such that $\tau_1^* = 0$ and $0 < \omega_s \tau_2^* \leq \theta_c \leq \pi$, and satisfying*

$$C_2^*(\omega_s) = -a. \tag{12}$$

Proof. Suppose there exists a density f_2' with two discrete delays τ_1' and τ_2', weights p_1' and p_2', mean E, satisfying $\tau_1' = 0$ and $\tau_2' > 0$. Necessarily, $p_2' \tau_2' = E$ (so f_2' has mean E). We are going to show that

$$C_2'(\omega_s) = -a. \tag{13}$$

By using $p_1' = 1 - p_2'$ and $p_2' = E/\tau_2'$, Eq. (13) is equivalent to

$$\cos(\omega_s \tau_2') = 1 - \frac{1+a}{\omega_s E} \omega_s \tau_2'. \tag{14}$$

From the definitions of the constant c and the function g (Definition 4.1), the equation $\cos(x) = 1 - (1+a)x/\omega_s E$ has positive solutions in $[0, \pi]$ if and only if $\cos(x) \geq 1 - cx$, that is

$$c \geq \frac{1+a}{\omega_s E}. \tag{15}$$

To see that inequality (15) is indeed satisfied, one can note that, using (11),

$$-a = C_2(\omega_s) = \sum_{i=1}^{2} p_i \cos(\omega_s \tau_i) \geq \sum_{i=1}^{2} p_i (1 - c\omega_s \tau_i) = 1 - c\omega_s E,$$

so $-a \geq 1 - c\omega_s E$. Thus (15) holds true. Consequently Eq. (14) has at least one solution satisfying $0 \leq \omega_s \tau_2' \leq \pi$.

Moreover, since θ_c is a tangent point (see Definition 4.1), there is exactly one solution satisfying

$$0 \leq \omega_s \tau_2' < \theta_c < \pi.$$

Denote by τ_2^* the smallest value of τ_2' that solves Eq. (14), and define $f^* = \sum_{i=1}^{2} p_i^* \delta(\tau - \tau_i^*)$, with $p_2^* = E/\tau_2^*$, $p_1^* = 1 - p_2^*$, and $\tau_1^* = 0$. From the definition of τ_2^*, f^* exists and is unique. It remains to show that f^* is a well-defined density, that is $p_2^* \in [0, 1]$. Since τ_2^* is the smallest and unique positive solution in the interval $[0, \theta_c]$ of (14), the sign of $\cos(x) - (1 - (1+a)x/(\omega_s E))$ determines whether x is smaller or larger than τ_2^* in the interval $[0, \theta_c]$. From Lemma 4.2, $\omega_s E < \theta_c$ and $\cos(\omega_s E) > -a$, or formulated equivalently, $\cos(\omega_s E) > 1 - (1+a)/(\omega_s E)\omega_s E$. Thus, $\cos(\omega_s E) - (1 - (1+a)\omega_s E/(\omega_s E)) > 0$, which implies that $\omega_s E < \omega_s \tau_2^*$. Since $E = p_2^* \tau_2^*$, we obtain the result $0 < p_2^* < 1$, which shows that f^* is a well-defined density. □

Lemma 4.4. *Assume $a \in]-1,1[$ and $E > 0$ satisfies (10). Suppose that there exists $\omega_s \in [0,\omega_c]$ and a density f_2 with mean E, such that equality (11) is satisfied. Then for any density f_2 with mean E and satisfying Eq. (11), we have*

$$S_2(\omega_s) \leq S^*(\omega_s),$$

where the density f^* is defined in Lemma 4.3.

Proof. We recast the problem in a slightly different way. Consider a density with two discrete delays τ_1 and τ_2 and mean E, such that $C_2(\omega_s) = -a$. Writing $u = \omega_s\tau_1$, $v = \omega_s\tau_2$ and $T = \omega_s E$, we can express the weights p_i in terms of u and v:

$$p_1 = \frac{v-T}{v-u} \quad \text{and} \quad p_2 = \frac{T-u}{v-u}.$$

By convention, $0 \leq u < T < v$. We consider $C_2(\omega_s)$ and $S_2(\omega_s)$ as functions of u and v; $C, S : [0,T) \times (T,\infty) \to [-1,1]$ with

$$C(u,v) = \frac{v-T}{v-u}\cos(u) + \frac{T-u}{v-u}\cos(v), \tag{16}$$

$$S(u,v) = \frac{v-T}{v-u}\sin(u) + \frac{T-u}{v-u}\sin(v). \tag{17}$$

The subscripts 2 have been dropped to ease the reading. Equation (17) is to be maximized with the restriction $C(u,v) = -a$. The equation $C(u,v) = -a$ defines a one-parameter family of solutions. For u fixed, $C(u,v) = -a$ has at most a finite number of solutions v, with $v > T$. As shown in Lemma 4.3, there is always a solution when $u = 0$ (equivalent to $\tau_1 = 0$). Fixing u and labeling the solutions in increasing order v_i, $i = 1,...,r$, $r \geq 1$, we have $S(u,v_1) \geq S(u,v_i)$ for all i. Indeed, the equality $C(u,v) = -a$ can be rewritten as

$$-\frac{a+\cos(u)}{T-u}v + \frac{au + T\cos(u)}{T-u} = \cos(v). \tag{18}$$

Since $0 \leq u < T < \pi$, $\cos(u)$ is decreasing, $\cos(u) > \cos(T)$, and $\cos(T) > -a$ (From Lemma 4.2, we know that $\cos(\omega_s E) > -a$), so $\cos(u) + a > 0$. Eq. (18) writes

$$\cos(v) = \alpha(u) - \beta(u)v, \tag{19}$$

where $\beta(u) > 0$ for all $u \in [0,T)$, $\alpha(0) = 1$ (in case $u = 0$, Eq. (19) reduces to Eq. (14)) and $\alpha(u)$ is increasing for $u \in [0,T)$. The slope of the right hand side of (19) is negative, $\cos(v_i)$ is decreasing with solutions v_i of (19) (Figure 1A). One may note that the points $\big(C(u,v_i), S(u,v_i)\big)$ are at the intersection of the chord i between the unit circle points $\big(\cos(u), \sin(u)\big)$ and $\big(\cos(v_i), \sin(v_i)\big)$ and the vertical secant at $-a$. From (16) with $C(u,v_i) = -a$, it is easy to see that $\cos(v_i) < -a$ since $\cos(u) > -a$. By displaying the above mentioned chords and the vertical secant on a unit circle (Figure 1B), it follows that all the chords i, $i > 1$, lie below chord 1, and thus $S(u,v_1) \geq S(u,v_i)$, $i \geq 1$.

It is therefore enough to look, for each u, at the smallest solution v_1 of the equation $C(u,v) = -a$. The solution, which exists for $u \in [0,T)$, can be parameterized by u, with $v_1 = v_1(u) = \min\{v | C(u,v) = -a\}$. At $u = 0$, the solution $v_1(0) = \omega_s\tau_2^*$. Therefore, we need to show that $S(0,v_1(0))$ maximizes $S(u,v_1(u))$. The total derivative of S with respect to u is

$$\frac{d}{du}S(u,v_1(u)) = \frac{\partial S}{\partial u} + \frac{\partial S}{\partial v}\frac{dv_1}{du}.$$

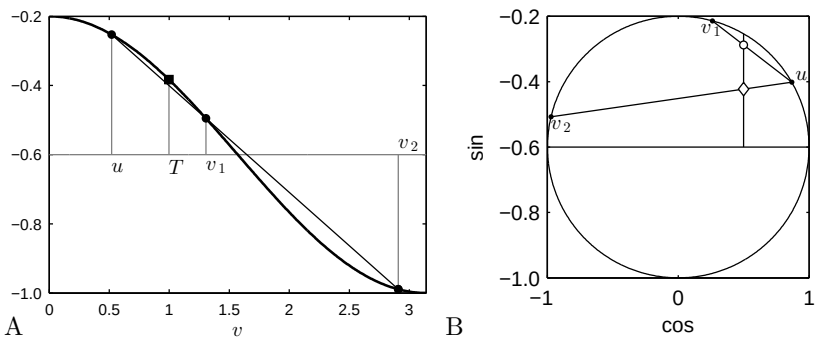

FIGURE 1. Two solutions in v of Eq. (19) for fixed u, with density $f_2(\tau) = 0.8\delta(\tau - 0.625) + 0.2\delta(\tau - 3.5)$ and $a = -0.5$ (parameter chosen to satisfy the conditions of Lemma 4.2). Then $\omega_c = \sqrt{1-a^2} = 0.8660$, $E = 1.2 < \arccos(-a)/\omega_c = 1.2092$. Eq. (11) was solved for $\omega_s = 0.8308 < \omega_c$ to yield $T = \omega_s E = 0.9969$ and $u = \omega_s \tau_1 = 0.5192$). The solution $v_2 = \omega_s \tau_2 = 2.9078$ corresponds to the density f_2 and $v_1 = 1.3056$, to the density $f^* = 0.3925\delta(\tau - 0.625) + 0.6075\delta(\tau - 1.5715)$. (A) Solutions along the cosine. (B) Solutions parametrized on the circle, illustrating that at the intersection of the secant at $-a$, the value of $S(u, v_1)$ ($\circ$) is strictly larger than $S(u, v_2)$ ($\diamond$).

If $\partial S/\partial v < 0$, the total derivative is strictly negative if and only if

$$\frac{dv_1}{du} > -\frac{\partial S}{\partial u} \Big/ \frac{\partial S}{\partial v}. \tag{20}$$

The partial derivative with respect to v is

$$\frac{\partial S}{\partial v} = \frac{T-u}{v-u}\left[\frac{\sin(u) - \sin(v)}{v-u} + \cos(v)\right].$$

One can see that v_1 always satisfies $v_1(u) \le \pi$. Indeed, if one assumes by contradiction $v_1(u) > \pi$, then first Eq. (19) has no root on the interval $[T, \pi]$, and second, since $\cos(T) > -a = \alpha(u) - \beta(u)T$, one gets $\cos(v) > \alpha(u) - \beta(u)v$ for $v \in [T, \pi]$. It follows that for all $v > \pi$,

$$\alpha(u) - \beta(u)v < \alpha(u) - \beta(u)\pi < \cos(\pi) = -1 \le \cos(v),$$

and Eq. (19) has no root, yielding a contradiction.

The sine function is strictly concave on the interval $[0, \pi]$ and this implies that

$$\sin(u) < \sin(v) + (u - v)\frac{d}{dv}\sin(v), \tag{21}$$

or equivalently that $(\sin(u) - \sin(v))/(v-u) + \cos(v) < 0$, for all $0 \le u < v \le \pi$. This shows that $\partial S/\partial v < 0$. Now,

$$\frac{dv_1}{du} = \frac{v-T}{T-u}\frac{\cos(v) - \cos(u) + (v-u)\sin(u)}{\cos(u) - \cos(v) - (v-u)\sin(v)},$$

$$-\frac{\partial S}{\partial u} \Big/ \frac{\partial S}{\partial v} = \frac{v-T}{T-u}\frac{\sin(v) - \sin(u) - (v-u)\cos(u)}{\sin(u) - \sin(v) + (v-u)\cos(v)}.$$

Inequality (20) can be re-expressed as

$$(v-u)\big[2-2\cos(v-u)-(v-u)\sin(v-u)\big]>0.$$

It can be verified that this inequality is satisfied for $v-u=z\in(0,\pi]$. The left-hand side vanishes when $z\to 0$, and the derivative is strictly positive for $0<z\leq\pi$:

$$\frac{d}{dz}\big[2-2\cos(z)-z\sin(z)\big]=\sin(z)-z\cos(z)>0.$$

The last inequality is obtained with inequality (21). Therefore, $dS/du<0$ and S is maximized for $u=\omega_s\tau_1^*=0$ and $v_1(0)=\omega_s\tau_2^*<\pi$. □

Now that we established the existence of a density f^* with two delays, one equal to zero the other one positive, and mean E which maximizes the quantity $S_2(\omega_s)$, we prove in the next theorem the stability of all densities with n discrete delays and mean E satisfying (10).

Theorem 4.5. *Assume $a\in\,]-1,1[$ and $E>0$ satisfies inequality (10). Let f_n be a discrete density with $n\geq 1$ delays and mean E, then the density f_n is stable.*

Proof. **Case $n=1$.** Single delay distributions ($n=1$) are stable by Theorem 2.5.

Case $n=2$. Consider a density f_2 with two delays $\tau_1<\tau_2$. If $C_2(\omega_s)>-a$ for every $\omega_s\in[0,\omega_c]$, Corollary 1 states that f_2 is stable. Suppose $C_2(\omega_s)=-a$ for a value $\omega_s\in[0,\omega_c]$. From Lemmas 4.3 and 4.4, there exists a density f^* with $\tau_1^*=0$ and $0<\tau_2^*\leq\pi/\omega_s$ such that $C^*(\omega_s)=C_2(\omega_s)$ and $S^*(\omega_s)\geq S_2(\omega_s)$.

Since S^* maximizes the value of S_2, if we are able to show that any distribution f^* with a zero and a positive delay, and $C^*(\omega_s)=-a$, satisfies $S^*(\omega_s)<\omega_s$, then from Corollary 1 all distributions with two delays will be stable.

Let the density $f^*(\tau)=(1-p)\delta(\tau)+p\delta(\tau-\tau^*)$ with $p\in(0,1]$ and $\tau^*\in[E,\pi/\omega_s]$. We have $C^*(\omega_s)=1-p+p\cos(\omega_s\tau^*)=-a$. We must show that $S^*(\omega_s)=p\sin(\omega_s)<\omega_s$. Summing up the squares of the cosine and the sine, we then obtain $p^2=(-a+p-1)^2+S^{*2}(\omega_s)$, so $S^*(\omega_s)=\sqrt{p^2-(-a+p-1)^2}$. Since E satisfies inequality (10), then $\tau^*<\arccos(-a)/p\sqrt{1-a^2}$. From $C^*(\omega_s)=-a$ we get $\omega_s=\arccos(-(a+1-p)p^{-1})/\tau^*$. Thus,

$$p\sqrt{1-a^2}\frac{\arccos\big(-(a+1-p)p^{-1}\big)}{\arccos(-a)}<\frac{\arccos\big(-(a+1-p)p^{-1}\big)}{\tau^*}=\omega_s.$$

Since $(a+1-p)p^{-1}\geq a$ for $p\in(0,1]$ and $a\in\,]-1,1[$, we have the following inequality

$$\frac{\arccos(-a)}{\sqrt{1-a^2}}\leq\frac{\arccos\big(-(a+1-p)p^{-1}\big)}{\sqrt{1-\big((a+1-p)p^{-1}\big)^2}},$$

which implies

$$p\sqrt{1-\big((a+1-p)p^{-1}\big)^2}\leq p\sqrt{1-a^2}\frac{\arccos\big(-(a+1-p)p^{-1}\big)}{\arccos(-a)}.$$

Thus,

$$S^*(\omega_s)=\sqrt{p^2-(-a+p-1)^2}\leq p\sqrt{1-a^2}\frac{\arccos\big(-(a+1-p)p^{-1}\big)}{\arccos(-a)}<\omega_s.$$

This completes the proof for the case $n=2$.

Case $n>2$. For densities f with $n>2$ delays, the strategy is also to find an upper bound for the value of $S(\omega_s)$ via a new distribution f^* that keeps $C(\omega_s)=-a$

constant. If, for the new distribution, $S(\omega_s) \leq S^*(\omega_s) < \omega_s$ holds true, then Corollary 1 can be applied. The construction of f^* requires two or three steps. In the first step, all delays $\tau_i > \pi/\omega_s$ are replaced by smaller delays $\tau_i' < \pi/\omega_s$, in order to use the concavity of the sine function on the interval $[0, \pi]$ as done in the proof of Lemma 4.4, in the following way:

$$\tau_i' = \begin{cases} \tau_i - 2k_i\pi/\omega_s & \text{if } \sin(\omega_s\tau_i) \geq 0, \\ 2(k_i+2)\pi/\omega_s - \tau_i & \text{if } \sin(\omega_s\tau_i) < 0, \end{cases}$$

where $k_i = \max\{j | 2j\pi/\omega_s \leq \tau_i\}$. This transformation preserves $C(\omega_s)$: $\cos(\omega_s\tau_i') = \cos(\omega_s\tau_i)$, and ensures that $S(\omega_s)$ increases: $\sin(\omega_s\tau_i') = |\sin(\omega_s\tau_i)|$. That way, we obtain an associated delay density f' with $C'(\omega_s) = -a$, $S'(\omega_s) \geq S(\omega_s)$, $E' \leq E$ and $\tau_i' \leq \pi/\omega_s$.

In the second step, we reduce the number of strictly positive delays. All pairs of delay $\tau_i' < \tau_j'$ for which the inequality

$$\frac{p_i\cos(\omega_s\tau_i') + p_j\cos(\omega_s\tau_j')}{p_i + p_j} \leq \cos\left(\omega_s\frac{p_i\tau_i' + p_j\tau_j'}{p_i + p_j}\right) \tag{22}$$

holds are iteratively replaced by one positive and one vanishing delay, as done in Lemma 4.3. We note that inequality (22) reduces to

$$C(\omega_s) = p_1\cos(\omega_s\tau_1) + p_2\cos(\omega_s\tau_2) \leq \cos(\omega_s E)$$

for a two discrete delay distribution, with delays τ_1 and τ_2 satisfying (9). This transformation preserves the values of mean E' and $C'(\omega_s)$, and increases the value of $S'(\omega_s)$. This step is repeated until one of the two situations occurs: (i) There remains one density f^* with exactly one delay $\tau_1^* = 0$ and one delay $\tau_2^* > 0$. Then the inequality $S^*(\omega_s) < \omega_s$ follows from the first part of the proof. Therefore, $S(\omega_s) \leq S'(\omega_s) \leq S^*(\omega_s) < \omega_s$, and, by Corollary 1 implies that f is stable. (ii) There remains a density $\bar{f}$ with one delay $\bar{\tau}_1 = 0$ and two or more delays $\bar{\tau}_k > 0$, $k = 2, \ldots, m$, $m \geq 3$, such that

$$\frac{\bar{p}_i\cos(\omega_s\bar{\tau}_i) + \bar{p}_j\cos(\omega_s\bar{\tau}_j)}{\bar{p}_i + \bar{p}_j} > \cos\left(\omega_s\frac{\bar{p}_i\bar{\tau}_i + \bar{p}_j\bar{\tau}_j}{\bar{p}_i + \bar{p}_j}\right),$$

for each pair $i \neq j \in 2, \ldots, m$. Since $\sum_{k=1}^m \bar{p}_k = 1$, the strictly positive delays now satisfy

$$\sum_{k=2}^m \frac{\bar{p}_k\cos(\omega_s\bar{\tau}_k)}{1-\bar{p}_1} > \cos\left(\omega_s\sum_{k=2}^m\frac{\bar{p}_k\bar{\tau}_k}{1-\bar{p}_1}\right), \tag{23}$$

while $\bar{C}(\omega_s) := \sum_{k=1}^m \bar{p}_k\cos(\omega_s\bar{\tau}_k) = -a \leq \cos(\omega_s\bar{E})$.

The third step is to replace all positive delays $\bar{\tau}_k$, $k = 2, \ldots, m$, with the single mean delay

$$\tau_2'' = \sum_{k=2}^m \frac{\bar{p}_k\bar{\tau}_k}{1-\bar{p}_1}.$$

Because the sine function is concave on the interval $[0, \pi]$, any averaging of delays can only increase the value of S. We now have a density f'' with $\tau_1'' = 0$ and $\tau_2'' > 0$, $p_1'' = \bar{p}_1$ and $p_2'' = 1 - \bar{p}_1$, $C''(\omega_s) < \bar{C}(\omega_s)$ (from inequality (23)), $E'' = \bar{E} \leq E$, and $S''(\omega_s) \geq \bar{S}(\omega_s)$. We now replace τ_2'' with a delay $\tau_2^* < \tau_2''$, so as to obtain a density f^* with $C^*(\omega_s) = \bar{C}(\omega_s) = -a$, and $E^* = E''$.

Indeed, this consists in finding (p_2^*, τ_2^*) such that $p_2^*\tau_2^* = E'' = p_2''\tau_2''$, $\tau_2^* < \tau_2''$, and $1 - p_2^* + p_2^*\cos(\omega_s\tau_2^*) = -a$. Hence, this is equivalent to finding $\tau_2^* \in]E'', \tau_2''[$ such that

$$\chi(\tau_2^*) := 1 - \frac{p_2''\tau_2''}{\tau_2^*} + \frac{p_2''\tau_2''}{\tau_2^*}\cos(\omega_s\tau_2^*) = -a.$$

Since χ is continuous, with $\chi(E'') = \cos(\omega_s E'') = \cos(\omega_s \bar{E}) \geq -a$, and $\chi(\tau_2'') = C_2''(\omega_s) < -a$, there is at least one $\tau_2^* \in]E'', \tau_2''[$ satisfying the above conditions, with $p_2^* := p_2''\tau_2''/\tau_2^*$. Moreover, since $\tau_2^* < \tau_2''$ and the function $\sin(x)/x$ is decreasing on $(0, \pi)$, one obtains, using $p_2^*\tau_2^* = E'' = p_2''\tau_2''$, that $p_2^*\sin(\omega_s\tau_2^*) \geq p_2''\sin(\omega_s\tau_2'')$, or equivalently, $S^*(\omega_s) \geq S''(\omega_s)$.

Consequently, this last change of delay has the effect of increasing the value $S^*(\omega_s) \geq S''(\omega_s)$, while maintaining the condition $C^*(\omega_s) = -a$. Since the mean E^* of density f^* satisfies inequality (10), we have $S^*(\omega_s) < \omega_s$ as shown for the case $n = 2$. Therefore $S(\omega_s) \leq S'(\omega_s) \leq \bar{S}(\omega_s) \leq S''(\omega_s) \leq S^*(\omega_s) < \omega_s$. Corollary 1 implies that f is stable. □

5. **Stability of a general distribution of delays.** We now show that the stability of discrete delays implies the stability of general distributions. First we need to bound the roots of the characteristic equation for general distributed delays.

Lemma 5.1. *Assume $a \in]-1, 1[$ and $E > 0$ satisfies inequality (10). Let η be a delay distribution with mean E and characteristic equation $D(\lambda) = 0$. There exists a sequence of distributions $\{\eta_n\}_{n\geq 1}$ with mean E, such that η_n converges weakly to η as $n \to \infty$, and λ is a root of the characteristic equation if and only if there exists a sequence of characteristic roots λ_n for η_n such that $\lim_{n\to\infty}\lambda_n = \lambda$. If $\{\mu_n\}_{n\geq 1}$ is a sequence of real parts of characteristic roots λ_n for η_n, $D_n(\lambda_n) = 0$, then $\limsup_{n\to\infty}\mu_n < 0$.*

Proof. Existence of a sequence $\{\eta_n\}_{n\geq 1}$ of distributions with n delays and mean E, such that η_n converges weakly to η as $n \to \infty$ is rather straightforward, this sequence can be built explicitly. We do not detail this part here.

Consider $\lambda_n = \mu_n + i\omega_n$ a root of the characterisitic equation for η_n. The mean E satisfies inequality (10), so $\mu_n < 0$. Then,

$$\begin{aligned}\Big|D(\lambda_n)\Big| &= \Big|\lambda_n + a + \int_0^\infty e^{-\lambda_n\tau}d\eta(\tau)\Big| \\ &= \Big|\lambda_n + a + \int_0^\infty e^{-\lambda_n\tau}d[\eta(\tau) - \eta_n(\tau)] + \int_0^\infty e^{-\lambda_n\tau}d\eta_n(\tau)\Big| \\ &= \Big|\int_0^\infty e^{-\lambda_n\tau}d[\eta(\tau) - \eta_n(\tau)]\Big| \to 0,\end{aligned}$$

as $n \to \infty$ by weak convergence. Thus any converging sub-sequence of roots converges to a root for η. The same way, if λ is a root for η,

$$\begin{aligned}\Big|D_n(\lambda)\Big| &= \Big|\lambda + a + \int_0^\infty e^{-\lambda\tau}d\eta_n(\tau)\Big| \\ &= \Big|\lambda + a + \int_0^\infty e^{-\lambda\tau}d[\eta_n(\tau) - \eta(\tau)] + \int_0^\infty e^{-\lambda\tau}d\eta(\tau)\Big| \\ &= \Big|\int_0^\infty e^{-\lambda\tau}d[\eta_n(\tau) - \eta(\tau)]\Big| \to 0,\end{aligned}$$

as $n \to \infty$. Convergence is guaranteed by inequality (4). Thus each root λ_n lies close to a corresponding root λ, and $\mu = \limsup_{n\to\infty} \mu_n$, with μ_n real part of a characteristic root λ_n, is the real part of a characteristic root for η. Since $\mu_n < 0$, we have that μ is non-positive. Suppose $\mu = 0$ and consider the scaled distribution $\eta_{a,\rho}(\tau)$ defined by (7), and the associated real parts $\mu_{a,\rho}$, where the subscript a is there to emphasize the dependence of the stability on the parameter a in the characteristic equation. Then, by continuity, there exists $(\bar{a}, \rho)$ in an ε-neighborhood of the point $(a, 1)$ for which $\mu_{\bar{a},\rho} > 0$. For sufficiently small $\varepsilon > 0$, inequality (10) is still satisfied:

$$\rho E < \frac{\arccos(-\bar{a})}{\sqrt{1-\bar{a}^2}}.$$

Additionally, the scaled discrete distributions $\eta_{n,\bar{a},\rho}$ converge weakly to $\eta_{\bar{a},\rho}$, so that the real parts $\mu_{n,\bar{a},\rho}$ of the roots converging to $\mu_{\bar{a},\rho}$ become eventually positive. That is, there is $N > 1$ such that $\eta_{n,\bar{a},\rho}$ is unstable for all $n > N$, a contradiction to Theorem 4.5, since inequality (10) still holds. Therefore $\mu < 0$. □

Theorem 5.2. *Assume $a \in]-1, 1[$ and $E > 0$ satisfies inequality (10). Let η be a delay distribution with mean E, then the distribution η is stable.*

Proof. Consider a sequence of distributions with n delays $\{\eta_n\}_{n\geq 1}$ where η_n converges weakly to η. By Lemma 5.1, the roots of the characteristic equation of η have strictly negative real parts. Therefore η is stable. □

The results obtained above provide the most complete picture of the stability of Eq. (2) when the only information about the distribution of delays is the mean. These results are summarized in the following theorem and illustrated in Fig. 2.

Theorem 5.3. *The zero solution of Eq. (2) is asymptotically stable if $a > -b$ and $a \geq |b|$, or if $b > |a|$ and the mean E of η satisfies*

$$E < \frac{\arccos(-a/b)}{\sqrt{b^2-a^2}}. \tag{24}$$

The zero solution of Eq. (2) may not be asymptotically stable (depending on the particular distribution) if $b > |a|$ and

$$E \geq \frac{\arccos(-a/b)}{\sqrt{b^2-a^2}}.$$

The zero solution of Eq. (2) is unstable if $a \leq -b$.

6. **Compartment model of hematopoiesis.** Circulating blood cells are continuously renewed by a hierarchical structure of cells maintained by hematopoietic stem cells (HSCs). Hematopoiesis consists in a complex set of feedback loops that control blood cell production. HSCs can either self-renew or differentiate to one of the three main blood cell lineages: white blood cells, platelets and red blood cells. Through successive division and differentiation stages, HSCs become progenitors (immature cells), precursors (differentiated cells), and then fully mature cells. At every stage of this hierarchy, feedback loops regulate cell differentiation, proliferation, and death. The process of red blood cell production is tightly controlled by erythropoietin, a growth factor released by the kidneys when blood oxygen is low, and whose action inhibits cell death [34]. Platelet production and white blood cell production processes are also controlled by growth factors (thrombopoietin [32] and G-CSF [7],

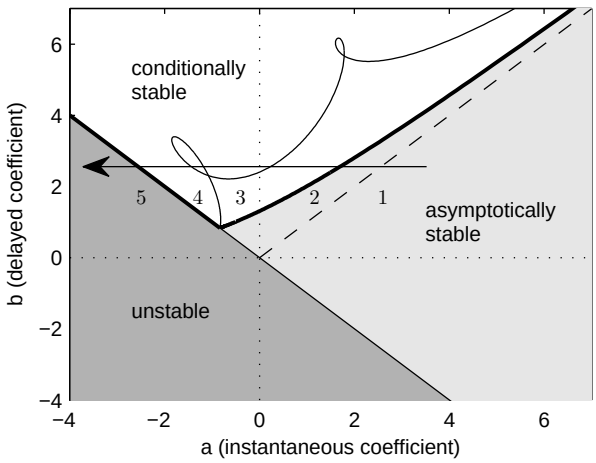

FIGURE 2. Stability chart of distributions of delay in the (a, b) plane, obtained from Theorem 5.3. The asymptotic stability region is composed of regions (1) to (3): a delay-independent stability region (*light grey*, (1)), delimited by the condition $a \geq |b|$; a discrete-delay stability region (*conditionally stable, light-grey*, (2)), delimited by condition 24; and a distributed-delay-dependent stability region (*white*, (3)). The instability region is composed of a distributed-delay-dependent instability region (*conditionally stable, white*, (4)) and a delay-independent instability region (*unstable, dark grey*, (5)), delimited by the curve $b = -a$. The discrete and distributed delay stability boundaries intersect at point $(a = -1/E, b = 1/E)$. The arrow pointing leftward shows that there exists a region, for $b > 1/E$, where a stable steady state can become unstable through a decrease of the value of a, independently of the shape of the delay distribution. The distributed delay is $f(\tau) = 0.8\delta(\tau - 0.625) + 0.2\delta(\tau - 3.5)$, with mean delay $E = 1.2$ (parameters as in Figure 1).

respectively). It is usually thought that mature blood cells act negatively, through growth factor release, on precursors, progenitors and HSCs dynamics [19, 20].

From a modeling viewpoint, the hierarchical structure of hematopoiesis can be described by a finite system of differential equations, each equation describing the dynamics of one cell generation [8, 14, 19, 20, 40, 49]. Such a view is largely accepted, both by modelers and biologists, even though mechanisms involved in cell differentiation processes are complex and there is no reason to believe that cells always go through a forward differentiation process.

In 2005, Colijn and Mackey [19, 20] proposed a compartment model of hematopoiesis, based on previous models of hematopoietic stem cell dynamics [40], white blood cell dynamics [14], platelet dynamics [4] and red blood cell dynamics [8]. This model consists in a system of 4 differential equations with discrete delays. Each equation describes the number of either HSCs, red blood cells, white cells or platelets. Cells spend a finite amount of time in each of these compartments during

which they mature and divide. Delays account for cell stage durations. Colijn and Mackey's model [19, 20] has been further justified and numerically analyzed by Colijn and Mackey [21] and Lei and Mackey [38], who showed that it exhibits multiple steady states. Stability analysis of this model is made difficult by the presence of several discrete delays. A simpler model, based on ordinary differential equations, can then be considered, similar to the one by Stiehl and Marciniak-Czochra [49]. However, even in this case, the structure of the system with several compartments induces a natural delay, and the stability analysis is not straightforward.

We consider a compartment model of hematopoiesis that encompasses the main dynamical properties existing hematopoiesis models, and focus on stability conditions for this system. The compartment model can be expressed as a single equation with a general distributed delay. We showed that among all delay distributions with a given fixed mean, the distribution with a single discrete delay (that is, the delay equals the mean) is the most unstable one. Consequently we can provide a condition for the stability of the hematopoiesis model by determining when the equation with a single delay is stable.

Let denote by $x(t)$ the number of HSCs at time t, and by $z_i(t)$, $i = 1, 2, 3$, the densities of circulating platelets, white cells, and red blood cells, respectively. We assume that x produces the quantities z_i through a linear chain process, describing the compartmental structure of each hematopoietic lineage. The number of mature cells z_i act on a negative feedback loop that represses the production of x. The disappearance rate of HSCs, α, is assumed constant. The HSC production rate P is a function that depends on x and a weighted average z of the repressors z_i. Namely $z = \sum_{i=1}^{3} p_i z_i$, where $p_i \geq 0$ and $\sum_{i=1}^{3} p_i = 1$. The HSC number x is governed by the equation

$$\dot{x} = P(x, z) - \alpha x. \tag{25}$$

Each mature cell number $z_i(t)$, $i = 1, 2, 3$, is assumed to be the product of a linear chain of differential equations of the type

$$\begin{cases} \dot{y}_i^{(1)} &= \beta_i\big(x - y_i^{(1)}\big), \\ \dot{y}_i^{(j)} &= \beta_i\big(y_i^{(j-1)} - y_i^{(j)}\big), \quad j = 1, \ldots, q_i - 1, \\ \dot{z}_i &= \beta_i\big(y_i^{(q_i-1)} - z_i\big). \end{cases} \tag{26}$$

In the i-th hematopoietic lineage, the cell number in generation j-th is denoted by $y_i^{(j)}$, $j = 1, \ldots, q_i - 1$. Mature cells z_i form compartment q_i, and immature cells x compartment 0. System (25)–(26) describes a hierarchical structure with parallel negative feedback loops of length q_i, with kinetic parameters β_i, $i = 1, 2, 3$. This situation hypothesizes that each compartment in each hematopoietic lineage depends only on the previous compartment and, except for the source term $\beta_i x$, lineages are independent from each other.

This system is an instance of a nonlinear system with a linear subsystem [22, 39]. For each lineage i, thanks to the usual chain trick in System (26), the repressors z_i can be expressed in terms of the history of x convoluted by a Gamma distribution,

$$z_i(t) = \int_0^\infty x(t - \tau) g(\tau, q_i, \beta_i) d\tau, \qquad \text{with} \qquad g(\tau, q_i, \beta_i) = \frac{\beta_i^{q_i}}{\Gamma(q_i)} \tau^{q_i - 1} e^{-\beta_i \tau}.$$

When one focuses only on one hematopoietic lineage, and $z = z_i$ ($p_j = 0$ for $j \neq i$), Eq. (25) can be expressed as a distributed delay equation with a Gamma distribution with mean $E_i = q_i/\beta_i$ and variance $V_i = q_i/\beta_i^2$. Two limiting cases are useful to consider. When $q_i = 1$, mature cells are produced directly from HSCs,

and the Gamma distribution becomes an exponential distribution with parameter β_i. When $E_i = q_i/\beta_i$ is made constant and $q_i \to \infty$, the Gamma distribution converges to a Dirac mass at E_i.

In addition to these three standard delay distributions, more general delay distributions are obtained by considering the above-mentioned linear parallel negative feedback loops. From System (26), the weighted repressor $z(t)$ remains a delayed version of $x(t)$,

$$z(t) = \int_0^\infty x(t-\tau) f_p(\tau) d\tau, \tag{27}$$

where the density of the distributed delay is a weighted average of Gamma densities,

$$f_p(\tau) = \sum_{i=1}^{3} p_i g(\tau, q_i, \beta_i).$$

The delay has a mean $E_p = \sum_{i=1}^{3} p_i q_i/\beta_i$. In the limiting case where the length q_i of each loop becomes infinite while keeping the ratio q_i/β_i constant, the distribution becomes a combination of discrete delays. Therefore, by a suitable choice and number of parallel negative feedback loops, one can obtain an arbitrary complex distribution of delays.

After expressing the repressor z as a function of the history of x in (27), one can then write the following equation for x, from (25) and (27),

$$\dot{x} = P\left(x, \int_0^\infty x(t-\tau) f_p(\tau) d\tau\right) - \alpha x. \tag{28}$$

The dynamics of System (25)–(26) is entirely contained in (28). Although the production term depends continuously on the history of x, the initial conditions need only to be known at a finite number of locations. Analyzing the stability of Eq. (28) is however as difficult as the stability of the System (25)-(26).

As a nonlinear production term P, we consider the case of a mixed feedback loop, observed when a repressor (mature cells) and an activator (immature cells) are competing. The nonlinear term in equation (28) is then

$$P(x, z) = \frac{k_0 x^r}{1 + z^h}. \tag{29}$$

The parameter r is related to the degree of cooperativity of the positive loop. For $r > 1$ the positive loop is positively cooperative and multiple stable steady states are possible. When $r = 1$ the positive loop is neutrally cooperative and at most one positive steady state exists. For $0 \le r < 1$, the positive loop is negatively cooperative and there is a single positive steady state. When $r = 0$, the dependence on x of the production rate P is lost. To ensure solutions are bounded, we set $r \le h$. The parameter h is the Hill coefficient describing the degree of cooperativity of the negative loop. The higher the value of h, the steeper the negative control. We assume $h > 1$. With these conditions, there is always at least one steady state $\bar{x} \ge 0$.

Eq. (28) linearized around a positive steady state $\bar{x} > 0$ is

$$\dot{x} = -\alpha(1-r)x - \frac{\alpha^2 h}{k_0} \bar{x}^{h-r+1} \int_0^\infty x(t-\tau) f_p(\tau) d\tau. \tag{30}$$

For positive cooperativity ($1 < r \le h$), there is a stable steady state $\bar{x}_0 = 0$. In addition, there are either zero, one or two positive steady states given by the roots of the equation $\alpha \bar{x}^h - k_0 \bar{x}^{r-1} + \alpha = 0$. In terms of Eq. (1), $a = \alpha(1-r) < 0$

and $b(\bar{x}) = \alpha^2 h \bar{x}^{h-r+1}/k_0 > 0$. The smaller positive steady state $\bar{x}_1$ satisfies $a \leq -b(\bar{x}_1)$ and, by Theorem 5.3, is always unstable. The larger steady state $\bar{x}_2$ satisfies $a > -b(\bar{x}_2)$ and the sufficient condition on stability of Theorem 5.3 can be applied in the following proposition.

Proposition 2 (positive cooperativity)**.** *Assume P is given by (29) and $1 < r \leq h$ (mixed feedback loop with positive cooperativity). When they exist and are distinct, the smaller positive steady state $\bar{x}_1$ of (28) is unstable, and the larger positive steady state $\bar{x}_2$ is linearly asymptotically stable if*

$$E_p := \sum_{i=1}^{3} p_i \frac{q_i}{\beta_i} < \frac{\arccos\left(\frac{(r-1)k_0}{\alpha h(\bar{x}_2)^{h-r+1}}\right)}{\alpha\sqrt{(\alpha h(\bar{x}_2)^{h-r+1}/k_0)^2 - (r-1)^2}}. \tag{31}$$

When $\bar{x}_1 = \bar{x}_2$, the positive steady state is unstable. The zero steady state $\bar{x}_0 = 0$ is always linearly stable.

For negative cooperativity ($0 \leq r < 1$), there exists a steady state $\bar{x}_0 = 0$ only if $r > 0$, in which case it is unstable. In addition, there is a unique positive steady state given by the root of the equation $\alpha(1 + \bar{x}^h)\bar{x}^{1-r} = k_0$. The linear equation is given by equation (30), and the instantaneous coefficient is $a = \alpha(1 - r) > 0$, the delayed coefficient is $b = \alpha^2 h \bar{x}^{h-r+1}/k_0 > 0$.

For neutral cooperativity ($r = 1$), there is a steady state $\bar{x}_0 = 0$, whose stability depends on the existence of a positive steady state. There exists a positive steady state $\bar{x} = ((k_0 - \alpha)/\alpha)^{1/h}$ only if $k_0 > \alpha$, and in this case $a = 0$ and $b = \alpha h(k_0 - \alpha)/k_0 > 0$. Theorem 5.3 can be applied in the following proposition to determine stability .

Proposition 3 (neutral and negative cooperativity)**.** *Assume P is given by (29). When $r = 1$ (mixed feedback loop with neutral cooperativity), a unique positive steady state, $\bar{x} = ((k_0 - \alpha)/\alpha)^{1/h}$, of (28) exists if $k_0 > \alpha$. If it exists, it is linearly asymptotically stable if*

$$E_p := \sum_{i=1}^{3} p_i \frac{q_i}{\beta_i} < \frac{k_0 \pi}{2\alpha h(k_0 - \alpha)}.$$

The zero steady state $\bar{x}_0 = 0$ is stable if $k_0 < \alpha$ and unstable otherwise.

When $0 \leq r < 1$ (negative cooperativity), a unique positive steady state $\bar{x}$ of (28) exists. It is linearly asymptotically stable if $\bar{x}^{h+1-r} \leq k_0(1 - r)/(\alpha h)$, or if $\bar{x}^{h+1-r} > k_0(1 - r)/(\alpha h)$ and (31) holds true. The zero steady state $\bar{x}_0 = 0$ is always unstable.

Similar models with negative ($r = 0$) and neutral cooperativity ($r = 1$) have been considered before by Mackey and Glass [41, equations 4a and 4b therein] in the context of blood cell production. The unique, positive, steady state of the negative cooperativity model ($r = 0$) can be destabilised by a discrete delay. Replacing the discrete delay by a general delay distribution cannot make the positive steady state unstable, as illustrated in Fig. 3. Neutral cooperativity arises when HSCs proliferate at a rate proportional to their number. In this situation, the steady state can be solved explicitly and the stability condition is relatively simple to state. The existence condition defines whether stem cells reproduce quickly enough to maintain their population ($k_0 > \alpha$) or not. The original Mackey-Glass equation contained a single discrete delay at E_p in both the negative and the positive loops. This is a particular case of a model with delayed mixed feedback loops for which

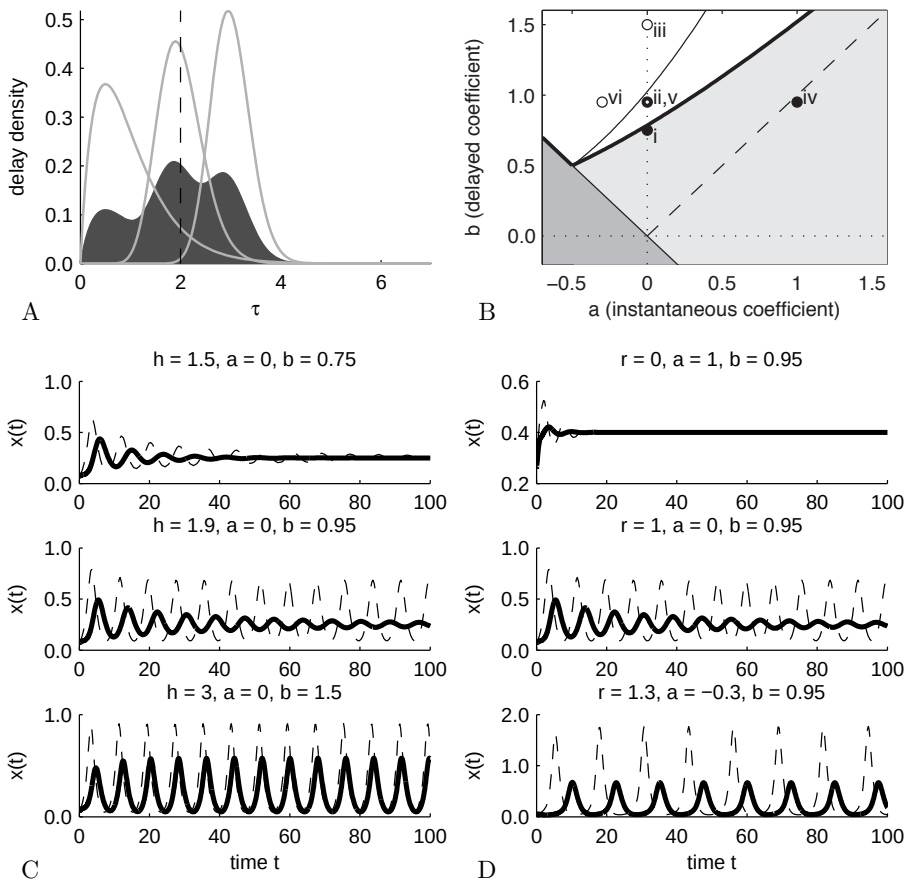

FIGURE 3. Comparison of solutions of Eq. (28) with a distributed delay and with a discrete delay for varying values of r and h. Fixed parameters values are $\alpha = 1$ and $k_0 = 2$ (so $\overline{x} = 1$ is a steady state of (28), whatever the values of r and h), and $q = \{2, 20, 60\}$, $\beta = \{2, 10, 20\}$, $p = \{0.3, 0.4, 0.3\}$. (A) The distributed delay (*shaded area*) is an average of three Gamma densities (*grey lines*) with mean delay $E = q/\beta = \{1, 2, 3\}$. The discrete delay is the mean delay $E_p = \sum_{i=1}^{3} p_i E_i = 2$ (*dashed*). (B) Stability chart of the positive steady state $\bar{x} = 1$, for varying r and h, and the stability condition is given in Proposition 3. The distributed delay is stable at points i, ii and iv, while the discrete delay is stable at points i and iv. Color coding is as in Fig. 2. (C, D) Time series of the system with distributed (*solid*) or discrete delay (*dashed*). (C) Neutral cooperativity, increasing Hill coefficient: $r = 1$ and $h = 1.5$ (i), 1.9 (ii) and 3.0 (iii). (D) Constant Hill coefficient, increasing cooperativity: $h = 1.9$ and $r = 0$ (iv), 1 (v) and 1.3 (vi).

stability results can be applied in a straightforward manner. This is not the case when the delay of the positive loop differs from the negative loop.

7. **Conclusion.** We have shown that for a given mean delay, the scalar linear differential equation with a distributed delay is asymptotically stable provided that the corresponding equation with a single discrete delay is asymptotically stable. Hence, linear systems with a discrete delay are "more" unstable than linear systems with distributed delay. This result provides a sufficient condition for the stability of a large class of linear systems, as instanced by a model of hematopoiesis with parallel lineages.

Quite often the aim of the modeling is not to reproduce stability but rather instability, via periodic oscillations. Pathological cases in hematopoiesis (blood diseases, leukemias) can for instance often be explained by the destabilization of the steady state which starts oscillating periodically. Our result shows that it is more difficult to reproduce periodic oscillations, observed experimentally, with a distributed delay than with a discrete delay.

Acknowledgments. This work has been supported by ANR grant ProCell ANR-09-JCJC-0100-01.

REFERENCES

[1] M. Adimy, F. Crauste and S. Ruan, A mathematical study of the hematopoiesis process with applications to chronic myelogenous leukemia, *SIAM J. Appl. Math.,* **65** (2005), 1328–1352.

[2] R. Anderson, Geometric and probabilistic stability criteria for delay systems, *Math. Biosci.,* **105** (1991), 81–96.

[3] R. Anderson, Intrinsic parameters and stability of differential-delay equations, *J. Math. Anal. Appl.,* **163** (1992), 184–199.

[4] R. Apostu and M. Mackey, Understanding cyclical thrombocytopenia: A mathematical modeling approach, *J. Theor. Biol.,* **251** (2008), 297–316.

[5] F. Atay, Distributed delays facilitate amplitude death of coupled oscillators, *Phys. Rev. Lett.*, **91** (2003), 094101.

[6] F. Atay, Delayed feedback control near Hopf bifurcation, *Discrete Contin. Dynam. Systems Ser. S,* **1** (2008), 197–205.

[7] S. Basu, A. Dunn and A. Ward, G-CSF: Function and modes of action, *Int. J. Mol. Med.,* **10** (2002), 3–10.

[8] J. Bélair, M. C. Mackey and J. M. Mahaffy, Age-structured and two-delay models for erythropoiesis, *Math. Biosci.,* **128** (1995), 317–346.

[9] R. Bellman and K. Cooke, *Differential-Difference Equations*, Academic press, 1963.

[10] E. Beretta and Y. Kuang, Geometric stability switch criteria in delay differential systems with delay dependent parameters, *SIAM J. Math. Anal.,* **33** (2002), 1144–1165.

[11] L. Berezansky and E. Braverman, Stability of linear differential equations with a distributed delay, *Comm. Pure Appl. Math.,* **10** (2011), 1361–1375.

[12] L. Berezansky and E. Braverman, Stability of equations with a distributed delay, monotone production and nonlinear mortality, *Nonlinearity,* **26** (2013), 2833–2849.

[13] S. Bernard, J. Bélair and M. C. Mackey, Sufficient conditions for stability of linear differential equations with distributed delay, *Discrete Contin. Dynam. Systems Ser. B,* **1** (2001), 233–256.

[14] S. Bernard, J. Belair and M. C. Mackey, Oscillations in cyclical neutropenia: New evidence based on mathematical modeling, *J. Theor. Biol.,* **223** (2003), 283–298.

[15] S. Bernard, B. Čajavec, L. Pujo-Menjouet, M. Mackey and H. Herzel, Modelling transcriptional feedback loops: The role of Gro/TLE1 in Hes1 oscillations, *Philos. Trans. R. Soc. London, Ser. A,* **364** (2006), 1155–1170.

[16] F. Boese, The stability chart for the linearized cushing equation with a discrete delay and gamma-distributed delays, *J. Math. Anal. Appl.,* **140** (1989), 510–536.

[17] S. Campbell, Time delays in neural systems, in *Handbook of Brain Connectivity*, (A. McIntosh and V. Jirsa, eds.), Springer, (2007), 65–90.

[18] S. Campbell and R. Jessop, Approximating the stability region for a differential equation with a distributed delay, *Math. Mod. Nat. Phenom.,* **4** (2009), 1–27.

[19] C. Colijn and M. Mackey, A mathematical model of hematopoiesis – I. Periodic chronic myelogenous leukemia, *J. Theor. Biol.,* **237** (2005), 117–132.
[20] C. Colijn and M. Mackey, A mathematical model of hematopoiesis – II. Cyclical neutropenia, *J. Theor. Biol.,* **237** (2005), 133–146.
[21] C. Colijn and M. Mackey, Bifurcation and bistability in a model of hematopoietic regulation, *SIAM J. App. Dynam. Sys.,* **6** (2007), 378–394.
[22] K. L. Cooke and Z. Grossman, Discrete delay, distributed delay and stability switches, *J. Math. Anal. Appl.,* **86** (1982), 592–627.
[23] F. Crauste, Stability and Hopf bifurcation for a first-order delay differential equation with distributed delay, in *Complex Time-Delay Systems*, (2010), 263–296, Springer, Berlin.
[24] T. Erneux, *Applied Delay Differential Equations*, Springer Verlag, 2009.
[25] C. Eurich, A. Thiel and L. Fahse, Distributed delays stabilize ecological feedback systems, *Phys. Rev. Lett.,* **94** (2005), 158104.
[26] J. Hale, Functional differential equations with infinite delays, *J. Math. Anal. Appl.,* **48** (1974), 276–283.
[27] J. Hale and J. Kato, Phase space for retarded equations with infinite delay, *Funkcial. Ekvac,* **21** (1978), 11–41.
[28] J. Hale and S. Verduyn Lunel, *Introduction to Functional Differential Equations*, Berlin: Springer, 1993.
[29] N. Hayes, Roots of the transcendental equation associated with a certain difference-differential equation, *J. Lond. Math. Soc.*, **25** (1950), 226–232.
[30] C. Huang and S. Vandewalle, An analysis of delay-dependent stability for ordinary and partial differential equations with fixed and distributed delays, *SIAM J. Sci. Comput.,* **25** (2004), 1608–1632.
[31] G. Hutchinson, Circular causal systems in ecology, *Ann. N.Y. Acad. Sci.,* **50** (1948), 221–246.
[32] K. Kaushansky, The molecular mechanisms that control thrombopoiesis, *J Clin Invest,* **115** (2005), 3339–3347.
[33] G. Kiss and B. Krauskopf, Stability implications of delay distribution for first-order and second-order systems, *Discrete Contin. Dynam. Systems Ser. B,* **13** (2010), 327–345.
[34] M. Koury and M. Bondurant, Erythropoietin retards DNA breakdown and prevents programmed death in erythroid progenitor cells, *Science,* **248** (1990), 378–381.
[35] T. Krisztin, Stability for functional differential equations and some variational problems, *Tohoku Math. J,* **42** (1990), 407–417.
[36] Y. Kuang, *Delay Differential Equations: With Applications in Population Dynamics*, Academic Pr, 1993.
[37] Y. Kuang, Nonoccurrence of stability switching in systems of differential equations with distributed delays, *Quart. Appl. Math.,* **52** (1994), 569–578.
[38] J. Lei and M. Mackey, Multistability in an age-structured model of hematopoeisis: Cyclical neutropenia, *J. Theor. Biol.*, **270** (2011), 143–153.
[39] N. MacDonald, *Biological Delay Systems: Linear Stability Theory*, Cambridge Studies in Mathematical Biology, 8. Cambridge University Press, Cambridge, 1989.
[40] M. C. Mackey, Unified hypothesis of the origin of aplastic anaemia and periodic hematopoiesis, *Blood,* **51** (1978), 941–956.
[41] M. C. Mackey and L. Glass, Oscillation and chaos in physiological control systems, *Science,* **197** (1977), 287–289.
[42] U. Meyer, J. Shao, S. Chakrabarty, S. Brandt, H. Luksch and R. Wessel, Distributed delays stabilize neural feedback systems, *Biol. Cybern.*, **99** (2008), 79–87.
[43] R. Miyazaki, Characteristic equation and asymptotic behavior of delay-differential equation, *Funkcial. Ekvac.*, **40** (1997), 471–481.
[44] N. Monk, Oscillatory expression of Hes1, p53, and NF-κB driven by transcriptional time delays, *Curr. Biol.,* **13** (2003), 1409–1413.
[45] H. Ozbay, C. Bonnet and J. Clairambault, Stability analysis of systems with distributed delays and application to hematopoietic cell maturation dynamics, in *Decision and Control, 2008. CDC 2008*, 47th IEEE Conference on, IEEE, (2008), 2050–2055.
[46] K. Rateitschak and O. Wolkenhauer, Intracellular delay limits cyclic changes in gene expression, *Math. Biosci.*, **205** (2007), 163–179.
[47] O. Solomon and E. Fridman, New stability conditions for systems with distributed delays, *Automatica J. IFAC,* **49** (2013), 3467–3475.

[48] G. Stépán, *Retarded Dynamical Systems: Stability and Characteristic Functions*, Longman Scientific & Technical New York, 1989.

[49] T. Stiehl and A. Marciniak-Czochra, Characterization of stem cells using mathematical models of multistage cell lineages, *Math. Comp. Models.*, **53** (2011), 1505–1517.

[50] X. Tang, Asymptotic behavior of a differential equation with distributed delays, *J. Math. Anal. Appl.,* **301** (2005), 313–335.

Received April 2014; revised February 2015.

E-mail address: bernard@math.univ-lyon1.fr
E-mail address: crauste@math.univ-lyon1.fr

9.2 Bergmann O, Bhardwaj R, Bernard S, Zdunek S, Barnabé-Heider F, Walsh S, Zupicich J, Alkass K, Buchholz B, Druid H, Jovinge S, Frisén J (2009) Evidence for cardiomyocyte renewal in humans. Science 324:98–102

References and Notes

1. D. J. Mangelsdorf *et al.*, *Cell* **83**, 835 (1995).
2. A. Antebi, J. G. Culotti, E. M. Hedgecock, *Development* **125**, 1191 (1998).
3. A. Antebi, W. H. Yeh, D. Tait, E. M. Hedgecock, D. L. Riddle, *Genes Dev.* **14**, 1512 (2000).
4. D. L. Motola *et al.*, *Cell* **124**, 1209 (2006).
5. N. Fielenbach, A. Antebi, *Genes Dev.* **22**, 2149 (2008).
6. D. P. Bartel, *Cell* **116**, 281 (2004).
7. R. C. Lee, R. L. Feinbaum, V. Ambros, *Cell* **75**, 843 (1993).
8. B. Wightman, I. Ha, G. Ruvkun, *Cell* **75**, 855 (1993).
9. A. E. Rougvie, *Development* **132**, 3787 (2005).
10. M. Chalfie, H. R. Horvitz, J. E. Sulston, *Cell* **24**, 59 (1981).
11. A. L. Abbott *et al.*, *Dev. Cell* **9**, 403 (2005).
12. B. J. Reinhart *et al.*, *Nature* **403**, 901 (2000).
13. Materials and methods are available as supporting material on *Science* Online.
14. Y. Shostak, M. R. Van Gilst, A. Antebi, K. R. Yamamoto, *Genes Dev.* **18**, 2529 (2004).
15. A. Esquela-Kerscher *et al.*, *Dev. Dyn.* **234**, 868 (2005).
16. B. Gerisch, C. Weitzel, C. Kober-Eisermann, V. Rottiers, A. Antebi, *Dev. Cell* **1**, 841 (2001).
17. K. Jia, P. S. Albert, D. L. Riddle, *Development* **129**, 221 (2002).
18. A. H. Ludewig *et al.*, *Genes Dev.* **18**, 2120 (2004).
19. G. D. Hayes, A. R. Frand, G. Ruvkun, *Development* **133**, 4631 (2006).
20. M. Li, M. W. Jones-Rhoades, N. C. Lau, D. P. Bartel, A. E. Rougvie, *Dev. Cell* **9**, 415 (2005).
21. H. Grosshans, T. Johnson, K. L. Reinert, M. Gerstein, F. J. Slack, *Dev. Cell* **8**, 321 (2005).
22. J. Varghese, S. M. Cohen, *Genes Dev.* **21**, 2277 (2007).
23. J. J. Repa *et al.*, *Science* **289**, 1524 (2000).

24. Our thanks go to G. Hayes, G. Ruvkun, V. Ambros, and A. Rougvie for strains; N. Timchenko for gel shift support; and D. Magner, S. Greene, and F. Schroeder for manuscript comments. This work was supported by NIH grant GM077201 and the Ellison Medical Foundation (A.A.), and the Howard Hughes Medical Institute and the Robert A. Welch Foundation (D.J.M.).

Supporting Online Material

www.sciencemag.org/cgi/content/full/324/5923/95/DC1
Materials and Methods
Figs. S1 to S5
Tables S1 and S2
References

20 August 2008; accepted 11 February 2009
10.1126/science.1164899

Evidence for Cardiomyocyte Renewal in Humans

Olaf Bergmann,[1]* Ratan D. Bhardwaj,[1]* Samuel Bernard,[2] Sofia Zdunek,[1] Fanie Barnabé-Heider,[1] Stuart Walsh,[3] Joel Zupicich,[1] Kanar Alkass,[4] Bruce A. Buchholz,[5] Henrik Druid,[4] Stefan Jovinge,[3,6] Jonas Frisén[1]†

It has been difficult to establish whether we are limited to the heart muscle cells we are born with or if cardiomyocytes are generated also later in life. We have taken advantage of the integration of carbon-14, generated by nuclear bomb tests during the Cold War, into DNA to establish the age of cardiomyocytes in humans. We report that cardiomyocytes renew, with a gradual decrease from 1% turning over annually at the age of 25 to 0.45% at the age of 75. Fewer than 50% of cardiomyocytes are exchanged during a normal life span. The capacity to generate cardiomyocytes in the adult human heart suggests that it may be rational to work toward the development of therapeutic strategies aimed at stimulating this process in cardiac pathologies.

Myocardial damage often results in chronic heart failure due to loss and insufficient regeneration of cardiomyocytes. This has prompted efforts to devise cardiomyocyte replacement therapies by cell transplantation or by the promotion of endogenous regenerative processes. The development of cell transplantation strategies is advancing rapidly, and some are currently being evaluated in clinical trials (*1*, *2*). Stimulating endogenous regenerative processes is attractive as it potentially could provide a noninvasive therapy and circumvent the immunosuppression required for allografts. However, it is unclear whether such regenerative strategies are realistic because it has been difficult to establish whether cardiomyocytes can be generated after the perinatal period in humans.

Stem/progenitor cells with the potential to generate cardiomyocytes in vitro remain in the adult rodent and human myocardium (*3*, *4*). Moreover, mature cardiomyocytes have been suggested to be able to reenter the cell cycle and duplicate (*5*). However, studies over several decades in rodents with labeled nucleotide analogs have led to conflicting results, ranging from no to substantial generation of cardiomyocytes postnatally (*6*). A recent genetic labeling study, which enabled detection of cardiomyocyte generation by stem/progenitor cells (but not by cardiomyocyte duplication), demonstrated cardiomyocyte renewal after myocardial injury, but not during 1 year in the healthy mouse (*7*).

It is possible that humans, who live much longer than rodents, may have a different requirement for cardiomyocyte replacement. Cell turnover has been difficult to study in humans because the use of labeled nucleotide analogs and other strategies commonly used in experimental animals cannot readily be adapted for studies in humans owing to safety concerns. The limited functional recovery after loss of myocardium and the fact that primary cardiac tumors are very rare indicate limited proliferation within the adult human heart (*8*). Several studies have described the presence of molecular markers associated with mitosis in the human myocardium (*5*), but this provides limited information because it is difficult to deduce the future fate of a potentially dividing cell in terms of differentiation and long-term survival.

We have measured carbon-14 (^{14}C) from nuclear bomb tests in genomic DNA of human myocardial cells, which allows retrospective birth dating (*9*–*11*). ^{14}C concentrations in the atmosphere remained relatively stable until the Cold War, when aboveground nuclear bomb tests caused a sharp increase (*12*, *13*). Even though the detonations were conducted at a limited number of locations, the elevated amounts of ^{14}C in the atmosphere rapidly equalized around the world as $^{14}CO_2$. After the Limited Nuclear Test Ban Treaty in 1963, the ^{14}C concentrations dropped exponentially, not primarily because of radioactive decay (half-life of 5730 years), but by diffusion from the atmosphere (*14*). Newly created atmospheric ^{14}C reacts with oxygen to form $^{14}CO_2$, which is incorporated by plants through photosynthesis. Humans eat plants, and animals that live off plants, so the ^{14}C concentration in the human body mirrors that in the atmosphere at any given time (*15*–*18*). Because DNA is stable after a cell has gone through its last cell division, the concentration of ^{14}C in DNA serves as a date mark for when a cell was born and can be used to retrospectively birth date cells in humans (*9*–*11*).

We first carbon-dated left ventricle myocardial cells, including cardiomyocytes and other cell types, to determine the extent of postnatal DNA synthesis in the human heart. DNA was extracted, and ^{14}C concentrations were measured by accelerator mass spectrometry (see tables S1 and S2 for ^{14}C values and associated data). The cellular birth dates can be inferred by determining the time at which the sample's ^{14}C concentration corresponded to the atmospheric concentration (Fig. 1A). ^{14}C concentrations from all individuals born around or after the nuclear bomb tests corresponded to atmospheric concentrations several years after the subjects' birth (Fig. 1B), indicating substantial postnatal DNA synthesis. Analysis of individuals born before the period of nuclear bomb tests allows for sensitive detection of any turnover after 1955, due to the marked increase in ^{14}C concentrations. By analyzing individuals born at different times before 1955 it is possible to establish the age up to which DNA synthesis occurs, or whether it continues beyond that age.

[1]Department of Cell and Molecular Biology, Karolinska Institutet, SE-171 77 Stockholm, Sweden. [2]CNRS UMR5208, Institut Camille Jordan, Université Claude Bernard Lyon 1, 69622 Villeurbanne cedex, France. [3]Lund Strategic Research Center for Stem Cell Biology and Cell Therapy, Lund University, SE-221 84 Lund, Sweden. [4]Department of Forensic Medicine, Karolinska Institutet, SE-171 77 Stockholm, Sweden. [5]Center for Accelerator Mass Spectrometry, Lawrence Livermore National Laboratory, 7000 East Avenue, L-397, Livermore, CA 94551, USA. [6]Department of Cardiology, Lund University Hospital, SE-221 85 Lund, Sweden.

*These authors contributed equally to this work.
†To whom correspondence should be addressed. E-mail: jonas.frisen@ki.se

Downloaded from www.sciencemag.org on April 3, 2009

In all studied cases, born up to 22 years before the onset of the nuclear bomb tests, ^{14}C concentrations were elevated compared to the levels before the nuclear bomb tests (Fig. 1C). Thus, DNA of myocardial cells is synthesized many years after birth, indicating that cells in the human heart do renew into adulthood.

Because cardiomyocytes constitute only about 20% of all cells within the human myocardium (*19*), it is not possible to infer from these data whether there is postnatal renewal of cardiomyocytes, or whether cell turnover in the myocardium is limited to other cell populations. We therefore set out to specifically birth date cardiomyocytes. Many cardiomyocytes are binucleated, and it is difficult to distinguish a binucleated cell from two aggregating mononucleated cells (of which one could be a noncardiomyocyte) in the flow cytometer. Hence, rather than separating myocardial cells on the basis of cell surface or cytoplasmic markers, we developed a strategy to isolate cardiomyocyte nuclei by flow cytometry.

We found that the well-characterized cardiomyocyte-specific proteins cardiac troponin I (cTroponin I, also known as TNNI3) and cardiac troponin T (cTroponin T, also known as TNNT2) [for review, see (*20*)] have evolutionar-

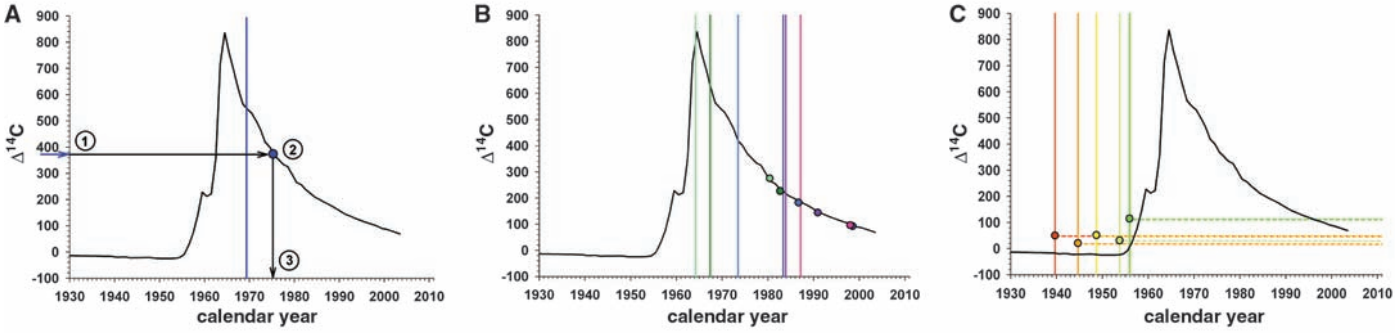

Fig. 1. Cell turnover in the heart. (**A**) Schematic figure demonstrating the strategy to establish cell age by ^{14}C dating. The black curve in all graphs shows the atmospheric concentrations of ^{14}C over the decades since 1930 [data from (*14*)]. The vertical bar indicates the date of birth of the individual. The measured ^{14}C concentration (1) is related to the atmospheric ^{14}C concentration by use of the established atmospheric ^{14}C bomb curve (2). The average birth date of the population can be inferred by determining where the data point intersects the *x* axis (3). ^{14}C concentrations in DNA of cells from the left ventricle myocardium in individuals born after (**B**) or before (**C**) the nuclear bomb tests correspond to time points substantially after the time of birth, indicating postnatal cell turnover. The vertical bar indicates the date of birth of each individual, and the similarly colored dots represent the ^{14}C data for the same individual. For individuals born before the increase in ^{14}C concentrations, it is not possible to directly infer an age because the measured concentration can be a result of ^{14}C incorporation during the rising and/or falling part of the atmospheric curve, and thus the concentration is indicated by a dotted horizontal line.

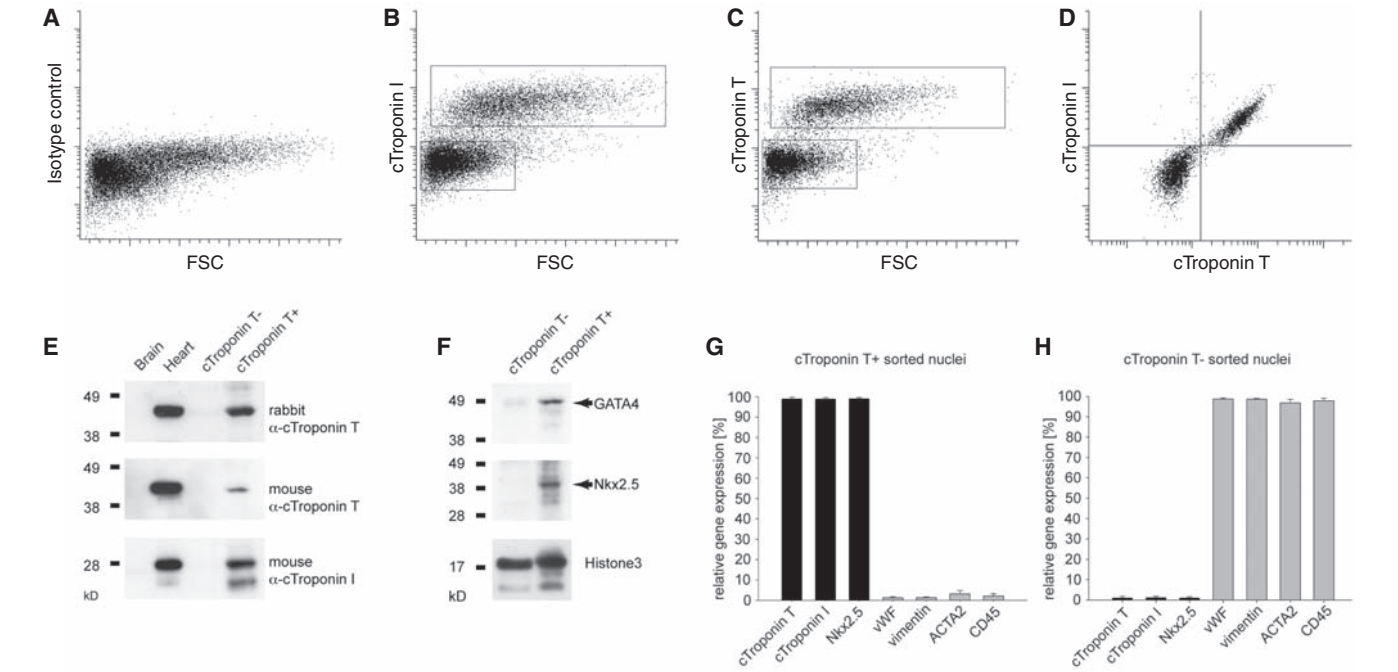

Fig. 2. Isolation of cardiomyocyte nuclei. (**A** to **C**) Flow cytometric analysis of cardiomyocyte nuclei from the left ventricle of the human heart with an isotype control antibody or antibodies to the cardiomyocyte-specific antigens cTroponin I or T. Boxes denote the boundaries for the positive and negative sorted populations. (**D**) cTroponin I and T are present in the same subpopulation of heart cell nuclei. (**E**) Western blot analysis of flow cytometry–isolated nuclei demonstrates nearly all detectable cTroponin T (analyzed with two different antibodies) and I protein in the cTroponin T–positive fraction. Brain and heart tissue were used as negative and positive controls, respectively. (**F**) The cardiac troponin T–positive population is enriched for the cardiomyocyte-specific transcription factors Nkx2.5 and GATA4. Both fractions contain similar amounts of the nuclear protein histone 3 (loading control). (**G**) Gene expression analysis of flow cytometry–isolated nuclei shows high expression of cardiomyocyte-specific genes in the cTroponin T–positive fraction (cTroponin I and T, Nkx2.5), whereas marker genes for endothelial cells (vWF), fibroblasts (vimentin), smooth muscle (ACTA2), and leukocytes (CD45) are highly expressed in the cTroponin T–negative fraction (**H**). Bars in (G) and (H) show the average from three independent experiments (±SD).

Downloaded from www.sciencemag.org on April 3, 2009

ily conserved nuclear localization signals and are partly localized in the nuclei of cardiomyocytes (figs. S1 and S2). Antibodies to cTroponin I and T identify the same subpopulation of nuclei in the myocardium (Fig. 2, A to D), and retrospective birth dating of nuclei isolated with antibodies against either epitope gave similar results (table S1). Western blot and quantitative reverse transcription polymerase chain reaction analysis of sorted nuclei demonstrated a high enrichment of cTroponin I and T in the positive fraction and a depletion in the negative, validating the efficiency of the strategy (Fig. 2, E to H). We assessed the potential transfer of cTroponin I and T during tissue processing by mixing cardiac tissue with another tissue devoid of these proteins, and found that there was negligible transfer of cTroponin I or T to noncardiomyocyte nuclei during tissue dissociation, nuclear preparation, or flow cytometric sorting (fig. S2).

We assessed the specificity of the isolation procedure with known cardiomyocyte-specific markers and markers of noncardiomyocytes present in the myocardium. There was a high enrichment of nuclei containing the known cardiomyocyte-specific nuclear markers Nkx2.5 and GATA4 in the cTroponin-positive fraction, with little contamination of nuclei expressing markers for fibroblasts, smooth muscle cells, endothelial cells, or hematopoietic cells (Fig. 2, F to H). Conversely, cardiomyocyte markers were depleted in the cTroponin-negative fraction (Fig. 2, F to H), indicating that nearly all cardiomyocytes were isolated in the positive fraction. Sorting whole cells with antibodies to a nonnuclear cardiomyocyte-specific epitope confirmed that nuclear cTroponin I and T are specific to cardiomyocytes, but resulted in lower purity compared to sorting nuclei (fig. S3). Flow cytometric reanalysis of all sorted samples demonstrated a DNA content-corrected cardiomyocyte purity of 96 ± 1.8% (mean ± SD; table S1 and fig. S4). Thus, flow cytometry with antibodies against cTroponin I or T allows specific isolation of cardiomyocyte and noncardiomyocyte nuclei.

We extracted DNA from cardiomyocyte nuclei [$(5 \pm 2) \times 10^7$, mean ± SD] and measured the ^{14}C concentration in genomic DNA. By analyzing the ^{14}C concentration also in unsorted myocardial nuclei ($>10^8$), we mathematically compensated for any contamination in the cardiomyocyte fraction in the individual cases, reducing the risk that contamination with a cell population with a different turnover rate would skew the result for cardiomyocytes. In all individuals born before the onset of the nuclear bomb tests, the ^{14}C concentrations in cardiomyocyte genomic DNA were higher than the pre-bomb atmospheric concentrations, demonstrating DNA synthesis after 1955 (Fig. 3A). Similarly, in all individuals born near or after the time of the nuclear bomb tests, the ^{14}C concentrations in cardiomyocyte DNA corresponded to the concentrations several years after their birth, establishing postnatal cardiomyocyte DNA synthesis (Fig. 3B).

There is no increase in the number of cardiomyocytes after the postnatal period but rather a slow, continuous decrease with age (*21*). About 25% of cardiomyocytes are binucleated in humans at birth, and this proportion stays constant throughout life (*22*). Thus, the postnatal cardiomyocyte DNA synthesis detected by ^{14}C analysis cannot be explained by an increase in cardiomyocyte number or binucleation. However, the heart grows during childhood, as the increasing demand of contractile capacity is met by hypertrophy of cardiomyocytes. Almost all cardiomyocyte nuclei are diploid at the time of birth, but the DNA of most nuclei is duplicated to become tetraploid in childhood when the cells undergo hypertrophy (Fig. 3C and fig. S5) (*23–25*). After the age of 10, there is no further increase in the DNA content of cardiomyocyte nuclei ($R = 0.135$, $P = 0.384$, Fig. 3C). The DNA synthesis associated with polyploidization of cardiomyocyte DNA results in incorporation of ^{14}C concentrations corresponding to the atmospheric levels during childhood.

Three of the individuals born before the nuclear bomb tests were more than 10 years old at the onset of the increase in atmospheric ^{14}C. That their ^{14}C concentration in cardiomyocyte DNA was above the prenuclear bomb test levels (Fig. 3A) cannot be explained by DNA synthesis associated with polyploidization, but indicates cardiomyocyte renewal after 1955. Moreover, in the individuals born after the nuclear bomb tests, the difference between the birth date of the person and the date corresponding to the ^{14}C concentration in cardiomyocyte DNA increased with the age of the individual (fig. S6 and table S1), demonstrating that cardiomyocyte DNA synthesis is not restricted to a limited period in childhood but continues in adulthood.

Polyploidization of cardiomyocyte DNA occurs in a stereotypical manner during a rather short period in childhood (Fig. 3C) (*23–25*), making it possible to calculate its impact on ^{14}C values in each individual [see supporting online text and (*26*)]. By subtracting the childhood polyploidization-associated ^{14}C incorporation from the measured value in each case, we could estimate polyploidization-independent ^{14}C values. In all cases, the polyploidization-independent ^{14}C values corresponded to time points after birth for each individual (Fig. 3D), indicating cardiomyocyte renewal. In the five oldest individuals, who all were born before or at the onset of the nuclear bomb tests, the ^{14}C values were lower than contemporary values (Fig. 3D), establishing that not all cardiomyocytes had been exchanged after 1955 but that a substantial fraction remains from early in life, even in the elderly.

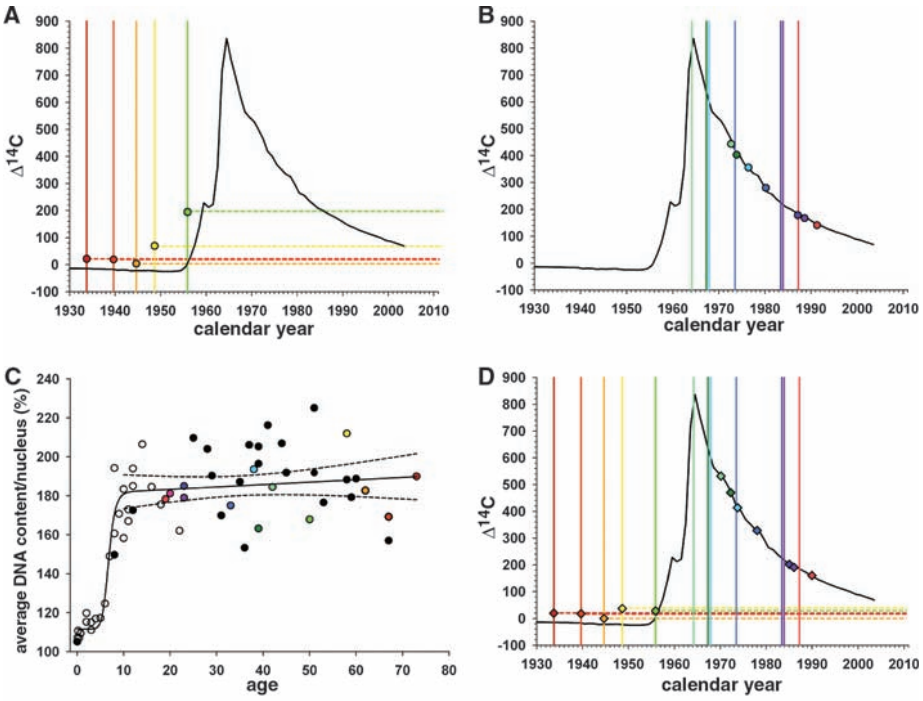

Fig. 3. Cardiomyocyte turnover in adulthood. (**A**) The ^{14}C concentrations in cardiomyocyte DNA from individuals born before the time of the atmospheric radiocarbon increase correspond to time points after the birth of all individuals. The vertical bar indicates year of birth, with the correspondingly colored data point indicating the $\Delta^{14}C$ value. (**B**) ^{14}C concentrations in cardiomyocyte DNA from individuals born after the time of the nuclear bomb test. (**C**) Average DNA content ($2n = 100\%$) per cardiomyocyte nucleus from individuals (without severe heart enlargement; see fig. S5) of different ages. Ploidy was measured by flow cytometry. Colored data points identify individuals analyzed for ^{14}C ($n = 13$). Black data points are from individuals analyzed only with regard to ploidy level ($n = 23$), and white data points are taken from Adler *et al.* ($n = 26$) (*24*, *26*). The dashed lines indicate the 95% confidence interval for the regression curve. (**D**) ^{14}C values corrected for the physiologically occurring polyploidization of cardiomyocytes during childhood for individuals born before and after the bomb-induced spike in ^{14}C concentrations, calculated on the basis of the individual average DNA content per cardiomyocyte nucleus. The ^{14}C content is not affected in individuals where the polyploidization occurred before the increase in atmospheric ^{14}C concentrations.

Downloaded from www.sciencemag.org on April 3, 2009

Increased cardiac workload in pathological situations often results in cardiomyocyte hypertrophy and heart enlargement, and at late stages can result in polyploidization in adulthood (fig. S5) (*24*). Although a few subjects had cardiac pathology (table S2), none had severe heart enlargement nor a pathological cardiomyocyte ploidy profile, and there was no significant difference in ^{14}C integration in cardiomyocyte DNA in the subjects with cardiac pathology (table S1, Fig. 3C, and fig. S5). Moreover, mathematical modeling of the kinetics of DNA synthesis and ^{14}C integration showed that the measured ^{14}C concentrations in cardiomyocyte DNA could not be a result of polyploidization during adulthood (see supporting online text). Furthermore, analysis of ^{14}C concentrations in DNA from only diploid or only polyploid cardiomyocyte nuclei demonstrated similar degrees of ^{14}C integration after childhood in both compartments, providing further evidence for cardiomyocyte renewal independently of polyploidization (see supporting online text, fig. S7, and table S3).

Several studies of sex-mismatched transplant recipients have indicated fusion of human cardiomyocytes with other cells (*27*). However, fusion appears to mainly occur transiently after transplantation, and even in the acute phase the fusion rate is too low to explain the ^{14}C data (fig. S8). DNA damage and repair are very limited in differentiated cells (*28*) and, at least in neurons, are well below the detection limit of the method used (*10*, *11*). Although cell fusion and DNA repair may affect ^{14}C concentrations in cardiomyocyte DNA, available data suggest that the magnitude of these processes makes them negligible in the current context and that the ^{14}C data we report here (after compensation for polyploidization) likely accurately reflects cell renewal.

Mathematical modeling of ^{14}C data from individuals born both before and after the nuclear bomb tests, which provides slightly different and complementary information, as well as of subjects of different age within these groups, can provide an integrated view on cell turnover (*9*). We used an analytical model that includes polyploidization in childhood to assess which one of many scenarios for cell birth and death best describes the data. Times at which cells are born, ploidize, and die are tracked. The atmospheric ^{14}C values corresponding to DNA synthesis events are integrated to yield a calculated ^{14}C level, on the basis of each subject's birth date, age at death, and DNA content. The calculated ^{14}C levels were fitted to the purity-corrected values to find the best renewal rates for each scenario (see supporting online text for a comprehensive description of the modeling). We first calculated what the annual turnover rate would be in each individual if the rate was constant throughout life. This indicated annual turnover rates of 0.2 to 2% (Fig. 4A). However, there was a clear negative correlation to age ($R = -0.84$; $P = 0.001$), establishing that the turnover rate declines with age. The strong negative correlation to age also indicates that there is limited interindividual variation in the cardiomyocyte turnover rate and its decrease with age.

We next tested a series of different models allowing turnover rates to change with age. The best fit was found with an inverse-linear declining turnover rate (Fig. 4B), in which younger cardiomyocytes were more likely than older ones to be replaced (see supporting online text). This model predicts that cardiomyocytes are renewed at a rate of ~1% per year at the age of 25 and 0.45% at the age of 75 (Fig. 4B). With this turnover rate, most cardiomyocytes will never be exchanged during a normal life span (Fig. 4C). At the age of 50, 55% of the cardiomyocytes remain from the time around birth and 45% have been generated later (Fig. 4C). The age of cardiomyocytes is on average 6 years younger than the individual (Fig. 4D). The ^{14}C data indicate a substantially higher renewal rate for noncardiomyocytes, with a median annual turnover of 18% and a mean age of 4.0 years (see supporting online text). Our data do not allow us to identify whether new cardiomyocytes derive from cardiomyocyte duplication or from a stem/progenitor pool, because both would result in similar ^{14}C integration in DNA.

Analysis of cell proliferation in the human myocardium has previously indicated a cardiomyocyte proliferation rate that could result in the exchange of all cardiomyocytes within 5 years (*29*), but the ^{14}C concentrations in DNA exclude such a high mitotic renewal rate. We asked whether cardiomyocytes may be heterogeneous, with an identifiable subpopulation turning over relatively fast and the rest not turning over at all. This scenario is incompatible with the data, and it is most likely that the vast majority of cardiomyocytes have a similar probability of being exchanged at a given age (see supporting online text).

The limited functional recovery in humans after myocardial injury clearly demonstrates insufficient regeneration of cardiomyocytes. The renewal of cardiomyocytes, indicated by the continuous integration of ^{14}C, suggests that the development of pharmacological strategies to stimulate this process may be a rational alternative or complement to cell transplantation strategies for cardiomyocyte replacement.

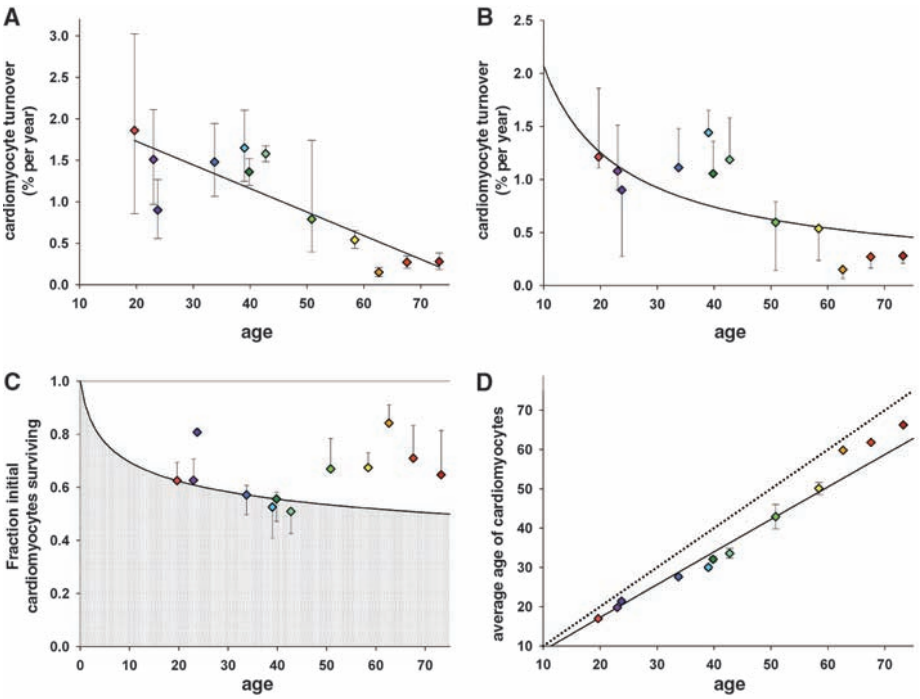

Fig. 4. Dynamics of cardiomyocyte turnover. (**A**) Individual data fitting assuming a constant turnover (see supporting online text) reveals an almost linear decline of cardiomyocyte turnover with age ($R = -0.84$; $P = 0.001$). A constant-turnover hypothesis might therefore not represent the turnover dynamics accurately. (**B**) Global fitting of all data points (see supporting online text, error sum of squares = 1.2×10^4) shows an age-dependent decline of cardiomyocyte turnover. (**C**) The gray area depicts the fraction of cardiomyocytes remaining from birth, and the white area is the contribution of new cells. Estimate is from the best global fitting. (**D**) Cardiomyocyte age estimates from the best global fitting. The dotted line represents the no-cell-turnover scenario, where the average age of cardiomyocytes equals the age of the individual. The black line shows the best global fitting. Colored diamonds indicate computed data points from ^{14}C-dated subjects. Error bars in (A) are calculated from the errors on ^{14}C measurements. Error bars in all other graphs are calculated for each subject individually and show the interval of possible values fitted with the respective mathematical scenario.

References and Notes

1. R. Passier, L. W. van Laake, C. L. Mummery, *Nature* **453**, 322 (2008).
2. M. A. Laflamme, C. E. Murry, *Nat. Biotechnol.* **23**, 845 (2005).
3. S. Martin-Puig, Z. Wang, K. R. Chien, *Cell Stem Cell* **2**, 320 (2008).
4. S. M. Wu, K. R. Chien, C. Mummery, *Cell* **132**, 537 (2008).
5. P. Anversa, B. Nadal-Ginard, *Nature* **415**, 240 (2002).

Downloaded from www.sciencemag.org on April 3, 2009

6. M. H. Soonpaa, L. J. Field, *Circ. Res.* **83**, 15 (1998).
7. P. C. Hsieh *et al.*, *Nat. Med.* **13**, 970 (2007).
8. J. Butany *et al.*, *Lancet Oncol.* **6**, 219 (2005).
9. K. L. Spalding *et al.*, *Nature* **453**, 783 (2008).
10. R. D. Bhardwaj *et al.*, *Proc. Natl. Acad. Sci. U.S.A.* **103**, 12564 (2006).
11. K. Spalding, R. D. Bhardwaj, B. Buchholz, H. Druid, J. Frisén, *Cell* **122**, 133 (2005).
12. H. De Vries, *Science* **128**, 250 (1958).
13. R. Nydal, K. Lovseth, *Nature* **206**, 1029 (1965).
14. I. Levin, B. Kromer, *Radiocarbon* **46**, 1261 (2004).
15. K. L. Spalding, B. A. Buchholz, L.-E. Bergman, H. Druid, J. Frisén, *Nature* **437**, 333 (2005).
16. W. F. Libby, R. Berger, J. F. Mead, G. V. Alexander, J. F. Ross, *Science* **146**, 1170 (1964).
17. D. D. Harkness, *Nature* **240**, 302 (1972).
18. E. M. Wild *et al.*, *Nucl. Instrum. Methods Phys. Res. B* **172**, 944 (2000).
19. M. Rubart, L. J. Field, *Annu. Rev. Physiol.* **68**, 29 (2006).
20. M. S. Parmacek, R. J. Solaro, *Prog. Cardiovasc. Dis.* **47**, 159 (2004).
21. G. Olivetti, M. Melissari, J. M. Capasso, P. Anversa, *Circ. Res.* **68**, 1560 (1991).
22. G. Olivetti *et al.*, *J. Mol. Cell. Cardiol.* **28**, 1463 (1996).
23. V. Brodsky, D. S. Sarkisov, A. M. Arefyeva, N. W. Panova, I. G. Gvasava, *Virchows Arch.* **424**, 429 (1994).
24. C. P. Adler, in *The Development and Regenerative Potential of Cardiac Muscle,* J. O. Oberpriller, J. C. Oberpriller, A. Mauro, Eds. (Harwood, New York, 1991), pp. 227–252.
25. P. Pfitzer, *Curr. Top. Pathol.* **54**, 125 (1971).
26. Materials and methods are available as supporting material on *Science* Online.
27. M. A. Laflamme, D. Myerson, J. E. Saffitz, C. E. Murry, *Circ. Res.* **90**, 634 (2002).
28. T. Nouspikel, P. C. Hanawalt, *DNA Repair (Amst.)* **1**, 59 (2002).
29. A. P. Beltrami *et al.*, *N. Engl. J. Med.* **344**, 1750 (2001).

30. We thank R. Lee, K. Spalding, and members of the Frisén lab for valuable discussions; M. Toro and K. Hamrin for help with flow cytometry; P. Reimer for assistance with radiocarbon interpretation; R. Cassidy, M. Müller, and E. Klaile for technical advice; M. Stahlberg and T. Bergman for help with high-performance liquid chromatography; and D. Kurdyla and P. Zermeno for producing graphite. This study was supported by grants from the Swedish Heart-Lung Foundation, the Swedish Research Council, Knut och Alice Wallenbergs Stiftelse, Human Frontiers Science Program, the Swedish Cancer Society, the Foundation for Strategic Research, the Karolinska Institutet, the Juvenile Diabetes Research Foundation, NIH/NCRR (RR13461), European Commission FP7 CardioCell, and the Tobias Foundation. This work was performed in part under the auspices of the U.S. Department of Energy by Lawrence Livermore National Laboratory under contract DE-AC52-07NA27344. R.D.B. and F.B.-H. were supported by fellowships from the Canadian Institutes of Health Research, and F.B.-H. was also supported by a fellowship from the Christopher and Dana Reeve Foundation.

Supporting Online Material
www.sciencemag.org/cgi/content/full/324/5923/98/DC1
Materials and Methods
SOM Text
Figs. S1 to S8
Tables S1 to S3
References

14 August 2008; accepted 29 January 2009
10.1126/science.1164680

S-Nitrosylation of Drp1 Mediates β-Amyloid–Related Mitochondrial Fission and Neuronal Injury

Dong-Hyung Cho,[1]*† Tomohiro Nakamura,[1]* Jianguo Fang,[1] Piotr Cieplak,[2] Adam Godzik,[2] Zezong Gu,[1]‡ Stuart A. Lipton[1]§

Mitochondria continuously undergo two opposing processes, fission and fusion. The disruption of this dynamic equilibrium may herald cell injury or death and may contribute to developmental and neurodegenerative disorders. Nitric oxide functions as a signaling molecule, but in excess it mediates neuronal injury, in part via mitochondrial fission or fragmentation. However, the underlying mechanism for nitric oxide–induced pathological fission remains unclear. We found that nitric oxide produced in response to β-amyloid protein, thought to be a key mediator of Alzheimer's disease, triggered mitochondrial fission, synaptic loss, and neuronal damage, in part via S-nitrosylation of dynamin-related protein 1 (forming SNO-Drp1). Preventing nitrosylation of Drp1 by cysteine mutation abrogated these neurotoxic events. SNO-Drp1 is increased in brains of human Alzheimer's disease patients and may thus contribute to the pathogenesis of neurodegeneration.

Disrupting the balance between mitochondrial fission and fusion can lead to excessive mitochondrial fragmentation. Fragmentation triggered by dysfunction of the fission-inducing protein Drp1 (dynamin-related protein 1), for example, contributes to synaptic damage and subsequent neuronal loss because of nitrosative/oxidative stress and impaired bioenergetics (*1*–*6*). Excessive fission results in abnormally small mitochondria with fragmented cristae (*2*), as observed in electron microscopy studies of neurons in human Alzheimer's disease (AD) (*7*). Drp1 homologs are S-nitrosylated, which regulates their activity (*8*, *9*). Furthermore, β-amyloid protein (Aβ) oligomers induce excessive mitochondrial fission and neuronal damage in a nitric oxide (NO)–mediated fashion (*2*, *10*). We sought to determine whether Drp1 is S-nitrosylated and thereby activated in AD.

Cerebrocortical neurons transfected with the mitochondrial marker mito-DsRed2 were exposed to the NO donor *S*-nitrosocysteine (SNOC) (*11*) and morphological changes in mitochondria were monitored by 3D-deconvolution fluorescence microscopy (*2*). Mitochondria normally displayed an elongated filamentous morphology, but addition of SNOC induced fragmented, smaller mitochondria in a dose-dependent manner, due to fission (Fig. 1, A and B) (*2*, *11*). Using a biotin-switch assay (*12*), we found that SNOC induced S-nitrosylation of Drp1 (forming SNO-Drp1) in neurons before inducing fission (Fig. 1C).

To investigate whether endogenously generated NO can induce SNO-Drp1, we used human embryonic kidney (HEK) 293 cells stably expressing neuronal NO synthase (nNOS). These cells were subjected to biotin-switch assay after incubation with the calcium ionophore A23187 to activate nNOS. Endogenous Drp1 was S-nitrosylated by endogenous NO; this reaction was blocked by the NOS inhibitor *N*-nitro-L-arginine (NNA; Fig. 2, A and B). SNO-Drp1 was not detected in controls performed without ascorbate to remove NO, thus preventing replacement of NO by biotin (which is detected in this assay), or without biotin-HPDP (*N*-[6-(biotinamido)hexyl]-3′-(2′-pyridyldithio)-propionamide).

Using the same conditions under which Aβ causes mitochondrial fragmentation and consequent neuronal damage (*2*), we found that Aβ could induce SNO-Drp1 formation. Cerebrocortical neurons were exposed to oligomers of the pathologically active fragment Aβ25-35 or, as a control, reverse-sequence Aβ35-25. Formation of SNO-Drp1 was observed only in Aβ25-35–treated neurons, not in the control (Fig. 2C). Additionally, we tested the effect of endogenously produced Aβ, generated from amyloid precursor protein (APP) in conditioned medium of N2a/APP695 stable neuronal cell lines or CHO cells stably expressing human APP with the $Val^{717} \rightarrow$ Phe mutation (designated 7PA2 cells). Exposing N2a cells to SNOC or conditioned medium resulted in SNO-Drp1 formation (Fig. 2C). We also found elevated levels of SNO-Drp1 in vivo in brains of the AD transgenic mouse model Tg2576, which expresses high levels of the Swedish APP mutation ($Lys^{670} \rightarrow$ Asn, $Met^{671} \rightarrow$ Leu) (fig. S1).

To extend these findings to humans, we examined brains obtained shortly after death from patients manifesting AD (table S1). We found increased SNO-Drp1 levels in 17 of 17 AD brains studied, but not in brains of deceased Parkinson's disease patients or controls who died of non-CNS causes (Fig. 2, D and E, and fig. S2). To determine whether the level of SNO-Drp1 in AD human

[1]Center for Neuroscience, Aging, and Stem Cell Research, Burnham Institute for Medical Research, 10901 North Torrey Pines Road, La Jolla, CA 92037, USA. [2]Bioinformatics and Systems Biology Program, Burnham Institute for Medical Research, 10901 North Torrey Pines Road, La Jolla, CA 92037, USA.

*These authors contributed equally to this work.
†Present address: Asan Medical Center, University of Ulsan College of Medicine, 388-1 Poongnap-2-dong Songpa-gu, Seoul 138-736, Korea.
‡Present address: University of Missouri–Columbia School of Medicine, Columbia, MO 65212, USA.
§To whom correspondence should be addressed. E-mail: slipton@burnham.org

Downloaded from www.sciencemag.org on April 3, 2009

9.3 Bernard S, Gonze D, Čajavec B, Herzel H, Kramer A (2007) Synchronization-induced rhythmicity of circadian oscillators in the suprachiasmatic nucleus. PLOS Comput Biol 3:e68

Synchronization-Induced Rhythmicity of Circadian Oscillators in the Suprachiasmatic Nucleus

Samuel Bernard[1*], Didier Gonze[2], Branka Čajavec[3], Hanspeter Herzel[3], Achim Kramer[4]

1 Institute of Applied and Computational Mathematics, Foundation for Research and Technology–Hellas, Heraklion, Crete, Greece, **2** Unité de Chronobiologie Théorique, Faculté des Sciences, CP 231, Université Libre de Bruxelles, Bruxelles, Belgium, **3** Institute for Theoretical Biology, Humboldt University, Berlin, Germany, **4** Laboratory of Chronobiology, Institute of Medical Immunology, Charité Universitätsmedizin Berlin, Berlin, Germany

The suprachiasmatic nuclei (SCN) host a robust, self-sustained circadian pacemaker that coordinates physiological rhythms with the daily changes in the environment. Neuronal clocks within the SCN form a heterogeneous network that must synchronize to maintain timekeeping activity. Coherent circadian output of the SCN tissue is established by intercellular signaling factors, such as vasointestinal polypeptide. It was recently shown that besides coordinating cells, the synchronization factors play a crucial role in the sustenance of intrinsic cellular rhythmicity. Disruption of intercellular signaling abolishes sustained rhythmicity in a majority of neurons and desynchronizes the remaining rhythmic neurons. Based on these observations, the authors propose a model for the synchronization of circadian oscillators that combines intracellular and intercellular dynamics at the single-cell level. The model is a heterogeneous network of circadian neuronal oscillators where individual oscillators are damped rather than self-sustained. The authors simulated different experimental conditions and found that: (1) in normal, constant conditions, coupled circadian oscillators quickly synchronize and produce a coherent output; (2) in large populations, such oscillators either synchronize or gradually lose rhythmicity, but do not run out of phase, demonstrating that rhythmicity and synchrony are codependent; (3) the number of oscillators and connectivity are important for these synchronization properties; (4) slow oscillators have a higher impact on the period in mixed populations; and (5) coupled circadian oscillators can be efficiently entrained by light–dark cycles. Based on these results, it is predicted that: (1) a majority of SCN neurons needs periodic synchronization signal to be rhythmic; (2) a small number of neurons or a low connectivity results in desynchrony; and (3) amplitudes and phases of neurons are negatively correlated. The authors conclude that to understand the orchestration of timekeeping in the SCN, intracellular circadian clocks cannot be isolated from their intercellular communication components.

Citation: Bernard S, Gonze D, Čajavec B, Herzel H, Kramer A (2007) Synchronization-induced rhythmicity of circadian oscillators in the suprachiasmatic nucleus. PLoS Comput Biol 3(4): e68. doi:10.1371/journal.pcbi.0030068

Introduction

In most mammalian cells, a set of "clock" genes and proteins forms a regulatory network that produces oscillations with a circadian period (≈24 h) [1]. Molecular and physiological rhythms are coordinated with the daily changes in the environment by a dominant circadian pacemaker, the suprachiasmatic nuclei (SCN) of the hypothalamus. The SCN neurons endogenously generate circadian rhythm and adapt that rhythm according to light–dark (LD) cycles of the environment (entrainment). The approximately 20,000 neurons in the SCN [2,3] vary (1) in their ability to sense the environmental timing cues, (2) in the neurotransmitters they express or respond to, and (3) in their connectivity properties. A desire to understand how such a heterogeneous network produces a coherent and synchronous circadian output has motivated extensive experimental and theoretical work.

Organotypic SCN slices or SCN neurons in high-density dispersal cultures express a coordinated rhythmic activity for as long as they are viable (a few weeks up to several months) [2]. SCN neurons in low-density dispersal cultures, however, do not show a coordinated activity but express a large variation in their free-running periods [4,5]. This has led to the conclusion that SCN neurons are self-sustained circadian oscillators that need a synchronization signal to produce a coherent output. Even before this experimental evidence, it had been hypothesized that the coupling of "sloppy" clocks improves the reliability of the output [6]. So far, all published mathematical models of the synchronization of the SCN rest on the coupling of self-sustained circadian oscillators.

Among candidate synchronization factors are the neuropeptides vasoactive intestinal polypeptide (VIP), gastrin-releasing peptide (GRP), [7] and prokineticin 2 [8], and the neurotransmitter GABA [9]. In addition, signals using the G-

Editor: Karl J. Friston, University College London, United Kingdom

Received October 20, 2006; **Accepted** February 27, 2007; **Published** April 13, 2007

A previous version of this article appeared as an Early Online Release on February 27, 2007 (doi:10.1371/journal.pcbi.0030068.eor).

Copyright: © 2007 Bernard et al . This is an open-access article distributed under the terms of the Creative Commons Attribution License, which permits unrestricted use, distribution, and reproduction in any medium, provided the original author and source are credited.

Abbreviations: DM, dorsomedial; LD, light–dark; SCN, suprachiasmatic nuclei; TTX, tetrodotoxin; VIP, vasoactive intestinal polypeptide; VL, ventrolateral

* To whom correspondence should be addressed. E-mail: samubernard@gmail.com

Author Summary

Circadian rhythms, characterized by a period close to 24 h, are observed in nearly all living organisms, from cyanobacteria to plants, insects, and mammals. In mammals, the central circadian clock is located in the suprachiasmatic nucleus (SCN) of the hypothalamus, where it receives light signals from the retina. In turn, the SCN controls circadian rhythms in peripheral tissues and behavioral activity. The SCN is composed of about 20,000 neurons characterized by a small size and a high density. Within each individual neuron, clock genes and proteins compose interlocked regulatory feedback loops that generate circadian oscillations on the molecular level. SCN neurons dispersed in cell cultures display cell-autonomous oscillations, with periods ranging from 20 h to 28 h. The ventrolateral part of the SCN receives light input from the retina, serving as a relay for the dorsomedial part. Coupling and synchronization among SCN neurons are ensured by neurotransmitters. A desire to understand how such a network of heterogeneous circadian oscillators achieves a synchronous and coherent output rhythm has motivated extensive experimental and theoretical work. In this paper, we present a molecular model combining intracellular and extracellular dynamics for the SCN circadian system, and propose a novel synchronization mechanism. Our results predict a dual role for the coupling factors within the SCN, both in maintaining the rhythmicity and in promoting the synchronization between the circadian oscillators.

protein subunit $G_{i/o}$ [10] as well as gap junctions [11] have been implicated in the intra-SCN synchronization mechanism. The concept of mutual coupling, in which the neurotransmitter is released in a circadian fashion and feeds back on the clock, has been put forward by different authors [9,12–18]. Two recent studies analyzed the consequences of targeted disruption of genes coding for VIP or its receptor, $VPAC_2$ [18,19]. In both cases, not only the synchrony between SCN neurons was lost, but, surprisingly, a majority of neurons also became arrhythmic. Similarly, inhibition of sodium channels by tetrodotoxin (TTX) desynchronizes and suppresses oscillatory activity in clock neurons [20]. In *Drosophila* also, electric disturbance of clock neurons can stop their free-running activity [21]. Activity at the neuronal membrane thus seems to play a role in maintenance of intracellular rhythms and coordination of neuronal clocks [22].

Here, we show that these results can be reproduced by a mathematical model of synchronization of coupled oscillators that are damped rather than self-sustained. Our model reproduces a number of experimental results well: (1) quick and robust synchronization under normal conditions; (2) loss of synchrony and rhythmicity in SCN slices after application of TTX, or in the absence of VIP signaling; and (3) entrainment by LD cycles. In addition, we show that if the number of oscillators is large enough and/or the connectivity between SCN neurons sufficiently strong, synchrony becomes a condition sine qua non for rhythmicity (i.e., the loss of coherent activity results in damped oscillations of individual neurons). Far from being coincidental, we suggest that synchrony-dependent rhythmicity in individual cells is a defining property of robustly synchronized systems like the SCN. Synchronization factors thus have a dual role in maintaining rhythmicity and synchronizing circadian oscillators.

Results

Structure of the Model

To simulate synchronization within the SCN, we constructed a network of coupled but damped molecular circadian oscillators. The model is built in two levels. First, on a single-cell level, we used a detailed molecular model to describe (1) the intracellular dynamics of clock genes and proteins, (2) the circadian neurotransmitter release by clock proteins, and (3) a simplified two-step signaling cascade leading to gene activation in response to neurotransmitter release (Figure 1). Second, on the "tissue" level, we placed the cells on a grid with the topology of a 2-D or 3-D SCN, and coupled them. We considered several coupling schemes mimicking different experimental conditions: (1) random sparse coupling (type 1, Figure 2A), (2) nearest-neighbor coupling (type 2, Figure 2B), and (3) SCN-like coupling combining nearest-neighbor and sparse coupling (type 3, Figure 2C).

Intracellular oscillator. The molecular oscillator consists of a set of seven differential equations describing the time evolution of the key genes of the circadian clock, including *Per/Cry* and *Bmal1*, as proposed in a model by Becker-Weimann et al. [23] (Figure 1; Materials and Methods). In the present study we assume that in absence of synchronization signaling, intracellular oscillators are damped rather than self-sustained (see Introduction). Damped oscillators display a circadian rhythmic activity with gradually decreasing amplitude; without extracellular signals, rhythms vanish within a few days. To achieve damping, we slightly modified the parameter values of the original Becker-Weimann model (see Materials and Methods). In addition, to reflect experimental findings [4], we randomly assigned to each oscillator an individual, intrinsic period distributed around 24 h.

Coupling of oscillators. The coupling between the molecular oscillators is assumed to be accomplished by a neurotransmitter released upon PER/CRY complex activity. The neurotransmitter triggers a signaling cascade that activates *Per/Cry* transcription both in the same cells as well as in coupled neighbors (Figure 1; Materials and Methods). The strength of the coupling signal depends on the average concentrations of neurotransmitter released by all coupled cells at a particular phase.

Topology of a population of oscillators. To simulate SCN-like topology, the oscillators are disposed in a two-lobe–shaped 2-D or 3-D grid (Figure 2C and 2D). Each lobe represents one suprachiasmatic nucleus. The average random periods of oscillators and the connection between oscillators depend on their position within the grid. We simulated three types of coupling to reproduce various experimental conditions (see Materials and Methods). Type 1 is a random coupling with a nominal connectivity c_0, which is the probability that two given oscillators are connected (Figure 2A). Such a coupling may be representative of conditions in neuron cultures dispersed at low or medium densities. Type 2 is a nearest-neighbor coupling, with connections only between oscillators that are separated by a distance smaller than a threshold d_{max}. Type 2 coupling covers a broad class of locally coupled networks, as in high-density neuronal cultures (Figure 2B). Type 3 is aimed to reflect SCN-like coupling entrained by a LD cycle, where the grid is divided into four

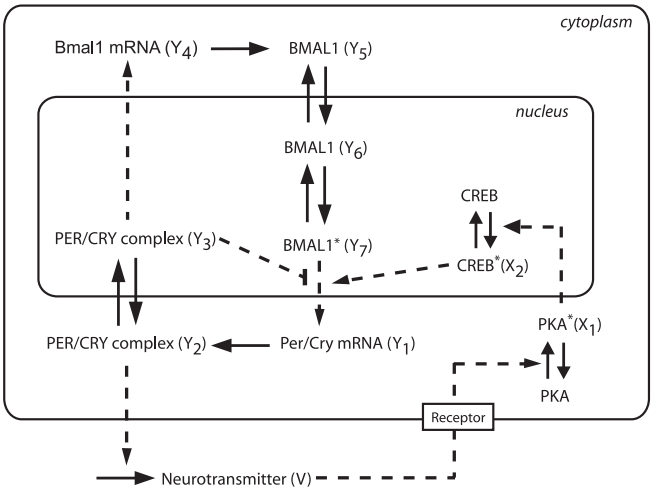

Figure 1. Scheme of the Single-Cell Circadian Oscillator, Including the Coupling Mechanism

The intracellular oscillator consists of interlocked positive and negative transcriptional/translational feedback loops. In the negative feedback loop, *Per* and *Cry* genes (treated as a single variable) inhibit their own transcription by preventing BMAL1 from promoting *Per/Cry* transcription. In the positive feedback loop, the PER/CRY complex activates the transcription of their common transcriptional activator, *Bmal1* [23]. We assumed that the release of the neurotransmitter in the extracellular medium is activated by PER/CRY. In turn, the neurotransmitter activates a signaling cascade (involving PKA and CREB) that activates *Per/Cry* expression. In this schematic representation, solid arrows denote transport, translation steps, or phosphorylation/dephosphorylation reactions, while dashed arrows denote transcriptional regulations. The stars indicate the active (phosphorylated or complexed) form of the proteins. For a full reasoning of modeling assumptions see main text and [23].

doi:10.1371/journal.pcbi.0030068.g001

regions: each lobe is divided in a "ventrolateral" (VL) core and "dorsomedial" (DM) shell region (Figure 2C). Thus, we can simulate a different coupling type for each of the regions as well as coupling between the regions.

Coupled Damped Oscillators Are Efficiently Synchronized

We studied the synchronization dynamics of coupled SCN neurons under four different conditions: high-density culture, low-density culture, presence of TTX, and loss of VIP/$VPAC_2$ receptor.

First, we wanted to test how well coupled oscillators can synchronize under normal conditions that mimic wild-type SCN slices or neuronal cultures (high-density, no mutation). We simulated this by a nearest-neighbor coupling (type 2; Figure 3A, 3B, and Video S1) in a 2-D SCN slice geometry. In these simulations, we ignored spatial heterogeneity of the SCN except that we set the periods of the DM cells to be slightly shorter (4%) than those of the VL cells, consistent with experimental findings [24], and we distributed the periods around 24 h with a standard deviation of 5% [4,5]. As a readout for synchrony, we defined an order parameter R (Equation 18 in Materials and Methods). R is a normalized variance of the average *Per/Cry* mRNA concentrations in all cells, and varies between 0 (no oscillator synchronized) and 1 (all oscillators synchronized in phase). To describe the strength of the synchronization signal, we introduced a parameter $K \geq 0$ that controls the overall coupling strength, and represents the sensitivity of cell to the neurotransmitter (for details, see Materials and Methods). With the coupling strength set to $K = 0.9$, the slice is well synchronized ($R = 0.83$), and the overall period is 24.4 h. The whole slice reached a stationary synchronized state less than 72 h after starting the oscillators from random initial conditions (Figure 3A and 3B; the first 72 h transients are not shown). Thus, the model reproduces well the high degree of synchrony seen in SCN slices.

The connectivity, defined as the average of the ratio between the number of connections and the maximal number of connections, is higher in 3-D (0.16) than in 2-D (0.10), as more neighbors are present within a given radius. Therefore, a complete SCN should synchronize even better than a 2-D slice. Indeed, simulations in a 3-D SCN geometry showed extremely well-synchronized cells ($R = 0.97$) with only a 2.5-h spread from the most advanced to the most delayed cells, compared with more than 4 h for a 2-D slice (Figure S2 and Video S2).

Second, having established that the model is well-synchronized under normal conditions, we wanted to know whether it could reproduce an SCN neuron culture dispersed at low density. To test this, we simulated a population of oscillators in which the neurotransmitter is only perceived by the cell that releases it (autocrine activation). Although individual oscillators are not self-sustained, simulations showed that isolated cells with autocrine activation become self-sustained oscillators, and oscillate with their intrinsic periods (Figure 3C and 3D). Thus, autocrine neurotransmitter activation seems to be sufficient to sustain oscillations in a dispersed cell culture. In addition, individual oscillators have an average intrinsic period of 24.3 ± 1.2 h that is very close to the period of the synchronized cells.

Third, we wanted to reproduce the loss of synchrony and rhythmicity in SCN slices after application of TTX. TTX blocks voltage-gated sodium channels and desynchronizes and suppresses oscillatory activity in clock neurons [20]. After removing TTX, the clock neurons resumed their oscillation and reestablished the same phase relationship as before TTX application. We simulated TTX experiments by using a weak coupling (K small) in a 2-D network with a nearest-neighbor coupling. We transiently decreased K from 0.9, as in normal conditions, to 0.3, and observed that all oscillators damped out. They quickly resumed their high-amplitude oscillations after restoration of full coupling (Figure 3E). Thus, the model reproduces the TTX experiments well.

Fourth, we simulated an SCN neuron culture in the absence of VIP signaling. Experimentally, in the absence of $VPAC_2$, neurons show desynchronized and low-amplitude oscillations, or no oscillations [18]. In some cases, low-amplitude behavioral rhythmicity is retained [10,18,19,25], so we assumed that weak cell-to-cell interaction subsists [7,10] and decreases with the distance between cells. With such a severely impaired coupling, most of the oscillators rapidly damped out, while a few remained irregularly rhythmic for a longer time (Figure 3F). Simulations over a longer time of multiple slices confirmed that these are not self-sustained oscillations (i.e., single cells eventually become arrhythmic). The rhythmic average output is preserved in the first 144 h, with $R = 0.78$. Later, from 144 h to 288 h, R is considerably reduced (to 0.20), indicating a severe disruption of the synchrony after a few days.

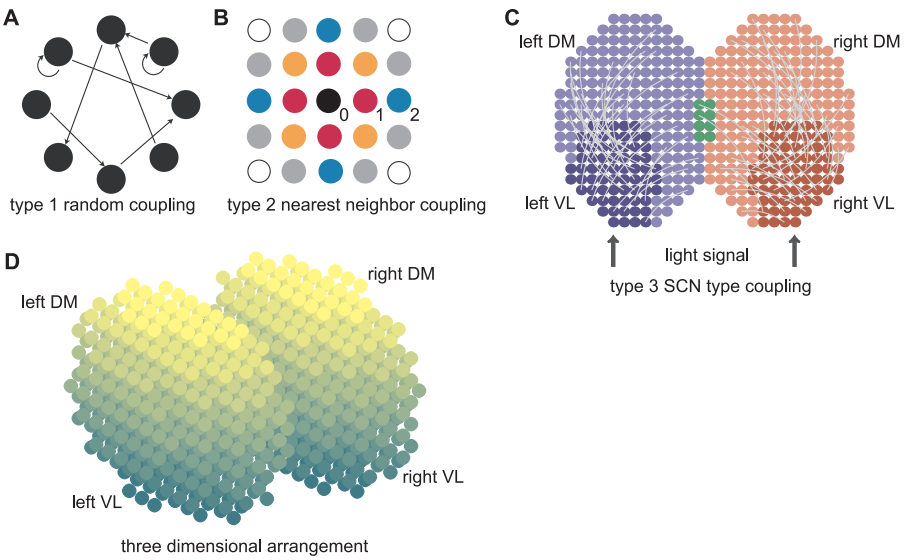

Figure 2. Organization of the Circadian Oscillator Networks

(A) Random coupling (type 1). The probability that two oscillators are connected is independent of their positions.

(B) Nearest-neighbor coupling (type 2). Oscillators are on a grid with a Euclidian distance d. Circle representing oscillators are color-coded for their distance from the central black oscillator. Black, red, orange, blue, gray, and white circles are at distances $d = 0, 1, \sqrt{2}, 2, \sqrt{5}$, and $2\sqrt{2}$, respectively. Two oscillators are connected if their distance is less than a threshold d_{max}.

(C) SCN-like coupling (type 3). The SCN is divided in four regions, left and right VL regions (dark blue and red, respectively), and left and right DM regions (light blue and red, respectively; the green part is the intersection between left and right DM regions). Each dot represents an oscillator. Projections from the VL regions to their respective DM regions are indicated by light gray arcs. Projections from one cell to another are assigned randomly, with probability 0.5 for a DM cell to receive a projection.

(D) Representation of a 3-D SCN. Each dot is a cell, and the color gradient indicates the VL–DM axis (dark cells are on the VL side and light cells are on the DM side, corresponding to the vertical axis in [C]). For type 3 coupling in a 3-D SCN, the regions are defined in the same way as in 2-D (C).

doi:10.1371/journal.pcbi.0030068.g002

Single-Cell Rhythmicity and Synchrony Are Codependent

After having established that oscillators can be efficiently synchronized, and that weak coupling leads to loss of synchrony and rhythmicity in individual oscillators, we wanted to investigate whether coupled damped oscillators indeed only have two dynamic states: rhythmic and synchronized, or arrhythmic and desynchronized. To do this, we first recapitulated the simulations made in the previous subsection with only two coupled oscillators to explore all the dynamic states they can take. We then confirmed that in a large population, individual oscillators could not be rhythmic if their neighbors are not synchronized.

We simulated possible dynamic outcomes of the coupling of two damped oscillators with random periods. We varied the coupling strength and the ability of the oscillators to sense autocrine or paracrine synchronization signals. First, if the oscillators sense strong autocrine and paracrine signals (K high enough, intercellular coupling), they synchronize (Figure 4A). Second, if the oscillators sense only autocrine signals (K high enough, no intercellular coupling), they oscillate, but do not synchronize (Figure 4B). Third, if the oscillators sense weak autocrine and paracrine signals (K small, intercellular coupling), their oscillations die out (Figure 4C). Despite many numeric simulations, we never encountered two normally coupled oscillators that are rhythmic but desynchronized. This indicates that in our model, rhythmicity is sufficient to induce synchronization, and vice versa.

A single oscillator in a large enough neighborhood of rhythmic but totally desynchronized cells would sense a constant average synchronization signal. In our model, the neurotransmitter activates the CREB protein in the signaling cascade. In simulations with constantly activated CREB protein (X_2, Equation 9), oscillations stopped and a stable steady state was reached (Figure 4D). Any transient oscillatory activity damped out to that state (Figure 4E). Hence, a variable input is required for sustained rhythmicity of individual oscillators. In a large population of well-coupled cells, the variable input can only come, by definition, from synchronized neighbors. Noise is another source of variability that might affect synchrony. Two kinds of noise can be distinguished and can have different effects on the synchronization of oscillators. First, the noise can affect individual properties of oscillators (e.g., the successive periods of a given oscillator) or their coupling (e.g., the neurotransmitter released by each cell). Such a local noise impairs the synchrony as the strength of noise increases (Figure S3A–S3D). Alternatively, a spatially uniform extracellular noise could contribute to synchronize the cells (Figure S3E and S3F), even in the absence of synchronization signals, in much the same way that was described by Zhou and coworkers [26]. This result shows that synchrony is necessary for rhythmicity of single oscillators (i.e., single-cell oscillator rhythmicity and synchrony are codependent).

Number of Oscillators and Connectivity Define Synchronization Properties

So far, we have looked at a large number of oscillators and found that robust synchronization is achieved when oscillators are appropriately coupled. To analyze the influence of the number of oscillators as well as the connectivity on synchronization dynamics, we used a uniform, random coupling (type

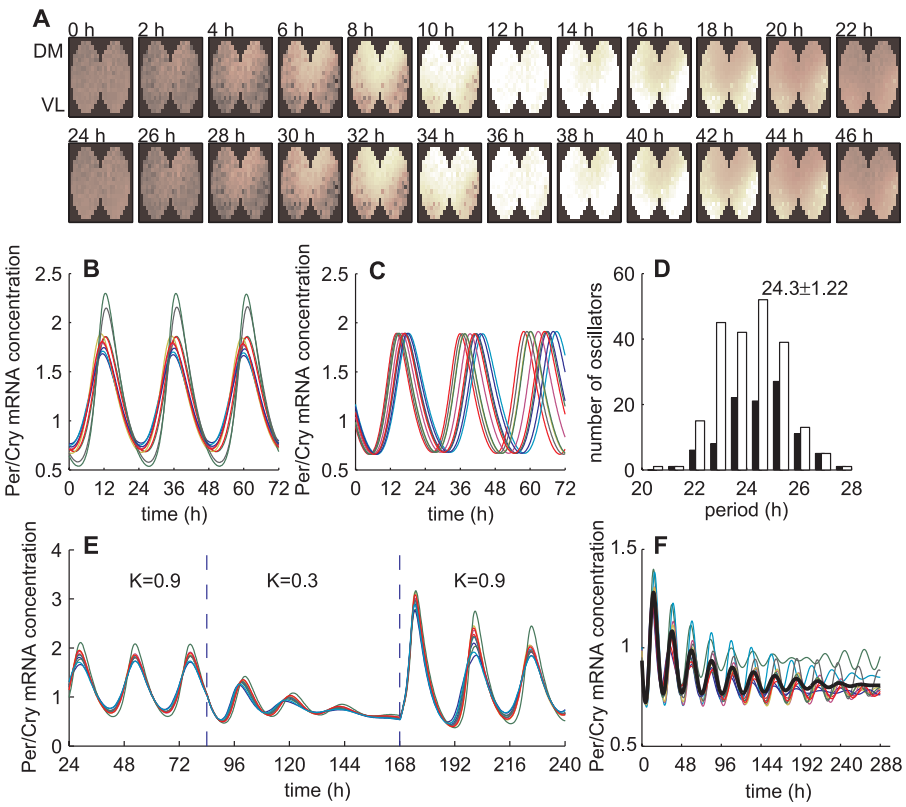

Figure 3. Synchronization of Damped Oscillators

(A) Simulated evolution of *Per/Cry* mRNA expression over 48 h of 309 coupled neurons in a 2-D SCN slice with a type 2 coupling (nearest-neighbor coupling; $d_{max} = 3.5$, $K = 0.9$). Dark brown corresponds to a low level of *Per/Cry* expression, while white corresponds to a high expression.
(B) Time series of ten randomly chosen oscillators from the slice shown in (A).
(C) Time series of ten randomly chosen uncoupled, free-running ($d_{max} = 0$, $K = 0.9$) oscillators.
(D) Distribution of cell-intrinsic periods (black, VL neurons; white, DM neurons; total number of cells, $n = 309$).
(E) Time series of ten transiently weakly coupled oscillators ($d_{max} = 3.5$, $K = 0.3$ between $t = 84$ and 168 h; $n = 309$).
(F) Evolution of ten randomly picked oscillators simulating loss of $VPAC_2$ receptor (f decreasing function of the distance, $d_{max} = 1$, $K = 0.45$, $n = 309$). The decreasing f (see Equation 15) means that the signal is stronger for autocrine coupling. The thick black lines represent the average output. The resulting period is 24.7 h, and the average period of individual oscillators is 24.6 ± 1.2 h.
doi:10.1371/journal.pcbi.0030068.g003

1), and we varied either the number of oscillators or the nominal connectivity (Figure 5) and measured the R values.

First, we considered the synchronization of ensembles consisting of six to 63 oscillators, with a nominal connectivity $c_0 = 0.1$. For the larger ensembles, strong synchronization was consistently achieved ($R > 0.8$ for $n > 40$). For smaller ensembles, the order parameter R shows a high variance, ranging from 0.15 to almost 1 for $n = 27$. High variability of R values denotes poor, nonrobust, network-dependent synchronization (Figure 5A). Representative average outputs for small cell numbers are damped or irregular compared with larger networks (Figure 5B, two top panels versus bottom panel).

Second, we tested the influence of the connectivity on synchronization properties (c_0 ranging from 0.005 to 1 with a fixed number of cells $n = 12$). For dense networks ($c_0 \geq 0.5$), synchronization was consistently excellent ($R > 0.9$). Sparsely connected networks ($c_0 < 0.5$) result in highly variable R values, as for small numbers of oscillators. For small c_0 values (<0.1), we observed better synchronization, perhaps because usually only one synchronized cluster forms (Figure 5C). Sparsely coupled networks show dynamics similar to small population networks, as the connectivity is varied (Figure 5D). These results show that in random networks, both a sufficient number of oscillators and connectivity contribute to strong and robust synchronization. In weakly coupled networks, in addition to a loss of rhythmicity, *Per/Cry* mRNA concentration decreases exponentially (Figure 5B and 5D, top panels), consistent with the relative "dark" cells observed in $VPAC_2$ receptor–deficient luciferase reporter mice [18].

For large numbers of SCN neurons, as in vivo (hundreds to thousands), we found that synchrony is achieved even for very small connectivity values. Therefore, a larger number of neurons in the network ensures that even a great reduction in connectivity will not impair synchrony.

Slow Oscillators Have a Higher Impact on the Period

Mutations in clock genes that modify the free-running period of the SCN provide a way to test the synchronization properties of neurons with different periods. Hamsters homozygous for the *tau* mutation have free-running periods of about 20 h compared with 24 h in wild-type hamsters [27]. The free-running periods in mutant and wild-type animals are determined by the average of periods of dispersed individual clock cells [28,29]. In a recent experiment by the Herzog lab, when dispersed SCN neurons of *tau* mutants and wild-type hamsters were mixed in cell cultures, the resulting period of the total population turned out to be longer than

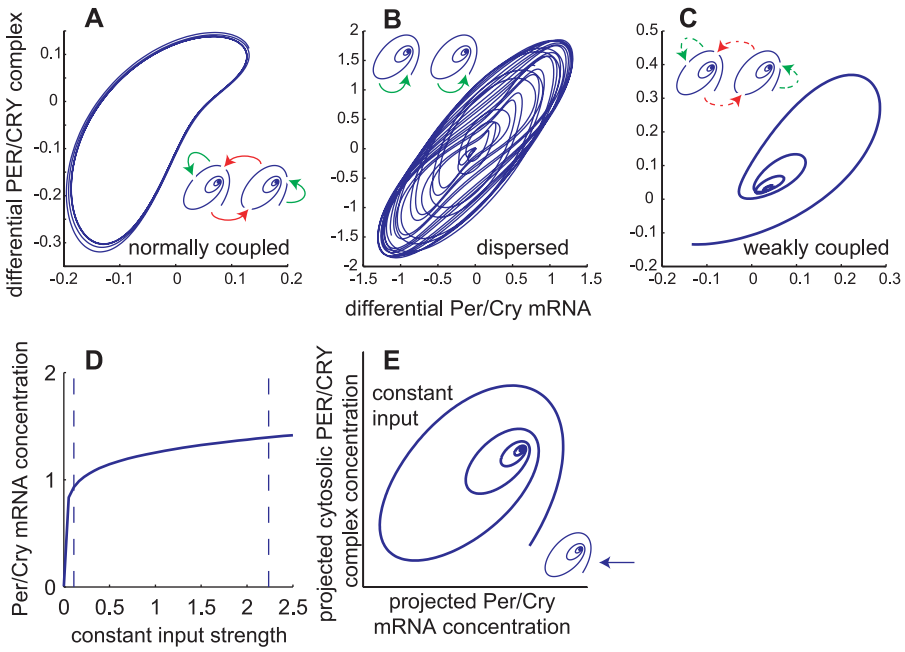

Figure 4. Single-Cell Rhythmicity Implies Synchrony

(A–C) Phase space of a network of two oscillators showing possible dynamic behaviors. Each panel represents a condition that was simulated in the previous subsection. The inlets show what kind of coupling was considered (spirals, damped oscillators; solid arrows, normal coupling [$K = 0.9$]; dashed arrows, weak coupling [$K = 0.3$]; red and green arrows, paracrine and autocrine coupling, respectively). The axes show the differences of *Per/Cry* mRNA and PER/CRY complex concentrations between the two oscillators. This way, two oscillators can be represented in a 2-D space.

(A) Normal, wild-type condition. The oscillators are normally coupled (autocrine and paracrine coupling), and the result is a regular, clock-like cycle denoting synchrony.

(B) Dispersed condition. Oscillators with autocrine activation only are rhythmic, but quickly run out of phase. The result is an irregular cycle as phase differences are not constant.

(C) Weak coupling. Oscillators with weak paracrine and autocrine coupling damp out to a steady state.

(D) Stable steady state of *Per/Cry* mRNA under constant input. The minimal and maximal values of rhythmic input signals (variable X_2) under normal coupling conditions are indicated by the dashed lines.

(E) Phase space of a single oscillator with constant input. Because the intracellular oscillator is 7-D, we had to reduce the phase space from seven to two dimensions, and we chose a projection plane for which the trajectory was closest to a spiral.

doi:10.1371/journal.pcbi.0030068.g004

the average period of the two unmixed populations, which would have been the naive prediction (S. Aton and E. Herzog, personal communication).

With this experimental observation in mind, we tested whether our model might be able to explain this nonintuitive result. We randomly mixed and connected a 24 h–period population with a 20 h–period population (total, $n = 100$; standard deviations of the periods, 0.1 h) in various ratios. The resulting period of the synchronized population was compared with the period that would have been expected from averaging the individual oscillator periods. For ratios between 0.2 and 0.8 (i.e., 20% and 80% wild-type cells), the resulting population period was systematically longer than expected (five runs per ratio, $R > 0.8$; Figure 6A and 6B). Thus, in mixed population, slow oscillators seem to have a higher impact on the period than the faster ones.

In a synchronized SCN neuron slice culture or a high-density SCN neuron dispersal culture, the intrinsic periods of the neurons (i.e., of the noncoupled neurons) cannot be determined experimentally, only the phases and amplitudes. Thus, we used our model to relate these two measures to the intrinsic periods of the neurons. To this end, we extracted the intrinsic periods of the neurons by uncoupling them and calculating their free-running periods. We saw that, when coupled, oscillators with short periods are phase-advanced, and oscillators with long periods are phase-delayed compared with the phase of the average output of the population (Figure 6C and 6D), consistent with the observation that the DM region is advanced with respect to the VL region [20]. We also saw that the amplitudes of oscillators are higher when their periods are longer (Figure 6E). Consequently, oscillators with high amplitudes are phase-delayed, and oscillators with low amplitudes are phase-advanced (Figure 6F). These findings explain why synchronized oscillators have a period longer than expected (i.e., because high-amplitude oscillators contribute more to the population than those with small amplitude).

The Light-Entrained Core Oscillators Can Entrain the Shell Oscillators

An important property of the circadian clock is its capability to be entrained by daily LD cycles. The light signal is conveyed from the retina to the SCN via the retino-hypothalamic tract [30]. Retino-hypothalamic cells release glutamate and PACAP, which activate *Per* gene expression in the target VL cells [31], which then relay the light signal to the DM cells [17]. After a phase-shift in the LD cycle, the light-responsive VL neurons re-entrain rapidly (~2 d) to the new schedule, while the DM neurons take much longer to readjust—up to 13 d after a 6-h advance in the LD cycle [32].

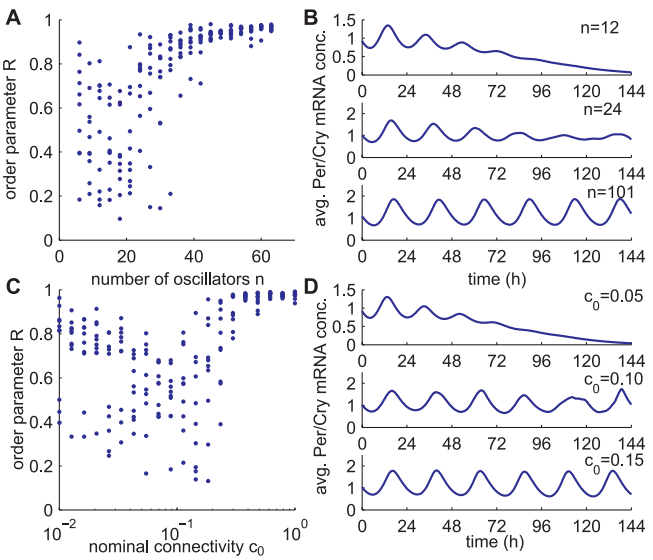

Figure 5. Effect of the Number of Oscillators as Well as the Connectivity on Synchronization

(A) Synchronization properties of randomly coupled networks with respect to the number of neurons n ($c_0 = 0.10$). Each dot represents the order parameter R for one realization of a random network and a simulation. Ten simulations were performed for each value of cell number n. The total length of the simulations was 312 h after starting with random initial conditions, and the order parameter was calculated over the last 240 h.

(B) Three examples of average output for $n = 12$, 24, and 101.

(C) Synchronization properties of randomly coupled networks with respect to the connectivity c_0 ($n = 12$). Ten simulations were performed for each value of nominal connectivity c_0. Other parameters as in (A).

(D) Three examples of average *Per/Cry* mRNA concentration for $c_0 = 0.05$, 0.10, and 0.15.

doi:10.1371/journal.pcbi.0030068.g005

To test whether our model is able to entrain to LD cycles and to analyze entrainment dynamics, we simulated a 12 h–12 h LD cycle in a 2-D SCN with a type 3 coupling by imposing a periodic forcing on the expression of *Per/Cry* gene in the VL cells. Through neuronal projections, VL cells entrained the DM cells (Figure 7A and 7B, and Video S3). Starting from completely desynchronized cells, high synchrony ($R = 0.92$) and phase-locking to the LD cycle (with a 24-h period) are reached very fast, within 72 h. The phases of DM cells were slightly more advanced than those of the light-inducible VL cells (unpublished data), as observed experimentally [20]. After a 12-h phase-shift in the LD cycle, VL cells resumed their phase quickly (after 2 d), while DM cells took more than 10 d to resynchronize to the LD cycle (Figure 7C). These results are in agreement with experimental findings [32], and show that entrainment by a LD cycle is efficient even if only a fraction of the cells can respond to the light signal (102 out of 309), but also that the light-insensitive cells take a longer time to adjust their phase.

Discussion

A Model for the SCN Circadian System

Recent technological advances made it possible to measure the oscillation dynamics of single neurons within a SCN tissue at a high resolution, thus providing experimental data to construct and support more realistic SCN models [3,19]. Several papers proposed models for the molecular mechanism underlying circadian oscillations at the single-cell level [23,33–35], but without considering intercellular communication. Other studies considered intercellular coupling mechanisms between generic oscillators without taking into account the influence of the rhythmicity of the intercellular coupling on the oscillators themselves. In two models, the intracellular oscillator is a van der Pol oscillator, which is a generic two-variable system displaying strong self-sustained oscillations. The models differ in the way cells are coupled: Kunz and Achermann [36] showed how uniformly locally coupled networks can robustly synchronize, while Antle and coworkers [37,38] proposed that a subset of gate cells provide daily inputs to rhythmic oscillators. Rougemont and Naef [39] used more abstract Kuramoto oscillators, in which only the phase (not amplitude) is described, with periods and phases randomly varying in time to characterize the source of phase dispersion. The first attempt to describe synchronization of circadian oscillators that are based on realistic genetic network was by Ueda et al. [40], who showed that synchronization factors confer noise resistance to circadian rhythms in populations of oscillators. Roenneberg and Merrow [41] proposed the concept of zeitnehmer, where the cellular circadian oscillator feeds back on the input pathways of the zeitgebers, blurring the distinction between intra- and extracellular components. Here, we present a molecular model for the SCN circadian system that combines intracellular and extracellular dynamics at the single-cell level.

So far, all published models assumed that individual oscillators are self-sustained. Recent experimental observations challenge that assumption. SCN slices treated with TTX, an inhibitor of sodium channels, lose both synchronization and rhythmicity [20]. In VIP and $VPAC_2$ receptor–deficient high-density neuron dispersals, about 70% of the neurons are no longer rhythmic [19]. Similarly, in the slices from mice lacking the $VPAC_2$ receptor, only a minority of neurons from the dorsal shell is rhythmic, and shows poorly organized and low-amplitude circadian gene expression [18]. These results suggest that synchronization factors are not only required for synchrony, but also for rhythmicity of individual cells. Therefore, in the present model, we considered a population of oscillators that are damped in the absence of synchronization signals.

We built a heterogeneous network of coupled damped circadian oscillators. On a single-cell level, we used a molecular model of the circadian clock [23], neurotransmitter release by clock proteins, and signaling cascade that leads to clock gene activation. We obtained a damped intracellular oscillator by reducing the steepness of the *Per/Cry* promoter feedback loop (Hill coefficient). The Hill coefficient represents the cooperative character of the transcriptional inhibition process. A lower Hill coefficient leads to a more gradual inhibition of the promoter, whereas a high Hill coefficient results more in a switch-like process. On a population level, we placed the cells on a grid with a flexible topology of a 2-D or 3-D SCN, and coupled them. The phenotypes of the neurons (period, amplitude, sustained or damped activity, neuropeptide release and receptor expression, connectivity, etc.) were specified according to their position in the grid.

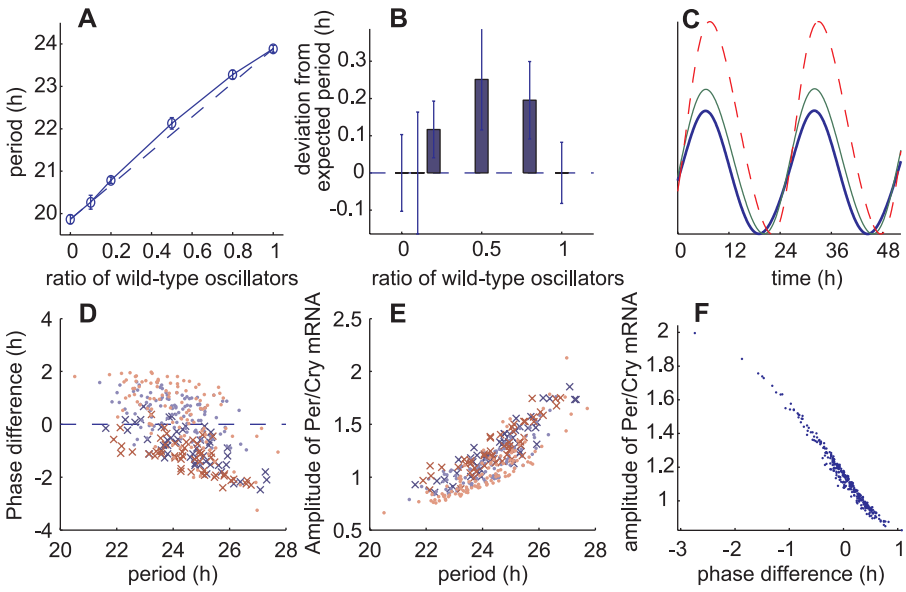

Figure 6. Effect of the Intrinsic Period on Amplitude and Phase

(A) Resulting periods of two mixed populations of oscillators, one with a 24 h period and one with 20 h period (type 1 coupling; $c_0 = 0.1$). The period was calculated with proportions of 24 h period cells of 0.0, 0.1, 0.2, 0.5, 0.8, and 1.0, and results of five runs for each proportion were averaged (total $n = 100$, [open circles] average period). The dashed line represents the average of the individual oscillators' periods.

(B) Deviation of the resulting population periods shown in (A) from the average of the individual oscillator periods (the error bars are the standard deviations).

(C) Three coupled oscillators with different intrinsic periods showing their phase and amplitude relationships: the short period oscillator (thick blue line) is phase-advanced and low amplitude compared with the average period oscillator (green line) and the long period oscillator (dashed red line).

(D) Phase difference from the average *Per/Cry* mRNA concentration with respect to the intrinsic periods, from the simulations shown in Figure 3A and 3B (dark blue ×, left VL neurons; light blue, left DM neurons; dark red ×, right VL neurons; light red, right DM neurons). A positive phase difference means phase-advanced compared with the phase of the population.

(E) Amplitude with respect to the intrinsic period from the simulations shown in Figure 3A and 3B (color code as in [D]).

(F) Amplitude phase relationship for type 1 coupling ($K = 0.9$, $c_0 = 0.1$, number of oscillators $n = 100$).

doi:10.1371/journal.pcbi.0030068.g006

Comparison with Experimental Results and Predictions

We verified that our model reproduces well-known behaviors of SCN. In high-density networks, the modeled coupled oscillators are rhythmic and well synchronized in absence of external cues (Figure 3A and 3B). We simulated TTX treatment of neurons [20] by lowering the coupling strength and showed that rhythmic activity in single oscillators disappeared and resumed quickly after the full coupling was restored (Figure 3E). Then, we simulated loss of VIP and $VPAC_2$ receptor [13,18,19] by lowering the coupling strength and reducing the range of connectivity, and showed that oscillators were slowly desynchronized and damped (Figure 3F). We assumed the presence of a short-range coupling because in the absence of the $VPAC_2$ receptor, mice express multiple circadian periods over more than 80 d when kept in constant darkness [19], suggesting the existence of isolated islands of synchronized, locally coupled SCN neurons. We also verified that a periodically entrained subset of neurons (the VL core) could entrain the rest of the neurons (the DM shell) to a 24-h period (Figure 7A and 7B). After simulating a 12-h phase-shift in the LD cycle, the light-inducible VL region reset its phase much faster than the DM region (2 d versus 10 d; Figure 7C).

Damped oscillators in a large coupled population can adopt two and only two dynamic behaviors, depending on the coupling: (1) damping if uncoupled or weakly coupled, or (2) synchrony if normally coupled (Figure 4). A direct consequence is that coupled cells cannot run out of phase and still oscillate (individual cells dispersed at low density are viewed as many independent synchronized systems). The coupling of damped oscillators produces a circadian pacemaker that is robustly synchronized: provided they are rhythmic, neurons will synchronize. If some neurons lose synchrony, they will damp out, leaving the rest of the SCN unperturbed.

We showed that to achieve robust synchronization, the number of neurons and the connectivity matter (Figure 5). In neuron dispersals, coherent rhythmic output is density-dependent [4,5,19]. In addition, Yamaguchi et al. [20] reported that the upper dorsal region of a SCN slice lost its rhythmicity when cut out from the ventral region, perhaps because of the small size of the separated region—25 neurons were measured in the cut piece. In $VPAC_2$ receptor–deficient or VIP-deficient mice, simultaneous multiple free-running periods in behavior could result from parallel, synchronized clusters in loosely connected networks.

Ohta et al. [42] reported that after 3–5 mo, 10% of the mice kept in constant light showed arrhythmicity. They showed that the arrhythmicity is due to desynchronization between rhythmic SCN neurons. The only way our model could reproduce these results is by decreasing paracrine coupling without interfering with autocrine coupling. But at present, there is no evidence that constant light could induce such a selective disruption.

In a driven harmonic oscillator like a pendulum, the highest amplitude is achieved when the driving period and the intrinsic period coincide [43]. Unexpectedly, in our

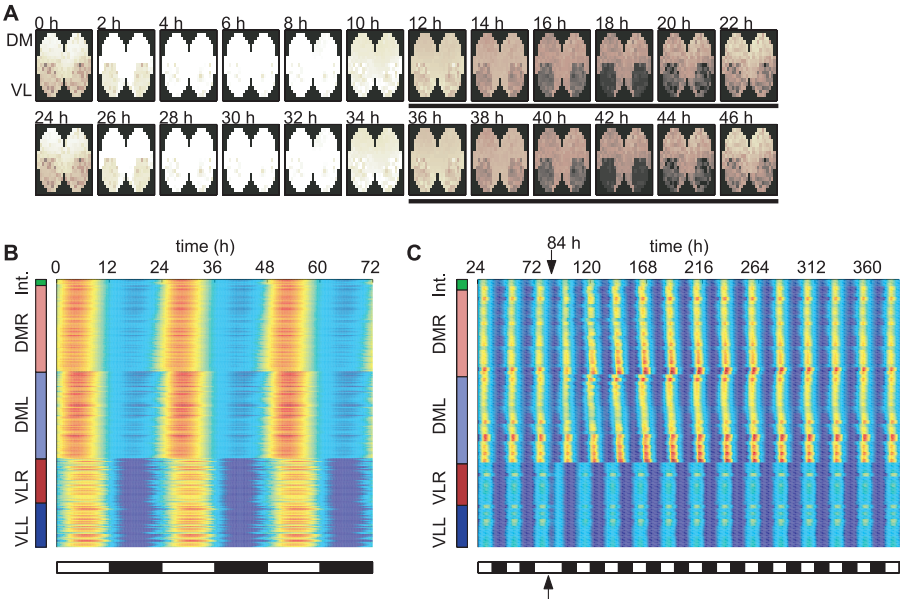

Figure 7. Simulation of Entrainment of a 2-D SCN Slice by a 12:12 LD Cycle

(A) Simulation of the evolution of *Per/Cry* mRNA over 48 h of 309 coupled cells (VL, $n = 102$; DM, $n = 207$) in a 2-D SCN slice with a type 3 coupling ($d_{max} = 3.5$, 50% of neuronal projections, 4% average period gradient, $K = 1.0$, $L_0 = 0.22$). The black bars indicate a dark phase (color code as in Figure 3A). Individual oscillators have an average period of 23.7 ± 1.2 h. Initial conditions were chosen randomly. The first 72 h of transient were discarded, and the time from 72 h to 144 h was retained.

(B,C) Raster plot of *Per/Cry* mRNA activity in oscillators, organized according to their regions (from bottom up: VLL, left VL region; VLR, right VL region; DML, left DM region; DMR, right DM region; and Int, intersection between left and right DM regions). The concentration of *Per/Cry* mRNA for each oscillator is represented by colors (blue, low concentration; red, high concentration).

(B) 12:12 LD cycle.

(C) 12:12 LD cycle with a 12 h phase shift at $t = 84$ h.

doi:10.1371/journal.pcbi.0030068.g007

model, we obtained a monotonic curve in which the amplitudes increase with the periods, possibly because of the interaction between *Per/Cry* gene activation by the synchronization signal and BMAL1 protein (Figure 6E). As a result, slow oscillators have a higher impact on the period in a mixed population, qualitatively reproducing the results from a mixed-genotype experiment (E. Herzog and S. Aton, personal communication). This contrasts with mutually coupled threshold-activated oscillators, where the fastest elements set the period [6]. In homogenous cell cultures, the difference between the free-running period and the average period of individual neurons is smaller than what is statistically detectable [29]. Our simulations also showed no statistical difference between average and synchronized periods (simulations from Figure 3A–3D, two-sided *t*-test, $p = 0.20$).

Based on our results, we propose three experimentally testable predictions. (1) Oscillations in a majority of $VPAC_2$ receptor–negative neurons dispersed at low density should rapidly damp out after induction by serum shock. If validated, this would confirm that loss of rhythmicity in a $VPAC_2$ receptor–negative SCN slice is not due to unexpected cell–cell interaction. To test that neurons need periodic synchronization signals to be rhythmic, one could treat VIP-deficient neurons with constant high levels of $VPAC_2$ agonist. We predict that arrhythmic neurons will stay arrhythmic. (2) A low number of neurons or a low connectivity should result in desynchrony. Medium-density neuron cultures with a small number of neurons should display variability in their synchrony levels (including nonoscillatory neurons as defined by the order parameter R). Increasing the density or the number of neurons would reduce the variability of synchronization levels and increase the average synchrony. Knife cuts in SCN slices to isolate different numbers of neurons could be a way to test size dependency. We predict that pieces that contain fewer than 40 neurons will display large variations in synchronization levels. In mice heterozygous in the gene coding for the $VPAC_2$ receptor, SCN neurons seem to have synchronization properties similar to those in wild-type mice [18]. However, if connectivity is subtly altered in heterozygous mice, a prediction is that asynchrony will occur in larger-cut SCN pieces than for wild-type mice. (3) In high-density dispersal cultures, normalized amplitudes [44] of oscillations should be negatively correlated with the phases as in Figure 6F, provided there is a small variation in the natural amplitudes of isolated neurons. This would be a way to estimate the free-running periods of individual neurons without the need to disperse them.

Synchronization Mechanism

The synchronization of damped oscillators is independent from the particular intracellular model used. Systems with a Goodwin-type model as used in [45], the Leloup-Goldbeter model [33], and other simple negative feedback oscillators have similar synchronization properties (Figure S4–S6). Numeric exploration of such models suggests that positive feedback loops facilitate, but are not necessary for, efficient synchronization (unpublished data). The variability of behavioral periods in *Rev-Erbα* knockout mice, in which the positive

loop is dysfunctional, could reflect that feature [46]. One could test whether synchronization properties of SCN neurons are altered in these mice by analyzing SCN neurons from *Rev-Erbα*$^{-/-}$Per2:luc double-transgenic mice. We predict that *Rev-Erbα* knockout mice will have lower amplitude and more spread-out synchronized SCN neurons. Li and coworkers [47] introduced "transient resetting" as a possible synchronization mechanism, in which uncoupled oscillators are synchronized by a force (which may be noise) that transiently moves them to a region where they have a stable steady state. In our model, the driving force was generated autonomously by the coupled oscillators. To our knowledge, it is the first time that synchronization-induced rhythmicity is described in a biological system. Damped but uncoupled oscillators have been considered before in a model of interaction between a clock and a zeitgeber input pathway [41]. Temporal and spatial rhythms can occur when identical stable systems are diffusively coupled together, giving rise to well-studied Turing instabilities [48,49]. Oscillations can also emerge from electrical coupling between nonoscillating cells [50,51]. Nonetheless, two features distinguish our work from that mentioned above. (1) In our system, temporal instabilities do not arise from spatial heterogeneity or local coupling because synchrony also holds in case of all-to-all coupling of identical oscillators. (2) Oscillators are directly coupled, instead of being diffusively coupled [52]. Direct coupling means that even under perfect synchrony, the coupling term is nonzero, unlike in the diffusive coupling case.

The question of how a coherent and robust circadian output is generated from a heterogeneous network of 20,000 oscillators in the SCN has led to many surprising results [2,3,18–20], bringing a better understanding of the interaction between the single-cell clock and its organization. To understand the orchestration of timekeeping in the SCN, intracellular circadian modules cannot be isolated from their intercellular communication components.

Materials and Methods

Single-cell oscillator model. The intracellular oscillator is a seven-variable model representing clock genes' mRNA and proteins [23]. It consists of interlocked transcriptional/translational feedback loops and reflects the essential features of the mammalian circadian oscillator (Figure 1). The circadian release of a neuropeptide mediates intercellular coupling of circadian cells in the SCN [9,12–18]. Here, we assumed that the release of the neuropeptide is induced by the cytosolic PER/CRY protein complex. The neuropeptide activates a two-step cascade in connected cells that leads to *Per/Cry* mRNA transcription. The assumption that the PER/CRY complex induces neuropeptide release was made to ensure that the transmitter is released quickly after *Per/Cry* gene activation. The cascade is schematized by PKA and CREB activation. With the neurotransmitter and the two-step cascade, the complete single-cell system has ten variables.

$$\frac{dY_1}{dt} = f_{Per/Cry} - k_{1d}Y_1 + L, \tag{1}$$

$$\frac{dY_2}{dt} = k_{2b}Y_1^q - (k_{2d} + k_{2t})Y_2 + k_{3t}Y_3, \tag{2}$$

$$\frac{dY_3}{dt} = k_{2t}Y_2 - k_{3t}Y_3 - k_{3d}Y_3, \tag{3}$$

$$\frac{dY_4}{dt} = f_{Bmal} - k_{4d}Y_4, \tag{4}$$

$$\frac{dY_5}{dt} = k_{5b}Y_4 - (k_{5d} + k_{5t})Y_5 + k_{6t}Y_6, \tag{5}$$

$$\frac{dY_6}{dt} = k_{5t}Y_5 - (k_{6t} + k_{6d})Y_6 + k_{7a}Y_7 - k_{6a}Y_6, \tag{6}$$

$$\frac{dY_7}{dt} = k_{6a}Y_6 - (k_{7a} + k_{7d})Y_7, \tag{7}$$

$$\frac{dV}{dt} = k_8Y_2 - k_{8d}V. \tag{8}$$

The nonlinear transcription functions are

$$f_{Per/Cry} = v_{1b}\frac{Y_7 + X_2^h}{k_{1b}(1 + (Y_3/k_{1i})^p) + (Y_7 + X_2^h)}, \tag{9}$$

$$f_{Bmal} = v_{4b}\frac{Y_3^r}{k_{4b}^r + Y_3^r} \tag{10}$$

The coupling term Q induces a signaling cascade leading to activation of *Per/Cry* promoter, and is proportional to the local mean field F.

$$Q = KF, \tag{11}$$

$$\frac{dX_1}{dt} = k_{x1}Q(X_{1T} - X_1) - k_{dx1}X_1, \tag{12}$$

$$\frac{dX_2}{dt} = k_{x2}X_1(X_{2T} - X_2) - k_{dx2}X_2. \tag{13}$$

The variables represent the following species: Y_1, *Per/Cry* mRNA; Y_2, PER/CRY cytosolic complex; Y_3, nuclear PER/CRY complex; Y_4, *Bmal1* mRNA; Y_5, cytosolic BMAL1; Y_6, nuclear BMAL1; Y_7, transcriptionally active BMAL1*; V, neurotransmitter; X_1, PKA; and X_2, CREB. F is the local mean field as defined in Equation 17, and K is a scalar determining the coupling strength. Equations for X and Y are replicated n times, where n is the number of cellular oscillators (we omitted the indices i for readability). The entry Q_i corresponds to the coupling term in cell i, $i = 1,...,n$. Furthermore, each system is scaled by a factor e_i to generate a distribution of periods. For e_i, we generated a sample g_i drawn from a Gaussian distribution centered at 1 with a standard deviation of 0.05. Additional heterogeneity was added in the form of a vector u_i that defines a linear or radial gradient of periods according to the position of the cells in the SCN. The scaling factor e_i is defined as

$$e_i = \frac{1}{g_i u_i}. \tag{14}$$

This produces a distribution of periods between 20 and 28 h.

The parameter values for the model are $v_{1b} = 9.0$, $k_{1b} = 1.0$, $k_{1i} = 0.56$, $p = 3$, $h = 2$, $k_{1d} = 0.18$, $k_{2b} = 0.3$, $q = 2$, $k_{2d} = 0.1$, $k_{2t} = 0.36$, $k_{3t} = 0.02$, $k_{3d} = 0.18$, $v_{4b} = 1.0$, $k_{4b} = 2.16$, $r = 3$, $k_{4d} = 1.1$, $k_{5b} = 0.24$, $k_{5d} = 0.09$, $k_{5t} = 0.45$, $k_{6t} = 0.06$, $k_{6d} = 0.18$, $k_{6a} = 0.09$, $k_{7a} = 0.003$, $k_{7d} = 0.13$, $k_8 = 1.0$, $k_{8d} = 4.0$, $K = 1.0$, $k_{x1} = 3.0$, $X_{1T} = 15.0$, $k_{dx1} = 4.0$, $k_{x2} = 0.25$, $X_{2T} = 15.0$, $k_{dx2} = 10.0$, and $L_0 = 0.22$. Rates k are in h^{-1} except k_{2b} ($h^{-1}nM^{-(q-1)}$), k_{1b} (nM), k_{1i} (nM), and v_{4b} (nM), k_{x1} and k_{x2} ($h^{-1}nM^{-1}$), v and L_0 (nM h^{-1}), and X_T (nM). Parameters were minimally adapted from the original model [23] to satisfy the following conditions: individual oscillators must be damped, and the coupled system must synchronize with a circadian period. Specifically, we reduced the Hill coefficient p from 8 to 3. A small Hill coefficient makes the periods longer, so we compensated the periods by increasing the degradation rates.

Coupling of neuronal circadian oscillators. Neuropeptide release and action in the intercellular medium are fast compared with the 24-h period of the neurons, allowing diffusion and transport delays between connected cells to be neglected. For a given neuron, we defined a local mean field as the average concentration of neurotransmitter released by the neighboring (connected) cells. This type of coupling is termed direct, as opposed to a diffusive coupling [52].

We considered two different shapes for the SCN. (1) The whole SCN is defined on a 3-D discrete cubic grid G, of size s, where each nonempty node represents a neuron (Figure 2D). Each neuron (node) is assigned a number from 1 to n, and empty nodes have a value 0. Functional or physical regions of the SCN are defined by subgrid E of

G by retaining as nonempty only the nodes belonging to the desired region. This way, various overlapping regions can be defined. (2) An SCN slice is defined on a 2-D square grid in a manner analog to the whole SCN (Figure 2C). Regions of the slice are constructed the same way as in 3-D. We used a Euclidian distance $d(i,j)$ to measure the distance between neurons i and j, with $d = 1$ for adjacent neurons (Figure 2B).

A coupling matrix M, which depends on the geometry of the SCN and a connectivity map C, describes the connections between cells. A neuron i, belonging to a population of size n, receives an input from neuron j if $C_{i,j}$ is 1. We considered three different types of coupling for C (Figure 2A–2C and Figure S1).

Random coupling (type 1): $C_{i,j} = 1$ with probability c_0 (the nominal connectivity) (Figures 2A and S1A). All-to-all coupling is a particular case of sparse coupling when $c_0 = 1$.

Nearest-neighbor coupling (type 2): $C_{i,j} = 1$ if $d_{i,j} < d_{max}$ and neuron i is downstream of neuron j (Figures 2B and S1B).

SCN-like coupling (type 3): we divided the SCN into four regions: left and right VL, and left and right DM regions. The VL part (the ventral core) corresponds to the light-inducible cells and has many projections into the DM region [3,53]. Neurons within the VL part are not coupled and are not spontaneously rhythmic [3,18]. The DM region (the dorsal shell) receives the input from the VL neuronal projections. We used a uniform type 2 coupling (nearest-neighbor) to couple DM cells (Figures 2C and S1C). We used this coupling type in conjunction with an LD cycle.

In addition to the connectivity, a function $f(d)$ determines the relative coupling strength between neurons separated by a distance d. Because of the mean field assumption, the effect of all neurons upstream of neuron i is averaged, so the coupling matrix $M \in \mathrm{R}^{n\times n}$ is

$$M = f(d) \cdot \tilde{C} \tag{15}$$

where the dot $(\cdot)$ denotes the element-wise matrix product and $\tilde{C}$ is normalized so that the sum of each line is 1,

$$\tilde{C}_i = \frac{C_i}{\sum_{j=1}^{n} C_{i,j}}, \qquad i = 1, \ldots, n. \tag{16}$$

The matrix C is normalized as a result of the local mean field assumption: the input to one cell is the average of the signal coming from upstream neurons. The fraction of nonzero entry of C is the connectivity, a scalar denoted by c. The input at each neuron in the SCN is described by the mean field vector $F \in \mathrm{R}^n$,

$$F = MV \tag{17}$$

where V is the transmitter concentration (Equation 8). To measure synchrony, we used an order parameter R [54] defined as

$$R = \frac{\langle \bar{X}^2 \rangle - \langle \bar{X} \rangle^2}{\frac{1}{n}\sum_{i=1}^{n}(\langle X_i^2 \rangle - \langle X_i \rangle^2)} = \frac{\mathrm{Var}_t(\bar{X})}{\mathrm{Mean}_i(\mathrm{Var}_t(\bar{X}_i))}, \tag{18}$$

where $\langle ... \rangle$ denotes the average over time, and $\bar{X} = \sum_{i=1}^{n} X_i/n$ is the average of the variable of interest among oscillators. For comparison with bioluminescence recordings, we chose the variable of interest to be *Per/Cry* mRNA concentration, Y_1 in Equation 1 (half-lives of the reporters are short enough for the reporter itself to be neglected [20]).

We simulated light entrainment by a clipped sine wave,

$$L(t) = \begin{cases} L_0 \sin\left(\frac{\pi t \mathrm{mod} t_{light}}{t_{light}}\right) & \text{if } (t \mathrm{mod} t_{light} + t_{dark}) \le t_{light} \\ 0 & \text{otherwise} \end{cases}, \tag{19}$$

($0 < L(t) \le L_0$ and $L(t) = 0$ alternating every t_{light} and t_{dark} h).

Unless specified, initial conditions for each simulation were randomly chosen, with each variable taking a value between 0 and 2 times the average value of the variable when the system is synchronized. Simulations and analysis were performed in the Matlab 6.5 environment (The MathWorks, http://www.mathworks.com). The ordinary differential equations were simulated with the medium-order adaptive step solver ode45. The codes are available on request.

Supporting Information

Figure S1. Coupling Matrices C for the Three Types of Coupling

In the "spy" matrix representation, the presence of a dot at position (i,j) denotes a directional coupling from cell j to cell i ($C_{i,j} = 1$), and a blank space means that there is no coupling ($C_{i,j} = 0$).
(A) Matrix C for the random coupling type (type 1).
(B) Matrix C for the nearest-neighbor coupling type (type 2). The matrix is symmetrical; hence, all coupling is bidirectional.
(C) Matrix C for the SCN coupling type (type 3). The red and blue shades represent DM intercellular coupling, and the black dots represent projections from the VL to the DM regions.

Found at doi:10.1371/journal.pcbi.0030068.sg001 (148 KB PDF).

Figure S2. Raster Plot of 625 Oscillators with Nearest-Neighbor (Type 2) Coupling in a 3-D SCN Geometry

SCN geometry is organized according to their regions (from bottom up, VLL: left VL region, VLR: right VL region, DML: left DM region, DMR: right DM region, and Int: intersection between left and right DM regions). The concentration of *Per/Cry* mRNA for each oscillators is represented by colors (blue, low concentration; red, high concentration). All other parameters are as in Figure 3A and 3B.

Found at doi:10.1371/journal.pcbi.0030068.sg002 (1.9 MB PDF).

Figure S3. Synchronization of Ten All-to-All Coupled Oscillators with Noisy Coupling and Noisy Intrinsic Periods

We used a multiplicative noise described by stationary Gaussian process (Ornstein-Uhlenbeck process; see Text S1) with noise strength S.
(A,B) Synchronization-coupled oscillators with noisy transmitter release and noisy intrinsic periods ($S = 0.03$, $K = 0.9$). Simulations were made over 2,400 h ([A]; gray lines, individual oscillators; blue line, average of the ten oscillators). Synchronization was good ($R = 0.89$) despite the variations in amplitudes and periods (B).
(C) Coupling improves temporal precision. Successive periods of the average output of synchronized oscillators (black bars, label P) show a better precision than individual oscillators in the synchronized state (gray bars, label C) and uncoupled oscillators (white bars, label U). The standard deviations were 0.5 h, 0.6 h, and 1.9 h, respectively, for data from simulations shown in (A) and (B).
(D) Effect of noise strength S on the order parameter R and the standard deviation of periods of the average output of coupled oscillators. Synchronization was good ($R > 0.8$; blue lines) and standard deviation limited (<2 h; red dashed lines) for S below 0.05. For S larger than 0.05, synchronization was still achieved, but the period became unreliable.
(E,F) Global noise can enhance synchrony. In the presence of strong noise ($S = 0.2$), weakly coupled oscillators ($K = 0.4$) maintained rhythmicity and synchrony ($R = 0.94$) (E). For weaker noise ($S = 0.05$), the same weakly coupled oscillators did not maintain rhythmicity (F).

Found at doi:10.1371/journal.pcbi.0030068.sg003 (273 KB PDF).

Figure S4. Synchronization of 309 Goodwin-Type Damped Oscillators with Nearest-Neighbor (Type 2) Coupling

The simulation is divided in four parts to show synchrony, damping, restoration of synchrony, and damping under constant signal. First, in constant darkness (DD) with normal coupling ($K = 1.5$), oscillators are well-synchronized. Second, in DD without coupling ($K = 0$), oscillators lose synchrony and rhythmicity. Third, in DD, normal coupling ($K = 1.5$) restores synchrony and rhythmicity. Fourth, in constant light (LL) without coupling, oscillators lose rhythmicity, showing that they are damped in the absence of a variable signal.

Found at doi:10.1371/journal.pcbi.0030068.sg004 (20 KB PDF).

Figure S5. Synchronization of 100 One-Variable Negative Feedback Loop Oscillators with Delay (All-to-All Coupling)

The simulation is divided into four parts to show synchrony, damping, restoration of synchrony, and damping under constant signal. First, in DD with normal coupling ($K = 0.1$), oscillators are well-synchronized. Second, in DD without coupling ($K = 0$), oscillators lose synchrony and rhythmicity. Third, in DD, normal coupling ($K = 0.1$) restores synchrony and rhythmicity. Fourth, in LL without coupling, oscillators lose rhythmicity, showing that they are damped in the absence of a variable signal.

Found at doi:10.1371/journal.pcbi.0030068.sg005 (21 KB PDF).

Figure S6. Synchronization of 40 Leloup-Goldbeter Oscillators with All-to-All Coupling

The simulation is divided into four parts to show synchrony, damping, restoration of synchrony, and damping under constant signal. First, in DD with normal coupling ($K = 1$), oscillators are well-synchronized. Second, in DD with weak coupling ($K = 0.6$), oscillators

lose synchrony and rhythmicity. Third, in DD, normal coupling ($K = 1$) restores synchrony and rhythmicity. We applied a light pulse to shorten the transients. Fourth, in LL without coupling, oscillators lose rhythmicity, showing that they are damped in the absence of a variable signal.

Found at doi:10.1371/journal.pcbi.0030068.sg006 (128 KB PDF).

Text S1. Supplementary Materials and Methods

Found at doi:10.1371/journal.pcbi.0030068.sd001 (50 KB PDF).

Video S1. 2-D Slice with Nearest-Neighbor (Type 2) Coupling over 72 h ($d_{max} = 3.5$, $K = 0.9$)

The time series are also shown in Figure 3A and 3B. Each dot is an oscillator. The concentration of *Per/Cry* mRNA for each oscillator is represented by colors (blue, low concentration, red, high concentration) and size.

Found at doi:10.1371/journal.pcbi.0030068.sv001 (2.0 MB AVI).

Video S2. 3-D SCN with Nearest-Neighbor (Type 2) Coupling over 72 h ($d_{max} = 3.5$, $K = 0.9$)

Except for the 3-D geometry, all parameters are as in Figure 3. Each dot is an oscillator. The concentration of *Per/Cry* mRNA for each oscillator is represented by colors (blue, low concentration; red, high concentration) and size. The SCN is slowly rotating to show the 3-D structure.

Found at doi:10.1371/journal.pcbi.0030068.sv002 (1.5 MB AVI).

Video S3. 2-D Slice with Type 3 Coupling over 72 h under a 12:12 LD Cycle

Total $n = 309$, VL regions $n = 102$, DM regions $n = 207$ $d_{max} = 3.5$, 50% of neuronal projections, 4% average period gradient, $K = 1.0$, $L_0 = 0.22$. The time series are also shown in Figure 7. Each dot is an oscillator. The concentration of *Per/Cry* mRNA for each oscillator is represented by color (blue, low concentration; red, high concentration) and size.

Found at doi:10.1371/journal.pcbi.0030068.sv003 (2.0 MB AVI).

Acknowledgments

We gratefully thank Dr. J. Locke and Professors E. Herzog and H. Okamura for stimulating discussions.

Author contributions. SB, DG, and HH conceived and designed the experiments. SB performed the experiments and contributed reagents/materials/analysis tools. SB, DG, HH, and AK analyzed the data. All authors contributed to writing the paper.

Funding. This work was supported by the European Commission (BioSim Network SHB-CT-2004.005137, Marie-Curie Research Training Network MRTN-CT-2004.503661) and the Deutsche Forschungsgemeinschaft (SFB 618). Research in AK's lab is supported by the 6th European Union framework program EUCLOCK. DG is funded by the Fonds National de la Recherche Scientifique (Belgium).

Competing interests. The authors have declared that there are no competing interests.

References

1. Reppert SM, Weaver DR (2002) Coordination of circadian timing in mammals. Nature 418: 935–941.
2. Aton SJ, Herzog ED (2005) Come together, right...now: Synchronization of rhythms in a mammalian circadian clock. Neuron 48: 531–534.
3. Antle MC, Silver R (2005) Orchestrating time: Arrangements of the brain circadian clock. Trends Neurosci 28: 145–151.
4. Welsh DK, Logothetis DE, Meister M, Reppert SM (1995) Individual neurons dissociated from rat suprachiasmatic nucleus express independently phased circadian firing rhythms. Neuron 14: 697–706.
5. Honma S, Nakamura W, Shirakawa T, Honma K (2004) Diversity in the circadian periods of single neurons of the rat suprachiasmatic nucleus depends on nuclear structure and intrinsic period. Neurosci Lett 358: 173–176.
6. Enright J (1980) Temporal precision in circadian systems: A reliable neuronal clock from unreliable components? Science 209: 1542.
7. Brown T, Hughes A, Piggins H (2005) Gastrin-releasing peptide promotes suprachiasmatic nuclei cellular rhythmicity in the absence of vasoactive intestinal polypeptide-$VPAC_2$ receptor signaling. J Neurosci 25: 11155–11164.
8. Cheng M, Bullock C, Li C, Lee A, Bermak J, et al. (2002) Prokineticin 2 transmits the behavioural circadian rhythm of the suprachiasmatic nucleus. Nature 417: 405–410.
9. Liu C, Reppert SM (2000) GABA synchronizes clock cells within the suprachiasmatic circadian clock. Neuron 25: 123–128.
10. Aton SJ, Huettner JE, Straume M, Herzog ED (2006) GABA and $G_{i/o}$ differentially control circadian rhythms and synchrony in clock neurons. Proc Natl Acad Sci U S A 103: 19188–19193.
11. Colwell CS (2000) Rhythmic coupling among cells in the suprachiasmatic nucleus. J Neurobiol 43: 379–388.
12. Reed HE, Meyer-Spasche A, Cutler DJ, Coen CW, Piggins HD (2001) Vasoactive intestinal polypeptide (VIP) phase-shifts the rat suprachiasmatic nucleus clock in vitro. Eur J Neurosci 13: 839–843.
13. Harmar AJ, Marston HM, Shen S, Spratt C, West KM, et al. (2002) The VPAC(2) receptor is essential for circadian function in the mouse suprachiasmatic nuclei. Cell 109: 497–508.
14. Cutler DJ, Haraura M, Reed HE, Shen S, Sheward WJ, et al. (2003) The mouse $VPAC_2$ receptor confers suprachiasmatic nuclei cellular rhythmicity and responsiveness to vasoactive intestinal polypeptide in vitro. Eur J Neurosci 17: 197–204.
15. Dardente H, Menet JS, Challet E, Tournier BB, Pevet P, et al. (2004) Daily and circadian expression of neuropeptides in the suprachiasmatic nuclei of nocturnal and diurnal rodents. Brain Res Mol Brain Res 124: 143–151.
16. Kalamatianos T, Kallo I, Piggins HD, Coen CW (2004) Expression of VIP and/or PACAP receptor mRNA in peptide synthesizing cells within the suprachiasmatic nucleus of the rat and in its efferent target sites. J Comp Neurol 475: 19–35.
17. Albus H, Vansteensel MJ, Michel S, Block GD, Meijer JH (2005) A GABAergic mechanism is necessary for coupling dissociable ventral and dorsal regional oscillators within the circadian clock. Curr Biol 15: 886–893.
18. Maywood E, Reddy A, Wong G, O'Neill J, O'Brien J, et al. (2006) Synchronization and maintenance of timekeeping in suprachiasmatic circadian clock cells by neuropeptidergic signaling. Curr Biol 16: 599–605.
19. Aton S, Colwell C, Harmar A, Waschek J, Herzog E (2005) Vasoactive intestinal polypeptide mediates circadian rhythmicity and synchrony in mammalian clock neurons. Nat Neurosci 8: 476–483.
20. Yamaguchi S, Isejima H, Matsuo T, Okura R, Yagita K, et al. (2003) Synchronization of cellular clocks in the suprachiasmatic nucleus. Science 302: 1408–1412.
21. Nitabach M, Blau J, Holmes T (2002) Electrical silencing of *Drosophila* pacemaker neurons stops the free-running circadian clock. Cell 109: 485–495.
22. Lundkvist G, Block G (2005) Role of neuronal membrane events in circadian rhythm generation. Methods Enzymol 393: 623–42.
23. Becker-Weimann S, Wolf J, Herzel H, Kramer A (2004) Modeling feedback loops of the mammalian circadian oscillator. Biophys J 87: 3023–3034.
24. Noguchi T, Watanabe K, Ogura A, Yamaoka S (2004) The clock in the dorsal suprachiasmatic nucleus runs faster than that in the ventral. Eur J Neurosci 20: 3199–3199.
25. Lundkvist G, Kwak Y, Davis E, Tei H, Block G (2005) A calcium flux is required for circadian rhythm generation in mammalian pacemaker neurons. J Neurosci 22: 350–356.
26. Zhou T, Chen L, Aihara K (2005) Molecular communication through stochastic synchronization induced by extracellular fluctuations. Phys Rev Lett 95: 178103.
27. Lowrey P, et al. (2000) Positional syntenic cloning and functional characterization of the mammalian circadian mutation *tau*. Science 288: 483–491.
28. Liu C, Weaver DR, Strogatz SH, Reppert SM (1997) Cellular construction of a circadian clock: Period determination in the suprachiasmatic nuclei. Cell 91: 855–860.
29. Herzog E, Aton S, Numano R, Sakaki Y, Tei H (2004) Temporal precision in the mammalian circadian system: A reliable clock from less reliable neurons. J Biol Rhythms 19: 35–46.
30. Hannibal J (2003) Neurotransmitters of the retino-hypothalamic tract. Cell Tissue Res 309: 73–88.
31. Nakamura W, Yamazaki S, Takasu N, Mishima K, Block G (2005) Differential response of period 1 expression within the suprachiasmatic nucleus. J Neurosci 25: 5481–5487.
32. Nagano M, Adachi A, Nakahama K, Nakamura T, Tamada M, et al. (2003) An abrupt shift in the day/night cycle causes desynchrony in the mammalian circadian center. J Neurosci 23: 6141.
33. Leloup JC, Goldbeter A (2003) Toward a detailed computational model for the mammalian circadian clock. Proc Natl Acad Sci U S A 100: 7051–7056.
34. Forger D, Peskin C (2003) A detailed predictive model of the mammalian circadian clock. Proc Natl Acad Sci U S A 100: 14806–14811.
35. Vanselow K, Vanselow J, Westermark P, Reischl S, Maier B, et al. (2006) Differential effects of PER2 phosphorylation: Molecular basis for the human familial advanced sleep phase syndrome (FASPS). Genes Dev 20: 2660.
36. Kunz H, Achermann P (2003) Simulation of circadian rhythm generation in the suprachiasmatic nucleus with locally coupled self-sustained oscillators. J Theor Biol 224: 63–78.
37. Antle MC, Foley DK, Foley NC, Silver R (2003) Gates and oscillators: A network model of the brain clock. J Biol Rhythms 18: 339–350.

38. Antle MC, Foley NC, Foley DK, Silver R (2007) Gates and oscillators II: Zeitgebers and the network model of the brain clock. J Biol Rhythms 22: 14–25.
39. Rougemont J, Naef F (2006) Collective synchronization in populations of globally coupled phase oscillators with drifting frequencies. Phys Rev E 73: 11104.
40. Ueda HR, Hirose K, Iino M (2002) Intercellular coupling mechanism for synchronized and noise-resistant circadian oscillators. J Theor Biol 216: 501–512.
41. Roenneberg T, Merrow M (1998) Molecular circadian oscillators: An alternative hypothesis. J Biol Rhythms 13: 167–179.
42. Ohta H, Yamazaki S, McMahon D (2005) Constant light desynchronizes mammalian clock neurons. Nat Neurosci 8: 267–269.
43. Tenenbaum M, Pollard H (1985) Ordinary differential equations. New York: Dover Publications. 808 p.
44. Izumo M, Sato TR, Straume M, Johnson CH (2006) Quantitative analyses of circadian gene expression in mammalian cell cultures. PLoS Comput Biol 2 (10): e136.
45. Gonze D, Bernard S, Waltermann C, Kramer A, Herzel H (2005) Spontaneous synchronization of coupled circadian oscillators. Biophys J 89: 120–129.
46. Preitner N, Damiola F, Zakany J, Duboule D, Albrecht U, et al. (2002) The orphan nuclear receptor REV-ERB controls circadian transcription within the positive limb of the mammalian circadian oscillator. Cell 110: 251–260.
47. Li C, Chen L, Aihara K (2006) Transient resetting: A novel mechanism for synchrony and its biological examples. PLoS Comput Biol 2 (8): e103.
48. Turing AM (1952) The chemical basis of morphogenesis. Phil Trans Roy Soc Lond, B 237: 37–72.
49. Smale S (1976) A mathematical model of two cells via Turing's equation. In: Marsden JE, McCracken M, editors The Hopf bifurcation and its applications. New York: Springer-Verlag. pp. 354–367.
50. Smolen P, Rinzel J, Sherman A (1993) Why pancreatic islets burst but single beta cells do not. The heterogeneity hypothesis. Biophys J 64: 1668–1680.
51. Manor Y, Rinzel J, Segev I, Yarom Y (1997) Low-amplitude oscillations in the inferior olive: A model based on electrical coupling of neurons with heterogeneous channel densities. J Neurophysiol 77: 2736–2752.
52. Aronson DG, Ermentrout GB, Kopell N (1990) Amplitude response of coupled oscillators. Physica D 41: 403–449.
53. Abrahamson E, Moore R (2001) Suprachiasmatic nucleus in the mouse: Retinal innervation, intrinsic organization and efferent projections. Brain Res 916: 172–191.
54. Garcia-Ojalvo J, Elowitz MB, Strogatz SH (2004) Modeling a synthetic multicellular clock: repressilators coupled by quorum sensing. Proc Natl Acad Sci U S A 101: 10955–10960.

9.4 Besse A, Clapp G, Bernard S, Nicolini F, Levy D, Lepoutre T (2017) Stability analysis of a model of interaction between the immune system and cancer cells in chronic myelogenous leukemia. Bull Math Biol *in press*

Bulletin of Mathematical Biology manuscript No.
(will be inserted by the editor)

Stability Analysis of a Model of Interaction Between the Immune System and Cancer Cells in Chronic Myelogenous Leukemia

Apollos Besse · Geoffrey D. Clapp · Samuel Bernard · Franck E. Nicolini · Doron Levy · Thomas Lepoutre

Received: date / Accepted: date

A. Besse
Inria Grenoble - Rhône-Alpes and Université de Lyon
Université Claude Bernard Lyon 1 CNRS UMR 5208
Institut Camille Jordan, 43 blvd. du 11 novembre 1918 F-69622 Villeurbanne cedex France,
E-mail: apollos.besse@inria.fr

G. D. Clapp
Department of Mathematics
University of Maryland, College Park, MD 20742, USA
E-mail: clappge1@umd.edu

S. Bernard
Inria Grenoble - Rhône-Alpes and Université de Lyon
Université Claude Bernard Lyon 1 CNRS UMR 5208
Institut Camille Jordan, 43 blvd. du 11 novembre 1918 F-69622 Villeurbanne cedex France,
E-mail: bernard@math.univ-lyon1.fr

F. E. Nicolini
Hematology department 1G, Centre Hospitalier Lyon Sud, Pierre Bénite, France
and INSERM U1052
Centre de Recherche en Cancérologie de Lyon, Centre Léon Bérard, Lyon, France
E-mail: franck-emmanuel.nicolini@chu-lyon.fr

D. Levy
Department of Mathematics
and Center for Scientific Computation and Mathematical Modeling (CSCAMM)
University of Maryland, College Park, MD 20742, USA
E-mail: dlevy@math.umd.edu

T. Lepoutre
Inria Grenoble - Rhône-Alpes and Université de Lyon
Université Claude Bernard Lyon 1 CNRS UMR 5208
Institut Camille Jordan, 43 blvd. du 11 novembre 1918 F-69622 Villeurbanne cedex France,
E-mail: thomas.lepoutre@inria.fr

Abstract: We describe here a simple model for the interaction between leukemic cells and the autologous immune response in chronic phase chronic myelogenous leukemia (CML). This model is a simplified version of the model we proposed in [Clapp *et al.*, Cancer Research, 75:4053-4062, 2015]. Our simplification is based on the observation that certain key characteristics of the dynamics of CML can be captured with a three compartments model: two for the leukemic cells (stem cells and mature cells) and one for the immune response. We characterize the existence of steady states and their stability for generic forms of immunosuppressive effects of leukemic cells. We provide a complete co-dimension one bifurcation analysis. Our results show how clinical response to tyrosine kinase inhibitors treatment is compatible with the existence of a stable low-disease, treatment-free steady state.

1 Introduction

Chronic myeloid leukemia is a clonal disease that arises from a discrete population of hematopoietic stem cells residing in the bone marrow harmed by a single fusion gene, *BCR-ABL*, encoding for a deregulated tyrosine kinase activity responsible for the disease [7]. Unlike most cancers, the measurement of the *BCR-ABL* transcripts can quantify precisely the tumor load and its evolution throughout time under targeted therapies (i.e. tyrosine kinase inhibitors (TKI)) over time. The first-in-class TKI Imatinib (Glivec®/Gleevec®, Novartis) is a targeted therapy that inhibits the deregulated tyrosine kinase activity of ABL in leukemic cells, and induces within 18 hours cell death by apoptosis [9]. This TKI and the other TKIs derived since 2005 from IM revolutionized the paradigms of treatment of CML and transformed this disease from a mostly fatal illness into a life-long indolent pathology [16]. However, in most cases, under TKI, the disease remains detectable at low levels. It is rare when the CML becomes undetectable, possibly cured. After stopping targeted therapies, most patients relapse and require a new TKI treatment. Yet, recent clinical trials [14, 17, 20] have shown that a long TKI treatment duration may result with remission after treatment withdrawal, and, in some cases, although detectable levels of transcripts might reappear, patients may end up in an indolent detectable disease not requiring further treatments.

There is increased evidence that such remissions (so-called treatment-free remissions) do not require disease eradication [19]. Such coexistence of low-level leukemic cell load and non-active relapse suggest the occurrence of leukemic cell control mechanisms. In CML, it is well-known that the autologous or allogeneic immune responses against the tumor have a critical importance in disease cure or long-term control. In an autologous setting, complete hematologic and cytogenetic remission, even in accelerated phase CML, has been observed after generating ex-vivo autologous leukemia-reactive cytotoxic T-lymphocyte infusions [8]. Nowadays, in successful treatment-free remission setting, elevated counts of natural killer cells [10] and plasmacytoid dendritic cells [1] at time of TKI withdrawal have been observed, supporting the hypothesis that the

autologous immune system might play a critical role in controlling the disease after TKI withdrawal.

Several mathematical models of the dynamics of CML during treatment and after treatment cessation have provided insight into the mechanism of remission and relapse. We briefly comment on some of these models. For a more comprehensive review of mathematical models for CML we refer to [4].

Michor *et al.* used a mathematical model to explain the failure of complete eradication of the disease under TKI treatments by the development of resistance [15]. Komarova and Wodarz proposed a model that incorporates the stem cell ability to become quiescent and to develop resistance to treatment [13]. An alternative model was proposed by Roeder *et al.* [18]. There, an agent-based model in which the fate of each cell is stochastically determined, according to its characteristics and its environment. The model describes the competition of leukemic stem cells versus disease-free stem cells in the bone marrow, and the effect of TKIs on competition [18]. The potential long-term effect of immune response was studied by Kim *et al.* in [12] by adding an immune compartment to the model of [15].

Recently, we proposed a model describing the interactions between leukemic cells and the autologous immune system in IM-treated patients [6] (see also [5]). The model was motivated by an observation that many patients who otherwise responded well to IM therapy still showed variations in their BCR-ABL transcripts. Our modeling results suggested that, at diagnosis, a patient's leukemic load is able to partially or fully suppress immune response developed in a majority of patients towards the CML clone(s). IM therapy drives the residual leukemic cell population into the "immune window", allowing the patient's autologous immune cells to expand and eventually mount an efficient recognition of the residual leukemic burden. This TKI drives the leukemic load below this immune window, allowing the residual leukemic population to partially recover until another weaker immune response is initiated. Thus, we suspect that the autologous immune response may explain the oscillations in the BCR-ABL transcripts regularly observed in patients on IM.

In this paper we propose a new model for describing the interaction between leukemic cells and the autologous immune system in chronic phase CML. This model is a simplified version of our original model from [6], in which we reduce the number of equations and simplify some of the interaction terms. Our simplification is based on the observation that certain key characteristics of the dynamics of CML can be captured with a three compartments model: two for the leukemic cells (proliferating stem cells and mature cells) and one for the immune response.

The new model is sufficiently accessible to allow us to conduct mathematical analysis. Indeed, we characterize the existence of steady states and their stability for generic forms of immunosuppressive effects of leukemic cells, and provide a complete co-dimension one bifurcation analysis. Our results show how clinical response to TKI treatment is compatible with the existence of a stable low-disease, treatment-free steady state.

The structure of this manuscript is as follows. In Section 2 we briefly overview the mathematical model of [6] after which we introduce our new model (4). The positive steady states of the system (4) are characterized in Section 2. A stability analysis of these steady states in conducted in Section 3. This section includes our main Theorems, Theorem 1 and 2, which describe the bifurcation diagrams of the steady states. Applications of the stability analysis are given in Section 4, and a concluding discussion is provided in Section 6.

2 The Model

2.1 The Clapp *et al.* model

The mathematical model of Clapp *et al.* described the dynamics of the interaction between cancer cells and the immune response in CML [6]. This model is given as a system of five ODEs, describing the dynamics of four states for the leukemic cells (quiescent and cycling stem cells, progenitor cells, and mature cells), and the dynamics of the immune response.

Let y_0 and y_1 represent the concentration of quiescent and cycling leukemic stem cells, respectively, y_2 the concentration of progenitor cells, y_3 the concentration of mature leukemic cells, and z the concentration of active immune cells. The model of [6] is written as the following system of ODEs:

$$\begin{cases} y_0' = b_1 y_1 - a_0 y_0 - \dfrac{\mu y_0 z}{1+\varepsilon y_3^2}, \\ y_1' = a_0 y_0 - b_1 y_1 + r y_1 \left(1 - \dfrac{y_1}{K}\right) - d_1 y_1 - \dfrac{\mu y_1 z}{1+\varepsilon y_3^2}, \\ y_2' = \dfrac{a_1}{inh_1} y_1 - d_2 y_2 - \dfrac{\mu y_2 z}{1+\varepsilon y_3^2}, \\ y_3' = \dfrac{a_2}{inh_2} y_2 - d_3 y_3 - \dfrac{\mu y_3 z}{1+\varepsilon y_3^2}, \\ z' = s - dz + \dfrac{\alpha y_3 z}{1+\varepsilon y_3^2}. \end{cases} \tag{1}$$

The model equations (1) describe transitions between leukemic populations (at rates b_1, a_0, a_1 and a_2). The different populations have associated death rates (d_1, d_2, d_3 and d). The cycling stem cells are assumed to grow logistically with growth rate r and carrying capacity K. The last terms in the first four equations in (1) represent the death of leukemic cells caused by an immune response. The mass action term $\mu y_i z$ represents the killing of leukemic cells by the immune system, where μ is the maximal rate (per immune cell) at which an immune cell will engage and kill a leukemic cell.

The last equation in (1) represents the concentration of autologous immune cells. The first term, s, is a constant source term for the immune cells, who die

at rate d. The mass action term $\alpha y_3 z$ represents the expansion (proliferation) of the immune cell pool in response to its leukemia stimulus, which occurs with maximal rate per leukemic cell. Only the contributions of the mature leukemic cells y_3 to immune stimulation are included since they are a much larger population than the immature leukemic cells.

This model is based on assuming that immunosuppression acts in two ways. First, mature leukemic cells inhibit the expansion of immune cells. In the last equation, the immune cell expansion term $\alpha y_3 z$ is divided by $1 + \varepsilon y_3^2$, where the constant ε determines the strength of the immunosuppression. Second, mature leukemic cells are assumed to decrease the killing capacity μ of activated immune cells, also by a factor of $1 + \varepsilon y_3^2$. By implementing immunosuppression in this way, Clapp *et al.* encoded an autologous immune response that is effective only with intermediate levels of leukemic cells. When the leukemic load is small, only a small number of immune cells is stimulated to respond. On the other hand, although large leukemic loads provide a stronger stimulus, the leukemic cells are able of suppressing the efficacy of the immune system. Thus, the immune response will be negligible when the leukemic load is either very small, at levels undetectable by the immune system, or very large, at levels that overwhelm and suppress the immune system. A strong immune response can occur only when the leukemic load y_3 is at an intermediate level, within a range $[y_{min}, y_{max}]$, the so-called *immune window*. The immune window is defined as the range of y_3 for which the rate of immune stimulation exceeds the death rate. The parameters inh_1 and inh_2 represent the inhibition of leukemic cell amplification by TKI treatment. TKI therapy may be used to drive the leukemic load into this immune window, allowing the autologous immune system to assist the drug in the elimination of the residual leukemic cells.

2.2 Introducing a simplified model

In [6] we provided no theoretical analysis of the model (1). Analysis of the model in its full generality is beyond the reach of this paper. Instead, we introduce in this subsection a reduced model which captures some of the essential features of the original model.

Our main simplification is to reduce the original system to three ODEs, keeping only two states for the leukemic cells. In addition, we assume that immunosuppression does not directly suppress the killing capacity μ of immune cells. These assumptions make the theoretical analysis accessible.

Let y_1 represent the concentration of cycling stem cells, y_2 the concentration of mature leukemic cells, and z the concentration of immune cells. We

consider the following system of ODEs:

$$\begin{cases} y_1' = ry_1\left(1 - \dfrac{y_1}{K}\right) - d_1 y_1 - \mu y_1 z, \\ y_2' = \dfrac{a_1}{k_{inh}} y_1 - d_2 y_2 - \mu y_2 z, \\ z' = s - f(y_2) z. \end{cases} \tag{2}$$

We note that the system (2) is a simplified version of system (1). We also note that y_2 in the system (2) plays the role of y_3 in the system (1). The parameter a_1 is the product of the stem cell differentiation rate and the amplification factor between stem and mature cells. The effect of the treatment is represented by dividing a_1 by an inhibition coefficient k_{inh}. The parameters r and K are the cycling stem cells growth rate and carrying capacity, respectively. The natural death rates of each population are given by d, d_1, d_2, and μ is the probability that an immune cell will interact with a leukemic cell and kill it.

The function f represents the net suppression effect of the leukemic cells on the immune system. It mixes the natural death rate of immune cells $d = f(0)$, the competitive (immune response) and the immunosuppressive effect of cancer cells. The suppression rate f can take negative values; in this case, immune response outbalances immunosuppression.

In all what follows, we assume

$$f \in C^2(\mathbb{R}_+),$$

and

$$\exists Y > 0, \quad f' < 0, \text{ on } [0, Y), \quad f' > 0, \text{ on } (Y, +\infty) \tag{3}$$

In words, we assume f to be strictly decreasing for low amount of cancer cells and strictly increasing for high amount of cancer cells (its monotony changes exactly once). An immediate important consequence of this hypothesis is the following result:

Proposition 1 (Zeros of f) *Let $f \in C^2(\mathbb{R}_+)$ satisfy (3), then either*

1. *f has no zero on $\mathbb{R}_+$,*
2. *f has one zero $y_{min} \in (0, Y]$,*
3. *f has two zeros $y_{min} \in (0, Y)$ and $y_{max} \in (Y, +\infty)$*

Notations of this proposition will be kept in the manuscript.

In order to eliminate the parameter d_1 from (2), we make a change of variables $r_{new} \leftarrow r_{old} - d_1$ and $K_{new} \leftarrow (r_{new}/r_{old})K_{old}$. We also set $a_1 \leftarrow a_1/k_{inh}$. This leads to the following system:

$$\begin{cases} y_1' = ry_1\left(1 - \dfrac{y_1}{K}\right) - \mu y_1 z, \\ y_2' = a_1 y_1 - d_2 y_2 - \mu y_2 z, \\ z' = s - f(y_2) z. \end{cases} \tag{4}$$

3 Steady states for the simplified model

We want to determine the positive steady states of the system (4). We start with a simple characterization.

Proposition 2 *The system (4) always has a unique, disease-free non-negative steady state* $(0, 0, \frac{s}{f(0)})$*. Other positive steady states are given by the solutions to the equations*

$$\bar{y}_1 = \frac{(r + d_2)\bar{y}_2}{a_1 + \frac{r}{K}\bar{y}_2}, \tag{5}$$

$$\bar{z} = \frac{s}{f(\bar{y}_2)}. \tag{6}$$

Here, $\bar{y}_2$ *is a positive zero of the function* P *given by*

$$P(X) = f(X)(X - M) + \frac{\mu s}{d_2}\left(M\frac{d_2}{r} + X\right), \tag{7}$$

with $M = \frac{a_1 K}{d_2}$*, such that* $f(\bar{y}_2) > 0$*. For any positive steady state, we have*

$$0 < \bar{y}_2 \leqslant M. \tag{8}$$

Proof The steady states of (4) are the solutions of the nonlinear system:

$$\begin{cases} 0 = ry_1\left(1 - \dfrac{y_1}{K}\right) - \mu y_1 z, \\ 0 = a_1 y_1 - d_2 y_2 - \mu y_2 z, \\ 0 = s - f(y_2)z. \end{cases} \tag{9}$$

The point $(0, 0, \frac{s}{f(0)})$ is always a steady state. It corresponds to the disease-free steady state, where the leukemic cell populations vanish and the immune system is maintained at a basal, surveillance level $\frac{s}{f(0)}$.

The positivity of all coefficients provides bounds for $\bar{y}_1$ and $\bar{y}_2$:

$$\bar{y}_1 \leqslant K, \qquad \bar{y}_2 \leqslant \frac{a_1 K}{d_2} := M.$$

Other steady states can be found by:

$$\begin{cases} \mu z = r\left(1 - \dfrac{y_1}{K}\right), \\ \mu y_2 z = a_1 y_1 - d_2 y_2, \\ f(y_2)z = s, \end{cases} \tag{10}$$

which leads to:

$$\bar{y}_1 = \frac{(r + d_2)\ \bar{y}_2}{a_1 + \frac{r}{K}\bar{y}_2}, \tag{11}$$

and

$$\bar{z} = \frac{s}{f(y_2)}. \tag{12}$$

As we are looking for non-negative steady states, equation (12) implies that $f(\bar{y}_2)$ must be non-negative. Since the steady state values $\bar{y}_1$ and $\bar{z}$ are uniquely determined by $\bar{y}_2$, and we reduce the problem to an equation on $\bar{y}_2$ alone. For $\bar{y}_1$, we have

$$1 - \frac{\bar{y}_1}{K} = \frac{M - \bar{y}_2}{M + \frac{r}{d_2}\bar{y}_2}.$$

Then, equations (10) and (12) imply:

$$\frac{\mu s}{f(\bar{y}_2)} = r\frac{M - \bar{y}_2}{M + \frac{r}{d_2}\bar{y}_2},$$

which means that,

$$\frac{\mu s}{r}\left(M + \frac{r}{d_2}\bar{y}_2\right) = f(\bar{y}_2)(M - \bar{y}_2).$$

This leads to the desired equation for $\bar{y}_2$:

$$f(\bar{y}_2)(\bar{y}_2 - M) + \frac{\mu s}{d_2}\left(M\frac{d_2}{r} + \bar{y}_2\right) = 0.$$

The following lemma precises the position of the steady states with respect to the zeros of f.

Lemma 1 *Keeping the notations of Proposition 1, positive steady states of the system satisfy $\bar{y}_2 \in (0, y_{min}]$, or $\bar{y}_2 \in [y_{max}, +\infty)$.*

Let name the condition

$$(\mathrm{C}_1) : d > \frac{\mu s}{r}.$$

Proposition 3 *Assume (C_1) is satisfied, there exists a disease steady state for (4) such that $\bar{y}_2 \in (0, M)$. Moreover, if f vanishes and (with notation of Proposition 1) $y_{min} < M$, there is a unique steady state for (4) that satisfies*

$$0 < \bar{y}_2 < y_{min} < M.$$

All other steady states satisfy $y_2 \geqslant y_{max}$ and $y_2 < M$

Proof Assuming (C_1), we have

$$P(0) = -\left(d - \frac{\mu s}{r}\right) M < 0,$$
$$P(M) = \frac{\mu s}{d_2}\left(\frac{d_2}{r} + 1\right) M > 0.$$

Thus, P changes sign in the interval $(0, M)$, which implies, from Proposition 2 that there is a steady state with $\bar{y}_2 \in (0, M)$. Moreover, $f(\bar{y}_2)$ must be positive, so the solution for $\bar{y}_2$ corresponds to a positive steady state, according to Proposition 2.

Keeping notations of proposition 1, assume $y_{min} \in (0, M)$. Because $f(0) = d$ is positive, $f(y_2)$ stays positive for $y_2 < y_{min}$. From the definition of P in (7), we have $P(y_{min}) > 0$. Since $P(0) < 0$ and since $y_{min} < M$, P admits at least one zero $\bar{y}_2 \in (0, y_{min})$.

To prove uniqueness, we highlight the fact that P is monotonous on $[0; y_{min}]$:

$$P'(X) = f(X) + f'(X)(X - M) + \theta,$$

is positive on $[0; y_{min}]$, since function f stays positive and strictly decreasing.

Moreover, at the unique zero $\bar{y}_2 < y_{min}$, $f(\bar{y}_2)$ is still positive, and Proposition 2 ensures that $\bar{y}_2$ corresponds to a positive steady state $\bar{x} = (\bar{y}_1, \bar{y}_2, \bar{z})$.

When $d > \frac{\mu s}{r}$, the smallest disease steady state (in terms of y_2) is denoted as the *low disease steady state*. When $d = \frac{\mu s}{r}$, $P(0) = 0$, and the low disease steady state becomes disease-free. For $d \leqslant \frac{\mu s}{r}$, the steady state becomes negative, and does not exists anymore.

4 A stability analysis

In order to draw a complete picture of the dynamics of the system (4), it is important to characterize the stability of the steady states. Because the system is bounded (positive cell concentrations cannot grow unbounded), we expect the system to converge either to a stable steady state or perhaps to a non-steady-state bounded attractor, such as a limit cycle. We will show that under biologically relevant assumptions, there always exists an asymptotically stable steady state, and that none of the steady states can be destabilized by a Hopf bifurcation. We are able to provide a complete local co-dimension 1 bifurcation diagram. Although more complex bifurcation diagrams are possible, they are non generic as they occur only for specific combinations of two or more parameters.

4.1 Stability of the disease-free steady state

In the disease-free steady state $(0, 0, \frac{s}{d})$, where $d = f(0)$, there are no leukemic cells, but the concentration of immune cells is positive, due to a basal cell production level s.

Proposition 4 *The disease-free steady state* $(0, 0, \frac{s}{d})$ *is asymptotically stable if and only if* $r < \frac{\mu s}{d}$. *If* $r = \frac{\mu s}{d}$, *then this disease-free steady state is locally attractive for positive solutions.*

Proof The linearized system around the disease-free steady state is

$$\begin{cases} y_1' = r y_1 - \dfrac{\mu s}{d} y_1, \\ y_2' = a_1 y_1 - d_2 y_2 - \dfrac{\mu s}{d} y_2, \\ z' = -dz + \dfrac{s}{d} f'(0) y_2. \end{cases} \tag{13}$$

The disease-free Jacobian matrix is

$$J_0 = \begin{pmatrix} r - \frac{\mu s}{d} & 0 & 0 \\ a_1 & -d_2 - \frac{\mu s}{d} & 0 \\ 0 & \frac{s}{d} f'(0) & -d \end{pmatrix}. \tag{14}$$

The matrix (14) is triangular, and its eigenvalues lie on the diagonal, which are all real coefficients. Two eigenvalues are always strictly negative. The third one, given by $r - \frac{\mu s}{d}$, can be either negative or positive. Therefore, the disease-free steady state is asymptotically stable if $rd < \mu s$, and it is unstable if $rd > \mu s$ (condition (C_1)).

In addition, if $rd = \mu s$, it is easy to verify that for $\varepsilon > 0$ small enough, $D_\varepsilon = [0; \varepsilon] \times [0; \frac{a_1}{d_2}\varepsilon] \times [\bar{z} - \frac{r}{K\mu}; +\infty)$ is a stable set for the equations. For solutions starting in D_ε, since f is non-increasing on $[0; \frac{a_1}{d_2}\varepsilon]$ and since $z' \geqslant s - f(0)z$, we have

$$\liminf_{+\infty} z \geqslant \bar{z}.$$

Finally, since $y_1' = -r y_1^2/K + \mu y_1(\bar{z} - z)$, we have

$$\limsup_{+\infty} y_1 \leqslant \frac{K\mu}{r} \limsup_{+\infty} (\bar{z} - z) \leqslant 0.$$

Hence, due to the non-negativity of y_1, $y_1(+\infty) = 0$, and using the equations (4), we conclude that $(y_1(t), y_2(t), z(t)) \to (0, 0, \bar{z})$.

From now on, we assume that the disease-free steady state is unstable, and we want to know if there are other stable steady states.

4.2 Stability of the disease steady states

We denote by $(\bar{y}_1, \bar{y}_2, \bar{z})$ a non-negative steady state of system (4), with $\bar{y}_1$ and/or $\bar{y}_2$ positive. The Jacobian matrix is

$$J = \begin{pmatrix} r - 2\frac{r}{K}\bar{y}_1 - \mu\bar{z} & 0 & -\mu\bar{y}_1 \\ a_1 & -d_2 - \mu\bar{z} & -\mu\bar{y}_2 \\ 0 & -f'(\bar{y}_2)\bar{z} & -f(\bar{y}_2) \end{pmatrix}. \tag{15}$$

Using (10) the matrix (15) becomes

$$J = \begin{pmatrix} -\frac{r}{K}\bar{y}_1 & 0 & -\mu\bar{y}_1 \\ a_1 & -a_1\frac{\bar{y}_1}{\bar{y}_2} & -\mu\bar{y}_2 \\ 0 & -f'(\bar{y}_2)\bar{z} & -f(\bar{y}_2) \end{pmatrix}. \tag{16}$$

In order to determine the stability of the steady state, we compute the characteristic polynomial χ_J

$$\begin{aligned}\chi_J(X) &= \left(X + \frac{r}{K}\bar{y}_1\right)\left((X + a_1\frac{\bar{y}_1}{\bar{y}_2})(X + f(\bar{y}_2)) - \mu\bar{y}_2\bar{z}f'(\bar{y}_2)\right) - a_1\mu\bar{y}_1\bar{z}f'(\bar{y}_2) \\ &= X^3 + \left(\frac{r}{K}\bar{y}_1 + a_1\frac{\bar{y}_1}{\bar{y}_2} + f(\bar{y}_2)\right)X^2 \\ &\quad + \left(\frac{r}{K}\bar{y}_1\left(a_1\frac{\bar{y}_1}{\bar{y}_2} + f(\bar{y}_2)\right) + a_1\frac{\bar{y}_1}{\bar{y}_2}f(\bar{y}_2) - \mu\bar{y}_2\bar{z}f'(\bar{y}_2)\right)X \\ &\quad + \left(\frac{r}{K}\bar{y}_1\left(a_1\frac{\bar{y}_1}{\bar{y}_2}f(\bar{y}_2) - \mu\bar{y}_2\bar{z}f'(\bar{y}_2)\right) - a_1\mu\bar{y}_1\bar{z}f'(\bar{y}_2)\right),\end{aligned}$$

and using the relation $\frac{r}{K}\bar{y}_1 + a_1\frac{\bar{y}_1}{\bar{y}_2} = r + d_2$,

$$\begin{aligned}\chi_J(X) =& X^3 + X^2\left(r + d_2 + f(\bar{y}_2)\right) \\ &+ \left((r + d_2)f(\bar{y}_2) - \mu\bar{z}\bar{y}_2f'(\bar{y}_2) + \frac{r}{K}\bar{y}_1a_1\frac{\bar{y}_1}{\bar{y}_2}\right)X \\ &+ \left(\frac{r}{K}\bar{y}_1a_1\frac{\bar{y}_1}{\bar{y}_2}f(\bar{y}_2) - (r + d_2)\mu\bar{z}\bar{y}_2f'(\bar{y}_2)\right).\end{aligned} \tag{17}$$

In what follows we will again keep notation of Proposition 1. In case 3 of proposition 1, we will distinguish the low steady state ($\bar{y}_2 \leqslant y_{min}$) and the others ($\bar{y}_2 \geqslant y_{max}$).

4.2.1 Stability of the low disease steady state

We are interested in proving the stability of the disease steady state given by Proposition 3 under condition (C_1). It is the only disease steady state $(\bar{y}_1, \bar{y}_2, \bar{z})$ such that $\bar{y}_2 \leqslant y_{min}$.

Proposition 5 *Assume the low disease steady state of (4) exists. It is asymptotically stable if and only if the disease-free steady state is unstable, i.e., if and only if $rd > \mu s$ (condition (C_1)). For $rd = \mu s$, there is a transcritical bifurcation between the disease-free steady state and the low disease steady state.*

Proof We can assume that the disease-free steady state is unstable, which implies that $rd > \mu s$ and the existence of the low disease steady state. Either f has no zero in $(0, M)$, or f admits a smallest zero $y_{min} \in (0, M)$. In either

case, at the low disease steady state, we have $f'(\bar{y}_2) < 0$. This means that the coefficients of χ_J are all positive. We need to prove that χ_J verifies the condition of Lemma 4 (in Appendix).

$$\begin{aligned} a_\chi b_\chi - c_\chi &= (r + d_2 + f(\bar{y}_2)) \left((r + d_2) f(\bar{y}_2) - \mu \bar{z} \bar{y}_2 f'(\bar{y}_2) + \frac{r}{K} \bar{y}_1 a_1 \frac{\bar{y}_1}{\bar{y}_2} \right) \\ &\quad - \left(\frac{r}{K} \bar{y}_1 a_1 \frac{\bar{y}_1}{\bar{y}_2} f(\bar{y}_2) - (r + d_2) \mu \bar{z} \bar{y}_2 f'(\bar{y}_2) \right) \\ &= (r + d_2) \left((r + d_2) f(\bar{y}_2) + \frac{r}{K} \bar{y}_1 a_1 \frac{\bar{y}_1}{\bar{y}_2} \right) \\ &\quad + f(\bar{y}_2) \left((r + d_2) f(\bar{y}_2) - \mu \bar{z} \bar{y}_2 f'(\bar{y}_2) \right) > 0. \end{aligned}$$

Here we used the fact that $f'(\bar{y}_2) < 0$.

By Lemma 4, we know that the dominating root of χ_J has a negative real part, which means that the dominating eigenvalue of J has a negative real part. Hence the low steady state is asymptotically stable.

For $rd = \mu s$, the low disease steady state crosses the disease-free steady state. At this point, the fusion steady state is locally stable for positive solutions (as seen in Subsection 4.1). For $rd < \mu s$, it becomes negative, and is necessarily unstable, i.e., it is a transcritical bifurcation.

The asymptotic stability of the low disease steady state corresponds to a state where the immune system is able to keep the leukemic cell population at a low level, even without treatment. However, we demonstrate numerically that the basin of attraction of low disease steady state is small, and solutions typically converge to the large disease steady state.

4.2.2 Stability of the other steady states

The existence of steady states other than the disease-free and the low disease steady states depends on the exact shape of the leukemia-induced immunosuppression function f. We assume that we are in the case 3 of Proposition 1 and moreover $y_{max} < M$. We denote this couple of conditions (C_2).

(C_2): f has two zeros y_{min} and y_{max} such that $0 < y_{min} < y_{max} < M$.

The assumption about the two zeros follows from the biological assumption that there exists a range of leukemic cell concentrations for which the immune system is able to mount an immune response (when f is negative, the growth rate of z is strictly positive). If $M \leqslant y_{max}$, the only possible disease steady state is the low disease steady state, which is asymptotically stable under (C_1). From now on, we assume that $M > y_{max}$, opening the door for other disease steady states to exist. All these disease steady states verify $f'(\bar{y}_2) > 0$.

We give a function that does not depend on s and μ, that gives both steady states and their stability.

Let denote $A(X) = f(X)(M - X)$, $B(X) = X + \frac{d_2}{r} M$, $\theta = \mu s / d_2$ and $\theta_{max} = \sup_{x \in (y_{max}, M)} \{ \frac{A}{B}(x) \}$.

All disease steady states are entirely determined by their component $\bar{y}_2$ defined as a zero of the function P defined in (7). We express P as a parametric linear combination of two functions A and B,

$$P_\theta(X) = -A(X) + \theta B(X). \tag{18}$$

Theorem 1 *If the function $\frac{A}{B}$ admits only one critical point, then the following holds:*

1. *For all θ in $[0, \theta_{max})$ there exist two disease steady states $\bar{x}^{(1)}$ and $\bar{x}^{(2)}$ with $y_{max} \leqslant \bar{y}_2^{(1)} < \bar{y}_2^{(2)} \leqslant M$. The disease steady state $\bar{x}^{(1)}$ is unstable and $\bar{x}^{(2)}$ is asymptotically stable.*
2. *For all $\theta > \theta_{max}$ there is no steady state with $\bar{y}_2$ in (y_{max}, M).*
3. *There is an saddle-node bifurcation for $\theta = \theta_{max}$, the corresponding double steady states is generically unstable.*

Proof The proof is constructed as follows:

- We give a necessary and sufficient condition for stability, that is based on condition (C_2) (Lemma 1).
- We connect this condition to functions A and B, which are independent of parameter θ (Lemma 2).
- We describe the bifurcation diagram depending on θ.

The parameter θ will be used as the bifurcation parameter. It has not any biological meaning, but allow the polynomial B to be unitary, and thus makes calculations simpler. Otherwise it could be feasible to use parameters μ or s that represent the immune system aggressiveness and the immune cells source, as we do in the Section 5. Parameter θ may vary in $[0; rd/d_2]$ to respect condition (C_1). The limit value $\theta = 0$ is allowed to be reached when $s = 0$, but not when $\mu = 0$. Indeed, in this last case the link between steady state and roots of polynomial P does not hold anymore.

The following lemma highlights the link between the stability of a steady state $\bar{x}$ and the sign of the jacobian matrix at $\bar{x}$, under (C_2). Its proof is given in Appendix.

Lemma 1 *Let $\bar{x} = (\bar{y}_1, \bar{y}_2, \bar{z})$ be a steady state of (4) such that $f'(\bar{y}_2) > 0$. The steady state $\bar{x}$ is asymptotically stable if, and only if,* $\det(J(\bar{x})) < 0$.

This lemma affirms that the key to stability is the Jacobian matrix determinant. The two following lemmas highlight the link between this determinant and the polynomials A and B. Their proofs are given in Appendix.

Lemma 2 *Let $\bar{x} = (\bar{y}_1, \bar{y}_2, \bar{z})$ be a steady state of (4). The determinant of the corresponding Jacobian matrix is:*

$$\det(J(\bar{x})) = -\frac{d_2(r + d_2)\bar{y}_2}{\left(M\frac{d_2}{r} + \bar{y}_2\right)^2}(A'B - AB')(\bar{y}_2).$$

Lemma 3 *Let $x \geqslant 0$. These following are equivalent:*

- $(A'B - AB')(x) = 0$
- *x is a double root of P_θ, where $\theta := \frac{A(x)}{B(x)}$.*

We first note that the unique zero of f' must lie between the zeros y_{min} and y_{max} of f. This implies that f is decreasing in $[0; y_{min}]$ and increasing in $[y_{max}; +\infty)$. Therefore, f' stays positive on $[y_{max}; M]$, steady states $\bar{x}^{(1)}$ and $\bar{x}^{(2)}$ verify the condition (C_2).

Hence, Lemma 1 ensures that stability of the steady state $\bar{x} = (\bar{y}_1, \bar{y}_2, \bar{z})$ is given by the sign of $\det(J(\bar{x}))$, which is equal to the sign of $-(A'B - AB')(\bar{y}_2)$ by Lemma 2.

The steady states are zeros of P_θ, so they satisfy $\frac{A(x)}{B(x)} = \theta$. Since A and B do not depend on θ, there exists a maximal value for θ such that this equation admits a solution in $(y_{max}; M)$, $\theta_{max} = \sup_{x \in (y_{max}, M)}\{\frac{A}{B}(x)\}$. This bound stands for a real $x_0 \in (y_{max}; M)$ because $\frac{A}{B}(y_{max}) = \frac{A}{B}(M) = 0$. The function $A'B - AB'$ vanishes in x_0 because it is an extremum for $\frac{A}{B}$.Then x_0 is a double zero of $P_{\theta_{max}}$.

We set $\theta < \theta_{max}$. A double zero x_1 for P_θ satisfies $\frac{A}{B}(x_1) = \theta$, and $(A' + \theta B')(x_1) = 0$. Then $(A'B - AB')(x_1) = 0$, so x_1 is a critical point of $\frac{A}{B}$. By our hypothesis $\frac{A}{B}$ admits a unique critical point, so $x_1 = x_0$. This is a contradiction since $\theta < \theta_{max}$. This means that P_θ admits only simple zeros in (y_{max}, M). We have

$$P_\theta(x_0) = -A(x_0) + \theta B(x_0) = B(x_0)\left(\theta - \frac{A}{B}(x_0)\right) = B(x_0)(\theta - \theta_{max}) < 0.$$

Since $P_\theta(y_{max}) > 0$ and $P_\theta(M) > 0$, P_θ admits exactly two zero in (y_{max}, M), distributed on both sides of x_0. A third zeros would induce to a second critical point for $\frac{A}{B}$, which is forbidden. The function $\frac{A}{B}$ changes its direction only at its critical point x_0. It is easy to verify that $(A'B - AB')(M) < 0$ and $(A'B - AB')(y_{max}) > 0$, hence $\frac{A}{B}$ is strictly increasing on $[y_{max}; x_0]$ and strictly decreasing on $[x_0; M]$. We can now explore the three cases of the theorem:

1. If $\theta < \theta_{max}$, there exist two distinct steady states $\bar{x}^{(1)}$ and $\bar{x}^{(2)}$ such that $\bar{y}_2^{(1)} < \bar{y}_2^{(2)}$. In addition $\bar{x}^{(1)}$ is unstable and $\bar{x}^{(2)}$ is asymptotically stable.
2. If $\theta > \theta_{max}$, P_θ cannot vanish on $[y_{max}, M]$, so only the disease-free and maybe the low disease steady state remains. We have seen in Proposition 5 that, as soon as the disease-free steady state is unstable, the low one is asymptotically stable.
3. If $\theta = \theta_{max}$, then there exists a unique steady state in $[y_{max}, M]$, resulting from the fusion of two steady states with different stabilities: it is a saddle-node bifurcation. Let $x = (y_1, y_2, z)$ be a perturbation of the steady state $\bar{x}$ such that y_2 stays in $[y_{max}, M]$. We have

$$z' = s - f(y_2)z = s - \frac{d_2}{\mu}\frac{A}{B}(y_2) > s - \frac{d_2}{\mu}\frac{A}{B}(\bar{y}_2) = 0,$$

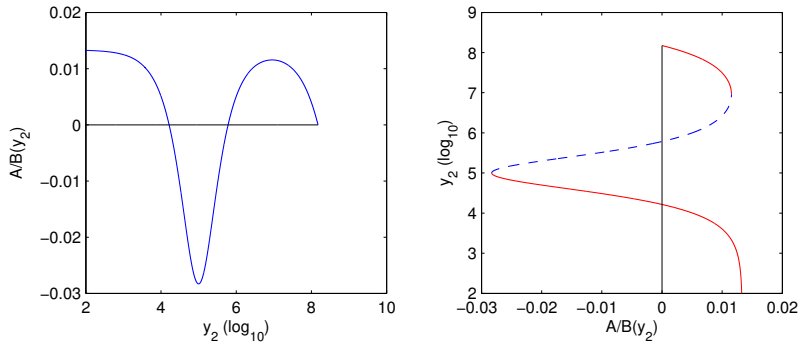

Fig. 1: The left graph represents $\frac{A}{B}$ as a function of y_2 in the interval $(0, M)$. The right graph represents $\bar{y}_2$ (corresponding to a steady state $\bar{x}$) as a function of θ. It is the bifurcation diagram, given by transposing the left graph. Stability is given by the sign of $\left(\frac{A}{B}\right)'$. Both graphs correspond to the case where f is given in Section 5.1.

because $\bar{y}_2$ is the maximum of $\frac{A}{B}$ on $[y_{max}, M]$. Hence z is always increasing near the steady state which, therefore, cannot be stable.

The next theorem is a stronger form of Theorem 1.

Theorem 2 *Denote by $\theta_1 < \cdots < \theta_n = \theta_{max}$ the extrema of $\frac{A}{B}$. Then*

1. *For all θ in $[0; \theta_{max}) \backslash \{\theta_1, \ldots, \theta_n\}$, there exist an positive even number of steady states with $\bar{y}_2$ in $(y_{max}; M)$. Their stability is alternated, the largest in term of value of $\bar{y}_2$ is asymptotically stable.*
2. *For all $\theta > \theta_{max}$ there is no steady state with $\bar{y}_2$ in $(y_{max}; M)$.*
3. *Generically, there is a saddle-node bifurcation for each $\theta \in \{\theta_1, \ldots, \theta_n\}$. Corresponding double steady states are generically unstable.*

Proof Using arguments identical to those used in proving Theorem 1, we conclude that x_0 is a double zero of P_θ. We set $\theta \in [0; \theta_{max}) \backslash \{\theta_1, \ldots, \theta_n\}$. The function P_θ cannot have any double root since θ does not correspond to a critical point of $\frac{A}{B}$. At x_0

$$P_\theta(x_0) = -A(x_0) + \theta B(x_0) = B(x_0)\left(\theta - \frac{A}{B}(x_0)\right) = B(x_0)(\theta - \theta_{max}) < 0.$$

Since $P_\theta(y_{max}) > 0$ and $P_\theta(M) > 0$, P_θ admits a positive even number of zeros in $(y_{max}; M)$. The function $\frac{A}{B}$ stays monotonic between two consecutive extrema. In addition, the sign of its derivative alternates between extrema. Calculations give $\frac{A}{B}(M) = 0$ and $(A'B - AB')(M) < 0$, so $\frac{A}{B}$ is locally positive and decreasing on the left side of M.

We fix $\theta < \theta_{max}$, and denote $x_\theta = \max\{x \geqslant 0 / \frac{A}{B}(x) = \theta\}$, which exists by continuity of $\frac{A}{B}$. Since $\frac{A}{B}(x_\theta) = \theta \geqslant 0 = \frac{A}{B}(M)$, $\frac{A}{B}$ must be locally decreasing near x_θ. We can now explore the three cases of the theorem:

1. If $\theta \in [0, \theta_{max}) \backslash \{\theta_1, \ldots, \theta_n\}$, the steady states set is

$$S_\theta = \{\bar{x} = (\bar{y_1}, \bar{y_2}, \bar{z}) \quad / \quad \frac{A}{B}(\bar{y_2}) = \theta \quad \& \quad \bar{y_1} \text{ and } \bar{z} \text{ verify 5 and 6}\}.$$

   Since $\frac{A}{B}$ is decreasing in $\max\{\bar{y_2} \ / \ \bar{x} \in S_\theta)$, that steady state is asymptotically stable by Lemmas 2 and 1. The stability of the other steady states alternates in terms of $\bar{y_2}$ value. Since $\#S_\theta$ is even, the lower steady state is unstable.
2. If $\theta > \theta_{max}$, P_θ cannot vanish on $[y_{max}, M]$, so only the disease-free and maybe the low disease steady state remains. We have seen in Proposition 5 that as soon as the disease-free steady state is unstable, the low one is asymptotically stable.
3. If $\theta = \theta_{max}$ then there exists a unique steady state, resulting from the fusion of two steady states with different stabilities: it is a saddle-node bifurcation.
4. If $\theta \in \{\theta_1, \ldots, \theta_n\}$, we let $x = (y_1, y_2, z)$ be a perturbation of the steady state $\bar{x}$ such that y_2 stays in $[y_{max}, M]$. Since $z' = s - f(y_2)z = s - \frac{d_2}{\mu}\frac{A}{B}(y_2)$, $z' > s - \frac{d_2}{\mu}\frac{A}{B}(y_2)$ if θ is a maximum of $\frac{A}{B}$ on $[y_{max}, M]$, and $z' < s - \frac{d_2}{\mu}\frac{A}{B}(y_2)$ if θ is a minimum of $\frac{A}{B}$ on $[y_{max}, M]$. In both cases, z is monotonic next to the steady state which, therefore, cannot be stable.

Corollary 1 *Let f be a rational fraction of the form $f = \frac{N}{D}$, where D is a positive polynomial with degree two or less, and N is a quadratic polynomial that admits two roots y_{min} and y_{max} in $[0, M]$, such that f' vanishes only once in $[0, M]$. Then there exists a value θ_{max} such that:*

1. *For any θ in $[0, \theta_{max})$ there exist two disease steady states with $\bar{y_2}$ in (y_{max}, M). The lower one is unstable and the higher one is asymptotically stable.*
2. *For any θ in $(\theta_{max}, +\infty)$ there is no steady state with $\bar{y_2}$ in (y_{max}, M).*
3. *There is an unstable saddle-node bifurcation at $\theta = \theta_{max}$.*

Proof The function f admits two zeros in $(0, M)$, which we denote as y_{min} and y_{max}. We write f as $f(x) = \frac{(x-y_{min})(x-y_{max})}{D(x)}$, and adapt Theorem 2: The first steady state is $(0, 0, \frac{s}{d})$. It is the disease-free steady state. Other steady states are given by:

$$\bar{y_1} = \frac{(r + d_2)\bar{y_2}}{a_1 + \frac{r}{K}\bar{y_2}}, \quad \text{and} \quad \bar{z} = \frac{sD(\bar{y_2})}{(\bar{y_2} - y_{min})(\bar{y_2} - y_{max})},$$

where $\bar{y_2}$ is a positive zero of the cubic polynomial:

$$P_\theta(X) = (X - y_{min})(X - y_{max})(X - M) + \theta\left(M\frac{d_2}{r} + X\right)D(X),$$

such that $\bar{y_2} \notin [y_{min}, y_{max}]$.

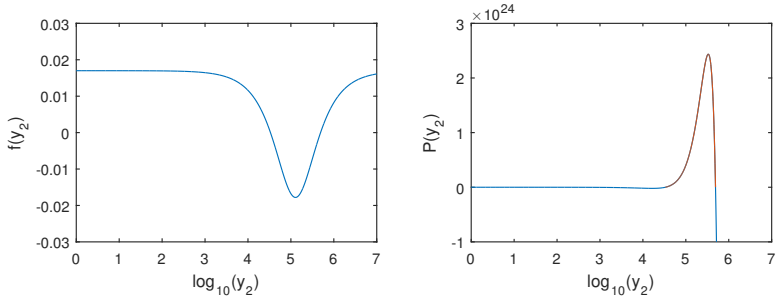

Fig. 2: Functions f and P profiles. The part where P is positive is represented in red.

We keep the previous notations: $A(X) = (X - y_{min})(X - y_{max})(X - M)$ and $B(X) = (M\frac{d_2}{r} + X)D(X)$. To prove the corollary, we only have to verify that $\frac{A}{B}$ has only one critical point in (y_{max}, M).

We assume that $\frac{A}{B}$ admits a second critical point x_1 in (y_{max}, M), and denote $\theta_1 = \frac{A}{B}(x_1)$. Then x_1 is a double root for P_{θ_1}. For all θ lower than θ_{max}, P_θ admits one root in $[0, y_{min}]$ and two distinct roots in $[y_{max}, M]$. Since it is a cubic polynomial, there are no more roots. Hence P_θ cannot have any double root in $[y_{max}, M]$.

This means that $\theta_1 = \theta_{max}$. Since $P_{\theta_{max}}$ is a cubic polynomial that admits x_0 and x_1 as double roots, necessarily $x_1 = x_0$. We showed that $\frac{A}{B}$ admits one and only one critical point. Applying Theorem 1 concludes the proof.

We have seen in this section that the bifurcation diagram is uniquely determined by transposing the function $\frac{A}{B}$ graph. It induces that no other branch could co-exist with the ones we highlight. An other consequence is that, at $\bar{y_2}$ fixed, the stability is known regardless of the value of parameters s and μ. We conducted the whole analysis by privileging the variable y_2 over y_1 and z because it is the only practical biologically measurable quantity. Our results are especially convenient since they only depend on this quantity.

5 Application of the stability analysis

In this section we will apply the previous stability analysis with two different functions modeling the immune system.

5.1 The original model

As in [6], we set $f(x) = d - \alpha\frac{x}{1+\varepsilon x^2}$. Its profile is represented in Figure 2.

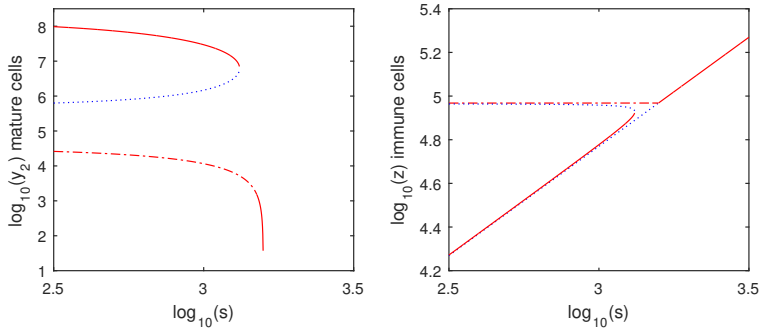

Fig. 3: Bifurcation diagram depending on parameter s variation (immune cells source). Solid red curves are for asymptotically stable steady states with real dominant eigenvalue, dashed red curves are for asymptotically stable steady states with complex dominant eigenvalue, and dotted curves are for unstable steady states. On the left graph the disease-free steady state corresponds to $\bar{y}_2 = 0$, so it does not appear with the log-scale. For s big enough, the two highest steady states disappear, then low and trivial steady states cross each other.

In this case, the derivative $f'(x) = -\alpha \frac{1-\varepsilon x^2}{(1+\varepsilon x^2)^2}$, vanishes only for $x = \varepsilon^{-1/2}$. We assume that $\alpha^2 \geqslant 4\varepsilon d^2$, and denote:

$$y_{min} = \frac{\alpha - \sqrt{\alpha^2 - 4\varepsilon d^2}}{2\varepsilon d}, \qquad y_{max} = \frac{\alpha + \sqrt{\alpha^2 - 4\varepsilon d^2}}{2\varepsilon d}.$$

As soon as $M > y_{max}$, we can apply Corollary 1. The function P_θ is then the third-order polynomial,

$$P_\theta = (X - y_{min})(X - y_{max})(X - M) + \frac{\theta}{\varepsilon d}\left(X + M\frac{d_2}{r}\right)(1 + \varepsilon X^2).$$

With this particular example, we can give an upper bound for $\frac{A}{B}$ on $\mathbb{R}_+$:

$$\frac{A}{B}(X \geqslant 0) = d\frac{(X^2 - (y_{min} + y_{max})X + \frac{1}{\varepsilon})(M - X)}{(X + \frac{d_2}{r}M)(X^2 + \frac{1}{\varepsilon})} \leqslant d\frac{M - X}{X + \frac{d_2}{r}M} \leqslant \frac{rd}{d_2}.$$

Hence, θ_{max} is bounded by $\frac{rd}{d_2}$. This value corresponds to the transcritical bifurcation between the low disease and the disease-free steady states. This means that the saddle-node bifurcation occurs for lower values of θ than the transcritical bifurcation.

The bifurcation diagram and stability chart given by Corollary 1 are reproduced in Figures 3 and 4.

We applied the simplified model (4) to the patient data from [6] in order to compare the relevance of two models in Figure 5.

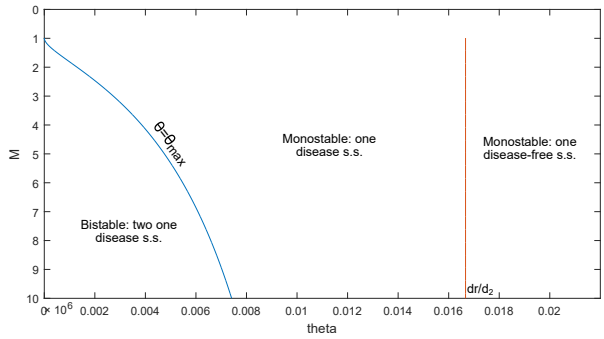

Fig. 4: Stability chart in the plan (θ, M), for Subsection 5.1.

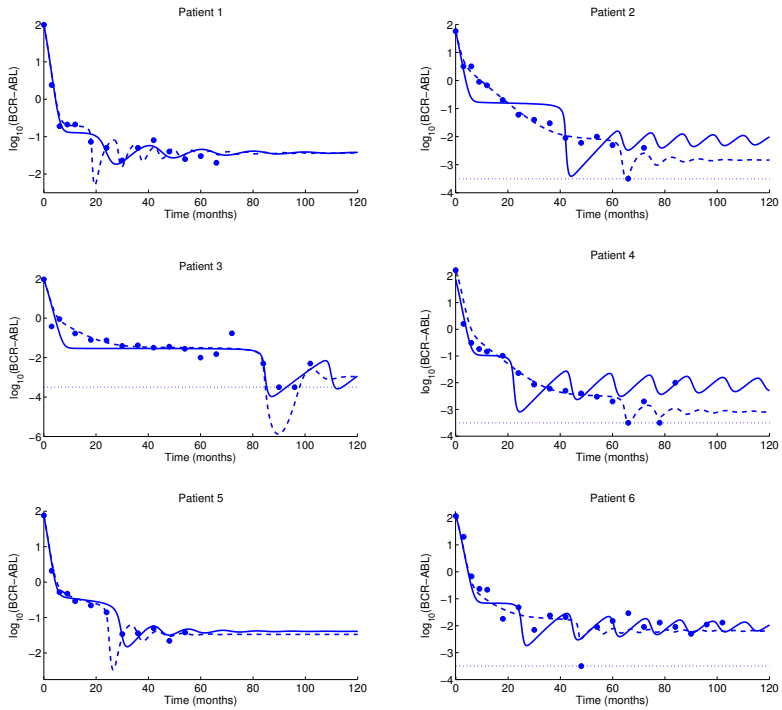

Fig. 5: Fits of the original (dashed line) and reduced (solid line) models to six patients treated with first-line Imatinib. The base-10 log of the BCR-ABL ratio is plotted against time, in months. Dots represent patient data. Dotted lines approximate the minimum leukemic level that is detectable by RT-PCR. Dots along this line represent zero measurements, meaning CML cells were not detected. The parameters used for the fits to the original and simplified model are respectively in Tables 2 and 3, universal parameters are in Table 1.

Table 1: Universal parameters values used in the reduced model.

Parameter	Value
r	0.007775
K	41.667
a_1	$1.350e5$
d_2	0.0375
s	$z(0) * d$
$y_1(0)$	K
$y_2(0)$	$1.5e8$
$z(0)$	120

Table 2: Estimated parameters with the original model (1)

Patient	inh_1	inh_2	d	μ	y_{min}	y_{max}
1	4.612	92.3215	0.031	9.964e-7	4.994e4	5.598e5
2	1.456	545.150	0.099	1.504e-8	3.765e4	2.759e5
3	591.591	14.568	0.040	2.371e-7	3.132e3	2.228e4
4	486.315	226.000	0.075	2.879e-8	3.536e2	1.684e3
5	50.988	79.645	0.005	1.271e-6	1.182e3	5.482e4
6	30.208	359.979	0.371	2.263e-7	4.959e3	1.353e4

Table 3: Estimated parameters with the simplified model (4)

Patient	k_{inh}	d	μ	y_{min}	y_{max}
1	2.521e2	0.051	3.647e-6	6.610e4	3.624e5
2	1.133e3	0.026	2.405e-8	3.831e4	3.055e5
3	4.205e2	0.054	4.224e-7	1.617e4	3.133e5
4	5.691e3	0.181	8.499e-6	1.206e3	1.090e4
5	4.594e3	0.038	5.723e-9	1.841e3	3.401e4
6	2.853e3	0.058	1.358e-9	7.143e3	7.576e4

For many patients, the fits in Figure 5 are comparable between the complete model (1) and the simplified model (4). Intriguingly, for some patients (such as Patients 1, 3 and 5), the fits seem more satisfactory with the simplified model. Typically when the initial decay is slow, it looks as if the oscillations are better controlled by the simplified model (4). It might be due to the fact that, in order to be consistent with [6], we decided to assume a priori that y_{min} and y_{max} exist, which then constrains the parameters. Compared with the full model, (1), the model (4) cannot capture rapid oscillations and sharp decays.

5.2 A mechanistic model

We apply here our procedure to a second example, a mechanistic model for describing the dynamics of CML [3]. In this model, there are no terms representing immunosuppression of the immune-leukemia interactions. Instead,

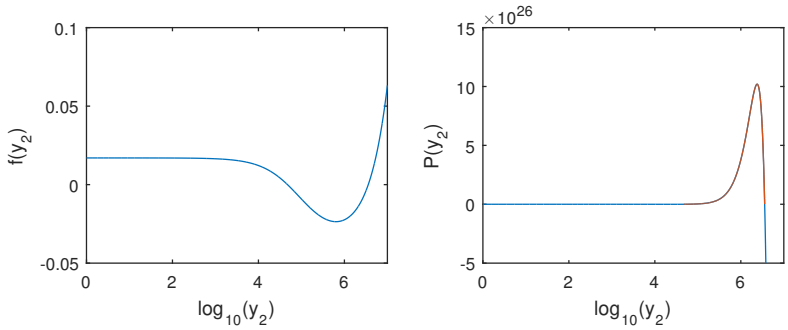

Fig. 6: Functions f and P profiles. The part where P is positive is represented in red.

mature leukemic cells are assumed to have two contrasting effects on immune cells: (i) a Michaelis-Menten term, $\alpha y_2 z/(1+\varepsilon y_2)$, that represents the stimulation of immune cells by leukemic cells, with maximum rate $\alpha\varepsilon^{-1}$ and Michaelis constant ε^{-1}; and (ii) a mass action term, $\nu y_2 z$, representing the killing of immune cells by leukemic cells, at a rate ν.

For the immune dynamics, f is given by $f(x) = d + \nu x - \alpha\frac{x}{1+\varepsilon x}$. Its profile is represented in Figure 6.

In this case, the derivative $f'(x) = \nu - \alpha(1+\varepsilon x)^{-2}$, vanishes only for $x = \frac{1}{\varepsilon}(\sqrt{\frac{\alpha}{\nu}} - 1)$. We assume that $(\alpha - \varepsilon d - \nu)^2 - 4\varepsilon\nu d > 0$, and denote:

$$y_{min} = \frac{(\alpha - \varepsilon d - \nu) - \sqrt{(\alpha - \varepsilon d - \nu)^2 - 4\varepsilon\nu d}}{2\varepsilon\nu},$$

$$y_{max} = \frac{(\alpha - \varepsilon d - \nu) + \sqrt{(\alpha - \varepsilon d - \nu)^2 - 4\varepsilon\nu d}}{2\varepsilon\nu}.$$

As soon as $M > y_{max}$, we can apply Corollary 1. The bifurcation diagram and stability chart given by Corollary 1 are reproduced in Figures 7 and 8.

6 Discussion and conclusion

In this manuscript we presented a simplified, analytically tractable version of a model for tumor-immune interaction recently proposed [6]. This simplification allows us to conduct a complete analytic study of the model. We showed the existence of a disease-free steady state and established conditions for the existence of disease steady states. We characterized the stability of each of these steady states, and identified the transitions in the number of steady states and in their stability.

It was anticipated that the simplified model would possess a disease-free steady state. This state corresponds to the asymptotic solution when treatment is effective. Whether the leukemic cells completely vanishes under treatment is a biological open question [2,19]. The model we analyze leads to a low disease

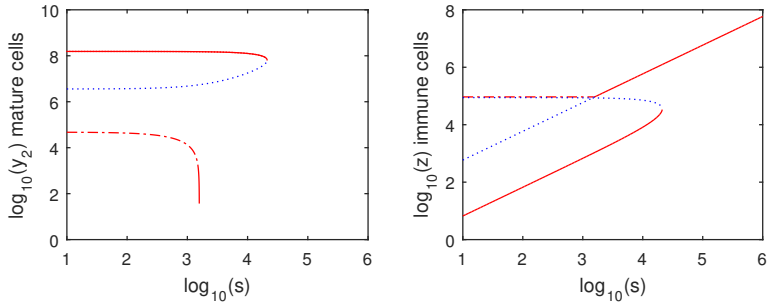

Fig. 7: Bifurcation diagram depending on parameter s variation (immune cells source). Solid red curves are for asymptotically stable steady states with real dominant eigenvalue, dashed red curves are for asymptotically stable steady states with complex dominant eigenvalue, and dotted curves are for unstable steady states. On the left graph the disease-free steady state corresponds to $\bar{y}_2 = 0$, so it does not appear with the log-scale. For s big enough, low and trivial steady states cross each other, then the two highest steady states disappear.

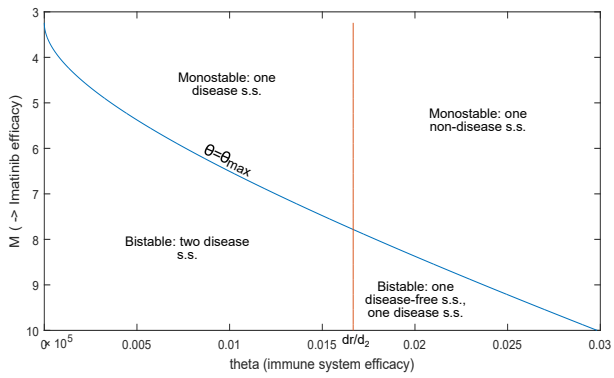

Fig. 8: Stability chart in the plan (θ, M), for Subsection 5.2, where $\theta = \frac{\mu s}{d_2}$. We still have the possibility of having two stable steady states (one with $y_2 < y_{min}$ one with $y_2 > y_{max}$). One of the main difference is that a stable disease free steady state may coexist with a stable disease steady state. In the first model, this is mainly due to the fact that the immunosuppression is not saturated and high levels of y_2 leads to very small values of z, below $\frac{s}{f(0)}$.

steady state (with leukemic load below the immune window) that corresponds to the asymptotic solution when treatment is not sufficiently efficient to eradicate the disease, but is sufficient to allow the immune system to keep it under control at a low level.

We obtained complete generic one-parameter bifurcation diagrams (Figures 3 and 7), and showed that a low-disease steady state exists for a wide range of parameters. When such a state exists, it is stable. The low-disease steady state becomes non-positive and disappear from the biologically relevant phase-space at a transcritical bifurcation with an unstable disease-free steady state, at which they exchange their stability. Large disease steady state can coexist; they are generically created and destroyed through saddle-node bifurcations. No steady state can ever be destabilized through a Hopf bifurcation. Although we have not shown that no limit cycles can occur, we could not find any non-local bifurcations leading to limit cycles, such homoclinic bifurcations, or saddle-node bifurcation on an invariant cycle (SNIC). The low-disease steady state is the only steady state that can be a focus, and it is always a stable focus.

Two qualitatively different bifurcation diagrams were identified: (i) a stable disease-free steady state and existence of a large disease steady state and mutually exclusive; and (ii) co-existence of a stable disease-free steady state and a large disease steady state possible.

The asymptotic stability we highlighted is a local stability of steady states, which does not guarantee the convergence of any solution to the steady state. We have not yet derived any theoretical result on the basin of attraction of asymptotically stable steady states. Numerically, the low steady state basin of attraction seems much smaller than the basin of attraction of the high steady state. That could be interpreted by the scarcity of solutions converging to the low disease steady state. For example, this model allows a state with low amount of leukemic cells and high amount of immune cells to converge to the highest disease steady state with high amount of leukemic cells and low amount of immune cells.

The stability results obtained in this paper could help in interpreting the clinical state of remission after treatment cessation. Indeed, remission could correspond to attraction by the low disease steady state, while relapse could correspond to attraction by a higher stable disease steady state. It is useful to see the weight of each parameter in the dynamics of solutions. For example, Figures 4 and 8 highlight the relevance controlling the autologous immune system efficacy in order to constrain solutions to converge to a low disease steady state or to a disease-free steady state.

Fitting either the original or the simplified model to individual patients yields excellent results in most cases (Figure 5). The simplified model has a tendency to predict oscillatory levels of BCR/ABL ratio, due to the focus nature of the low disease steady state. Whether the fluctuations in clinical BCR/ABL ratio correspond to deterministic oscillations or to stochastic fluctuations is not clear, but our steady state analysis suggests that oscillations are a signature of the immune control of the CML.

The bifurcation diagrams suggest three possible scenarios for the outcome of a treatment cessation. In any of these scenarios, relapse is possible. First, if there is co-existence of a stable large disease steady state and a stable low steady state, no cure is possible and the success of treatment cessation is determined by how attractive the low-disease steady state is. Second, if there is co-existence of a large disease steady state and a stable disease-free steady state, it is possible that treatment cessation (or continuation) could actually lead to eradication of the tumor. Third, no large steady state exists, and the low-disease steady state is the clinical disease state. In this case, the disease-free steady state is always unstable, and treatment cessation is bound to fail.

Our stability analysis is adaptable to a large class of functions modeling the immune system degradation. The double-monotony of this function is a biologically acceptable condition, corresponding to immune activation and immunosuppression.

Acknowledgements The work of GC was supported by the National Science Foundation Graduate Research Fellowship under Grant No. DGE1322106. The work of DL was supported in part by the John Simon Guggenheim Memorial Foundation. The work was supported by the Inria Partnerships Program grant "Modelling Leukemia".

References

1. Burchert, A. Inselmann, S. Saussele, S. Dietz, C.T. Müller, M.C. Eigendorff, E. Brümmendorf, T.H. Waller, C. Dengler, J. Goebeler, M.E. Herbst, R. Freunek, G. Hanzel, S. Illmer, T. Wang, Y. Neubauer, A. Lange, T. Hochhaus, A. Florian, F. Brendel, C.A. Guilhot, J. Mahon, F.X. & Schütz, C. Frequency of CTLA-4 Receptor Ligand (CD86, B7.2)-Positive Plasmacytoid Dendritic Cells Predicts Risk of Disease Recurrence after Tyrosine-Kinase Inhibitor Discontinuation in Chronic Myeloid Leukemia: Results from a Prospective Substudy of the Euroski Trial. *Blood*, 126(23):599, dec 2015.
2. Chu, S. McDonald, T. Lin, A. Chakraborty, S. Huang, Q. Snyder, D.S. & Bhatia, R. Persistence of leukemia stem cells in chronic myelogenous leukemia patients in prolonged remission with imatinib treatment. *Blood*, 118(20):5565–5572, 2011.
3. Clapp, G.D. Applying Mathematical Models to Study the Role of the Immune System in Chronic Myelogenous Leukemia, Ph.D. Dissertation, University of Maryland, College Park, 2016.
4. Clapp, G.D. & Levy, D. A Review of Mathematical Models for Lymphoma and Leukemia. *Drug Discovery Today: Disease Models*, 16:1–6, 2015.
5. Clapp, G.D., Lepoutre, T., Nicolini, N. & Levy, D. BCR-ABL transcript variations in chronic myelogenous leukemia patiens on imatinib first-line: Possible role of the autologous immune system. *Oncoimmunology*, 5(5), e1122159, 2016.
6. Clapp, G.D., Lepoutre, T., El Cheikh, R., Bernard, S., Ruby, J., Labussière-Wallet, H., Nicolini, F., & Levy, D. Implication of the autologous immune system in BCR-ABL transcript variations in chronic myelogenous leukemia patients treated with imatinib. *Cancer Research*, 75(19):4053-4062, 2015.
7. Deininger, M.W. Goldman, J.M. & Melo, J.V. The molecular biology of chronic myeloid leukemia *Blood*, 96(10):3343–3356, 2000.
8. Falkenburg, J.H. Wafelman, A.R. Joosten, P. Smit, W.M. van Bergen, C.A. Bongaerts, R. Lurvink, E. van Der Hoorn, M. Kluck, P. Landegent, J.E. Kluin-Nelemans, H.C. Fibbe, W.E. & Willemze, R. Complete remission of accelerated phase chronic myeloid leukemia by treatment with leukemia-reactive cytotoxic T lymphocytes *Blood*, 94(4):1201–8, aug 1999.

9. Graham, S.M. Jørgensen, H.G. Allan, E. Pearson, C. Alcorn, M.J. Richmond, L. & Holyoake, T.L. Primitive, quiescent, Philadelphia-positive stem cells from patients with chronic myeloid leukemia are insensitive to STI571 in vitro. *Blood*, (January):319–325, 2008.

10. Ilander, M. Kreutzman, A. & Mustjoki, S. IFNα induces prolonged remissions modeling curative immunologic responses in chronic myeloid leukemia *Oncoimmunology*, 3(April):e28781, 2014.

11. Kim, P.S. Lee, P.P. & Levy, D. A PDE model for imatinib-treated chronic myelogenous leukemia *Bulletin of mathematical biology*, 70(7):1994–2016, oct 2008.

12. Kim, P.S. Lee, P.P. & Levy, D. Dynamics and potential impact of the immune response to chronic myelogenous leukemia *PLoS computational biology*, 4(6):e1000095, jun 2008.

13. Komarova, N. & Wodarz, D. Effect of cellular quiescence on the success of targeted CML therapy *PloS one*, 2(10):e990, jan 2007.

14. Mahon, F-X. Réa, D. Guilhot, J. Guilhot, F. Huguet, F. Nicolini, L. Legros, L. Charbonnier, A. Guerci, A. Varet, B. Etienne, G. Reiffers, J. & Rousselot, P. Discontinuation of imatinib in patients with chronic myeloid leukaemia who have maintained complete molecular remission for at least 2 years: the prospective, multicentre Stop Imatinib (STIM) trial *The Lancet Oncology*, 11(11):1029–35, nov 2010.

15. Michor, F. Hughes, T.P. Iwasa, Y. Branford, S. Shah, N.P. Sawyers, C.L. & Nowak, M.A. Dynamics of chronic myeloid leukaemia *Nature*, 435(7046):1267–70, jun 2005.

16. O'Brien, S.G. Guilhot, F. Larson, R.A. Gathmann, I. Baccarani, M. Cervantes, F. Cornelissen, J.J. Fischer, T. Hochhaus, A. Hughes, T. Lechner, K. Nielsen, J.L. Rousselot, P. Reiffers, J. Saglio, G. Shepherd, J. Simonsson, B. Gratwohl, A. Goldman, J.M. Kantarjian, H. Taylor, K. Verhoef, G. Bolton, A.E. Capdeville, R. & Druker, B.J. Imatinib compared with interferon and low-dose cytarabine for newly diagnosed chronic-phase chronic myeloid leukemia *The New England journal of medicine*, 348(11):994–1004, mar 2003.

17. Preudhomme, C. Guilhot, J. Nicolini, F.E. Guerci-Bresler, A. Rigal-Huguet, F. Maloisel, F. Coiteux, V. Gardembas, M. Berthou, C. Vekhoff, A. Rea, D. Jourdan, E. Allard, C. Delmer, A. Rousselot, P. Legros, L. Berger, M. Corm, S. Etienne, G. Roche-Lestienne, C. Eclache, V. Mahon, F.X. & Guilhot, F. Imatinib plus peginterferon alfa-2a in chronic myeloid leukemia *The New England journal of medicine*, 363(26):2511–21, dec 2010.

18. Roeder, I. Horn, M. Glauche, I. Hochhaus, A. Mueller, M. & Loeffler, M. Dynamic modeling of imatinib-treated chronic myeloid leukemia: functional insights and clinical implications *Nature medicine*, 12(10):1181–4, oct 2006.

19. Ross, D.M. Branford, S. Seymour, J.F. Schwarer, A.P. Arthur, C. Bartley, P.A. Slader, C. Field, C. Dang, P. Filshie, R.J. Mills, A.K. Grigg, A.P. Melo, J.V. & Hughes, T.P. Patients with chronic myeloid leukemia who maintain a complete molecular response after stopping imatinib treatment have evidence of persistent leukemia by DNA PCR *Leukemia*, 24(10):1719–1724, 2010.

20. Rousselot, P. Huguet, F. Rea, D. Legros, L. Cayuela, J.M. Maarek, O. Blanchet, O. Marit, G. Gluckman, E. Reiffers, J. Gardembas, M. & Mahon F.X. Imatinib mesylate discontinuation in patients with chronic myelogenous leukemia in complete molecular remission for more than 2 years *Blood*, 109(1):58–61, 2007.

APPENDIX

The following equations are satisfied by positive steady states. They will be used in technical lemmas.

$$\bar{z} = \frac{s}{f(\bar{y}_2)},$$

$$\bar{z} = \frac{d_2}{\mu}\frac{M - \bar{y}_2}{M\frac{d_2}{r} + \bar{y}_2},$$

$$\frac{r}{K}\bar{y}_1 = \frac{(r+d_2)\bar{y}_2}{M\frac{d_2}{r} + \bar{y}_2},$$

$$a_1\frac{\bar{y}_1}{\bar{y}_2} = M\frac{d_2}{r}\frac{(r+d_2)}{M\frac{d_2}{r} + \bar{y}_2}.$$

Lemma 1 Let $\bar{x} = (\bar{y}_1, \bar{y}_2, \bar{z})$ be a steady state of (4) such that $f'(\bar{y}_2) > 0$. The steady state $\bar{x}$ is asymptotically stable if, and only if, $\det(J(\bar{x})) < 0$.

Proof The determinant of $J(\bar{x})$ is the product of all its eigenvalues, so it is equal to $-\chi_J(0)$. We note that the polynomial χ_J is convex on $\mathbb{R}^+$, and that

$$\begin{aligned}
\chi_J'(0) - \frac{\chi_J(0)}{r+d_2} &= \left((r+d_2)f(\bar{y}_2) - \mu\bar{z}\bar{y}_2 f'(\bar{y}_2) + \frac{r}{K}\bar{y}_1 a_1\frac{\bar{y}_1}{\bar{y}_2}\right) \\
&\quad - \frac{1}{r+d_2}\left(\frac{r}{K}\bar{y}_1 a_1\frac{\bar{y}_1}{\bar{y}_2}f(\bar{y}_2) - (r+d_2)\mu\bar{z}\bar{y}_2 f'(\bar{y}_2)\right) \\
&= (r+d_2)f(\bar{y}_2) + \frac{r}{K}\bar{y}_1 a_1\frac{\bar{y}_1}{\bar{y}_2} - \frac{1}{r+d_2}\frac{r}{K}\bar{y}_1 a_1\frac{\bar{y}_1}{\bar{y}_2}f(\bar{y}_2) \\
&= \frac{r}{K}\bar{y}_1 a_1\frac{\bar{y}_1}{\bar{y}_2} + \frac{f(\bar{y}_2)}{r+d_2}\left((r+d_2)^2 - \frac{r}{K}\bar{y}_1 a_1\frac{\bar{y}_1}{\bar{y}_2}\right) \\
&= \frac{r}{K}\bar{y}_1 a_1\frac{\bar{y}_1}{\bar{y}_2} + \frac{f(\bar{y}_2)}{r+d_2}\left(\left(\frac{r}{K}\bar{y}_1 + a_1\frac{\bar{y}_1}{\bar{y}_2}\right)^2 - \frac{r}{K}\bar{y}_1 a_1\frac{\bar{y}_1}{\bar{y}_2}\right) \\
&= \frac{r}{K}\bar{y}_1 a_1\frac{\bar{y}_1}{\bar{y}_2} + \frac{f(\bar{y}_2)}{r+d_2}\left(\left(\frac{r}{K}\bar{y}_1\right)^2 + \left(a_1\frac{\bar{y}_1}{\bar{y}_2}\right)^2 + \frac{r}{K}\bar{y}_1 a_1\frac{\bar{y}_1}{\bar{y}_2}\right) > 0.
\end{aligned}$$

Here we used $f(\bar{y}_2) > 0$ given by Proposition 2. We consider two cases:

Case 1: If $\chi_J(0) < 0$, then there exists a root in $\mathbb{R}_+^*$. In this case the steady state $\bar{x}$ is unstable.

Case 2: If $\chi_J(0) > 0$, then $\chi_J'(0) > 0$ and, by convexity, χ_J stays non-negative on $\mathbb{R}_+^*$. If χ_J admits three real roots, they are all negative, and the steady state is asymptotically stable. Otherwise, there exists two conjugate complex

roots. In this case, we denote by x the negative real root, and by z one of the two complex roots. First, note that since $f'(\bar{y}_2) > 0$, we have:

$$\chi_J(-\frac{r}{K}\bar{y}_1) = -a_1\bar{y}_1\mu\bar{z}f'(\bar{y}_2) < 0.$$

As χ_J has only one sign change on $\mathbb{R}$, at x, we deduce that $-\frac{r}{K}\bar{y}_1 < x$. Yet,

$$2\,\mathrm{Re}(z) + x = -\frac{r}{K}\bar{y}_1 - a_1\frac{\bar{y}_1}{\bar{y}_2} - \frac{s}{f(\bar{y}_2)} < x - a_1\frac{\bar{y}_1}{\bar{y}_2} - \frac{s}{f(\bar{y}_2)}.$$

Hence

$$\mathrm{Re}(z) < -\frac{1}{2}\left(a_1\frac{\bar{y}_1}{\bar{y}_2} + \frac{s}{f(\bar{y}_2)}\right) < 0.$$

We showed that complex roots have negative real parts in the case where $f'(\bar{y}_2)$ is positive. Therefore, the steady state is asymptotically stable.

Lemma 2 Let $\bar{x} = (\bar{y}_1, \bar{y}_2, \bar{z})$ be a steady state of (4). The determinant of the corresponding Jacobian matrix $\det(J(\bar{x}))$ has a sign opposite to that of $A'B - AB'$.

Proof We compute

$$\begin{aligned} A'B - AB' &= (f'(X)(M-X) - f(X))\left(X + \frac{d_2}{r}M\right) - f(X)(M-X) \\ &= f'(X)(M-X)\left(X + \frac{d_2}{r}M\right) - f(X)M\left(1 + \frac{d_2}{r}\right). \end{aligned}$$

Let $\bar{x} = (\bar{y}_1, \bar{y}_2, \bar{z})$ be a steady state for the system (4). The determinant of the Jacobian matrix at $\bar{x}$ is

$$\begin{aligned} \det(J(\bar{x})) &= \frac{r}{K}\bar{y}_1 a_1\frac{\bar{y}_1}{\bar{y}_2}f(\bar{y}_2) - (r+d_2)\mu\bar{z}\bar{y}_2 f'(\bar{y}_2) \\ &= \frac{(r+d_2)\bar{y}_2}{M\frac{d_2}{r} + \bar{y}_2}M\frac{d_2}{r}\frac{(r+d_2)}{M\frac{d_2}{r} + \bar{y}_2}f(\bar{y}_2) - (r+d_2)d_2\frac{M - \bar{y}_2}{M\frac{d_2}{r} + \bar{y}_2}\bar{y}_2 f'(\bar{y}_2) \\ &= \frac{d_2(r+d_2)\bar{y}_2}{\left(M\frac{d_2}{r} + \bar{y}_2\right)^2}\left(M\left(1 + \frac{d_2}{r}\right)f(\bar{y}_2) - (M - \bar{y}_2)\left(M\frac{d_2}{r} + \bar{y}_2\right)f'(\bar{y}_2)\right) \\ &= -\frac{d_2(r+d_2)\bar{y}_2}{\left(M\frac{d_2}{r} + \bar{y}_2\right)^2}(A'B - AB')(\bar{y}_2). \end{aligned}$$

Hence $sign(\det(J(\bar{x}))) = -sign((A'B - AB')(\bar{y}_2))$.

Lemma 3 Let $x \geqslant 0$. These following are equivalent:

- $(A'B - AB')(x) = 0$,
- x is a double root of P_θ, where $\theta := \frac{A(x)}{B(x)}$.

Proof Let x be a positive zero of $A'B - AB'$. We fix $\theta := \frac{A(x)}{B(x)}$. Then,

$$P_\theta(x) = -A(x) + \theta B(x) = 0,$$
$$P'_\theta(x) = -A'(x) + \theta B'(x) = -\frac{A'B - AB'}{B}(x) = 0.$$

Hence x is a double zero of P_θ.

Reciprocally, let (θ, x) be such that x is a double zero of P_θ. Since $P_\theta(x) = 0$, $\theta = \frac{A}{B}(x)$. Also, since $P'_\theta(x) = 0$, $(A'B - AB')(x) = 0$, which means that x is a zero of $A'B - AB'$.

Lemma 4 *Consider the polynomial $P = X^3 + aX^2 + bX + c$, where $a, b, c \in \mathbb{R}_+^*$. If $ab > c$, then all roots of P have negative real part.*

Proof First, positivity of all coefficients ensures that the real roots of P cannot be positive. Second, as $P(0) = c > 0$, P necessarily admits a real, negative root. It remains to characterize the two other roots. If real and negative, then the dominating root is negative and the lemma is proven. Therefore we may assume that the two remaining roots are complex, and we need to determine the sign of their real part.

Let λ be the first negative root of P. We can factor

$$P = \big(X - \lambda\big)\big(X^2 + (a + \lambda)X + (b + a\lambda + \lambda^2)\big).$$

By our assumption, P admits a pair of complex roots. We want to compare $\big(X^2 + (a+\lambda)X + (b + a\lambda + \lambda^2)\big)$ and $(X - z)(X - \bar{z})$, where $z \in \mathbb{C}$. Separating the real and imaginary parts leads to

$$a + \lambda = -2\,\mathrm{Re}(z),$$
$$b + a\lambda + \lambda^2 = (\mathrm{Re}(z))^2 + (\mathrm{Im}(z))^2.$$

In order to find the sign of $\mathrm{Re}(z)$, we need to compare a and λ. We have $P(-a) = -ab + c$. Since we assume that, $ab > c$, we obtain $P(-a) < 0$. As P has only one real root λ, we obtain $-a < \lambda$. This leads to $\mathrm{Re}(z) < 0$, and the dominating root of P has its real part negative.

9.5 Chauhan A, Lorenzen S, Herzel H, Bernard S (2011) Regulation of mammalian cell cycle progression in the regenerating liver. J Theor Biol 283:103–112

Author's personal copy

Journal of Theoretical Biology 283 (2011) 103–112

Contents lists available at ScienceDirect

Journal of Theoretical Biology

journal homepage: www.elsevier.com/locate/yjtbi

Regulation of mammalian cell cycle progression in the regenerating liver

Anuradha Chauhan [a], Stephan Lorenzen [c], Hanspeter Herzel [a], Samuel Bernard [b,*]

[a] Institute for Theoretical Biology, Humboldt University, Invalidenstrasse 43, 10115 Berlin, Germany
[b] Institut Camille Jordan, CNRS UMR5208, Université de Lyon, Université Lyon 1, 43, boulevard du 11 novembre 1918, F-69622 Villeurbanne Cedex, France
[c] AG Systems Biology, Charité Center for Cardiovascular Research, Hessische Strasse 3-4, 10115 Berlin, Germany

ARTICLE INFO

Article history:
Received 10 November 2010
Received in revised form
6 May 2011
Accepted 17 May 2011
Available online 26 May 2011

Keywords:
Liver regeneration
Mitosis
Bandpass filter
G2 delay
Cyclin

ABSTRACT

The process of cell division in mammalian cells is orchestrated by cell-cycle-dependent oscillations of cyclin protein levels. Cyclin levels are controlled by redundant transcriptional, post-translational and degradation feedback loops. How each of these separate loops contributes to the regulation of the key cell cycle events and to the connection between the G1-S transition and the subsequent mitotic events is under investigation. Here, we present an integrated computational model of the mammalian cell cycle based on the sequential activation of cyclins. We validate the model against experimental data on liver cells (hepatocytes), which undergo one or two rounds of synchronous circadian-clock gated cell divisions during liver regeneration, after partial hepatectomy (PH). The model exhibits bandpass filter properties that allow the system to ignore strong but transient, or sustained but weak damages after PH. Bifurcation analysis of the model suggests two different threshold mechanisms for the progression of the cell through mitosis. These results are coherent with the notion that the mitotic exit in mammalian cells is bistable, and suggests that Cdc20 homologue 1 (Cdh1) is an important regulator of mitosis. Regulation by Cdh1 also explains the observed G2/M phase prolongation after hepatocyte growth factor (HGF) stimulation during S phase.

© 2011 Elsevier Ltd. All rights reserved.

1. Introduction

The cell division cycle is a highly organized and structured mechanism in mammals. Because of its dynamical nature, it has been subject to several computational models. The first computational models pertained to the cell cycle in amphibian embryos and yeast (Tyson, 1991; Goldbeter, 1991; Novak and Tyson, 1993; Sha et al., 2003; Pomerening et al., 2003; Chen et al., 2004). More recently, computational models were proposed for specific parts of the mammalian cell cycle, particularly the G1/S phase transition and the restriction point (Aguda and Tang, 1999; Qu et al., 2003a,b; Swat et al., 2004; Novak and Tyson, 2004). A generic model for the eukaryotic cell cycle has also been presented (Csikasz-Nagy et al., 2006).

Few detailed, integrative models coupling the main events of the cell cycle, DNA synthesis and mitosis have been proposed. Models of this sort have been proposed for yeast, in which growth of cell mass is playing a key role in regulating mitosis (Chen et al., 2004), and more recently for mammals (Gerard and Goldbeter, 2009). In mammals, however, cell mass is not a major determinant for the control of cell cycle. Rather, mammalian cells possess multiple control mechanisms that prevent them from proliferating outside specific conditions. Mammalian cells vary in type and degree of differentiation, each one having different proliferative potential and mechanism. This makes the task of modelling mammalian cells challenging, as there is no universal experimental model. In vitro systems of dividing cells provide a way to study synchronized cell populations, which are suitable for modelling cell cycle events. However, cell cycle specific events are obtained under variable experimental conditions and different cell cycle synchronization procedures, which are difficult to reproduce on models. During liver regeneration, liver cells (hepatocytes) divide in a highly synchronized manner. We have taken advantage of the wealth of experimental data on the cell cycle during liver regeneration to construct the first integrative model of the mammalian cell cycle in the regenerating livers.

Liver regeneration is a process by which the liver can recover its normal mass and function following injury. After the surgical removal of two-third of the liver (partial hepatectomy), 90% of the hepatocytes re-enter the cell cycle synchronously to complete one or two divisions and restore the liver mass. Partial hepatectomy (PH) triggers the release of pro-inflammatory cytokines (PICs). In the presence of PICs, hepatocytes leave a quiescent state, denoted G0, to enter a primed state, a process denoted *priming*. Primed cells, which are in the early G1 phase, are then driven by growth factors (GFs) to cross the restriction point, a point of no return beyond which they

* Corresponding author. Tel.: +33 472 44 83 17.
E-mail address: bernard@math.univ-lyon1.fr (S. Bernard).

0022-5193/$ - see front matter © 2011 Elsevier Ltd. All rights reserved.
doi:10.1016/j.jtbi.2011.05.026

Author's personal copy

are irreversibly engaged in the cell cycle and do not require growth factors any more to complete mitosis (Taub, 2004). Progression within the cell cycle is controlled by the sequential activation of a family of cyclin dependent kinases (cdks) that allow an ordered succession of the cell cycle phases: G1, S, G2, and M (Morgan, 2007). The cdk proteins are only active when they form a complex with their corresponding cyclin proteins. Cyclin D/Cdk4-6, Cyclin E/Cdk2, Cyclin A/Cdk2, and Cyclin B/Cdk1 complexes promote, respectively, progression in G1 phase, the transition from G1 to S phase, progression in S and G2 phase, and finally the G2/M phase transition, allowing entry into mitosis (Morgan, 2007). Cyclin/cdk complexes are the workhorses of the cell cycle machinery, and as such, they need regulators. Cyclin/cdk regulation, which we henceforth mention as cyclin regulation for simplicity, is achieved through a variety of mechanisms. These include transcriptional regulation [E2F transcription factor 1 (E2F)], association with protein inhibitors [cyclin dependent kinase inhibitor (CKI)], phosphorylation/dephosphorylation [Wee1 and cell division cycle 25 (Cdc25)] and cyclin degradation [complexes formed with anaphase promoting complex (APC) and Cdc20 homologue 1 (Cdh1) or Cell division cycle 20 (Cdc20) (APC^{Cdh1}, APC^{Cdc20}), Skp1/cullin/F-box protein related complexes (SCF)] (Morgan, 2007) (Fig. 1).

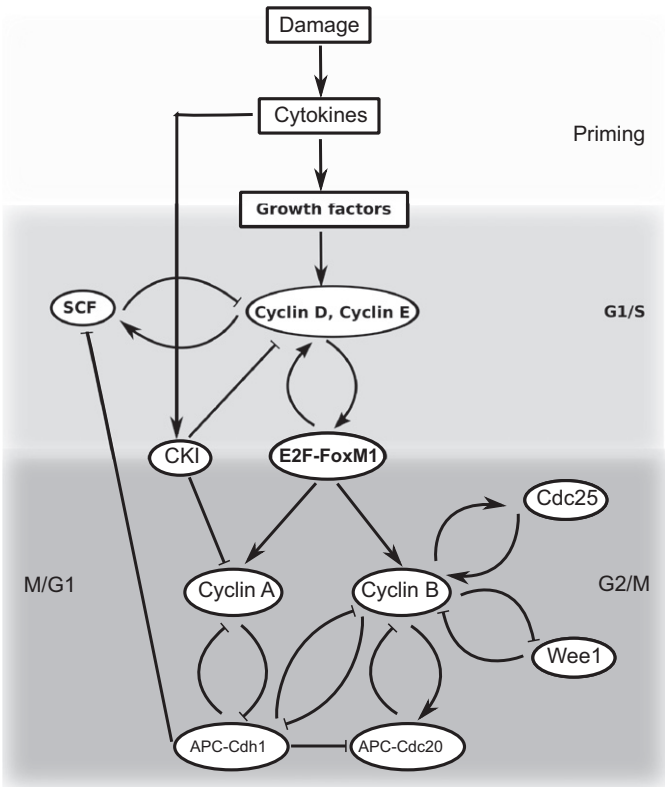

Fig. 1. Damage induced model of the cell cycle during liver regeneration based on sequential cyclin activation and degradation. The PH-induced damage primes quiescent cells via cytokine signaling. Primed cells then activate growth factor-induced signaling cascades. Cytokine- and growth factor-induced pathways act in concert to provide mitogenic signals for Cyclin D activation in early G1 phase. Cyclin D initiates a chain of sequential phosphorylation of Rb/E2F which leads to sequential transcription of further G1-S (Cyclin E), S (Cyclin A) and M (Cyclin B) phase cyclins. As early as G1 phase, stoichiometric inhibitors of cyclins, CKI, are also activated by cytokines. The G1-S proteolytic degradation machinery, SCF, is activated by Cyclin E. Entry to mitosis is initiated by the abrupt activation of Cyclin B by Cdc25 and Wee1 in a positive feedback loop fashion at G2-M transition. Cdc25- and Wee1-mediated positive feedback loops also regulate the rapid exit from mitosis by swiftly inactivating Cyclin B at M-G1 in coordination with a positive feedback loop from the M-G1 degradator APC^{Cdh1}. Mitotic degradator APC^{Cdc20} exerts a negative feedback loop. All cyclin-cdk complexes are depicted by their respective activating cyclin partner for simplicity. E2F in the scheme represents all three forms of E2F, *viz*, unphosphorylated, hypophosphorylated and hyperphosphorylated.

2. The model

DNA synthesis and mitosis: After both PH and CCl_4 treatment, liver regeneration exhibits well-synchronized DNA synthesis and mitosis (Deguchi et al., 2002). The temporal proliferation pattern of the cells in regenerating rodent livers consists of two waves of mitosis (Fabrikant, 1968). During the first round, hepatocytes synchronously undergo DNA replication and mitosis. It is then followed by a second round of division of less synchrony (Faktor, 1971). In mice, the first peak of DNA synthesis occurs 36 h after PH and the mitotic peak, 4–12 h after the peak of DNA synthesis (Matsuo et al., 2003).

E2Fs regulating sequential activation of cyclins: E2F activity is tightly controlled by binding to the retinoblastoma protein (Rb). Rb sequesters E2F and inhibits its transcriptional activity. Cyclins sequentially phosphorylate Rb and activate E2F in a positive feedback loop manner. Only hyperphosphorylated forms of Rb-E2F transactivates Cyclin A and Cyclin B (Lundberg and Weinberg, 1998) (see Appendix A.2 for the derivation of the Rb/E2F equations).

CKI at the interphase of S phase and mitosis: CKI stoichiometrically inhibits Cyclin D, Cyclin E and Cyclin A by forming complexes with their cdk partners (Harper et al., 1995). CKIs are predominantly transcriptionally regulated by cytokine-dependent signaling (Gartel and Tyner, 1999; Coller et al., 2000). For further details on modelling CKI activation refer to (Chauhan et al., 2008). Degradation of CKI is mediated by SCF and APC-Cdc20 (Bashir et al., 2004; Amador et al., 2007). For simplicity, we do not model SCF and/or APC^{Cdc20} dependent degradation of CKI, but use a general degradation term for CKI.

Cyclins: The whole process of cell division is orchestrated by the sequential activation of cyclins. Cyclin D and Cyclin E are the G1-S cyclins that trigger DNA synthesis. G1-S cyclins are induced by cytokine- and growth factor-dependent pathways and their degradation is controlled by SCF. For further details on Cyclin D and Cyclin E modelling refer to (Chauhan et al., 2008). The rise of G1-S cyclins is accompanied by the appearance of Cyclin A during S phase. In the late G2 phase, a transient activation of Cyclin B is observed enabling swift G2-M transition. This transient activation is enabled by regulatory feedbacks imposed on Cyclin B by Cdc25 and Wee1. At metaphase, sufficiently high levels of active Cyclin B phosphorylates Cdc20 to form an active complex with APC, which in turn, degrades Cyclin B. Inactivation of Cyclin B allows mitotic exit and return to the G1 phase (Morgan, 2007). Inactivation of Cyclin B also leads to dephosphorylated Cdh1 which then forms an active complex with APC to degrade Cyclin B and Cyclin A during G1 phase.

APC and SCF: the degradators controlling the cell cycle: APC is a proteasomal degradation machinery that needs to form complexes with subunits to be activated. During the cell cycle, APC is successively activated by two of its subunits, Cdc20 and Cdh1, which have separate windows of activity, each regulated by feedback loops. Cdc20 is activated by Cyclin B during mitosis through a negative feedback loop. Cdh1 becomes active at the end of mitosis through a positive feedback loop, when Cyclin B is degraded, and assembles with APC to further degrade Cyclin A, Cyclin B, Cdc20 and SCF (Wäsch et al., 2010). Cdh1 also acts as a G1 regulator by destroying mitotic cyclins during G1 phase and maintaining the cell in G1 by the destruction of SCF (Bashir et al., 2004; Wei et al., 2004). Cdh1 controls Cyclin A and B at two levels: first by a direct cyclin-Cdh1 double feedback loop and second by a CyclinB-Cdc20 negative feedback. Cdh1 controls G1 cyclins, Cyclin D and E by degrading their degradator SCF.

SCF can degrade G1-S cyclins, Cyclin D and Cyclin E (Nakayama and Nakayama, 2005). SCF is down-regulated during M and G1 phases and is induced by Cyclin E near the S phase when its

Author's personal copy

degradator Cdh1 is degraded (Bashir et al., 2004). Cdh1 connects the SCF-driven G1-S proteolytic machinery with the APC-dependent mitotic and G1 proteolysis. Therefore, at the core of the cell cycle lies Cdh1-driven degradation that results in a proteolytic oscillator setting the pace of the cell cycle progression.

Using the existing knowledge about cyclin control mechanisms and their temporal organization during liver regeneration, we designed the network controlling the cyclin-dependent kinase activity at all stages of the cell cycle (Fig. 1). The model is a system of ordinary differential and algebraic equations describing the concentration of key players of the cell cycle (see Appendix A for a description of the model variables). To make the model as tractable as possible, the variables were sorted according to the time scale on which they evolve. The time-scale of reference is the duration of one cell cycle (in hours). Variables that change on a shorter time-scale were approximated by their steady state (quasi-steady state assumption). For instance, concentrations of phosphorylated proteins were approximated by their steady states. To limit the number of variables in the model, we considered explicitly protein concentrations but not their corresponding mRNA concentrations. The kinetic parameters (see Appendix B) were adjusted so that the model could represent the experimentally observed temporal dynamics of respective model species. The induction of gene expression by pro-inflammatory cytokines, growth factors and by Rb-E2F (here called E2F) was incorporated directly by time-dependent input functions modulating the synthesis of cyclins (see (Chauhan et al., 2008) and Appendix A.2). Post-translational regulation through phosphorylation-dephosphorylation or through complex formation is explicitly included in the model. For simplicity, we do not distinguish between the nuclear and cytosolic compartments of the cell. The model describes the dynamics of the intracellular cyclin/cdk network and represents an average hepatocyte during liver regeneration. Our aim is to address one cycle of division during liver regeneration triggered by a decaying damage (Hayashi et al., 2003; Blindenbacher et al., 2003). All concentrations in the model are expressed in arbitrary units (a.u.) since for most of the regulatory proteins, the actual concentrations are not known.

Numerical simulations of the full model were performed with Matlab. Bistability analysis of the model was done with the numerical bifurcation continuation process of XPPAUT.

3. Results

3.1. Sequential activation of cyclins and proteolytic degradators

The computational model is able to reproduce the sequential activation of cyclins and proteolytic degradators along the cell cycle (Fig. 2). Damage activates cytokine- and growth factor-induced pathways which lead to the activation of Cyclin D during late G1 and the subsequent activation of Cyclin E, indicating entry into S phase (Chauhan et al., 2008). Step-wise activation of E2F via Cyclin D and Cyclin E leads to the sequential transcription of Cyclin A in the S phase and Cyclin B during mitosis (Morgan, 2007) (for equations see Appendix A.2). CKI is activated in early G1 and is maximally elevated at late S phase (Behrens et al., 2002). E2F activity peaks at S phase (Chen et al., 2009). APC^{Cdh1} is active during late mitosis and early G1 phase, degrading Cyclin A and Cyclin B. APC^{Cdc20}, which is a degradator of mitotic substrates, is activated during late mitosis, once Cyclin B is sufficiently activated. Degradator of G1-S cyclins, SCF, becomes active at the end of S phase, leading to the degradation of Cyclin D and Cyclin E. Also, mitotic regulators Cyclin B active, Wee1, Cdc25 and APC^{Cdc20} exhibit a delayed switch-like activation (Morgan, 2007) (Fig. 2).

3.2. A switch in Cyclin B activity drives M phase progression

A switch-like increase in the activity of Cyclin B enables entry into mitosis, whereas subsequent Cyclin B proteolysis promotes exit from mitosis (Morgan, 2007). This switch-like behaviour is made possible by the presence of controls on Cyclin B activation,

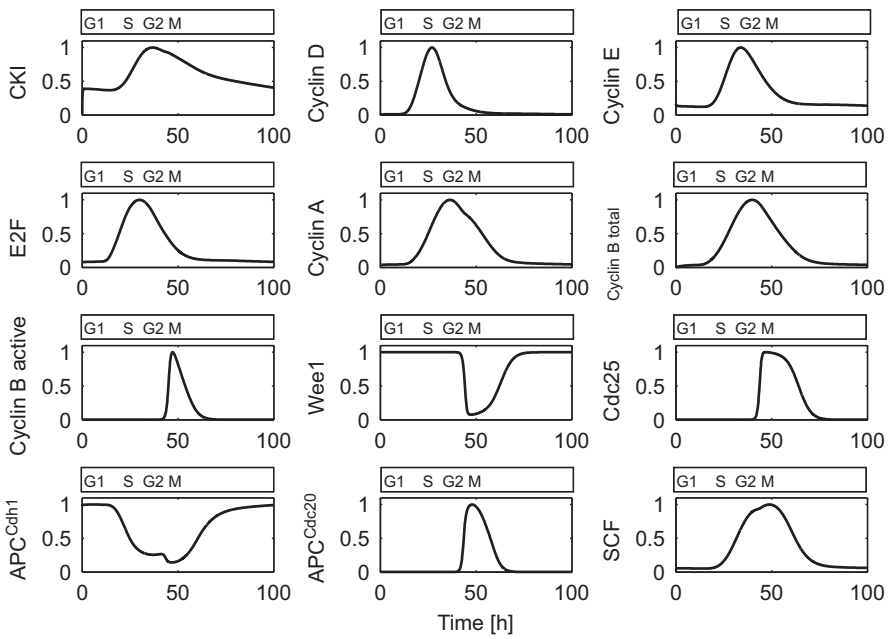

Fig. 2. Sequential activation and degradation of cyclins and their key regulators. Cyclin D appears at the late G1, Cyclin E at the G1-S transition, Cyclin A in the S phase and Cyclin B in the late S phase and mitosis. At the G2-M interface, transient activation of Cyclin B active, Cdc25 and inactivation of Wee1, leads to abrupt mitotic entry. At the M-G1 interface, Cdc25 and Wee1 are, respectively, rapidly inactivated and activated, leading to swift exit from mitosis. APC^{Cdc20} is also transiently activated once enough Cyclin B has accumulated at mitosis. APC^{Cdh1} is active from late mitosis to G1 phase keeping Cyclin A and Cyclin B degraded in a positive feedback loop fashion during late mitosis and G1. SCF is activated by Cyclin E during G1-S phase leading to degradation of G1-S cyclins. All concentrations are normalized by their maximum concentrations.

Author's personal copy

which conserves the total amount of Cyclin B, and on total Cyclin B concentration.

Two feedback loops control Cyclin B activity: a double negative feedback loop from the inhibitory kinase Wee1, which is itself inhibited by Cyclin B, and a positive feedback loop from the activating phosphatase Cdc25, which is further activated by Cyclin B (Tyson et al., 2003). Recently, Potapova et al. (2009) have shown that the exit from mitosis was also a switch phenomenon, due to the Wee1 and Cdc25-dependent positive feedback loops acting during G1 phase.

Total Cyclin B concentration is controlled through synthesis, by E2F, and degradation, by APC^{Cdh1} and APC^{Cdc20}. E2F promotes Cyclin B synthesis. At low E2F activity, there is not enough Cyclin B for any of it to be activated. If E2F reaches a threshold value, Cyclin B gets activated. This threshold activation is achieved through a transcritical bifurcation (Fig. 3a) (Guckenheimer et al., 1997). At any E2F values, two steady states for Cyclin B exist, one zero and one either negative (below the threshold) or positive (above the threshold). The zero steady state is stable below the threshold and the positive steady state is stable above it. This transcritical bifurcation is possible because of the Cdc25 loop. When this loop is switched off by setting Cdc25 to a low constant level (set at 0.01), the transcritical bifurcation disappears. No effect was observed when Wee1 loop was removed (results not shown). Downregulation of APC^{Cdh1} is responsible for the activation of Cyclin B, while APC^{Cdc20} is mainly responsible for its degradation at the exit of mitosis. Varying the strength of the Cdh1-mediated Cyclin B degradation rate, d_{CB}^{Cdh1}, revealed a bistable switch that allows rapid activation and inactivation of Cyclin B (Fig. 3). At high degradation rate, there is a small total amount of Cyclin B, and no active Cyclin B. When the degradation rate is reduced, a second stable steady state appears through a saddle-node bifurcation. These two stable steady states co-exist until the low level steady state becomes unstable, through a reverse pitchfork bifurcation (Guckenheimer et al., 1997). For degradation rates below that level, there is only high Cyclin B activity. This combination of bifurcations form a bistable switch whereby low and high levels of Cyclin B are possible.

Thus, the model includes two mechanisms for controlling Cyclin B activity: a transcritical activation by E2F and a bistable switch induced by APC^{Cdh1}-mediated Cyclin B degradation. The transcritical activation ensures active Cyclin B levels remain to zero whenever total Cyclin B level are low, therefore preventing accidental entry into mitosis. The bistable switch is responsible for the rapid activation of Cyclin B at the entry to mitosis, and its rapid elimination at the end of mitosis.

3.3. Liver regeneration and cell cycle progression are robust processes

Liver regeneration is a robust process. After PH, the liver grows back to its normal mass even in the absence of important cell cycle players. Therefore, we expect Cyclin E and Cyclin B activity, as a measure of total DNA synthesis and mitosis, respectively, to be robustly activated. We analysed the sensitivity of Cyclin E and Cyclin B activity with respect to changes in biochemical parameters. Both Cyclin E and Cyclin B were robust to parameter change except when parameters immediately downstream of the damage, such as degradation of PIC, were varied. In case of these sensitive parameters, Cyclin E and Cyclin B peaks showed a bell-shaped response to systematic variation in these sensitive parameters (results now shown).

We further went on to study the response of the model to systematic changes in the damage. We varied the damage from strong-transient to weak-sustained input keeping the the total amount of damage, i.e. the integral under the curve, constant

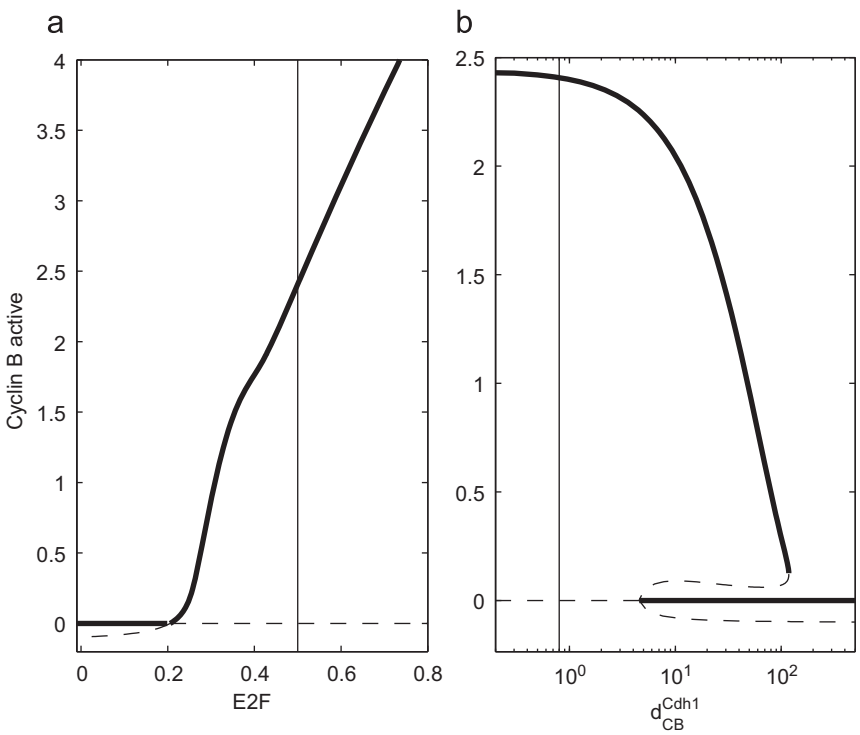

Fig. 3. Threshold activation of Cyclin B driving M phase progression. (a) Bifurcation diagram with respect to E2F activity. Steady states in Cyclin B activity are plotted as a function of E2F activity. At any E2F level, Cyclin B activity has two steady states, one zero and one either negative or positive. The two steady states exchange their stability when they meet. The largest (zero or positive) steady state is always stable and the smallest always unstable. (b) Bifurcation diagram with respect to the degradation rate d_{CB}^{Cdh1}. Steady states in Cyclin B activity are plotted as a function of the degradation rate d_{CB}^{Cdh1}. Over a large range of degradation rates, Cyclin B activity has two stable steady states. In a and b, thick solid lines represent stable steady states and dashed lines, unstable steady states. The vertical lines represent the set values of E2F and d_{CB}^{Cdh1} for the bifurcation diagrams for d_{CB}^{Cdh1} and E2F, respectively.

Author's personal copy

(Fig. 4a). Both DNA synthesis (Cyclin E) and mitosis (Cyclin B) responded as a bandpass filter to such a systematic variation in damage (Fig. 4b and c, upper panels). Weak-sustained and strong-transient damages were rejected and the cells did not progress through both DNA synthesis and mitosis in both cases. The timing of cell cycle events was robust to varying nature of damage (Fig. 4b and c, lower panels).

Bandpass filtering properties have been studied previously in a G1/S model (Chauhan et al., 2008). The damage was transmitted through two pathways: (1) direct ultrasensitive induction of Cyclin E, which filtered out the weak-sustained damages and (2) Cytokine mediated delayed pathway, which consisted of nested feedforward loops. Incoherent feedforward loops via CKI and HGF filtered out sharp-transient damages. In the present model, changing the strength of feedback loops during G2/M/G1 phases did not change bandpass filtering behaviour of the model. However, the range of the bandpass filter was affected. Decreasing the positive feedback loop strength of the Cdh1-Cyclin A loop by reducing the two Cyclin A and Cdh1 mutual negative regulation parameters to one-half, one-fourth and zero, respectively, had two distinct filtering effects: it decreased the range of the filter in case of Cyclin B (Fig. 5b), while for Cyclin E (Fig. 5a), it increased the range of filter. This opposite control of cell cycle events: DNA synthesis (Cyclin E) and mitosis (Cyclin B) with respect to varying damage, has not been systematically studied to our knowledge.

3.4. The circadian clock gates mitosis but not DNA synthesis

Cell division in many mammalian tissues is associated with the circadian clock, a ~ 24 h rhythm regulating physiology and behaviour (Reppert and Weaver, 2002). In hepatocytes, Wee1 is the gatekeeper of this circadian control of cell cycle (Matsuo et al., 2003). Wee1 is a clock-controlled gene (its expression is modulated over 24 h), and regulates the timing and efficiency of the cell cycle. In mice hepatocytes, Wee1 synthesis peaks around ZT12 (ZT0 represents lights on and ZT12, lights off, in a 24 h light-dark cycle) (Matsuo et al., 2003). To simulate the circadian expression of Wee1, we used a sinusoidal-shaped synthesis rate of Wee1, with a maximal synthesis rate at ZT12 (Fig. 6a, see Appendix A.6). We simulated PHs performed on mice at ZT8 or ZT0, and used peak of activity in Cyclin B and E as markers of mitosis and S phase. We found that mitotic activity

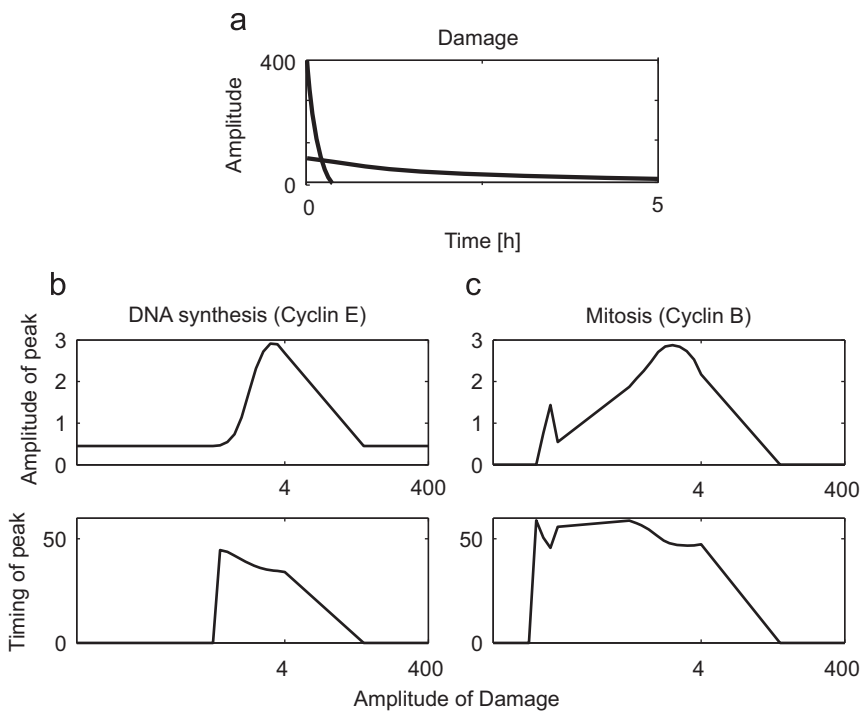

Fig. 4. Bandpass filter characteristics of the model. Both DNA synthesis (Cyclin E) (b, top) and mitosis (Cyclin B) (c, top) exhibit bandpass filtering properties when the damage (a) is changed systematically from weak-sustained damage to strong-transient damage, keeping the total amount of damage constant. Timing remains relatively constant (b and c, bottom).

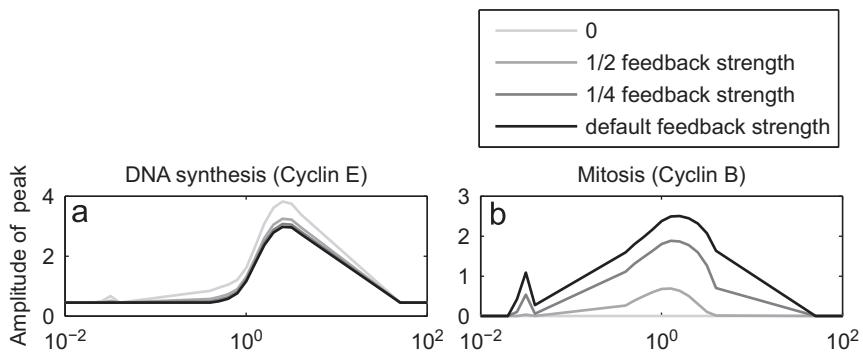

Fig. 5. Opposite bandpass filtering effect on DNA synthesis (a) and mitosis (b) with respect to changing feedback strength of Cdh1-Cyclin A loop.

Author's personal copy

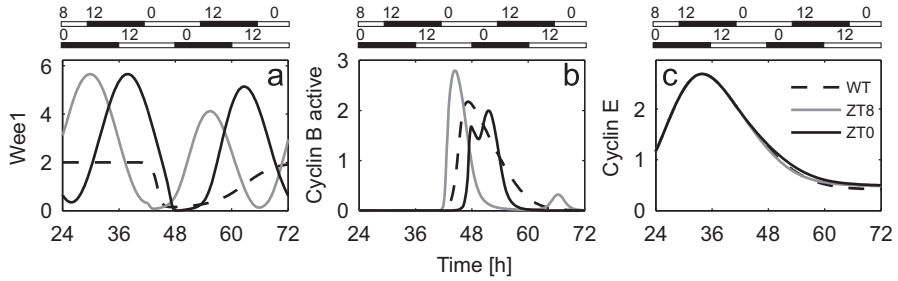

Fig. 6. Wee1 (a) and Cyclin B (b) activity in response to PH performed at different times of the day (ZT8 represents 8 h after light is on; ZT0 represents 0 h after light is on, in a 12 h light-dark cycle). In ZT8 mice, Wee1 peaks 8 h earlier than in ZT0 mice; that leads to a 7.5 h-advanced peak of Cyclin B activity. Cyclin E (c) shows no change in activity between ZT0 and ZT8.

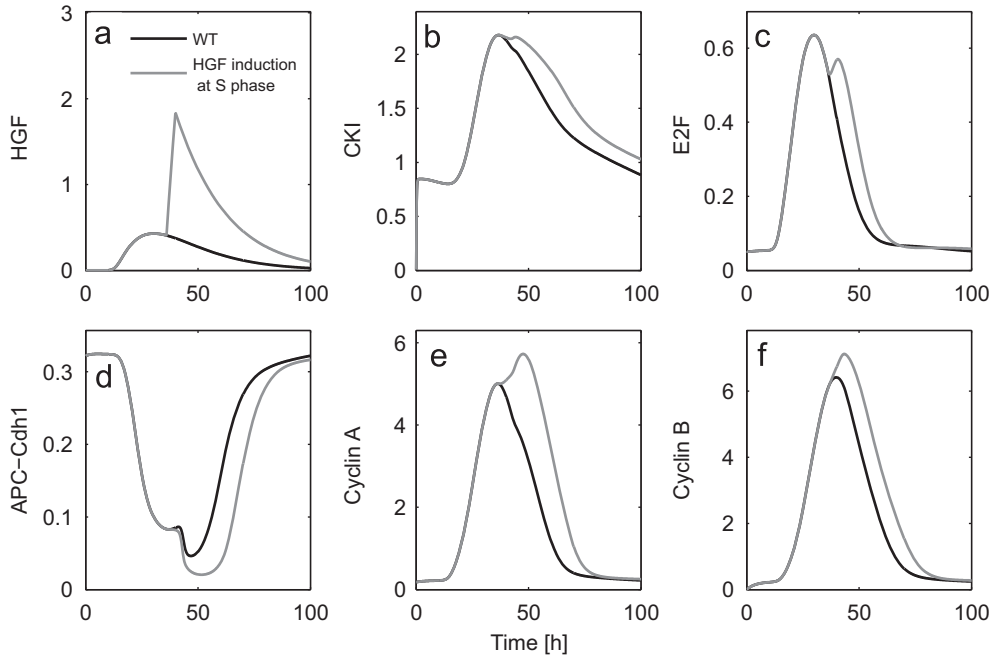

Fig. 7. Growth factor induction at S phase. Induction of HGF at S phase (a) leads to delay in the degradation of Cyclin A (e) and Cyclin B (f). CKI (b), E2F (c) and APC^{Cdh1} (d) contribute together in causing this delayed degradation of G2-M cyclins.

induced by Cyclin B at ZT8 or ZT0 changes from 44.5 to 51.5 h (Fig. 6b). These results reproduce well the gating properties of Wee1 observed experimentally (Matsuo et al., 2003).

In our model, DNA synthesis is directly coupled to mitosis via a Cdh1-SCF loop. Nevertheless, Cyclin E activity, which is representative of DNA replication, was independent from Zeitgeber time PH (Fig. 6c). Imposition of circadian control on Wee1 maintains DNA synthesis as an independently controlled property of hepatocytes (Matsuo et al., 2003).

3.5. HGF treatment at S phase causes prolonged Cyclin A and Cyclin B activity

Growth factors are well known to promote the transition from G1 to S phase in cell cycle progression. Beyond G1-S transition though, growth factors have been considered non-essential during the cell cycle (Jones and Kazlauskas, 2001). However, when injected at S and G2 phases, hepatocyte growth factor induces a prolongation of G2. Increased ERK activation and delayed degradation of Cyclin A and Cyclin B are observed when the cells are induced with HGF at S and G2 phase (Park et al., 2007; Nam et al., 2008). It is not intuitive how HGF induction at S phase might lead to delayed degradation of Cyclin A and Cyclin B, but CKI up-regulation has been implicated (Dangi et al., 2006).

We went on to simulate growth factor induction at S phase by giving an extra HGF pulse during S phase between 36 and 40 h (see Appendix A.7). Our model was able to reproduce the observed delay in the degradation of Cyclin A and Cyclin B (Fig. 7e and f). Our simulations suggest that HGF treatment at S phase prolongs CKI (Fig. 7b) and E2F-FoxM1 (Fig. 7c) expression and delays APC^{Cdh1} activation (Fig. 7d). Thus, growth factor leads to E2F-FoxM1 dependent Cyclin A up-regulation. As long as Cyclin A is active at G2, APC-Cdh1 cannot be activated due to its antagonistic control by Cyclin A. This leads to delayed Cdh1 activation. Delayed Cdh1 activation leads to delayed degradation of Cyclin A and Cyclin B (Fig. 7b–d). More recently, CKI (Dangi et al., 2006), FoxM1 (Alvarez-Fernandez et al., 2010) and APC^{Cdh1} (Holt et al., 2010) have been directly implicated in G2 arrest. CKI and FoxM1 are activated through growth factor induced MAPK signaling at G2 (Dangi et al., 2006; Ma et al., 2005).

4. Discussion

4.1. Computational model for mammalian cell cycle

We have developed a computational model for the cell cycle of hepatocytes during liver regeneration that couples different

Author's personal copy

cyclins and proteolytic degradators in a sequential manner. The model recapitulates the temporal profile of dividing hepatocytes following partial hepatectomy: the sequential activation of cyclins and proteolytic degradators; the effect of the circadian clock on the timing of mitosis; the G2 phase delay caused by HGF treatment during S phase and the effect of Cdh1 on cell cycle progression.

Gerard and Goldbeter (2009) recently presented a mammalian cell cycle model describing the sequential cyclin-cdk activation. The model demonstrates repetitive cell cycling in the presence of suprathreshold amounts of growth factors. The emphasis was on the Rb-E2F network during G1 phase and Cyclin A-dependent activation of Cyclin B during mitotic entry. Our model is also structurally able to generate sustained oscillations like many other cell cycle models (Csikasz-Nagy et al., 2006; Gerard and Goldbeter, 2009). However, the focus of the model presented here is to simulate one or two cycles of cell division observed during liver regeneration after injury.

4.2. Threshold activation of Cyclin B

Entry to and exit from M phase display a switch-like behaviour in Cyclin B levels. It is rapidly switched on at the G2-M phase transition and rapidly switched off at the end of mitosis. Threshold activation provides a robust mechanism for switch. We have shown that total Cyclin B concentration and activity is regulated by two threshold processes: a transcritical bifurcation, mediated by E2F and a bistable loop, mediated by APC^{Cdh1}. Both the transcritical bifurcation and the bistable loop allowed active Cyclin B to be kept at zero levels outside the specific time window of activity during G2/M phases. Although transcritical activation is qualitatively different from a bistable switch, it also provides a sharp activation threshold.

4.3. Bandpass filter of damage input

The model exhibits bandpass filter properties which allows the system to ignore strong-transient and weak-sustained damages (Chauhan et al., 2008). Thus, if the damage is too transient (short) or too weak, cells will not enter the cell cycle events of DNA synthesis and mitosis. This is in agreement with observations that liver regeneration is proportional to the amount of PH, but does not occur if the PH is too small or too large (Lambotte et al., 1997). Also, varying the feedback strength of the Cdh1-Cyclin A positive feedback loop in the model tunes the range of filtering for Cyclin E and Cyclin B in an opposite manner. Such an opposite control of DNA synthesis and mitosis with varying strength of the Cdh1-Cyclin A positive feedback loop has not been systematically studied to our knowledge. Opposite control of filtering range for Cyclin E and Cyclin B can have some interesting physiological implications. Certain environmental conditions promote DNA synthesis while suppressing mitosis, inducing endoreplication and polyploidization (Nevzorova et al., 2009). Cdh1-mediated control of cyclins during endoreplication has been widely reported in mammals, Drosophila and plants (Garcia-Higuera et al., 2008; Sorensen et al., 2000; Sigrist and Lehner, 1997; Kasili et al., 2010). It would be interesting to study Cdh1-mediated feedback loop control of cell cycle with respect to endoreplication and polyploidization, which are common forms of cell cycle progression during liver regeneration (Duncan et al., 2010).

4.4. Circadian control of Wee1

Our model is consistent with a circadian control of Wee1 synthesis, affecting the timing of mitosis but not of DNA synthesis. When the entrainment to light-dark cycle is simulated by varying Wee1 synthesis with a 24 h period, the time at which PH is performed has a impact on the timing of mitosis. In agreement with Matsuo et al. (2003) results, we found that in PH performed at ZT0 and ZT8 (at lights on and 8 h later, respectively), cells enter mitosis roughly at the same time (around 60 h after ZT0). This shows that circadian regulation of Wee1 induces a gating process by which cells cannot divide at any time of the day. The timing of DNA synthesis was independent from the timing of PH, and occurred 36 h after PH, coherent with experimental results. In hepatocytes, Wee1 is a major link between the circadian clock and the cell cycle and S phase is largely a circadian clock-independent process, despite the presence of a feedback loop linking G1/S and G2/M phases via Cdh1 and SCF. In continuously dividing cells this independence might not be preserved as gating mitosis might affect subsequent phases.

4.5. HGF treatment during S phase causes prolonged G2/M phase

HGF promotes and accelerates cell cycle progression but has been mostly assumed to be non-essential beyond the G1-S transition. However, HGF injection during S phase leads to a prolongation of G2 resulting in the delayed degradation of cyclins during G2-M phase. The model was able to reproduce the prolonged activation of Cyclin A and Cyclin B, caused by a delayed reactivation of APC^{Cdh1} during M phase. Moreover, activation of Cyclin A and Cyclin B was not delayed after HGF injection, consistent with experimental results (Nam et al., 2008). The delay in G2-M transition is explained by a delay in Cyclin B-associated kinase activity, due to a delay in nuclear translocation. Our model is not refined enough to reproduce intracellular compartimentalization results, although it is consistent with total Cyclin B time courses.

Erk signaling is known to mediate G2 delay via CKI (Han et al., 2005; Dangi et al., 2006; Park et al., 2007). Our simulations suggest that CKI, APC^{Cdh1} and E2F-FoxM1 contribute in delaying the degradation of Cyclin A and Cyclin B. This leads us to the conclusion that induction of growth factors during S phase might lead to prolonged transcriptional activity of E2F-FoxM1 resulting in increased Cyclin A activity. Since the antagonistic players Cyclin A and APC^{Cdh1} cannot coexist, APC^{Cdh1} activation is delayed. Thus the APC^{Cdh1}-dependent degradation machinery might also be responsible for the delayed Cyclin A and Cyclin B degradation during G2 phase delay.

4.6. Conclusion

Mounting evidences demonstrate that Cdh1 plays an important role in the control of proliferation, differentiation and maintenance of genomic integrity by timely and coordinated degradation of several substrates (Wäsch et al., 2010). Cdh1 maintains the stability of G1 phase by degrading the degradator of G1-S cyclins and SCF. Cdh1 is required for the G2 DNA-damage checkpoint (Wäsch et al., 2010). Cdh1 is implicated in genomic instability and cancers, and is under investigation as a therapeutic target. Cdh1 also plays a role in specialised cell division cycles of endoreplication and polyploidy, widely observed during liver regeneration. These observations call for a better characterization of the role of Cdh1 in the control of G2 phase. It will be interesting to refine the model presented here around Cdh1 in order to understand the G2 delay and get a better understanding of the fate of the cell division cycle.

Acknowledgments

AC was supported by the German Ministry Federal Ministry of Education and Research (BMBF, Hepatosys, 0313078A) and by SFB

Author's personal copy

618 Grant of the Deutsche Forschungsgesellschaft (DFG). SL was supported by the German Ministry Federal Ministry of Education and Research (BMBF, Hepatosys, 0313078A). SB was supported by the Project-Team INRIA Dracula (France), the French National Research Agency (ProCell, ANR-09-JCJC-0100-01), and acknowledges support from Rhône-Alpes Complex Systems Institute (IXXI, France). We thank two anonymous reviewers for their useful suggestions.

Appendix A. Model equations

The model contains 25 dynamical variables and 84 parameters. The 25 variables are the concentrations of the following players involved in the cell cycle control: Damage (D) induced pro-inflammatory cytokine pathways (PIC and PGE); pro-inflammatory cytokine induced growth factor pathways (PAI, HGF, HB-EGF); Cyclins D, E, A, and B; the inhibitor CKI and its complexes with the active cyclin-cdk complexes; the active and inactive forms of phosphatase Cdc25 and of kinase Wee1; the SCF proteasomal ligases involved in the degradation of cyclin D, Cyclin E and CKI; and the active and inactive forms of the proteins Cdh1 and Cdc20 involved in the degradation of cyclins A and B.

A.1. G1-S model

$$[D] = I_0 \cdot e^{-d_0 \cdot t} \tag{A.1}$$

$$\frac{d[PIC]}{dt} = \frac{v_1}{1+\left(\frac{[PGE]}{k_1^-}\right)^2} \cdot \frac{[D]}{k_1+[D]} - d_1 \cdot [PIC] \tag{A.2}$$

$$\frac{d[PGE]}{dt} = v_2 \cdot [PIC] - d_2 \cdot [PGE] \tag{A.3}$$

$$\frac{d[IEG]}{dt} = \frac{v_3 \cdot [PIC]^3}{k_3^3+[PIC]^3} - d_3 \cdot [IEG] \tag{A.4}$$

$$\frac{d[PAI]}{dt} = \frac{v_4 \cdot [PIC]^3}{k_4^3+[PIC]^3} - d_4 \cdot [PAI] \tag{A.5}$$

$$\frac{d[HGF]}{dt} = \frac{v_5 \cdot [IEG]}{1+\left(\frac{[PAI]}{k_5^-}\right)^4} \cdot \left(1+\frac{f_5 \cdot [HGF]}{k_5+[HGF]}\right) - d_5[HGF] \tag{A.6}$$

$$\frac{d[HBEGF]}{dt} = v_6 \cdot \frac{[D]^4}{k_{61}^4+[D]^4} \cdot \frac{[IEG]}{k_{62}+[IEG]} \cdot \frac{[HGF]}{k_{63}+[HGF]} \tag{A.7}$$

$$-d_6[HBEGF] \tag{A.8}$$

$$\frac{d[CKI]}{dt} = v_7 \cdot \frac{PIC}{k_7+PIC} - d_7 \cdot [CKI] - \frac{d[CycD|CKI]}{dt} - \frac{d[CycE|CKI]}{dt} - \frac{d[CycA|CKI]}{dt} \tag{A.9}$$

$$\frac{d[CycD]}{dt} = \frac{v_8 \cdot [IEG] \cdot [HGF]}{k_8+[IEG]} + d_{10} \cdot [CycD|CKI] - (d_8 \cdot [SCF] + v_{10} \cdot [CKI]) \cdot [CycD] \tag{A.10}$$

$$\frac{d[CycE]}{dt} = \frac{v_{91} \cdot [HBEGF]^2}{k_{91}^2+[HBEGF]^2} + \frac{v_{92} \cdot [CycD]^4}{k_{92}^4+[CycD]^4} + d_{11} \cdot [CycE|CKI] - (d_9 \cdot [SCF] + v_{11} \cdot [CKI]) \cdot [CycE] \tag{A.11}$$

$$\frac{d[CycD|CKI]}{dt} = v_{10}[CKI][CycD] - d_{10}[CycD|CKI] \tag{A.12}$$

$$\frac{d[CycE|CKI]}{dt} = v_{11}[CKI][CycE] - d_{11}[CycE|CKI] \tag{A.13}$$

$$\frac{d[SCF]}{dt} = v_{12} \cdot CycE - d_{122} \cdot SCF \cdot [APC|Cdh1] - d_{12} \cdot SCF \tag{A.14}$$

A.2. E2F steady state

Rb phosphorylation is initiated by Cyclin D, releasing E2F in sufficient quantity for Cyclin E activation. Cyclin E further phosphorylates Rb (Rb_P) resulting in hyperphosphorylated Rb_{pp}, releasing higher amounts of E2F required for transcriptional activation of further Cyclins. Phosphorylation/dephsophorylation reactions of Rb and association/dissociation of its three phosphorylated forms with E2F are fast enough to be in the steady state equilibrium:

$$[Rb_T] = [Rb] + [Rb_p] + [Rb_{pp}] + [Rb \cdot E2F] + [Rb_p \cdot E2F] + [Rb_{pp} \cdot E2F]$$

$$[E2F_T] = [E2F] + [Rb \cdot E2F] + [Rb_p \cdot E2F] + [Rb_{pp} \cdot E2F]$$

$$[Rb_p] = p_1 \cdot [Rb] \cdot [CycD]$$

$$[Rb_{pp}] = p_1 p_2 \cdot [Rb] \cdot [CycD] \cdot [CycE]$$

$$[Rb \cdot E2F] = k_1 \cdot [Rb] \cdot [E2F]$$

$$[Rb_p \cdot E2F] = p_1 k_2 \cdot [Rb] \cdot [CycD] \cdot [E2F]$$

$$[Rb_{pp} \cdot E2F] = p_1 p_2 k_3 \cdot [Rb] \cdot [CycD] \cdot [CycE] \cdot [E2F]$$

Substituting the steady state values, we solve the equation for E2F as

$$E2F = -\frac{Rb_T - E2F_T + C}{2} + \sqrt{\frac{(Rb_T - E2F_T + C)^2}{4} + C} \tag{A.15}$$

where

$$C = \frac{1 + p_1 \cdot [CycD] + p_1 p_2 \cdot [CycD] \cdot [CycE]}{k_1 + k_2 p_1 \cdot [CycD] + k_3 p_1 p_2 \cdot [CycD] \cdot [CycE]}$$

A.3. APC steady state

$$[APC_T] = [APC] + [APC|Cdh1] + [APC|Cdc20_p] \tag{A.16}$$

$$[APC|Cdh1] = k_{APC}^{Cdh1} \cdot [Cdh1] \cdot [APC] \tag{A.17}$$

$$[APC|Cdc20_p] = k_{APC}^{Cdc20} \cdot [Cdc20_p] \cdot [APC] \tag{A.18}$$

Substituting the steady state values, we solve the equation for APC as

$$[APC] = \frac{[APC_T]}{1 + k_{APC}^{Cdh1} \cdot [Cdh1] + k_{APC}^{Cdc20} \cdot [Cdc20_p]} \tag{A.19}$$

A.4. Cyclin B steady state

Cyclin B exists in two forms in our model: $CycB_{act}$ (active Cyclin B) and $CycB_{inact}$ (inactive Cyclin B). Inactive Cyclin B equation is adapted from Pomerening et al. (2005) with the simplification that the phosphorylation/dephosphorylation of the three inactive forms of Cyclin B *viz* transcribed Cyclin B (*CycB*), Tyrosine phosphorylated ($CycB^Y$), and Tyrosine and Threonine phosphorylated ($CycB^{YT}$) is fast enough to be always in equilibrium; so that equation for $CycB^{YT}$ can be algebraically

Author's personal copy

solved:

$$[CycB_{inact}] = [CycB] + [CycB^{Y}] + [CycB^{YT}] \tag{A.20}$$

$$[CycB] = k_2 \cdot \frac{[Cdc25_p]}{[Wee1]} \cdot [CycB^{Y}] \tag{A.21}$$

$$[CycB^{Y}] = k_1 \cdot \frac{CycB^{YT}}{Wee1} \tag{A.22}$$

$$[CycB^{YT}] = \frac{CycB_{inact} \cdot Wee1^2}{Wee1^2 + k1 \cdot Wee1 + k1 \cdot k2 \cdot Cdc25_p} \tag{A.23}$$

A.5. Mitosis

$$\frac{d[CycA]}{dt} = v_{CA}^{E2F} \cdot E2F - d_{CA}^{Cdh1} \cdot [APC|Cdh1] \cdot [CycA] - d_{CA} \cdot [CycA] - \frac{d[CycA|CKI]}{dt} \tag{A.24}$$

$$\frac{d[CycA|CKI]}{dt} = v_{CA}^{CKI} \cdot [CycA] \cdot [CKI] - d_{CA}^{CKI} \cdot [CycA|CKI] \tag{A.25}$$

$$\frac{d[CycB_{inact}]}{dt} = v_{CB}^{E2F} \cdot E2F - k_{a1} \cdot [Cdc25_p] \cdot [CycB^{YT}] + P_{CB}^{Wee1} \cdot [Wee1] \cdot [CycB_{act}] - d_{CB}^{Cdh1} \cdot [APC|Cdh1] \cdot [CycB_{inact}] - d_{CB}^{Cdc20} \cdot [APC|Cdc20_p] \cdot [CycB_{inact}] - d_{CB} \cdot [CycB_{inact}] \tag{A.26}$$

$$\frac{d[CycB_{act}^{T}]}{dt} = -P_{CB}^{Wee1} \cdot [Wee1] \cdot [CycB_{act}] + k_{a1} \cdot [Cdc25_p] \cdot [CycB^{YT}] - d_{CB}^{Cdh1} \cdot [APC|Cdh1] \cdot [CycB_{act}] - d_{CB}^{Cdc20} \cdot [APC|Cdc20_p] \cdot [CycB_{act}] - d_{CB} \cdot [CycB_{act}] \tag{A.27}$$

$$\frac{d[Wee1]}{dt} = Wee1_b - P_{Wee1}^{CB} \cdot [CycB_{act}] \cdot [Wee1] + P_{Wee1}^{dephos} \cdot [Wee1_p] - d_{Wee1} \cdot [Wee1] \tag{A.28}$$

$$\frac{d[Wee1_p]}{dt} = P_{Wee1}^{CB} \cdot [CycB_{act}] \cdot [Wee1] - P_{Wee1}^{dephos} \cdot [Wee1_p] - d_{Wee1} \cdot [Wee1_p] \tag{A.29}$$

$$\frac{d[Cdc25]}{dt} = Cdc25_b - P_{Cdc25}^{CB} \cdot [CycB_{act}] \cdot [Cdc25] + p_{Cdc25}^{dephos} \cdot [Cdc25_p] - d_{Cdc25} \cdot [Cdc25] \tag{A.30}$$

$$\frac{d[Cdc25_p]}{dt} = P_{Cdc25}^{CB} \cdot [CycB_{act}] \cdot [Cdc25] - P_{Cdc25}^{dephos} \cdot [Cdc25_p] - d_{Cdc25} \cdot [Cdc25_p] \tag{A.31}$$

$$\frac{d[Cdh1]}{dt} = Cdh1_b - P_{Cdh1}^{CA} \cdot [CycA] \cdot [Cdh1] - P_{Cdh1}^{CB} \cdot [CycB_{act}] \cdot [Cdh1] + P_{Cdh1}^{dephos} \cdot [Cdh1_p] - k_{Cdh1} \cdot [APC] \cdot [Cdh1] - d_{Cdh1} \cdot [Cdh1] \tag{A.32}$$

$$\frac{d[Cdh1_p]}{dt} = P_{Cdh1}^{CA} \cdot [CycA] \cdot [Cdh1] + P_{Cdh1}^{CB} \cdot [CycB_{act}] \cdot [Cdh1] - P_{Cdh1}^{dephos} \cdot [Cdh1_p] - d_{Cdh1} \cdot [Cdh1_p] \tag{A.33}$$

$$\frac{d[Cdc20]}{dt} = Cdc20_b - P_{Cdc20}^{CB} \cdot [CycB_{act}] \cdot [Cdc20] + p_{Cdc20}^{dephos} \cdot [Cdc20_p] - d_{Cdc20}^{Cdh1} \cdot [APC|Cdh1] \cdot [Cdc20] - d_{Cdc20} \cdot [Cdc20] \tag{A.34}$$

$$\frac{d[Cdc20_p]}{dt} = P_{Cdc20}^{CB} \cdot [CycB_{act}] \cdot [Cdc20] - P_{Cdc20}^{dephos} \cdot [Cdc20_p] - d_{Cdc20}^{Cdh1} \cdot [APC|Cdh1] \cdot [Cdc20_p] - k_{Cdc20} \cdot [APC] \cdot [cdc20_p] - d_{Cdc20} \cdot [Cdc20_p] \tag{A.35}$$

A.6. Wee1 gated circadian regulation

$$\frac{d[Wee1]}{dt} = Wee1_c \cdot (1 + sin(2\pi/24 \cdot (t-6))) - P_{Wee1}^{CB} \cdot [CycB_{act}] \cdot [Wee1] + P_{Wee1}^{dephos} \cdot [Wee1_p] - d_{Wee1} \cdot [Wee1] \tag{A.36}$$

A.7. HGF injection

$$d[HGF] = \frac{V_{HGF}^{IEG} \cdot [IEG]}{1 + \left(\frac{[PAI]}{Km_{HGF}^{PAI}4}\right)} \cdot \left(1 + \frac{f \cdot [HGF]}{Km_{HGF}^{IEG} + [HGF]}\right) - d_{HGF} \cdot [HGF] + hgfs \cdot (t < 40) \cdot (t > 36) \tag{A.37}$$

Appendix B. Parameters

G_1–S	v_6 15	d_{12} 0.025	k_1 0.03	P_{Cdh1}^{dephos} 0.01
I_0 4	k_{61} 0.9	d_{122} 0.75	k_2 5	k_{Cdh1} 0.1
d_0 0.05	k_{62} 0.0005	**E2F**	k_{a1} 60	$Cdc20_b$ 15
v_1 1.5	k_{63} 1.0	$E2F_T$ 0.05	v_{CB}^{E2F} 1.2	d_{Cdc20} 0.005
k_1^- 0.9	d_6 0.05	Rb_T 1	d_{CB} 0.01	d_{Cdc20}^{Cdh1} 20
k_1 0.5	v_7 8	$p1$ 3	d_{CB}^{Cdh1} 0.8	P_{Cdc20}^{CB} 10
d_1 0.5	d_7 8	p_2 4	d_{CB}^{Cdc20} 0.2	P_{Cdc20}^{dephos} 0.01
v_2 0.6	v_8 3	k_1 25	P_{CB}^{Wee1} 8	k_{Cdc20} 0.1
d_2 0.006	k_8 0.001	k_2 1	$Wee1_b$ 1	**HGF injection**
v_3 4.5	d_8 0.03	k_3 0.1	d_{Wee1} 0.5	$hgfs$ 0.4
k_3 0.7	v_{91} 5	**APC**	P_{Wee1}^{CB} 3	**Wee1–gated**
d_3 6	k_{91} 30	APC_T 1	P_{Wee1}^{dephos} 0.02	$Wee1_c$ 1.5
v_4 45	v_{92} 5	k_{APC}^{Cdh1} 0.5	$Cdc25_b$ 0.03	$dphos_{Cdc25}$ 0.3
k_4 0.5	k_{92} 30	k_{APC}^{Cdc20} 0.1	d_{Cdc25} 0.2	**Bifurcation E2F**
d_4 6	d_9 0.01	**Mitosis**	P_{Cdc25}^{CB} 5	D 4
v_5 5	v_{10} 0.008	v_{CA}^{E2F} 1.75	P_{Cdc25}^{dephos} 0.3	**Bifurcation Cdh1**
f_5 5	d_{10} 0.0008	d_{CA}^{Cdh1} 1	$Cdh1_b$ 0.2	D 4
k_5 0.25	v_{11} 2	d_{CA} 0.1	d_{Cdh1} 0.1	$E2F$ 0.5
k_5^- 0.18	d_{11} 6	v_{CA}^{CKI} 0.01	P_{Cdh1}^{CA} 0.2	
d_5 0.05	v_{12} 0.56	d_{CA}^{CKI} 0.1	P_{Cdh1}^{CB} 0.01	

References

Aguda, B.D., Tang, Y., 1999. Cell Prolif. 32 (5), 321.

Alvarez-Fernandez, M., Halim, V., Krenning, L., Aprelia, M., Mohammed, S., Heck, A., Medema, R., 2010. EMBO Report.

Amador, V., Ge, S., Santamaria, P.G., Guardavaccaro, D., Pagano, M., 2007. Mol. Cell 27 (3), 462.

Bashir, T., Dorrello, N.V., Amador, V., Guardavaccaro, D., Pagano, M., 2004. Nature 428 (6979), 190.

Author's personal copy

Behrens, A., Sibilia, M., David, J.-P., Möhle-Steinlein, U., Tronche, F., Schütz, G., Wagner, E.F., 2002. EMBO J. 21 (7), 1782 (c-jun cyclineD).
Blindenbacher, A., Wang, X., Langer, I., Savino, R., Terracciano, L., Heim, M.H., 2003. Hepatology 38 (3), 674.
Chauhan, A., Legewie, S., Westermark, P.O., Lorenzen, S., Herzel, H., 2008. J. Theor. Biol. 252 (3), 465.
Chen, H.-Z., Tsai, S.-Y., Leone, G., 2009. Nat. Rev. Cancer. 9 (11), 785.
Chen, K.C., Calzone, L., Csikasz-Nagy, A., Cross, F.R., Novak, B., Tyson, J.J., 2004. Mol. Biol. Cell 15 (8), 3841.
Coller, H.A., Grandori, C., Tamayo, P., Colbert, T., Lander, E.S., Eisenman, R.N., Golub, T.R., 2000. Proc. Natl. Acad. Sci. USA 97 (7), 3260.
Csikasz-Nagy, A., Battogtokh, D., Chen, K.C., Novak, B., Tyson, J.J., 2006. Biophys. J. 90 (12), 4361.
Dangi, S., Chen, F.M., Shapiro, P., 2006. Cell Prolif. 39 (4), 261.
Deguchi, M., Shiraki, K., Inoue, H., Okano, H., Ito, T., Yamanaka, T., Sugimoto, K., Sakai, T., Ohmori, S., Murata, K., Furusaka, A., Hisatomi, H., Nakano, T., 2002. Biochem. Biophys. Res. Commun. 297 (1), 59.
Duncan, A.W., Taylor, M.H., Hickey, R.D., Hanlon Newell, A.E., Lenzi, M.L., Olson, S.B., Finegold, M.J., Grompe, M., 2010. Nature 467 (7316), 707.
Fabrikant, J.I., 1968. J. Cell Biol. 36 (3), 551.
Faktor, V.M., 1971. Biull. Eksp. Biol. Med. 72 (9), 97.
Garcia-Higuera, I., Manchado, E., Dubus, P., Canamero, M., Mendez, J., Moreno, S., Malumbres, M., 2008. Nat. Cell Biol. 10 (7), 802.
Gartel, A.L., Tyner, A.L., 1999. Exp. Cell Res. 246 (2), 280.
Gerard, C., Goldbeter, A., 2009. Proc. Natl. Acad. Sci. USA 106 (51), 21643.
Goldbeter, A., 1991. Proc. Natl. Acad. Sci. USA 88 (20), 9107.
Guckenheimer, J., Harris-Warrick, R., Peck, J., Willms, A., 1997. J. Comput. Neurosci. 4 (3), 257.
Han, J., Tsukada, Y.-i., Hara, E., Kitamura, N., Tanaka, T., 2005. J. Biol. Chem. 280 (36), 31548.
Harper, J.W., Elledge, S.J., Keyomarsi, K., Dynlacht, B., Tsai, L.H., Zhang, P., Dobrowolski, S., Bai, C., Connell-Crowley, L., Swindell, E., 1995. Mol. Biol. Cell 6 (4), 387.
Hayashi, E., Yasui, A., Oda, K., Nagino, M., Nimura, Y., Nakanishi, M., Motoyama, N., Ikeda, K., Matsuura, A., 2003. J. Surg. Res. 111 (2), 196.
Holt, J.E., Weaver, J., Jones, K.T., 2010. Development 137 (8), 1297.
Jones, S.M., Kazlauskas, A., 2001. FEBS Lett. 490 (3), 110.
Kasili, R., Walker, J.D., Simmons, L.A., Zhou, J., De Veylder, L., Larkin, J.C., 2010. Genetics 185 (1), 257.
Lambotte, L., Saliez, A., Triest, S., Tagliaferri, E.M., Barker, A.P., Baranski, A.G., 1997. Am. J. Physiol. 273 (4 Pt 1), G905.
Lundberg, A.S., Weinberg, R.A., 1998. Mol. Cell Biol. 18 (2), 753.
Ma, R.Y.M., Tong, T.H.K., Cheung, A.M.S., Tsang, A.C.C., Leung, W.Y., Yao, K.-M., 2005. J. Cell Sci. 118 (Pt 4), 795.
Matsuo, T., Yamaguchi, S., Mitsui, S., Emi, A., Shimoda, F., Okamura, H., 2003. Science 302 (5643), 255.
Morgan, D.O., 2007. The Cell Cycle: Principles of Control. New Science Press in association with Oxford University Press, London.
Nakayama, K.I., Nakayama, K., 2005. Semin. Cell Dev. Biol. 16 (3), 323.
Nam, H.-J., Kim, S., Lee, M.-W., Lee, B.-S., Hara, T., Saya, H., Cho, H., Lee, J.-H., 2008. Cell Signal. 20 (7), 1349.
Nevzorova, Y.A., Tschaharganeh, D., Gassler, N., Geng, Y., Weiskirchen, R., Sicinski, P., Trautwein, C., Liedtke, C., 2009. Gastroenterology 137 (2), 691.
Novak, B., Tyson, J.J., 1993. J. Cell Sci. 106 (Pt 4), 1153.
Novak, B., Tyson, J.J., 2004. J. Theor. Biol. 230 (4), 563.
Park, Y.Y., Nam, H.-J., Lee, J.-H., 2007. Biochem. Biophys. Res. Commun. 356 (1), 300.
Pomerening, J.R., Kim, S.Y., Ferrell, J.E.J., 2005. Cell 122 (4), 565.
Pomerening, J.R., Sontag, E.D., Ferrell, J.E.J., 2003. Nat. Cell Biol. 5 (4), 346.
Potapova, T.A., Daum, J.R., Byrd, K.S., Gorbsky, G.J., 2009. Mol. Biol. Cell 20 (6), 1737.
Qu, Z., MacLellan, W.R., Weiss, J.N., 2003a. Biophys. J. 85 (6), 3600.
Qu, Z., Weiss, J.N., MacLellan, W.R., 2003b. Am. J. Physiol. Cell Physiol. 284 (2), C349.
Reppert, S.M., Weaver, D.R., 2002. Nature 418 (6901), 935.
Sha, W., Moore, J., Chen, K., Lassaletta, A.D., Yi, C.-S., Tyson, J.J., Sible, J.C., 2003. Proc. Natl. Acad. Sci. USA 100 (3), 975.
Sigrist, S.J., Lehner, C.F., 1997. Cell 90 (4), 671.
Sorensen, C.S., Lukas, C., Kramer, E.R., Peters, J.M., Bartek, J., Lukas, J., 2000. Mol. Cell Biol. 20 (20), 7613.
Swat, M., Kel, A., Herzel, H., 2004. Bioinformatics 20 (10), 1506.
Taub, R., 2004. Nat. Rev. Mol. Cell Biol. 5 (10), 836.
Tyson, J.J., 1991. Proc. Natl. Acad. Sci. USA 88 (16), 7328.
Tyson, J.J., Chen, K.C., Novak, B., 2003. Curr. Opin. Cell Biol. 15 (2), 221.
Wäsch, R., Robbins, J.A., Cross, F.R., 2010. Oncogene 29 (1), 1.
Wei, W., Ayad, N.G., Wan, Y., Zhang, G.-J., Kirschner, M.W., Kaelin, W.G.J., 2004. Nature 428 (6979), 194.

9.6 El Cheikh R, Bernard S, El Khatib N (2014) Modeling circadian clock-cell cycle interaction effects on cell population growth rates. J Theor Biol 363:318–331

Journal of Theoretical Biology 363 (2014) 318–331

Contents lists available at ScienceDirect

Journal of Theoretical Biology

journal homepage: www.elsevier.com/locate/yjtbi

Modeling circadian clock–cell cycle interaction effects on cell population growth rates

R. El Cheikh [a,b], S. Bernard [a,b], N. El Khatib [c,*]

[a] CNRS UMR 5208, Institut Camille Jordan, Université Lyon 1, 43 blvd. du 11 novembre 1918, F-69622 Villeurbanne cedex, France
[b] DRACULA Inria Grenoble Rhône-Alpes, Montbonnot F-38322, France
[c] Lebanese American University, Department of Computer Science and Mathematics, Byblos, P.O.Box 36, Byblos, Lebanon

HIGHLIGHTS

- We develop a mathematical model for cell cycle–circadian clock coupling.
- We characterize multiple regions of cell cycle entrainment by the circadian clock.
- Influence of coupling on cell proliferation is studied.
- Coupling increases growth rate for cell cycle period around 24 h and >48 h.
- Effects of mutating clock genes on the growth rate are studied.

ARTICLE INFO

Article history:
Received 13 February 2014
Received in revised form
28 July 2014
Accepted 2 August 2014
Available online 23 August 2014

Keywords:
Chronotherapy
Age-structured equations

ABSTRACT

The circadian clock and the cell cycle are two tightly coupled oscillators. Recent analytical studies have shown counter-intuitive effects of circadian gating of the cell cycle on growth rates of proliferating cells which cannot be explained by a molecular model or a population model alone. In this work, we present a combined molecular-population model that studies how coupling the circadian clock to the cell cycle, through the protein WEE1, affects a proliferating cell population. We show that the cell cycle can entrain to the circadian clock with different rational period ratios and characterize multiple domains of entrainment. We show that coupling increases the growth rate for autonomous periods of the cell cycle around 24 h and above 48 h. We study the effect of mutation of circadian genes on the growth rate of cells and show that disruption of the circadian clock can lead to abnormal proliferation. Particularly, we show that *Cry* 1, *Cry* 2 mutations decrease the growth rate of cells, *Per* 2 mutation enhances it and *Bmal* 1 knockout increases it for autonomous periods of the cell cycle less than 21 h and decreases it elsewhere. Combining a molecular model to a population model offers new insight on the influence of the circadian clock on the growth of a cell population. This can help chronotherapy which takes benefits of physiological rhythms to improve anti-cancer efficacy and tolerance to drugs by administering treatments at a specific time of the day.

© 2014 Elsevier Ltd. All rights reserved.

1. Introduction

The circadian clock regulates body daily rhythmic activities, from the wake–sleep phases succession and hormone production to blood pressure and body temperature. Several epidemiological studies have shed light on the fact that individuals with disrupted circadian rhythms have increased risk of developing tumorigenic diseases (Kubo et al., 2006; Filipski et al., 2002, 2004, 2009; Fu et al., 2002; Gery et al., 2006; Grèchez-Cassiau et al., 2008). Studies made on yeast revealed restriction of cell division to the reductive phases of the yeast metabolic cycle. This type of control was shown to be involved in circadian regulation and may be a general strategy for the robust maintenance of cellular processes. This regulation insures that the cell cycle evades the potentially mutagenic redox environment of the oxidative respiratory phase, helping us to minimize the occurrence of futile reactions (Murray et al., 2007; Tu et al., 2005).

The circadian clock interacts with the cell cycle through multiple molecular pathways (Edmunds, 1988; Johnson, 2010; Yang et al., 2010; Pando and van Oudenaarden, 2010; Hunt and Sassone-Corsi, 2007; Nagoshi et al., 2004). Hence, a disruption of the circadian clock can lead to abnormal cell proliferation and enhances tumor development.

Circadian rhythms are generated at the cellular level by a finely regulated gene network that produces sustained 24 h period

* Corresponding author.
E-mail address: nader.elkhatib@lau.edu.lb (N. El Khatib).

http://dx.doi.org/10.1016/j.jtbi.2014.08.008
0022-5193/© 2014 Elsevier Ltd. All rights reserved.

oscillations in clock gene and protein expression. This network involves several genes and relies on transcriptional, translational and post-translational mechanisms. Oscillations arise from an autoregulatory negative feedback loop system in which a clock protein inhibits the expression of its own gene by inactivating a transcription factor (Lee et al., 2001; Reppert and Weaver, 2002; Eide et al., 2005; Cardone et al., 2005; Sato et al., 2006; Partch et al., 2006; Gonze, 2011).

The cell cycle is usually divided into four phases G1, S, G2, M. Progression through each phase depends on the activity of cyclins and cyclin-dependent protein kinase complexes (Cdks) and a mitosis promoting factor (MPF). When MPF activity is high, the cell progresses through the cycle. When it is low, progression stops (Morgan, 1995). Each phase of the cell cycle is controlled by a different cyclin/Cdk complex: G1 is controlled by cyclin D/Cdk4-6, G1/S transition by cyclin E/Cdk2, S phase by cyclin A/Cdk2 and G2/M transition by cyclin B/Cdk1 (Hunt and Sassone-Corsi, 2007).

The circadian clock and the cell cycle are tightly connected. The circadian clock gates the cell cycle through the regulation of different Cdks. It has been reported that BMAL1/CLOCK activates the transcription of the kinase WEE1 to regulate the G2/M transition (Matsuo et al., 2003). The circadian clock, via the protein REV-ERBα, regulates the transcription of p21, which inhibits Cdk2 and blocks the G1/S transition (Grèchez-Cassiau et al., 2008). The circadian clock is also involved in direct control of DNA damage and apoptosis pathways by virtue of its regulation of Chk2 and other related factors (Gery et al., 2006; Chen and McKnight, 2007).

Two main approaches have been used to model the coupling between the cell cycle and the circadian clock oscillators. The first approach is to model the molecular machinery of the cell. It is usually based on ordinary differential equations, where the variables describe the intracellular molecular concentrations of both oscillators. Chauhan and colleagues constructed such a model to account for the regulation of mammalian cell cycle progression and its gating by the circadian clock in the regenerating liver (Chauhan et al., 2011). Zamborszky and colleagues used a minimal model for circadian rhythms coupled to a cell cycle model that had been originally developed for the yeast cell cycle. Their model revealed quantized cell cycles and they suggested that cell size control is influenced by the clock (Zamborszky et al., 2007). More recently, Gérard and colleagues used a detailed computational model for the Cdk network driving the mammalian cell cycle to study the effect of multiple molecular links to the circadian clock (Gérard and Goldbeter, 2012). They characterized the domains of autonomous periods where the cell cycle can be brought to oscillate to 24 or 48 h periods, and determined conditions for switching between these two patterns of entrainment.

The second approach is to model a cell population, leaving aside molecular details. This approach is based on PDEs, especially the category of physiologically structured models, or on individual-based models and cellular automata. In these models, the cell cycle is divided into multiple, discrete phases and the circadian clock is coupled via time-periodic parameters, such as the transition coefficients or phases duration. Altinok and colleagues used a cellular automaton model to examine the entrainment of the cell cycle by the circadian clock (Altinok et al., 2011). Clairambault and colleagues used an age-structured PDE system to model a population of cells under the control of the circadian clock (Clairambault et al., 2009, 2011). The circadian clock was taken into account through periodic cell cycle phase transition coefficients into the equations.

Compared to population models, molecular models capture more details of the fine regulation of the cell cycle, and in particular, can predict the effect of mutations on the cell cycle regulation. However, molecular models rarely describe explicitly dividing cell populations and it is not clear how growth rates are affected by disruptions at the molecular level.

Here, we present a mathematical model that combines the molecular and the population levels, to study the influence of the circadian clock on the growth of a population of cells. We study the influence of circadian clock gene mutations on the net growth rate of a dividing population. We show that disruption of circadian rhythms can lead to abnormal proliferation. Depending on autonomous cell cycle properties and the nature of the disruption, circadian clock gene mutations can lead to faster or slower growth rates. We characterize the effect of circadian clock gene mutations, and show that combined molecular/population model brings to the dynamics of cell proliferation a picture more complete than a molecular model alone.

2. Coupling the cell cycle and the circadian clock

Becker-Weimann and colleagues developed a simple model that takes into consideration molecular information and analyzed the roles of feedback loops on the oscillatory dynamics (Becker-Weimann et al., 2004). This model was used to explore the role of the negative feedback loop created by the transcription factor complex BMAL1/CLOCK that activates the *Period* and *Chryptochrome* genes (*Per* 1, *Per* 2, *Cry* 1 and *Cry* 2) (Fig. 1A). After several hours, PER and CRY proteins form a complex in the cytoplasm, go back to the nucleus and downregulate their own synthesis by inhibiting BMAL1/CLOCK. Once the latter protein complex is inhibited, transcription of PER and CRY stops. Hence, BMAL1/CLOCK is no longer inhibited and the cycle starts its process again. The model also includes a positive feedback loop where *Bmal* 1 transcription is positively regulated by PERs and CRYs because the complex PER/CRY also inhibits the transcription of *Rev-erb*α, which inhibits the transcription of *Bmal* 1.

Here, we focus on the coupling between the cell cycle and the circadian clock through the protein WEE1. The combined molecular/population model consists of two coupled systems of equations: one system of ordinary differential equations that describes the molecular dynamics of the cell cycle and the circadian clock, and one system of partial differential equations that describes the growth of a cell population. The molecular model itself is a coupled system of two core networks, one for the circadian clock, and one for the cell cycle.

According to Nagoshi et al. (2004), cultured fibroblasts harbor self-sustained and cell autonomous circadian clocks similar to those operative in the neurons of the suprachiasmatic nuclei. Similar results were obtained for yeast, where the regulation of oscillations is not the result of a central oscillator, but rather it emerges from numerous subgraphs with the potential to oscillate with stable periodicity (Murray et al., 2007). Also, circadian gene expression continues during cell division and daughter cells resume the rhythms of mother cells after mitosis. We assume that cell cycle divisions do not alter the molecular concentration of the circadian components, neither their rhythms, which can be linked to the fact that daughter cells inherit the same circadian expressions of their mothers.

For the circadian clock, we used the model proposed by Becker-Weimann and colleagues (2004). It consists of seven nonlinear ordinary differential equations describing the concentrations of *Per*/*Cry* mRNA and PER/CRY protein complexes, and *Bmal* 1/*Clock* mRNA and protein complexes (y_i, $i=1,\ldots,7$).

For the cell cycle, we used a system of three ordinary differential equations based on MPF activity (z_i, $i=8,\ldots,10$). This model was inspired by a model by Novak et al. (2001) (The original model is for fission yeast cell cycle, we adapt the notations for mammalian cell cycle). The core of the Tyson and

Novak model is based on the activity of the cyclin-dependent protein kinase complexes CyclinB/Cdk1 (also called MPF for mitosis promoting factor), which are the engine needed to start DNA replication and mitosis. The cell cycle is divided into three phases: G1, S/G2, and M. Transitions from one phase to the other depend on the concentration of MPF and its enemies. When the activity of MPF is high, the cell progresses through the cell cycle; when it is low, the cell blocks its progression. Each phase transition of the cycle is regulated by specific enemies and helpers, which decide whether MPF will win or lose. Transition from G1 to S is governed by the antagonistic interaction between MPF and its enemies APC^{G_1} and CKI. In the G2/M transition, the enemy of MPF is the tyrosine kinase WEE1, which can inactivate Cdk1. At cell division, or M to G1 transition, MPF activity shuts down to let the cell exit mitosis and enter the G1 phase. The helper molecule for this transition is the APC^M complex, which promotes the degradation of CyclinB. In the model, three players are included explicitly: MPF (z_8), WEE1 (z_9) and the inhibitor of MPF (z_{10}). We supposed that cells enter S/G2 phase when MPF increases above a fixed threshold (θ_1), enter mitosis (M phase) when MPF activity rises above that of WEE1, and divide when MPF reaches back a low threshold level (θ_2), as it happens during mitosis. Even though the cell cycle model presented here is not quantitative due to the small number of kinetic parameters, it still reproduces a correct qualitative behavior of the cell cycle dynamics. Since we were interested in the effects of coupling the circadian clock to the cell cycle through the protein WEE1, we only considered the antagonistic relation of WEE1 and MPF to avoid simulation artifacts, which may come from other interactions that are not related to our study. Our model reproduces well the evolution of MPF activity, which oscillates in an antagonistic way with the activity of WEE1. Once MPF activity surpasses WEE1 activity, it activates its inhibitor (variable z_{10} in our model, which can be associated with APC^M in the Tyson and Novak model, Fig. 1 in Novak et al., 2001) to help shutting down its own activity and forces the cell to exit mitosis.

The full, 10-variable molecular system, reads

$$\frac{dy_1}{dt} = \frac{\nu_{1b}(y_7+c)}{k_{1b}(1+\left(\frac{y_3}{k_{1i}}\right)^p)+y_7+c} - k_{1d}y_1, \tag{1}$$

$$\frac{dy_2}{dt} = k_{2b}y_1^q - k_{2d}y_2 - k_{2t}y_2 + k_{3t}y_3, \tag{2}$$

$$\frac{dy_3}{dt} = k_{2t}y_2 - k_{3t}y_3 - k_{3d}y_3, \tag{3}$$

$$\frac{dy_4}{dt} = \frac{\nu_{4b}y_3^r}{k_{4b}^r+y_3^r} - k_{4d}y_4, \tag{4}$$

$$\frac{dy_5}{dt} = k_{5b}y_4 - k_{5d}y_5 - k_{5t}y_5 + k_{6t}y_6, \tag{5}$$

$$\frac{dy_6}{dt} = k_{5t}y_5 - k_{6t}y_6 - k_{6d}y_6 + k_{7a}y_7 - k_{6a}y_6, \tag{6}$$

$$\frac{dy_7}{dt} = k_{6a}y_6 - k_{7a}y_7 - k_{7d}y_7, \tag{7}$$

$$\frac{dz_8}{dt} = \frac{k_{0mpf}k_{1mpf}^n}{k_{1mpf}^n+z_8^n+sz_{10}^n}(1-z_8) - d_{wee1}z_9z_8, \tag{8}$$

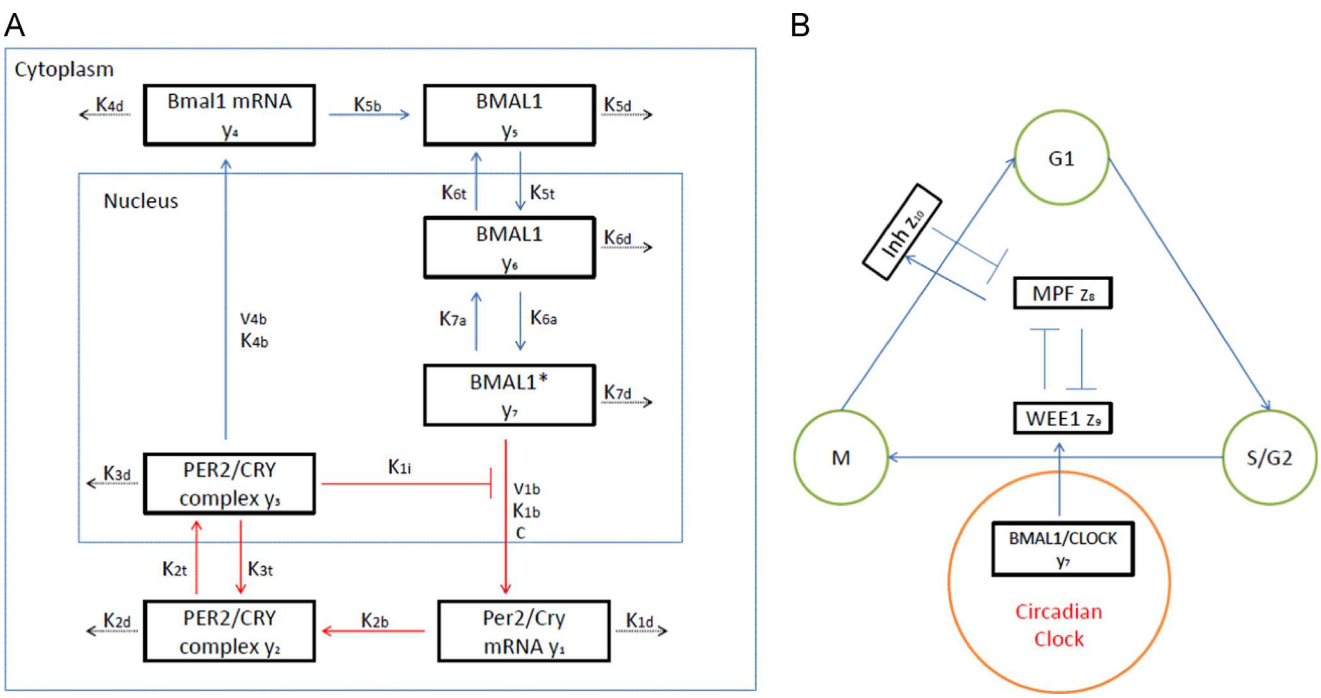

Fig. 1. (A) Scheme of the circadian clock network: the activated heterodimer BMAL1/CLOCK (BMAL1*, y_7) activates *Per* 2 and *Cry* genes, which produce *Per2/Cry* mRNA (y_1). PER2 and CRY proteins are synthesized and bind in the cytosol to form a complex (y_2) to be transported into the nucleus (y_3). This complex inhibits the activity of BMAL1/CLOCK complex, thus destroying its own source of transcription and closing the negative feedback loop. The nuclear complex PER2/CRY (y_3) also activates *Bmal* 1 transcription, which produces an increase in *Bmal* 1 mRNA (y_4), and cytosolic protein concentration (y_5). The BMAL1/CLOCK complex is then transported to the nucleus (y_6), where it is activated. The activated BMAL1/CLOCK complex (BMAL1*, y_7) restarts the activation process of *Per2/Cry*. (B) Schematic representation of the coupling between the cell cycle and the circadian clock through the protein WEE1 (z_9) (Matsuo et al., 2003). In the model, the cell cycle is divided into three successive phases G1, S/G2, M. Transitions from one phase to another depend on the activity of MPF (z_8). For cells to leave G1 and enter S/G2, MPF activity must exceed a fixed threshold $\theta_1 = 0.09$. For cells to leave S/G2 and enter M phase, MPF activity must exceed that of WEE1 (z_9). In the M phase, MPF activates its inhibitor (z_{10}), which represses MPF activity, letting it shut down and forcing the cell to exit mitosis. Division occurs once MPF activity reaches a low threshold level $\theta_2 = 0.06$. Coupling between the cell cycle and the circadian clock is achieved by the transcriptional activation of *Wee1*, which induces WEE1 activity (z_9) by the active BMAL1/CLOCK complex (y_7).

$$\frac{dz_9}{dt} = \frac{k_{actw}}{k_{actw}+d_{w1}}(c_w + Cy_7) + \left(\frac{k_{actw}}{k_{actw}+d_{w1}} - 1\right)\frac{k_{inactw} z_8^n z_9}{k_{1wee1}^n + z_8^n} - d_{w2} z_9, \quad (9)$$

$$\frac{dz_{10}}{dt} = k_{act}(z_8 - z_{10}). \quad (10)$$

The dynamical variables of the circadian clock are the following: y_1 *Per* 2 or *Cry* mRNA and proteins; y_2 PER2/CRY complex (cytoplasm); y_3 PER2/CRY complex (nucleus); y_4 *Bmal* 1 mRNA; y_5 BMAL1 cytoplasmic protein; y_6 BMAL1 nuclear protein; y_7 Active BMAL1. The dynamical variables of the cell cycle are the following: z_8 Active MPF; z_9 Active WEE1; z_{10} Active MPF inhibitor.

For the cell population system, we used age-structured equations described in the next section. The molecular model entrains the cell population system through cell cycle phase transition rates, which depend on an average molecular state of the cells.

We first studied the influence of the coupling strength between the circadian clock and the cell cycle. The coupling describes the BMAL1/CLOCK-mediated rate of WEE1 activation (parameter C in Eq. (9). Cell cycle durations reported in the literature range from around 8 h for fast dividing lymphocytes to more than 60 h for slow tumor cells (Milo et al., 2010). Thus, characteristic division times of most mammalian cells coincide with the 24 h period of the day. To see how cells could entrain to the circadian clock period, we chose a cell cycle with an autonomous period (period without coupling to the circadian clock) close, but not equal to 24 h. The cell cycle period was set by scaling the time in the cell cycle equations to obtain the right period. This means that all kinetic events (activation and deactivation) are scaled uniformly. We simulated the influence of the coupling on a cell cycle with an autonomous period of 18 h, for different coupling strengths $C = 0, 0.5, 1, 1.5$. We observed that when the coupling strength increases, the period of the cell cycle increases (Fig. 2). This behavior was expected for two reasons: (i) WEE1 blocks the cell cycle in G2 phase, and hence slows it down, and (ii) the period of entrainment of the circadian clock is longer than the autonomous period of the cell cycle.

We then asked whether coupling to the circadian clock always slows down the cell cycle, or whether it could speed it up. To answer this question, we looked at the influence of the coupling strength on the cell cycle for autonomous cell cycle period ranging from 8 to 60 h. Our simulations led to different modes of locking between the circadian clock and the cell cycle. For certain combinations of coupling strength and autonomous periods, the cell cycle can entrain to the circadian clock with a rational period ratio, referred to as *n:m* phase-locking or entrainment (Fig. 3A). For a *n:m* locking, the cell divides *n* times each *m* days. These regions of the coupling strength/autonomous periods are called Arnold tongues (Pikovsky et al., 2001). Arnold tongues show that the cell cycle can

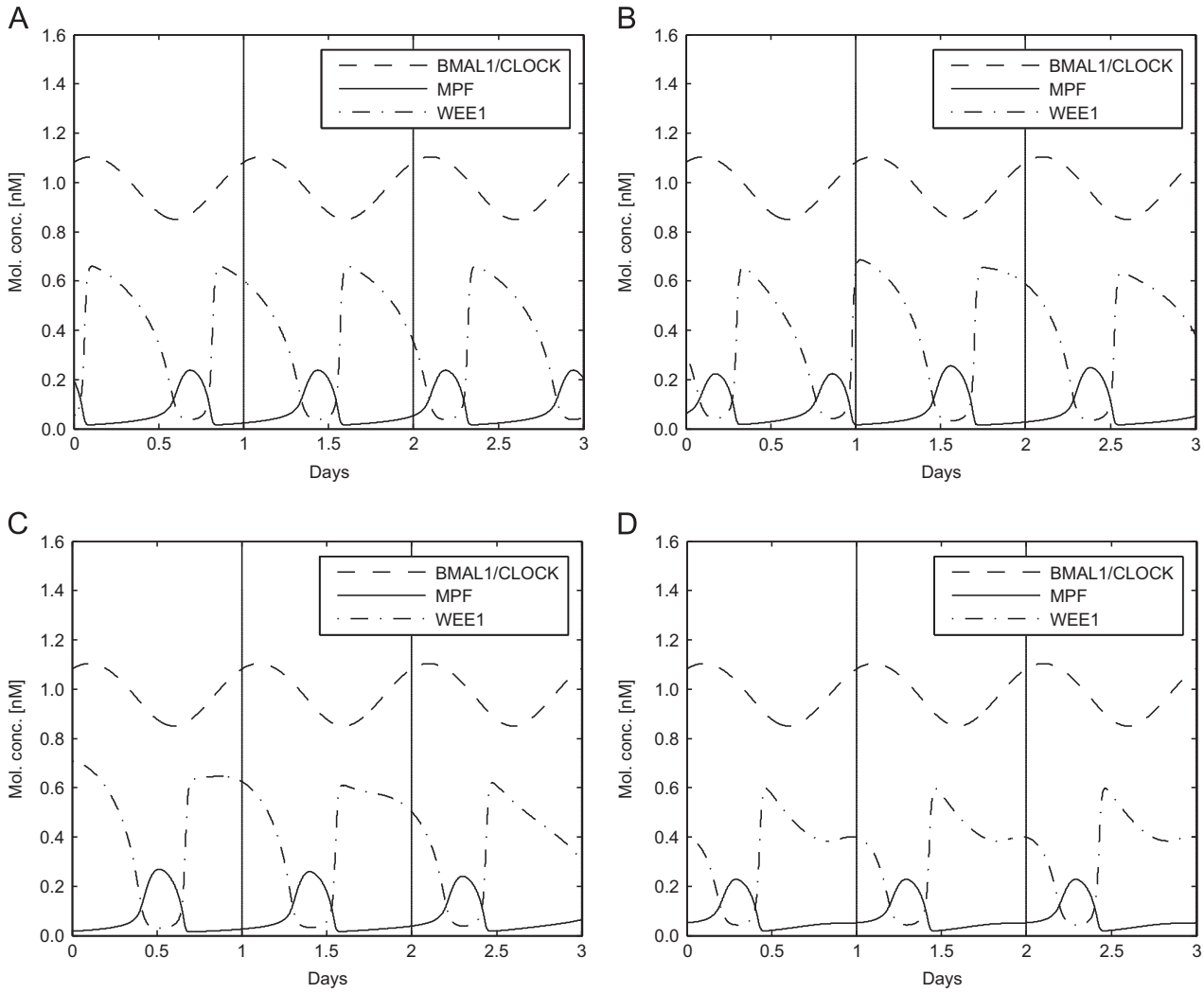

Fig. 2. Cell cycle dynamics with coupling to the circadian clock. Autonomous period of the cell cycle is equal to 18 h in this example. Increasing the coupling strength tends to regulate the cell cycle to 24 h. Coupling strength: (A) 0, (B) 0.5, (C) 1, (D) 1.5.

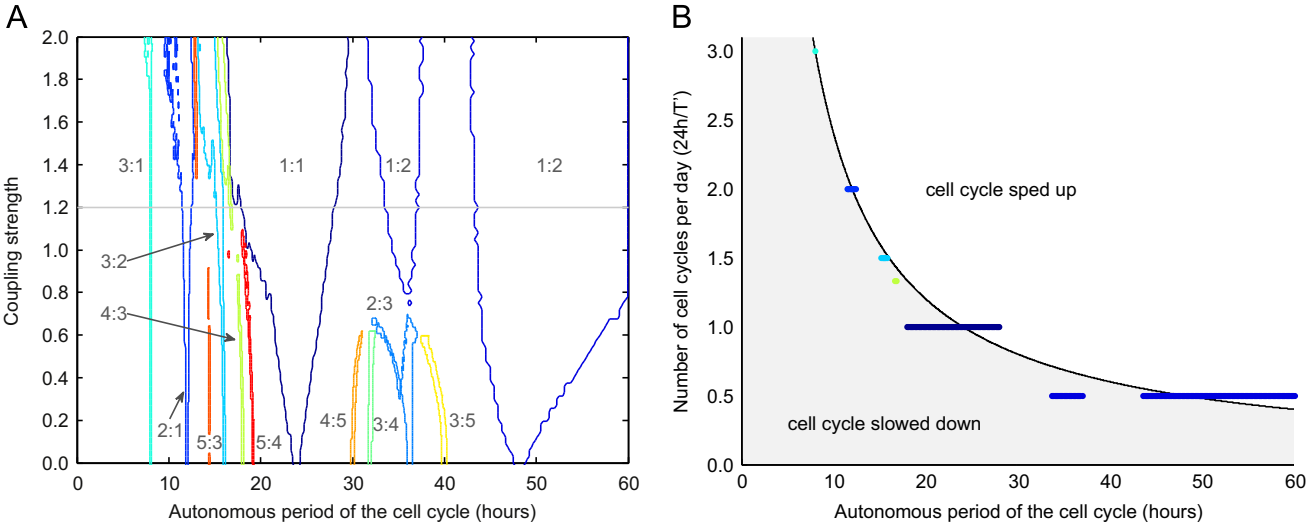

Fig. 3. (A) Arnold tongues showing the regions of *n:m* entrainment for different coupling strengths and autonomous periods. Each region corresponds to an order of entrainment. The order *n:m* means that cells divide *n* times every *m* days. Hence, the 1:1 phase-lock region contains all cell cycles that are entrained to one division per day, or a cycle of 24 h, under an appropriate coupling strength. (B) The 24 h/T' vs T plot for a fixed coupling strength ($C=1.2$) has a characteristic shape, the *devil's staircase* (Pikovsky et al., 2001). T' is the period after entrainment by the circadian clock and T is the autonomous period of the cell cycle.

phase-lock to a wide range of orders with m up to 5. 1:1 and 1:2 phase-locks have the widest range of entrainment, but other ratios can be found for large coupling strengths, such as 2:1 and 3:2.

For a fixed coupling strength ($C=1.2$), the graph of the domains of entrainment leads to a devil's staircase (Fig. 3B). The devil's staircase shows the frequencies (in number of cell cycles per day) of the phase-locked cell cycles as a function of the autonomous period. Phase-locked frequencies are distributed below (Fig. 3B, shaded region) and above the autonomous frequencies (white region), indicating that entrainment by the circadian clock can either slow down, or speed up the cell cycle. The cell cycle is accelerated for intervals of autonomous periods above 24 and 48 h. Therefore, although in our model the circadian clock only acts as a break for cell cycle progression, cells with autonomous periods above 24 or 48 h can cycle faster under circadian entrainment.

3. From molecular concentrations to population growth

The simulations so far show that the circadian clock could make the cell cycle model run faster or slower, depending on its autonomous period. How does this translate into a net growth rate in a dividing cell population is unclear, and recent analytical results have shown counter-intuitive effects of periodic forcing on growth rates of proliferating cells. There is no systematic inequality when comparing growth rates of a population under circadian control versus a population with a constant, average control (Clairambault et al., 2009, 2011), but it seems that populations under circadian control that have a cell cycle period close to multiples of 24 h proliferate faster (Bernard and Herzel, 2006).

We would expect the cell cycle period to be inversely proportional to the growth rate, as in the devil's staircase (Fig. 3B). If this were so, the knowledge of the clock-entrained period should be enough to determine the cell population dynamics, without the need of population models. To test that hypothesis, we set up a cell population model entrained by the circadian clock. We used an age-structured model that tracks the time elapsed by cells in each cell cycle phase (Brikci et al., 2007, 2008; Doumic, 2007). We divided the cell cycle model into three phases corresponding to the three phases of the molecular model: G1, S/G2, and M phases. The equations read

$$\partial_t n_i(t,x)+\partial_x n_i(t,x)+K_i(y,z)n_i(t,x)=0, \tag{11}$$

$$n_{i+1}(t,0)=\int_0^\infty K_i(y,z)n_i(t,x)\,\mathrm{d}x, \tag{12}$$

for $i=1,2$, and

$$n_1(t,0)=2\int_0^\infty K_3(y,z)n_3(t,x)\,\mathrm{d}x, \tag{13}$$

The variable $n_i(x,t)$ represents the density of cells in phase i. The variable x represents the time spent by a cell in a phase. The parameter K_i is the transition rate from phase i to the next phase. The transition between phase $i=3$ and phase $i=1$ marks the cell division, which accounts for the coefficient 2 in the boundary condition for n_1. Each transition rate K_i depends on an average molecular state of the cells. The molecular state is given by the coupled systems of ODEs for the circadian clock and the cell cycle (Eqs. (1)–(10)). The functional form of the transition rates is a Goldbeter–Koshland function:

$$K(y,z)=\frac{2yJ_i}{z-y+zJ_a+yJ_i+\sqrt{(z-y+zJ_a+yJ_i)^2-4yJ_i(z-y)}}. \tag{14}$$

This function has been used to generate a switching behavior (Novak et al., 2001). If the ratio y/z becomes larger than one, the function switches to the upper state and the transition occurs. J_a and J_i are two constants that determine the stiffness of the switch, if they tend to zero, the switch tends to a step function. The transition rate from G1 ($i=1$) to S/G2 ($i=2$) is switched ON when the concentration of MPF reaches a certain threshold value θ_1 that instructs the cell to start DNA synthesis ($K_1=K(z_8,\theta_1)$). The G2 to M ($i=3$) transition rate depends on the balance between MPF and WEE1. The cell is blocked in S/G2 and cannot transit to mitosis until MPF concentration exceeds that of WEE1 ($K_2=K(z_8,z_9)$). The transition from M to G1, and cell division, occurs when the activity of MPF goes back to baseline level ($K_3=K(\theta_3,z_8)$). The total cell number in each phase is given by

$$N_i(t)=\int_0^\infty n_i(t,x)\,\mathrm{d}x, \tag{15}$$

$i=1,\ldots,3$ and the total cell number is $N(t)=\sum_{i=1}^3 N_i(t)$.

To examine the effect of coupling on the growth rate, we made simulations with and without coupling to the circadian clock. Based on

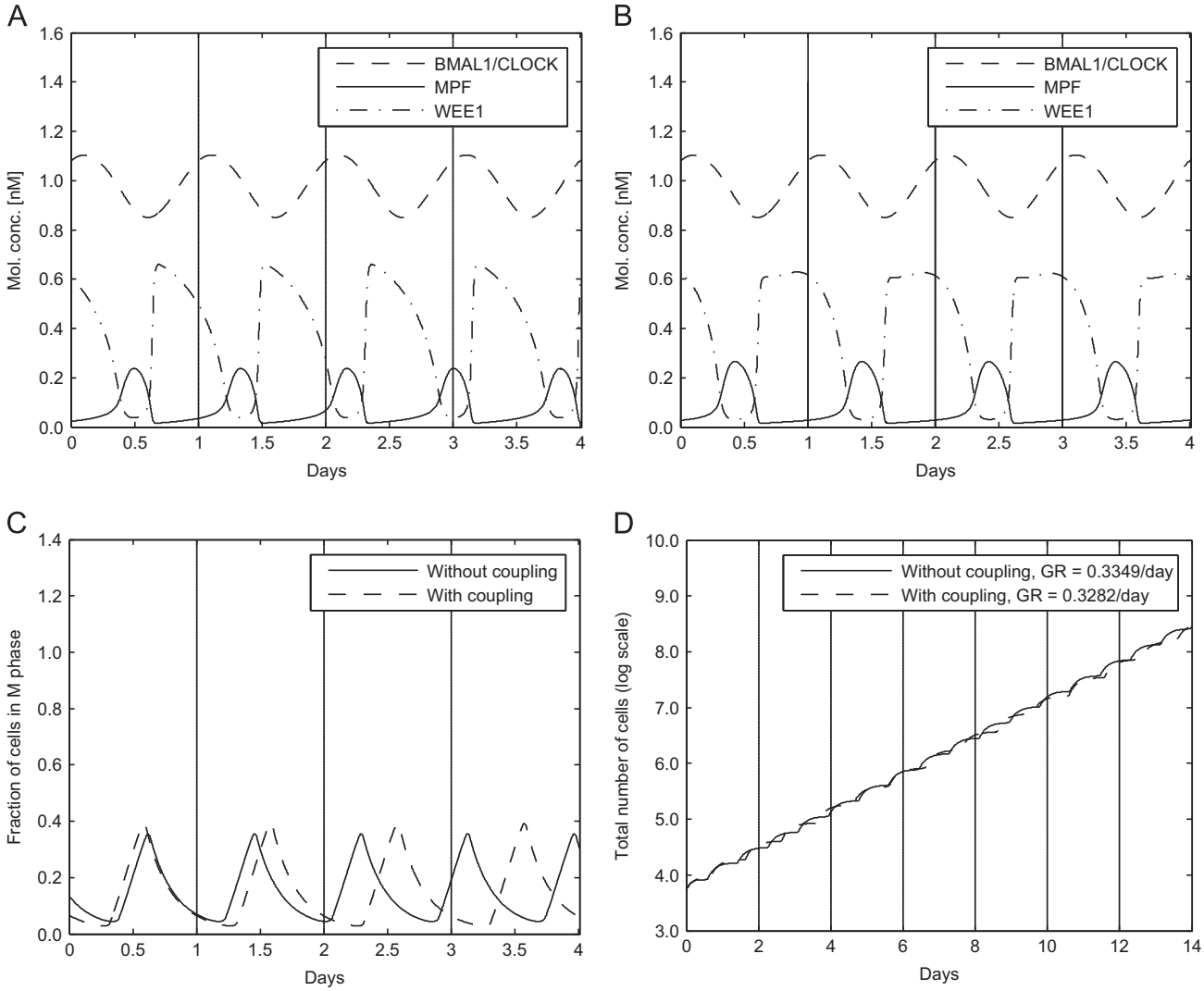

Fig. 4. Effects of coupling the circadian clock to the cell cycle with autonomous period of 20 h. (A) Without coupling ($C=0$): MPF activity follows a 20-h autonomous cycle. BMAL1/CLOCK period is equal to 24 h. (B) With coupling ($C=1.2$): the cell cycle period is entrained to 24 h. (C) The population in M phase is entrained to 24 h, hence cells have a division cycle of 24 h instead of 20 h. (D) With coupling, the growth rate does not decrease even though the cell cycle period becomes longer.

the Arnold tongues for $C=1.2$, the autonomous period of the cell cycle was set to 20 h, inside the 1:1 phase-lock region (Fig. 3A). When coupled to the circadian clock, the activity of MPF and WEE1 is well entrained and follows a rhythm of 24 h (Fig. 4A and B). Driven by the new rhythm of MPF and WEE1, the fraction of dividing cells follow a rhythm of 24 h (Fig. 4C). Even though the coupling slows down the cell cycle, the population growth rate stays practically unchanged (Fig. 4D). This can be justified by the fact that not all cells divide at each cycle. Indeed, there was 0.38 cell division per cell per cycle with coupling, while there was 0.32 cell division per cell per cycle without coupling. Therefore, a longer cell cycle can be compensated by a larger number of division at each cycle, resulting in a higher growth rate than would be inferred from the cell cycle duration only.

To gain more insight on this non-intuitive result, we examined the impact of the coupling strength on the growth rate, for autonomous cell cycle periods ranging from 8 to 60 h. In the absence of circadian coupling, the growth rate decreases almost linearly with the cell cycle period (Fig. 5A, solid line). In the presence of circadian coupling, the growth rate is decreased for most of the autonomous cell cycle periods (Fig. 5A, non-solid lines). A notable exception is the interval between 20 h and 31 h, where the growth rate is elevated compared to the growth rate without coupling. This interval corresponds to the range of 1:1 phase-lock (Fig. 3). For the larger coupling strengths ($C \geq 1.2$), the growth rate is almost constant on this interval, as is to be expected from a synchronized population. The elevated growth rate in phase-locked populations is not systematic. For autonomous cell cycle periods above 31 h, which include the 1:2 phase-lock region, the growth rate is almost constant. In this phase-lock region, the cell cycle is entrained on a 48 h period, and the growth rate is close to the autonomous growth rate at 48 h. These results are in agreement with previous theoretical studies made with population models (Clairambault et al., 2009, 2011; Bernard and Herzel, 2006), which showed that under circadian forcing, the growth rate was elevated near 24 h. Taken together, these results show that the growth rate is related to the entrainment of the molecular cell cycle, but that it is not possible to compare the growth rates with or without coupling.

To test the robustness and genericity of these results, we performed the same simulations on the effect of the coupling strength with two other published models for the circadian clock, one by Mirsky et al. (2009), and the other by Leloup and Goldbeter (2004). For the Leloup and Goldbeter (2004) model, we used parameter set 4. Both models showed the same qualitative result for the impact of the coupling strength on the growth rate. The coupling to the circadian clock increases the growth rate for periods around 24 h, over 48 h and decreases it elsewhere (Fig. 5B and C).

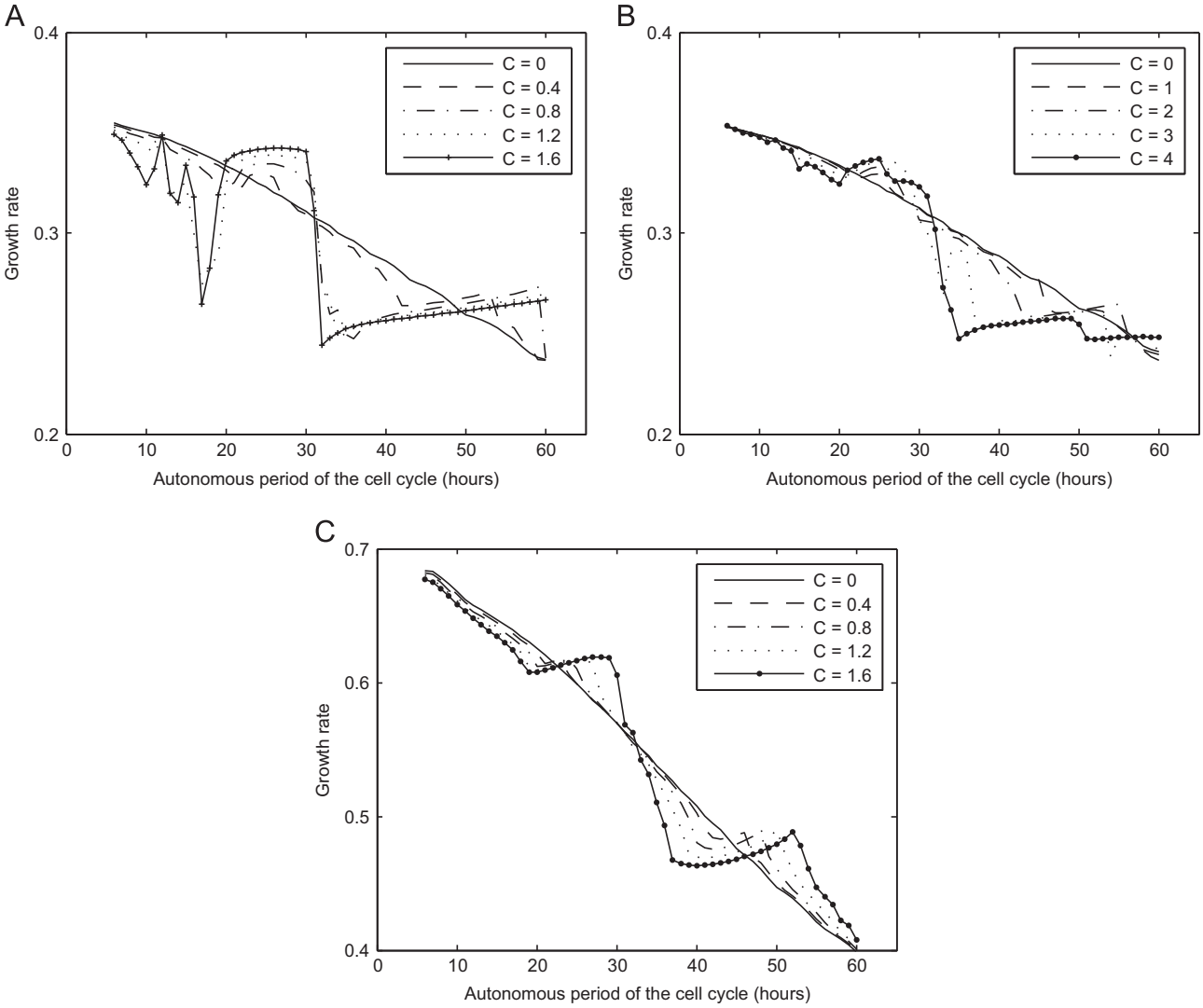

Fig. 5. Effects of coupling on the growth rate. (A) Present model. (B and C) Effects of coupling on the growth rate with other models chosen from the literature for the circadian clock: Mirsky et al. (2009) (B), and Leloup and Goldbeter (2004) (C).

4. Circadian clock and cancer

To investigate the role of the circadian clock in tumor development, we looked at the effect of mutations or deletions of circadian genes on the growth rate. Different types of mutations were examined, namely *Per* 2, *Bmal* 1, *Cry* 2 mutations and *Per* 2/*Cry* 2 double mutations. *Per2 and Bmal1 mutations abolished circadian clock rhythmicity, while Cry2 and Per2/Cry2 mutations maintained rhythmicity, in agreement with experimental data (Table 1 and reference Becker-Weimann et al., 2004, details on simulating mutants are below)*. Two cases were studied, one considering an autonomous period of the cycle equal to 28 h and one equal to 20 h. By choosing an appropriate coupling strength ($C=1.2$ for example) to the circadian clock, these two cycles could be entrained to a 1:1 cycle (Fig. 3). We looked at changes that occurred after simulating a mutation in the circadian clock. Finally, to have a more global view, we investigated the effect of mutations for autonomous periods ranging from 8 to 60 h.

We studied the effect of mutating *Per* 2 gene by considering that PER2 is a main actor in the negative feedback loop and simulated *Per* 2 mutation by decreasing the rate of PER2/CRY complex formation (we set $k_{2b}=0.01$). Simulations showed that *Per* 2 mutants have a slower division cycle (Fig. 6A and B, dash-dotted lines). This mutation tends to increase the growth rate in the case of 20 h autonomous cell cycle and keeps it almost equal to that of wild type cells for autonomous period of 28 h (Table 2). *Even though the cell cycle becomes much slower in mutants, in the case of 28 h autonomous period, 1.05 cell divisions occur during each 56 h-cycle, compared to 0.4 divisions per cycle in wild type cells. This means that for Per2 mutants, some cells must divide more than once during the cycle and explains why the mutants proliferate at the same rate as the wild-type*. We also supposed that PER2 activates *Bmal* 1 transcription and simulated *Per* 2 mutation by decreasing *Bmal* 1 transcription rate (we set $\nu_{4b}=1.5$). Similarly, we obtained that *Per* 2 mutants have a slower division cycle and an increased growth rate (Fig. 7, dot-dashed lines).

Table 1
Effects of mutations on the period of the circadian clock: comparison between experimental data and simulations.

Mutation	Circadian clock period	
	Experimental	Simulation
Per 2	Arrhythmic (Mirsky et al., 2009)	Arrhythmic
Bmal 1	Arrhythmic (Mirsky et al., 2009)	Arrhythmic
Cry 2	Rhythmic, long period (Mirsky et al., 2009)	Rhythmic, $T=24.2$ h
Per 2/*Cry* 2	Rhythmic (Oster et al., 2002)	Rhythmic, $T=22.7$ h

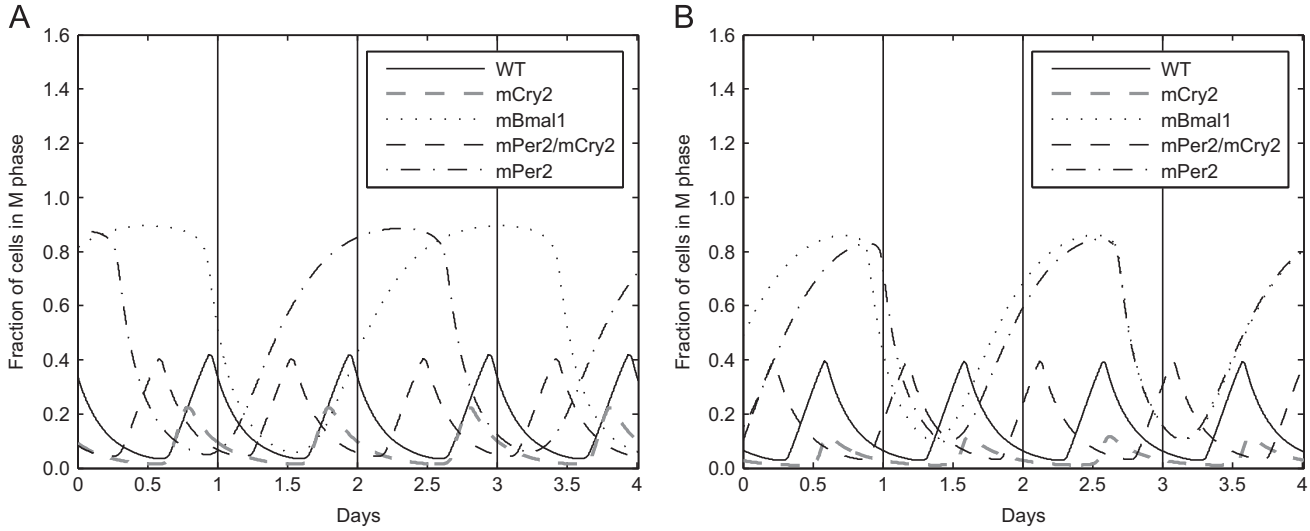

Fig. 6. Effects of mutating circadian genes on the fraction of cells entering mitosis. (A) Autonomous period of the cell cycle is equal to 28 h. (B) Autonomous period of the cell cycle is equal to 20 h.

Table 2
Effects of mutations on the period of the M phase (column period) and the growth rate (column g.r.).

Mutation	Autonomous period 28 h		Autonomous period 20 h	
	Period (h)	g.r. (d^{-1})	Period (h)	g.r. (d^{-1})
Wild-type	28.0	0.3389	20.0	0.3282
Per 2	56.4	0.3364	38.4	0.3954
Bmal 1	60.0	0.2938	42.7	0.3558
Cry 2	24.2	0.1895	24.2	0.0986
Per 2/*Cry* 2	22.6	0.3348	22.7	0.3289

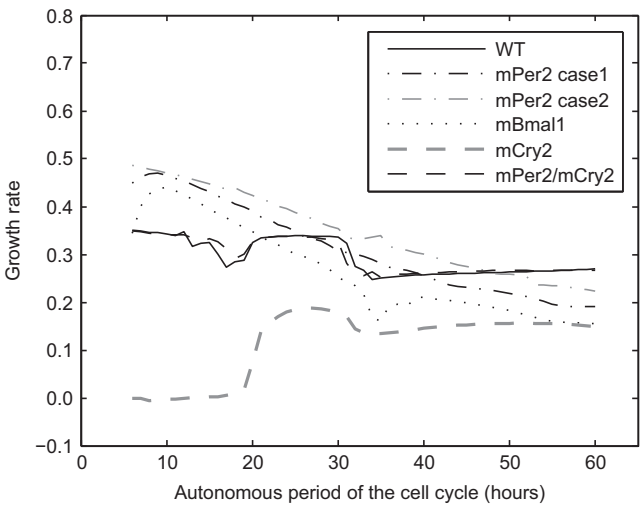

Fig. 7. Effects of mutating circadian genes on the growth rate. Mutation of *Per* 2, assuming its role in the negative feedback loop (dot-dashed line), decreases the growth rate for periods ranging from 27 to 31 h, for periods larger than 40 h and increases it elsewhere. Mutation of *Per* 2 assuming its positive regulation of *Bmal* 1 (gray dot-dashed line) increases the growth rate almost everywhere. *Bmal* 1 knockout (dotted line) increases the growth rate for periods shorter than 21 h and decreases it elsewhere. *Cry* 2 mutation (gray dashed line) decreases the growth rate everywhere. *Per* 2/*Cry* 2 double mutation (dashed line) maintains a normal proliferation.

We simulated Bmal1 knockout by setting the transcription rate of Bmal1 ν_{4b} equal to 0. Simulations showed that this mutation tends to slow the cell division cycle for both 20 and 28 h autonomous period (Fig. 6A and B, dotted lines). We observed that this mutation decreases the growth rate for autonomous periods of 28 h and increases it for autonomous periods of 20 h (Table 2).

We simulated deficient *Cry* 2 mutants by decreasing the strength of the negative feedback loop (the constant k_{1i} was increased to $k_{1i}=0.8$). *Cry* 2 mutation preserves the periods of mitotic divisions (Fig. 6A and B, gray-dashed lines), but decreases the growth rate for both 20 and 28 h-autonomous the cell cycle periods (Table 2).

We simulated *Per* 2/*Cry* 2 double mutants by assuming that *Per* 2 mutation decreases the rate of PER2/CRY complex formation, and that *Cry* 2 mutation decreases the strength of the negative feedback loop (we set $k_{1i}=0.8$ and $k_{2b}=0.01$). Our simulations showed that these double mutants have recovered a mitotic division cycle similar to that of wild type. They also have the same growth rate (Fig. 6A and B, dashed lines; Table 2).

Finally, we compared the growth rates for mutants and wild type cells for autonomous cell cycle periods ranging between 8 and 60 h. *Per* 2 mutation generally increases the growth rate. *Cry* 2 mutation decreases it, and *Bmal* 1 mutation increases it for autonomous periods less than 21 h and decreases it elsewhere. Our simulations also predict that *Per* 2/*Cry* 2 double mutants recover a normal proliferation rate and have approximately the same growth rate for all autonomous periods of the cell cycle (Fig. 7).

We tested the robustness and the genericity of these results by performing the same simulations on the effect of circadian genes mutations with the models proposed by Mirsky et al. (2009) and Leloup and Goldbeter (2004). Results given by the model proposed by Mirsky et al. (2009) were consistent with current model. Namely, *Per* 2 mutation increases the growth rate, *Cry* 1 decreases it, *Bmal* 1 mutation increases it for autonomous periods less than 22 h and decreases it elsewhere. Simulations on *Per* and *Cry* mutations done with the model proposed by Leloup and Goldbeter (2004) did not show a difference in growth rate compared to the wild type (Fig. 8). These results may be explained by the fact that this model is relatively robust to parameter variations. For the parameter set 4 in Leloup and Goldbeter (2004), the circadian clock was most sensitive to parameters related to Bmal1, for which the effect on the population growth rate was similar to the current model and the model by Mirsky et al. (2009).

Taken together, these results predict a differential effect of certain clock gene mutations, depending on the autonomous cell

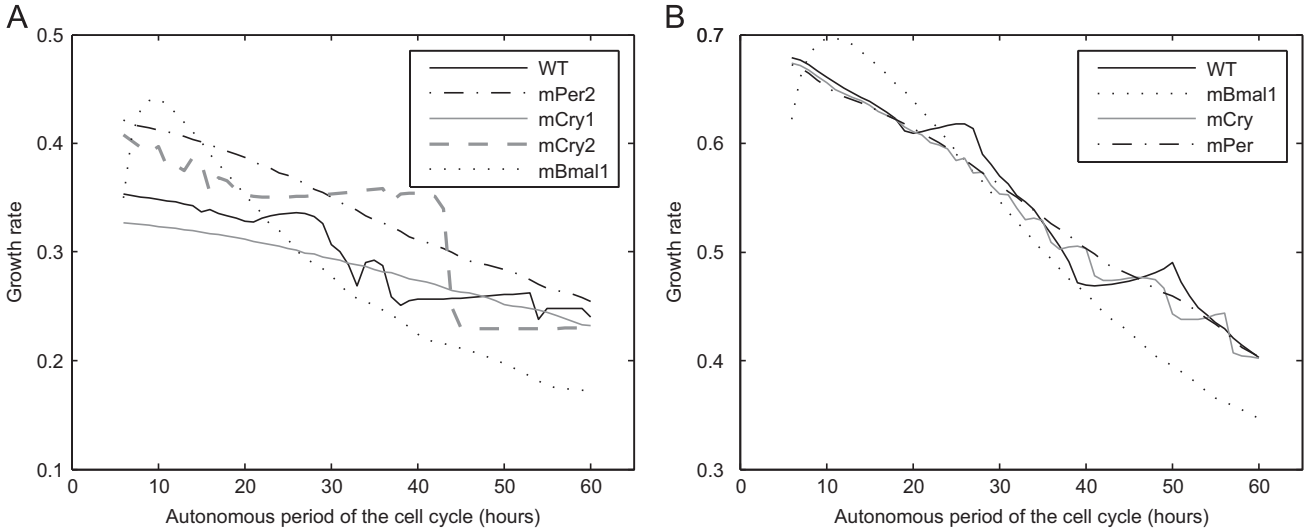

Fig. 8. Effects of mutating circadian genes on the growth rate. Simulations were performed with other models chosen from the literature for the circadian clock (Mirsky et al., 2009 (A), and Leloup and Goldbeter, 2004 (B)). Both models gave a result for *Bmal* 1 mutants similar to our result, *Bmal* 1 mutation increases the growth rate for autonomous periods less than 22 h and decreases it elsewhere. For other types of mutations, the first model is more consistent with our model. It gave similar result for *Per* 2 mutants, *Per* 2 mutation increases the growth rate (dot-dashed line (A)). Results for *Cry* 1 mutation were also in agreement with our results. *Cry* 1 mutation (gray solid line (A)) seems to decrease the growth rate for a large interval of autonomous periods. Results for *Cry* 2 mutation are not in agreement with ours, since *Cry* 2 mutation (gray dashed line (A)) seems to increase the growth rate and does not decrease it as it was predicted by our model. Simulations on *Per* and *Cry* mutations done with the model proposed by Leloup et al. did not show much difference for the growth rate compared to wild type cells (dot-dashed and gray solid lines (B)).

cycle period of the cell population. For instance, *Per* 2 mutant populations grow faster when the autonomous period is shorter than 40 h, but can also grow more slowly if their autonomous period is longer. Other mutations, such as *Cry* 2, systematically slow down the population growth rate.

These results can be explained by looking at the impact of mutations on the MPF/WEE1 dynamics, which dictates the rhythm for cells to enter into mitosis and then divide. Mutation-induced change in BMAL1/CLOCK dynamics, either its period or concentration, directly influences WEE1 activity and the cell cycle dynamics. For example, in case of a 28 h autonomous period, even though the cell cycle becomes longer for *Per* 2 mutants, the growth rate does not change. *Per* 2 mutation produces an arrhythmic clock with low BMAL1/CLOCK concentration (Fig. A1B, dash-dotted line). A comparison of MPF/WEE1 dynamics between mutants and wild type cells shows how the transition rates for the M phase differ (Fig. A2). For *Per* 2 mutants, the transition rate is at a high level for a longer time. This means that even though the cell cycle is longer, much more cells will have the time to enter M phase and divide. This explains why growth rates are similar in *Per* 2 mutants, even though the cell cycle period is longer. For *Cry* 2 mutants, growth rate decreases. *Cry* 2 mutation leads to higher rates of BMAL1/CLOCK, which in turn increases WEE1 activity (Fig. A1B, gray-dashed line). Increasing WEE1 activity will decrease the activity of MPF (Fig. A1A, gray-dashed line), which means that cells are blocked in G2 phase for a longer time and are prevented from transiting into mitosis. A comparison of the transition rate between wild type and *Cry* 2 mutants shows that transition rate for wild type cells stays on a high level for a longer time than for mutant cells (Fig. A3).

5. Discussion and conclusion

5.1. Mathematical model for the regulation of the cell cycle by the circadian clock

We developed a combined molecular/population mathematical model to study how the coupling of the circadian clock to the cell cycle, through the protein WEE1, affects a proliferating cell population. The model has the novelty of combining both intracellular and population levels. We investigated the influence of coupling on the period of the molecular cell cycle and on the growth rate of the population. The molecular model displays wide ranges of entrainment to the circadian clock, where there is a *n:m* ratio in the number of cell cycles and the number of circadian oscillations. We found that molecular information about the cell cycle was not always sufficient to predict how the growth rate in a dividing cell population is affected. The combined molecular/population could predict an increase in growth rate in *Per* 2 mutants that could not be explained by the molecular model alone. We used the combined model to look at the influence of circadian clock gene mutations on the population growth rate. We found a differential effect of clock gene mutations, depending on the autonomous cell cycle period of the cell population.

5.2. Entraining the cell cycle by the circadian clock

We examined the influence of coupling the cell cycle to the circadian clock on the number of cell cycle divisions per day. We showed that for certain combinations of coupling strength and autonomous periods, the cell cycle can entrain to the circadian clock with a rational period ratio, referred to as *n:m* phase locking or entrainment. These regions in the coupling strength/autonomous periods space are the Arnold tongues already introduced (Fig. 3A). Gérard and colleagues characterized domains of entrainment to 24 and 48 h periods (Gérard and Goldbeter, 2012), which correspond to 1:1 and 1:2 phase-locking, respectively. While their model and the current model both predict wide ranges of 1:1 and 1:2 entrainment, there are small differences. In the current model, the 1:2 entrainment region is larger than the 1:1, while the converse is true for the model by Gérard and Goldbeter (2012) (their Fig. 4B, our Fig. 3A). In the current model, 1:2 entrainment is observed at large coupling strength in an autonomous period range where 2:3 occurs (around autonomous periods of 36 h). It looks like that in the Gérard and Goldbeter model, the 1:1 entrainment takes over for larger coupling strengths. Recently, Feillet et al. used multispectral imaging of single live cells and mathematical modeling to investigate how the temporal

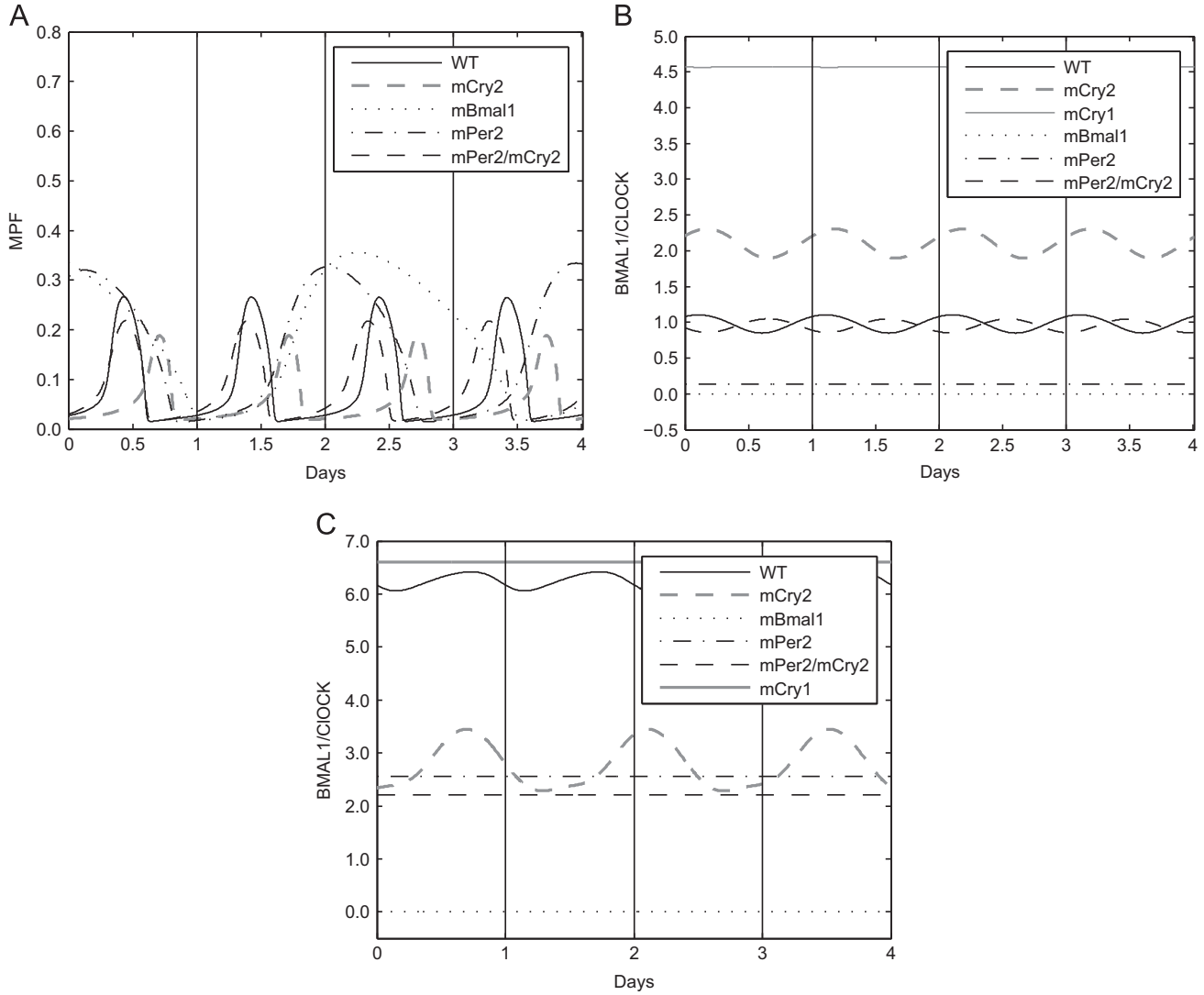

Fig. A1. Effects of mutating circadian genes. (A) MPF activity under different clock mutations. (B) BMAL1/CLOCK activity under different clock mutations, current model (Becker-Weimann et al., 2004). (C) BMAL1/CLOCK activity under different clock mutations, model of Mirsky et al. (2009).

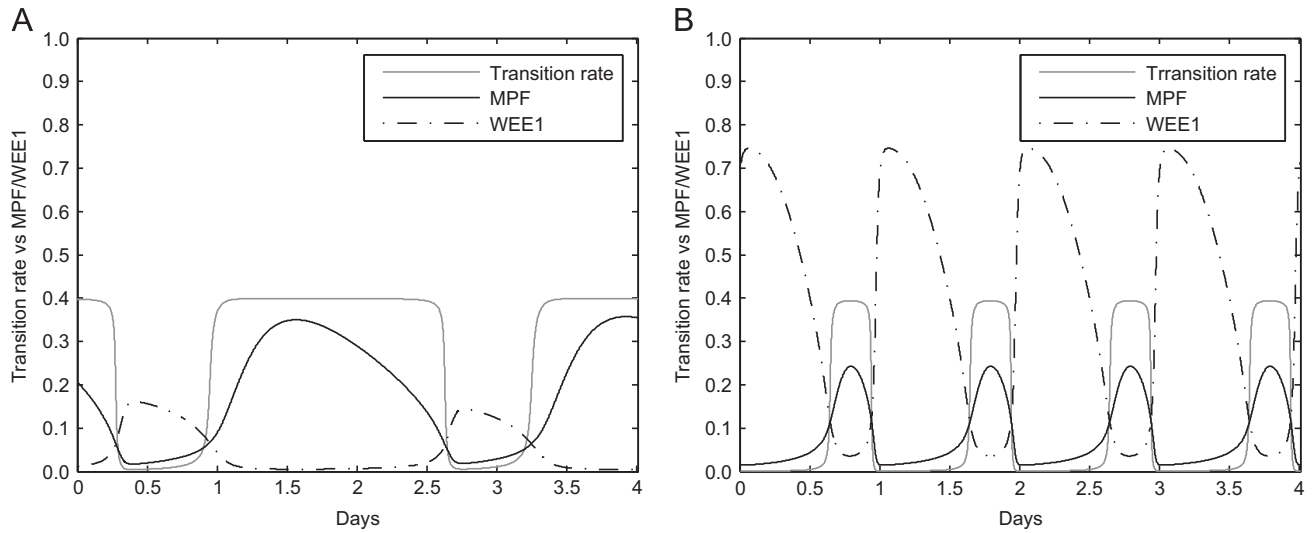

Fig. A2. (A) *Per* 2 mutants. (B) Wild type cells.

organization of cell division at the single cell level produces daily rhythms at the population level (Feillet et al., 2014). They demonstrated that there are multiple coexisting robust oscillatory dynamical states of the coupled clock and cell cycle in proliferating mammalian cells, namely 1:1, 5:4 and 3:2 phase locking states. We have characterized a wide range of entrainment modes, including

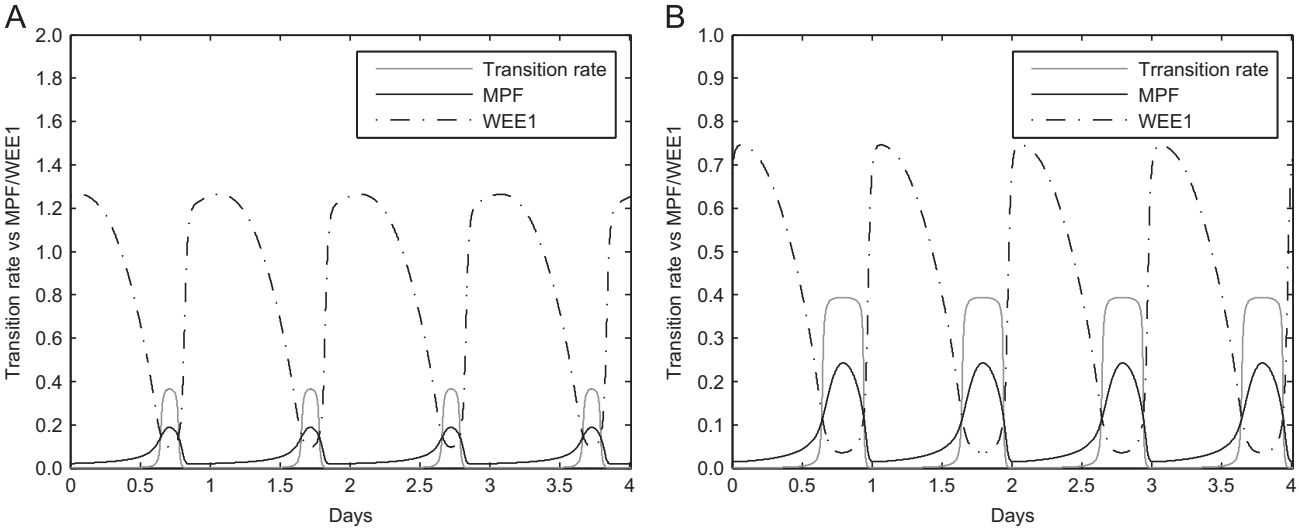

Fig. A3. (A) *Cry* 2 mutants. (B) Wild type cells.

high order phase-locking (3:5, 4:5, 5:4, 5:3), which is consistent with the experimental data of Feillet et al. and which may partly explain the observed quantized cell cycle times discussed previously (Zamborszky et al., 2007). The devil's staircase provides a way to predict the frequency of cell divisions as a function of the autonomous cell cycle period. Although the circadian clock acts as a break by activating the inhibitor WEE1, for certain autonomous periods, the cell cycle frequency can still be higher with the clock than without (Fig. 3B).

5.3. Modulation of population growth rate by the clock

We investigated the influence of coupling on the growth rate for autonomous periods of the cell cycle varying from 8 to 60 h. Clairambault and colleagues (2011) showed, using population models, that there is no general inequality between growth rates with and without coupling to the circadian clock. Bernard and Herzel (2006) found that cells under circadian control that have an interdivision time close to multiples of 24 h proliferate faster. Here, we showed that coupling increases the growth rate for autonomous periods of the cell cycle around 24 h and above 48 h. For most other periods, the growth rate is decreased. These results could not have been obtained based only on the molecular model, which predicted a smaller growth rate for autonomous periods just below 24 h.

5.4. Effect of mutating clock genes on the growth rate

We investigated the effect of single or double circadian clock gene mutations on a cell population growth rate. Fu and colleagues showed that loss of *Per* 2 functions increased tumor development (Fu et al., 2002). The roles of PER2 in the circadian clock mechanism have been unclear. It is usually considered as a main actor in the negative feedback loop, repressing the activity of BMAL1/CLOCK through the complex PER2/CRY. But some studies also suggest that PER2 activates *Bmal* 1 transcription in an indirect manner (Shearman et al., 2000; Yu et al., 2002; Akashi et al., 2014). We first examined *Per* 2 mutation by considering that PER2 plays a repressive role in the negative feedback loop. Our simulations are in agreement with experimental results and show that *Per* 2 mutation increases the growth rate for a wide range of autonomous periods of the cell cycle. When a positive action of PER2 on *Bmal* 1 was assumed, we also obtained an increased growth rate for this mutation. We examined *Cry* 2 mutation. We showed that *Cry* 2 mutation decreases the growth rate for almost all periods of the cell cycle. This may explain the experimental results obtained by Matsuo and colleagues, who showed that the weight of regenerating liver in *Cry* deficient mice was significantly lower than in wild type mice (Matsuo et al., 2003).

We examined *Per* 2/*Cry* 2 double mutation. We showed that *Per* 2/*Cry* 2 double mutants recover normal proliferation rates and have similar growth rates for all autonomous periods of the cell cycle. Oster et al. showed that inactivation of *Cry* 2 gene in *Per* 2 mutant mice restored circadian rhythmicity as well as normal clock gene expression patterns (Oster et al., 2002). They showed that both the period and the amplitude of *Bmal* 1 (also of *Per* 1 and *Cry* 1) expressions in *Per* 2/*Cry* 2 double mutant animals were comparable to those of wild types. Hence, if both period and amplitude of *Bmal* 1 are comparable to those of wild type, WEE1 profile will not be changed for these double mutants, preserving normal dynamics for the cell cycle.

We also explored *Cry* 1 mutation and *Cry* 1/*Cry* 2 double mutation, based on the assumption that CRY1 plays a more important role in the negative feedback loop (Langmesser et al., 2008). In the current model, these mutations completely abolished cell proliferation (data not shown). There is no experimental evidence that disruption of the circadian clock can totally prevent cell cycle progression, and it is likely that the cell cycle relies on factors not included in the current model to proceed through division.

5.5. Robustness of the results

To test the robustness of our results, we performed our main simulations with two other models for the circadian clock (Mirsky et al., 2009; Leloup and Goldbeter, 2004). We simulated the effect of coupling and circadian genes mutation on the growth rate. Both models show the same qualitative result that we obtain for the impact of the coupling on the growth rate. Results on mutating circadian genes obtained with the model proposed by Mirsky et al. were more consistent with our results. The model proposed by Leloup et al. did not show a difference between mutated and wild type cells. This may be explained by the fact that the model proposed by Mirsky et al. was designed to study the effects of mutating circadian genes, whereas the model proposed by Leloup et al. was designed to generate sustained oscillations, which makes it more robust about parameter variation.

The current circadian clock model (Becker-Weimann et al., 2004) shows limitations in reproducing experimental data that are inherent to models with simplifying assumptions and distinct molecular species lumped together. To check how the simplifying assumptions affect the results,we made a detailed comparison between the current model and the model by Mirsky et al. (2009) on the effects of circadian gene mutations. What it is critical in our model is the effect specific mutations on the activity of BMAL1/CLOCK (period and concentration),which regulates directly WEE1 and the cell cycle. Hence,we simulated the effects of circadian gene mutations on BMAL1/CLOCK using Mirsky et al. model (in the same way the authors did it in the original study,Table S3 in Mirsky et al., 2009) and compared the results with those obtained by the current model. Both models showed similar effects for *Bmal* 1 and *Per* 2 mutations. *Bmal* 1 mutation results in an arrhythmic clock with zero concentration of BMAL1/CLOCK and *Per* 2 mutation results in an arrhythmic clock with a low BMAL1/CLOCK concentration (Fig. A1B and C, and Tables A2 and A3). Consequently, *Bmal* 1 and *Per* 2 mutations have similar effects on the growth rates (Figs. 7 and 8A, dotted and dash-dotted lines). *Cry* 2 mutation results in a rhythmic clock with a longer period for both models. However, the period obtained with the model of Mirsky et al. is longer than with the current model ($T=32.1$ h vs $T=24.2$ h, Table A2). The effect on BMAL1/CLOCK concentration is different: the Mirsky et al. model showed a lower concentration compared to wild type,while the current model showed a higher concentration (Fig. A1B and C, and Table A3). This results in different growth rates for the two models (Figs. 7 and 8A, gray dashed lines). *Per* 2/*Cry* 2 double mutation results in a rhythmic clock with the current model ($T=22.7$ h),with a concentration similar to wild type,while it results in an arrhythmic clock using the model of Mirsky et al. (Fig. A1B and C, and Tables A2, A3). Finally, both models gave an arrhythmic clock for *Cry* 1 mutation, with higher BMAL1/CLOCK concentration compared to wild type (Fig. A1B and C, gray solid line).

The main differences between the two models are the effects of *Cry* 2 and *Per* 2/*Cry* 2 mutations. Mirsky et al. predict a longer period for *Cry* 2 mutants, which may be more realistic in the case of lung explants and fibroblasts. The model by Mirsky et al. predicts an arrhythmic clock for *Per* 2/*Cry* 2 double mutation, in contrast to the current model and experiments showing normal rhythmicity for these double mutants (Oster et al., 2002). The model by Forger and Peskin also predicts a rhythmic clock for this double mutation (Forger and Peskin, 2003). The main limitation of the current model is the way that *Cry* 1 mutation and *Cry* 1/*Cry* 2 double mutation are approached. Both are simulated in the same way, by decreasing further the strength of the negative feedback loop. This leads to an arrhythmic clock with high constitutive BMAL1/CLOCK concentration inhibiting cell proliferation, which cannot be supported by experimental data (data not shown). Results given on the growth rate by the model of Mirsky et al. on *Cry* 1 mutation seems to be more coherent. *Cry* 1 mutants have a decreased growth rate compared to wild types for a wide interval of autonomous periods of the cell cycle (Fig. 8A, gray solid line).

5.6. Conclusion

Combining a molecular model to a population model offers new insight on the influence of the circadian clock on the growth of a cell population. Disruption of the circadian clock can increase or decrease the growth rate, as well as the period of mitotic divisions, depending on which clock gene is affected. In some cases, even though the cell cycle slows down, the growth rate can still increase, making the combination of a molecular model and population model unavoidable to study the effect of circadian clock disruption. This can have beneficial impacts on chronotherapy, which aims to develop new strategies in cancer therapies by a better understanding of the circadian clock and its impact on cell proliferation.

The combined model presented in this study is the first step in developing a fully multiscale model for the interaction between the circadian clock and the cell cycle. The multiscale model describes a cell population p structured with a molecular content (y,z) describing the circadian clock and the cell cycle. Heterogeneity among cells can be fully taken into account in a multiscale model, but at the cost of a high-dimensional phase space (here 10D). Even though it has limitations, the current molecular model is simple enough to be amenable to a multiscale description, which, in our view, is essential.

Several studies have shown that the tolerance and the toxicity of drugs vary according to their administration time (Focan, 1995; Hrushesky and Bjarnason, 1993; Lévi, 2000). Clinical studies showed that compared to standard chemotherapies, chronomodulated chemotherapies, which aim to deliver drugs at an optimal time of the day, could be more efficient and better tolerated by patients (Focan et al., 1999, 2000). In a recent work, Bernard et al. (2010) used a simple cell population model under chronomodulated treatment and developed a quantitative method to identify biological parameters important for the successful design of a chronotherapy strategy. They found that optimal times depend not only on the circadian status but also on the cell cycle kinetics of the tumor. They suggested that the length of the cell cycle is important to determine the best treatment times and intervals. For fast growing tumors, with short S phase, administering a drug that targets the S phase of the cell cycle at 28.8 h intervals may be safer than treating at 24 h intervals, and that for slow growing tumors, with a long S phase, treating at 24 h intervals would be the best option. The circadian clock is often disrupted in advanced stage cancers, perhaps because this gives a competitive advantage to growing tumor cells (Savvidis and Koutsilieris, 2012). The current model could be useful to predict how the cell cycle is modified following circadian clock disruption. Combined with the method proposed by Bernard et al. (2010), this may be of great importance to determine the right time for drug delivery. By taking into account complex interactions between the cell cycle, the circadian clock and the treatment, the combined molecular/population model can be a helpful tool for chronotherapy.

Acknowledgment

The authors gratefully acknowledge the support of CAMPUS FRANCE and the Lebanese National Council of Scientific Research for funding this work under the PHC Cèdre Grant 30097ZA.

Appendix A. Supplementary figures and tables

Effects of mutating circadian genes on MPF and BMAL1/CLOCK activities and on transition rates are given in Figure A1 and Figure A2 respectively. The parameters description is given in Table A1, the effects of mutations on circadian clock period and BMAL1/CLOCK concentration are given in Tables A2 and A3.

Table A1
Parameters description.

Parameters	Values	Units	Description
Circadian clock			
c	0.01	nM	Concentration of constitutive activator
p	8	Unit less	Hill coefficient
ν_{1b}	9	nM h^{-1}	Maximal rate of Per2/Cry transcription
k_{1b}	1	nM	Michaelis constant of Per2/Cry transcription
k_{1d}	0.12	h^{-1}	Degradation rate of Per2/Cry mRNA
k_{1i}	0.56	nM	Inhibition constant of Per2/Cry transcription
k_{2b}	0.3	nM^{-1} h^{-1}	Formation rate of cytoplasmic PER2/CRY complex
k_{2d}	0.05	h^{-1}	Degradation rate of cytoplasmic PER2/CRY complex
k_{2t}	0.24	h^{-1}	Nuclear import rate of PER2/CRY complex
k_{3t}	0.02	h^{-1}	Nuclear export rate of PER2/CRY complex
q	2	Unit less	Number of PER2/CRY2 complex forming subunits
k_{3d}	0.12	h^{-1}	Degradation rate of nuclear PER2/CRY complex
ν_{4b}	3.6	nM^{-1} h^{-1}	Maximal rate of Bmal1 transcription
r	3	Unit less	Hill coefficient of Bmal1 transcription
k_{4b}	2.16	nM	Michaelis constant of Bmal1 transcription
k_{4d}	0.75	h^{-1}	Degradation rate
k_{5b}	0.24	h^{-1}	Translation rate of BMAL1
k_{5d}	0.06	h^{-1}	Degradation rate of BMAL1
k_{5t}	0.45	h^{-1}	Nuclear import rate of BMAL1
k_{6t}	0.06	h^{-1}	Nuclear export rate of BMAL1
k_{6d}	0.12	h^{-1}	Degradation rate of nuclear BMAL1
k_{6a}	0.09	h^{-1}	Activation rate of nuclear BMAL1
k_{7a}	0.003	h^{-1}	Deactivation rate of nuclear BMAL1*
k_{7d}	0.09	h^{-1}	Degradation rate of nuclear BMAL1*
Cell cycle			
k_{0mpf}	10	h^{-1}	Activation rate of MPF
k_{1mpf}	0.05	nM	Activation rate of MPF
s	20	nM	Inhibition constant of MPF
$d_{wee\ 1}$	5	h^{-1}	Degradation rate
n	2	Unit less	Hill coefficient
k_{actw}	1	h^{-1}	Activation rate of WEE1 due to BMAL1/CLOCK
$d_{w\ 1}$	1	nM	Michaelis constant
c_w	0.5	nM	Concentration of constant activator
C	0	nM	Coupling strength to the circadian clock
k_{inactw}	200	h^{-1}	Deactivation rate
k_{1wee1}	0.5	nM	Michaelis constant
$d_{w\ 2}$	1	h^{-1}	Degradation rate
k_{act}	0.01	h^{-1}	Activation rate of MPF inhibitor
Population model			
θ_1	0.09	nM	Threshold value for G1 to S/G2 transition
θ_2	0.06	nM	Threshold value for mitotic division (M to G1)
J_a	0.1	Unit less	Stiffness of the switch
J_i	0.1	Unit less	Stiffness of the switch

Table A2
Effects of mutations on the period of the circadian clock: comparison between the current model (Becker-Weimann et al., 2004) and the model of Mirsky et al. (2009).

Mutation	Circadian clock rhythmicity	
	Current	Mirsky et al.
Per 2	Arrhythmic	Arrhythmic
Bmal 1	Arrhythmic	Arrhythmic
Cry 2	Rhythmic, $T=24.2$ h	Rhythmic, $T=32.1$ h
Per 2/*Cry* 2	Rhythmic, $T=22.7$ h	Arrhythmic
Cry 1	Arrhythmic	Arrhythmic

Table A3
Effects of mutations on the BMAL1/CLOCK concentration compared to wild type: comparison between the current model (Becker-Weimann et al., 2004) and the model of Mirsky et al. (2009).

Mutation	BMAL1/CLOCK	
	Current	Mirsky et al.
Per 2	Lower	Lower
Bmal 1	Lower	Lower
Cry 2	Higher	Lower
Per 2/*Cry* 2	Similar	Lower
Cry 1	Higher	Higher

References

Akashi, M., Okamoto, A., Tsuchiya, Y., Todo, T., Nishida, E., Node, K., 2014. A positive role for PERIOD in mammalian circadian gene expression. Cell Rep 7 (4), 1056–1064. http://dx.doi.org/10.1016/j.celrep.2014.03.072.

Altinok, A., Gonze, D., Lévi, F., Goldbeter, A., 2011. An automaton model for the cell cycle. Interface Focus 1, 36–47.

Becker-Weimann, S., Wolf, J., Herzel, H., Kramer, A., 2004. Modeling feedback loops of the mammalian circadian oscillator. Biophys. J. 87 (5), 3023–3034.

Bernard, S., Herzel, H., 2006. Why do cells cycle with a 24 hour period? Genome Inf. 17 (1), 72–79.

Bernard, S., Bernad, B.C., Lévi, F., Herzel, H., 2010. Tumor growth rate determines the timing of optimal chronomodulated treatment schedules. PLoS Comput. Biol. 6, e1000712.

Brikci, F., Clairambault, J., Ribba, B., Perthame, B., 2007. An age-and-cyclin-structured cell population model for healthy and tumoral tissues. J. Math. Biol. 57, 91–110.

Brikci, F., Clairambault, J., Perthame, B., 2008. Analysis of a molecular structured population model with possible polynomial growth for the cell division cycle. Math. Comput. Model. 47, 699–713.

Cardone, L., Hirayama, J., Giordanao, F., Tamaru, T., Palvino, J., Sassone-Corsi, P., 2005. Circadian clock control by SUMOylation of BMAL1. Science 309, 1390–1394.

Chauhan, A., Lorenzen, S., Herzel, H., Bernard, S., 2011. Regulation of mammalian cell cycle progression in the regenrating liver. J. Theor. Biol. 283, 103–112.

Chen, Z., McKnight, S., 2007. A conserved DNA damage response pathway responsible for coupling the cell division cycle to the circadian and metabolic cycles. Cell Cycle 6 (23), 2906–2912.

Clairambault, J., Gaubert, S., Lepoutre, T., 2009. Comparison of Perron and Floquet eigenvalues in age structured cell division models. Math. Comput. Model. 4, 183–209.

Clairambault, J., Gaubert, S., Lepoutre, T., 2011. Circadian rhythm and cell population growth. Math. Comput. Model. 53, 1558–1567.

Doumic, M., 2007. Analysis of a population model structured by the cells molecular content. Math. Model. Nat. Phenom. 2, 121–152.

Edmunds, J., 1988. LN, Cellular and Molecular Bases of Biological Clocks: Models and Mechanisms for Circadian Timekeeping. Springer, NY, USA.

Eide, J.E., Woolf, M.F., Kang, H., Hurst, W., Camacho, F., et al., 2005. Control of mammalian circadian rhythm by cki_{ε}-regulated proteasome-mediated per2 degradation. Mol. Cell. Biol. 25, 2795–2807.

Feillet, C., et al., 2014. Phase locking and multiple oscillating attractors for the coupled mammalian clock and cell cycle. Proc. Natl. Acad. Sci. 111 (27), 9828–9833.

Filipski, E., King, V., Li, X., Granda, T., Mormont, M., Liu, X., Claustrat, B., Hastings, M., Lévi, F., 2002. Host circadian clock as a control point in tumor progression. J. Natl. Cancer. Inst. 94, 690–697.

Filipski, E., Delaunay, F., King, V., Wu, M.-W., Claustrat, B., Gréchez-Cassiau, A., Guettier, C., Hastings, M., Lévi, F., 2004. Effects of chronic jet lag on tumor progression in mice. Cancer Res. 64, 7879–7885.

Filipski, E., Subramanian, P., Carriére, J., Guettier, C., Barbason, H., Lévi, F., 2009. Circadian disruption accelerates liver carcinogenesis in mice. Mutat. Res. 680, 95–105.

Focan, C., 1995. Circadian rhythms and cancer chemotherapy. Pharmacol. Ther. 67, 1–52.

Focan, C., Lévi, F., Kreutz, F., 1999. Continuous delivery of venous 5-fluorouracil and arterial 5-fluorodeoxyuridine for hepatic metastases from colorectal cancer: feasibility and tolerance in a randomized phase II trial comparing flat versus chronomodulated infusion. Anticancer Drugs 10, 385–392.

Focan, C., Kreutz, F., Focan-Henrard, D., Moeneclaey, N., 2000. Chronotherapy with 5-fluorouracil, folinic acid and carboplatin for metastatic colorectal cancer; an interesting therapeutic index in a phase II trial. Eur. J. Cancer 36, 341–347.

Forger, D.B., Peskin, C.S., 2003. A detailed predictive model of the mammalian circadian clock. Proc. Natl. Acad. Sci. 100 (25), 14806–14811.
Fu, L., Pelicano, H., Liu, J., Huang, P., Lee, C., 2002. The circadian gene Period2 plays an important role in tumor suppression and DNA damage response in vivo. Cell 11, 41–50.
Gérard, C., Goldbeter, A., 2012. Entrainment of the mammalian cell cycle by the circadian clock: modeling two coupled cellular rhythms. PLoS Comput. Biol. 8 (5), e1002516.
Gery, S., Komatsu, N., Baldjyan, L., Yu, A., Koo, D., Koeffler, H., 2006. The circadian gene per1 plays an important role in cell growth and DNA damage control in human cancer cells. Mol. Cell 22, 375–382.
Gonze, D., 2011. Modeling circadian clocks: from equations to oscillations. Cent. Eur. J. Biol. 6, 699–711.
Grèchez-Cassiau, A., Rayet, B., Guillaumond, F., Teboul, M., Delaunay, F., 2008. The circadian clock component BMAL1 is a critical regulator of $p21^{waf1/cip1}$ expression and hepatocyte proliferation. J. Biol. Chem. 283, 4535–4542.
Hrushesky, W., Bjarnason, G., 1993. The application of circadian chronobiology to cancer chemotherapy. Cancer 2666–2686.
Hunt, T., Sassone-Corsi, P., 2007. Riding tandem: circadian clocks and the cell cycle. Cell 129, 461–464.
Johnson, C., 2010. Circadian clocks and cell division. What's the pacemaker? Cell Cycle 9, 3864–3873.
Kubo, T., Ozasa, K., Mikami, K., Wakai, K., Fujino, Y., Watanabe, Y., Miki, T., Nakao, M., Hayashi, K., Suzuki, K., Mori, M., Washio, M., Sakauchi, F., Ito, Y., Yoshimura, T., Tamakoshi, A., 2006. Prospective cohort study of the risk of prostate cancer among rotating-shift workers: findings from the japan collaborative cohort study. Am. J. Epidemiol. 164 (6), 549–555.
Langmesser, S., Tallone, T., Bordon, A., Rusconi, S., Albrecht, U., 2008. Interaction of circadian clock proteins PER2 and CRY with BMAL1 and CLOCK. BMC Mol. Biol. 9, 41–57.
Lee, C., Etchegaray, J., Cagampang, F., Loudon, A., Reppert, S., 2001. Posttranslational mechanisms regulate the mammalian circadian clock. Cell 107, 855–867.
Leloup, J.-C., Goldbeter, A., 2004. Modeling the mammalian circadian clock: sensitivity analysis and multiplicity of oscillatory mechanisms. J. Theor. Biol. 230, 541–562.
Lévi, F., 2000. Therapeutic implications of circadian rhythms in cancer patients. Novartis Found. Symp. 227, 136–142.
Matsuo, T., Yamaguchi, S., Mitsui, S., Emi, A., Shimoda, F., Okamura, H., 2003. Control mechanism of the circadian clock for timing of cell division in vivo. Science 302, 255–259.
Milo, et al., 2010. Bionumbers. Nucl. Acids Res. 38, D750–D753 (BNID 100685).
Mirsky, H., Liu, A., Welsh, D., Kay, S., Doyle, F., 2009. A model of the cell-autonomous mammalian circadian clock. Proc. Natl. Acad. Sci. 106, 11107–11112.
Morgan, D., 1995. Principles of cdk regulation. Nature 374, 131–134.
Murray, D., Beckmann, M., Kitano, H., 2007. Regulation of yeast oscillatory dynamics. Proc. Natl. Acad. Sci. 104, 2241–2246.
Nagoshi, E., Saini, C., Bauer, C., Laroche, T., Naef, F., et al., 2004. Circadian gene expression in individual fibroblasts: cell-autonomous and self-sustained oscillators pass time to daughter cells. Cell 119, 693–705.
Novak, B., Pataki, Z., Ciliberto, A., Tyson, J., 2001. Mathematical model of the cell division cycle of fission yeast. Chaos 11 (1), 277–286.
Oster, H., Yasui, A., van der Horst, G., Albrecht, U., 2002. Disruption of *mCry* 2 restores circadian rhythmicity in *mPer* 2 mutant mice. Genes Dev. 16, 2633–2638.
Pando, B., van Oudenaarden, A., 2010. Coupling cellular oscillators—circadian and cell division cycles in cyanobacteria. Curr. Opin. Genet. Dev. 20, 613–618.
Partch, C., Shields, K., Thompson, C., Selby, C., Sancar, A., 2006. Posttranslational regulation of mammalian circadian clock by chryptochrome and protein phosphatase 5. Proc. Acad. Sci. USA 103, 10467–10472.
Pikovsky, A., Rosenblum, M., Kurths, J., 2001. Synchronization. Cambridge University Press, New York, USA.
Reppert, S., Weaver, D., 2002. Coordination of circadian timing in mammals. Nature 418, 935–941.
Sato, T., Yamada, R., Ukai, H., Baggs, J., Miraglia, L., Kobayashi, T., et al., 2006. Feedback repression is required for mammalian circadian clock function. Nat. Genet. 38, 212–219.
Savvidis, C., Koutsilieris, M., 2012. Circadian rhythm disruption in cancer biology. Mol. Med. 18 (1), 1249–1260.
Shearman, L., Sriram, S., Weaver, D., Maywood, E., Chaves, I., Zheng, B., Kume, K., Lee, C., van der Horst, T., Hastings, M., Reppert, S., 2000. Interacting molecular loops in the mammalian circadian clock. Science 288, 1013–1019.
Tu, B., Kudlicki, A., Rowicka, M., Mcknight, S., 2005. Logic of the yeast metabolic cycle: temporal compartmentalization of cellular processes. Science 310, 1152–1158.
Yang, C., Bernardo, F., Dong, G., Golden, S., van Oudenaarden, A., 2010. Circadian gating of the cell cycle revealed in single cyanobacterial cells. Science 327, 1522–1526.
Yu, W., Nomura, M., Ikeda, M., 2002. Interacting feedback loops within the mammalian clock: BMAL1 is negatively autoregulated and upregulated by CRY1, CRY2, and PER2. Biochem. Biophys. Res. Commun. 290 (3), 933–941.
Zamborszky, J., Csikasz-Nagy, A., Hong, C., 2007. Computational analysis of mammalian cell division gated by a circadian clock: quantized cell cycles and cell size. J. Biol. Rhythms 22, 542–553.

Bibliography

[1] Altrock PM, Liu LL, Michor F (2015) The mathematics of cancer: integrating quantitative models. Nature Reviews Cancer 15(12):730–745

[2] Ananthasubramaniam B, Herzel H (2014) Positive feedback promotes oscillations in negative feedback loops. PLOS ONE 9(8):1–11, DOI 10.1371/journal.pone.0104761

[3] Antle MC, Foley DK, Foley NC, Silver R (2003) Gates and oscillators: a network model of the brain clock. Journal of Biological Rhythms 18(4):339–350

[4] Antle MC, Foley NC, Foley DK, Silver R (2007) Gates and oscillators ii: zeitgebers and the network model of the brain clock. Journal of Biological Rhythms 22(1):14–25

[5] Arner P, Bernard S, Salehpour M, Possnert G, Liebl J, Steier P, Buchholz B, Eriksson M, Arner E, Hauner H, Skurk T, Rydén M, Frayn K, Spalding K (2011) Dynamics of human adipose lipid turnover in health and metabolic disease. Nature 478:110–113

[6] Ashford NA, Bauman P, Brown HS, Clapp RW, Finkel AM, Gee D, Hattis DB, Martuzzi M, Sasco AJ, Sass JB, et al (2015) Cancer risk: Role of environment. Science 347(6223):727–727

[7] Aton SJ, Colwell CS, Harmar AJ, Waschek J, Herzog ED (2005) Vasoactive intestinal polypeptide mediates circadian rhythmicity and synchrony in mammalian clock neurons. Nat Neurosci 8(4):476–483

[8] Battogtokh D, Tyson JJ (2006) Periodic forcing of a mathematical model of the eukaryotic cell cycle. Physical Review E 73(1):011,910

[9] Becker-Weimann S, Wolf J, Herzel H, Kramer A (2004) Modeling feedback loops of the mammalian circadian oscillator. Biophys J 87(5):3023–3034

[10] Bélair J, Mackey MC, Mahaffy JM (1995) Age-structured and two-delay models for erythropoiesis. Math Biosci 128(1):317–346

[11] Bergmann O, Bhardwaj R, Bernard S, Zdunek S, Barnabé-Heider F, Walsh S, Zupicich J, Alkass K, Buchholz B, Druid H, Jovinge S, Frisén J (2009) Evidence for cardiomyocyte renewal in humans. Science 324:98–102

[12] Bergmann O, Liebl J, Bernard S, Alkass K, Yeung M, Steier P, Kutschera W, Johnson L, Landén M, Druid H, Spalding K, Frisén J (2012) The age of olfactory bulb neurons in humans. Neuron 74:634–639

[13] Bergmann O, Zdunek S, Felker A, Salehpour M, Alkass K, Bernard S, Sjostrom S, Szewczykowska M, Jackowska T, dos Remedios C, Malm T, Andr M, Jashari R, Nyengaard J, Possnert G, Jovinge S, Druid H, Fris n J (2015) Dynamics of Cell Generation and Turnover in the Human Heart. Cell 161:1566–1575

[14] Bernard S (2013) How to Build a Multiscale Model in Biology. Acta Biotheoretica 61:291–303

[15] Bernard S (2016) Moving the Boundaries of Granulopoiesis Modelling. Bull Math Biol 78:2358–2363

[16] Bernard S, Crauste F (2015) Optimal linear stability condition for scalar differential equations with distributed delay. Discrete Contin Dynam Systems Ser B 20:1855–1876

[17] Bernard S, Herzel H (2006) Why do cells cycle with a 24 hour period? Genome Info 17:72–79

[18] Bernard S, Bélair J, Mackey M (2001) Sufficient conditions for stability of linear differential equations with distributed delay. Discrete Contin Dynam Systems Ser B 1:233–256

[19] Bernard S, Čajavec B, Pujo-Menjouet L, Mackey M, Herzel H (2006) Modelling transcriptional feedback loops: the role of Gro/TLE1 in Hes1 oscillations. Phil Trans Roy Soc A 364:1155–1170

[20] Bernard S, Gonze D, Čajavec B, Herzel H, Kramer A (2007) Synchronization-induced rhythmicity of circadian oscillators in the suprachiasmatic nucleus. PLOS Comput Biol 3:e68

[21] Bernard S, Frisén J, Spalding K (2010) A mathematical model for the interpretation of nuclear bomb test derived ^{14}C incorporation in biological systems. Nucl Instr Meth B 268:1295–1298

[22] Besse A, Clapp G, Bernard S, Nicolini F, Levy D, Lepoutre T (2017) Stability analysis of a model of interaction between the immune system and cancer cells in chronic myelogenous leukemia. Bull Math Biol *in press*

[23] Burnham KP, Anderson DR (2003) Model selection and multimodel inference: a practical information-theoretic approach. Springer Science & Business Media

[24] Campbell SA, Ncube I (2017) Stability in a scalar differential equation with multiple, distributed time delays. Journal of Mathematical Analysis and Applications 450(2):1104–1122

[25] Chauhan A, Lorenzen S, Herzel H, Bernard S (2011) Regulation of mammalian cell cycle progression in the regenerating liver. J Theor Biol 283:103–112

[26] Clairambault J, Gaubert S, Lepoutre T (2009) Comparison of perron and floquet eigenvalues in age structured cell division cycle models. Mathematical Modelling of Natural Phenomena 4(3):183–209

[27] Clapp GD, Lepoutre T, El Cheikh R, Bernard S, Ruby J, Labussière-Wallet H, Nicolini FE, Levy D (2015) Implication of the autologous immune system in BCR–ABL transcript variations in chronic myelogenous leukemia patients treated with Imatinib. Cancer Research 75(19):4053–4062

[28] El Cheikh R, Bernard S, El Khatib N (2014) Modeling circadian clock-cell cycle interaction effects on cell population growth rates. J Theor Biol 363:318–331

[29] Elser JA, Margulies KB (2012) Hybrid mathematical model of cardiomyocyte turnover in the adult human heart. PloS One 7(12):e51,683

[30] Enright J (1984) Mutual excitation of damped oscillators and self-sustainment of circadian rhythms. Mathematical models of the circadian sleep-wake cycle, Raven Press, New York pp 1–17

[31] Ernst A, Alkass K, Bernard S, Salehpour M, Perl S, Tisdale J, Possnert G, Druid H, Frisén J (2014) Neurogenesis in the striatum of the adult human brain. Cell 156:1072–1083

[32] Friedman SH, Anderson AR, Bortz DM, Fletcher AG, Frieboes HB, Ghaffarizadeh A, Grimes DR, Hawkins-Daarud A, Hoehme S, Juarez EF, et al (2016) Multicellds: a community-developed standard for curating microenvironment-dependent multicellular data. bioRxiv p 090456

[33] Fu L, Pelicano H, Liu J, Huang P, Lee CC (2002) The circadian gene Period2 plays an important role in tumor suppression and DNA damage response in vivo. cell 111(1):41–50

[34] Gonze D, Bernard S, Waltermann C, Kramer A, Herzel H (2005) Spontaneous synchronization of coupled circadian oscillators. Biophys J 89:120–129

[35] Goodwin B (1965) Oscillatory behavior in enzymatic control processes. Advances in enzyme regulation 3:425–438

[36] Hale JK, Huang W (1993) Global geometry of the stable regions for two delay differential equations. Journal of Mathematical analysis and applications 178(2):344–362

[37] Huttner H, Bergmann O, Salehpour M, Rácz A, Tatarishvili J, Lindgren E, Csonka T, Csiba L, Hortobágyi T, Méhes G, Englund E, Solnestam B, Zdunek S, Scharenberg C, Ström L, Støahl P, Sigurgeirsson B, Dahl A, Schwab S, Possnert G, Bernard S, Kokaia Z, Lindvall O, Lundeberg J, Frisén J (2014) The age and genomic integrity of neurons after cortical stroke in humans. Nat Neurosci 17:801–803

[38] Kajstura J, Rota M, Cappetta D, Ogórek B, Arranto C, Bai Y, Ferreira-Martins J, Signore S, Sanada F, Matsuda A, et al (2012) Cardiomyogenesis in the aging and failing human heart. Circulation 126(15):1869–1881, retraction published 2014 Circulation 129: e466

[39] Ko CH, Yamada YR, Welsh DK, Buhr ED, Liu AC, Zhang EE, Ralph MR, Kay SA, Forger DB, Takahashi JS (2010) Emergence of noise-induced oscillations in the central circadian pacemaker. PLoS Biol 8(10):e1000,513

[40] Kress R, Maz'ya V, Kozlov V (1989) Linear integral equations, vol 17. Springer

[41] Kunz H, Achermann P (2003) Simulation of circadian rhythm generation in the suprachiasmatic nucleus with locally coupled self-sustained oscillators. Journal of theoretical biology 224(1):63–78

[42] Kuznetsov VA, Makalkin IA, Taylor MA, Perelson AS (1994) Nonlinear dynamics of immunogenic tumors: parameter estimation and global bifurcation analysis. Bulletin of mathematical biology 56(2):295–321

[43] Leloup JC, Goldbeter A (2003) Toward a detailed computational model for the mammalian circadian clock. Proceedings of the National Academy of Sciences 100(12):7051–7056

[44] Levin I, Kromer B, Hammer S (2013) Atmospheric $\delta 14CO2$ trend in western european background air from 2000 to 2012. Tellus B: Chemical and Physical Meteorology 65(1):20,092, DOI 10.3402/tellusb.v65i0.20092

[45] Liu AC, Welsh DK, Ko CH, Tran HG, Zhang EE, Priest AA, Buhr ED, Singer O, Meeker K, Verma IM, et al (2007) Intercellular coupling confers robustness against mutations in the scn circadian clock network. Cell 129(3):605–616

[46] Mahaffy JM, Joiner KM, Zak PJ (1995) A geometric analysis of stability regions for a linear differential equation with two delays. International Journal of Bifurcation and Chaos 5(03):779–796

[47] Mahon FX, Réa D, Guilhot J, Guilhot F, Huguet F, Nicolini F, Legros L, Charbonnier A, Guerci A, Varet B, et al (2010) Discontinuation of imatinib in patients with chronic myeloid leukaemia who have maintained complete molecular remission for at least 2 years: the prospective, multicentre stop imatinib (stim) trial. The lancet oncology 11(11):1029–1035

[48] Matsuo T, Yamaguchi S, Mitsui S, Emi A, Shimoda F, Okamura H (2003) Control mechanism of the circadian clock for timing of cell division in vivo. Science 302(5643):255–259

[49] Maywood ES, Reddy AB, Wong GK, O'Neill JS, O'Brien JA, McMahon DG, Harmar AJ, Okamura H, Hastings MH (2006) Synchronization and maintenance of timekeeping in suprachiasmatic circadian clock cells by neuropeptidergic signaling. Curr Biol 16(6):599–605

[50] Monk N (2003) Oscillatory expression of Hes1, p53, and NF-κB driven by transcriptional time delays. Curr Biol 13(16):1409–1413

[51] Nagoshi E, Saini C, Bauer C, Laroche T, Naef F, Schibler U (2004) Circadian gene expression in individual fibroblasts: cell-autonomous and self-sustained oscillators pass time to daughter cells. Cell 119(5):693–705

[52] Ohta H, Yamazaki S, McMahon DG (2005) Constant light desynchronizes mammalian clock neurons. Nat Neurosci 8(3):267–269

[53] Pett JP, Korenčič A, Wesener F, Kramer A, Herzel H (2016) Feedback loops of the mammalian circadian clock constitute repressilator. PLOS Computational Biology 12(12):e1005,266

[54] Reimer PJ, Baillie MG, Bard E, Bayliss A, Beck JW, Bertrand CJ, Blackwell PG, Buck CE, Burr GS, Cutler KB, et al (2004) IntCal04 terrestrial radiocarbon age calibration, 0-26 cal kyr BP. Radiocarbon

[55] Ruan S, Wei J (2003) On the zeros of transcendental functions with applications to stability of delay differential equations with two delays. Dynamics of Continuous Discrete and Impulsive Systems Series A 10:863–874

[56] Ruoff P, Vinsjevik M, Monnerjahn C, Rensing L (2001) The goodwin model: simulating the effect of light pulses on the circadian sporulation rhythm of neurospora crassa. J Theor Biol 209(1):29–42

[57] Spalding K, Arner E, Westermark P, Bernard S, Buchholz B, Bergmann O, Blomqvist L, Hoffstedt J, Näslund E, Britton T, Concha H, Hassan M, Rydén M, Frisén J, Arner P (2008) Dynamics of fat cell turnover in humans. Nature 453:783–787

[58] Spalding K, Bergmann O, Alkass K, Bernard S, Salehpour M, Huttner H, Boström E, Westerlund I, Vial C, Buchholz B, Possnert G, Mash D, Druid H, Frisén J (2013) Dynamics of hippocampal neurogenesis in adult humans. Cell 153:1219–1227

[59] Spalding KL, Bhardwaj RD, Buchholz BA, Druid H, Frisén J (2005) Retrospective birth dating of cells in humans. Cell 122(1):133–143

[60] To TL, Henson MA, Herzog ED, Doyle FJ (2007) A molecular model for intercellular synchronization in the mammalian circadian clock. Biophysical journal 92(11):3792–3803

[61] Tomasetti C, Vogelstein B (2015) Variation in cancer risk among tissues can be explained by the number of stem cell divisions. Science 347(6217):78–81

[62] Tomasetti C, Li L, Vogelstein B (2017) Stem cell divisions, somatic mutations, cancer etiology, and cancer prevention. Science 355(6331):1330–1334

[63] Tsai TYC, Choi YS, Ma W, Pomerening JR, Tang C, Ferrell JE (2008) Robust, tunable biological oscillations from interlinked positive and negative feedback loops. Science 321(5885):126–129

[64] Webb AB, Angelo N, Huettner JE, Herzog ED (2009) Intrinsic, nondeterministic circadian rhythm generation in identified mammalian neurons. Proceedings of the National Academy of Sciences 106(38):16,493–16,498

[65] Weiss JN (1997) The hill equation revisited: uses and misuses. The FASEB Journal 11(11):835–841

[66] Welsh DK, Logothetis DE, Meister M, Reppert SM (1995) Individual neurons dissociated from rat suprachiasmatic nucleus express independently phased circadian firing rhythms. Neuron 14(4):697–706

[67] Wild C, Brennan P, Plummer M, Bray F, Straif K, Zavadil J (2015) Cancer risk: role of chance overstated. Science 347(6223):728–728

[68] Wu S, Powers S, Zhu W, Hannun YA (2016) Substantial contribution of extrinsic risk factors to cancer development. Nature 529(7584):43–47

[69] Yamaguchi S, Isejima H, Matsuo T, Okura R, Yagita K, Kobayashi M, Okamura H (2003) Synchronization of cellular clocks in the suprachiasmatic nucleus. Science 302(5649):1408–1412

[70] Yeung M, Zdunek S, Bergmann O, Bernard S, Salehpour M, Alkass K, , Frisén J (2014) Dynamics of Oligodendrocyte Generation and Myelination in the Human Brain. Cell 159:766–774

Index

14C, 36

Akaike Information Criterion, 40
Asymptotic stability, 24
Atmospheric 14C, 36

Birth rate, 36
Birth-and-death model, 36
Bistability, 45

Cardiomyocyte renewal, 40
Cell division, 44
Characteristic equation, 20, 24–26
Chronological age, 37
Circadian clock, 28
Connectivity matrix, 30
Cooperativity, 25
Coupling strength, 30
Coupling, diffusive, 30
Coupling, direct, 30
Cyclin B, 45

Death rate, 36
Delay differential equations, 20
Dirac mass, 21, 38
Discrete delay, 21
Distributed time delay, 20

G$\langle n \rangle$, 23
G$\langle n \rangle$M, 23
Gamma distribution, 20, 24
Goodwin model, 22, 25

Heart, 40
Hill coefficient, 22
Hill function, 22
Homeostasis, 45
Hopf bifurcation, 29

Least-square, 39
Least-square problem, 39
Linear chain trick, 23

Mean field, 33
Mixed feedback, 26
Multiscale, 44

Negative feedback, 23
Non-identical oscillators, 30

Partial hepatectomy, PH, 45
Phase synchronization, 30
Positive feedback, 25

Quasi-periodic solution, 30

Relaxation oscillator, 28
Renewal equation, 37

Scenario, 40
SCN, suprachiasmatic nucleus, 28
Simuscale, 46
Sinusoidal oscillator, 30
Stability chart, 21
Stability switch, 26
Structured model, 36

Tangled monster, 21
Torus, 30
Transcritical bifurcation, 45
Transport equation, 37
Tumor suppressor, 45
Turnover rate, 40

van der Pol oscillator, 28
Volterra equation, 38

Weak solution, 38
Wee1, 44

Approches équations différentielles structurées et multiéchelles pour la dynamique de populations cellulaires chez l'humain

Résumé: Tout d'abord, nous étudions la stabilité d'une boucle de rétroaction négative générique avec retard, qui est sensible aux instabilités et aux oscillations. La boucle de rétroaction négative peut décrire aussi bien des oscillateurs génétiques que la régulation négative d'une population de cellules. Comprendre ce qui affecte la stabilité (ou l'instabilité) est donc pertinent pour les deux échelles de modélisation (intracellulaire et population de cellule) d'intérêt ici. Ensuite, nous montrons comment l'interaction (communication cellule-cellule par un facteur diffusible) peut transformer une collection d'oscillateurs mous en une horloge robuste et résistante au bruit. Des données expérimentales soutiennent cette interprétation. Par la suite, nous évaluons le potentiel de renouvellement des tissus humains à long-terme. Nous discutons comment estimer l'étendue du renouvellement cellulaire dans le muscle cardiaque. Nous avons trouvé que le cœur humain avait une capacité limitée de se regénérer. Des dizaines d'essais cliniques basés sur des traitement d'accidents cardiaques par cellules souches sont en cours; nos résultats montrent que ces thérapies sont sûrement sur-estimées. Nous étudions aussi un modèle récent pour l'interaction tumeur-immune, et le rôle du système immunitaire dans la rémission à long terme de la leucémie myéloïde chronique. Enfin, nous discutons des approches intégratives et multiéchelles (moléculaire/population). Dans une première étude, nous utilisons un modèle moléculaire du cycle cellulaire pour explorer comment la division cellulaire est modulée par l'horloge circadienne. Dans une deuxième étude, nous caractérisons les effets de la dérégulation de l'horloge circadienne sur la prolifération cellulaire.

Mots clés: Modèles de naissance-mort; Horloge circadienne; Synchronisation; Équations différentielles à retard; Équations de transport; datation 14C; renouvellement cellulaire

Structured differential equations and multiscale approaches for human cell population dynamics

Abstract: First, we study the stability of a generic negative feedback loop with a delay, which is known to be prone to instabilities and oscillations. The negative feedback loop can describe equally genetic oscillators and nonlinear feedback regulation of cell population numbers. Understanding what affects stability (or instability) is thus relevant for the two biological scales (intracellular and cell population) of interest here. Then, we show how interaction (cell-cell communication though a diffusible factor) can transform a collection of sloppy oscillators into a robust, noise-resistant clock. There is evidence that the clock neurons follow this design principle. We then look at the long-term renewal capacity of tissues in human. We discuss how we can estimate the extent of cell renewal in the human hippocampus or the heart ventricle. The human heart has a limited capacity to regenerate after a stroke or during chronic heart failure, and tens of clinical trials involving stem cells injection in the heart are being conducted without clear understanding of fate of these cells after transplant. We also discuss a recent model for the tumor-immune interaction, and the role of the immune system in long-term remission in chronic myelogenous leukemia. Finally, we discuss integrative approaches for multiscale (molecular/population) models. In a first study, we looked at how cell division during liver regeneration is gated by the circadian clock based on a molecular model of the cell cycle. In a second study, we looked at the effect of a disruption of the circadian clock of cell proliferation.

Keywords: Birth-and-death models; Circadian clock; Synchronization; Delay differential equations; Transport equations; 14C dating; cell renewal

Image en couverture : Solutions quasi-périodiques d'oscillateurs couplés. Crédit image : S Bernard.

ED 512 INFOMATHS Ecole doctorale

UNIVERSITÉ DE LYON